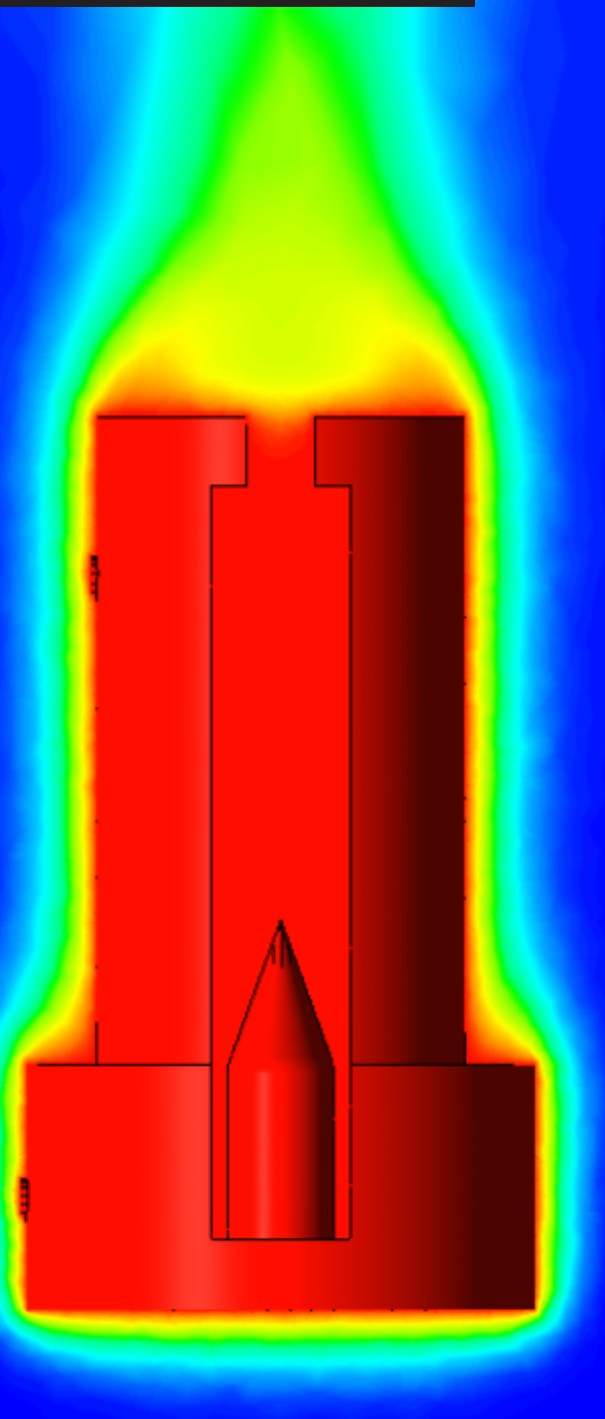


Development of a high-temperature Solar Thermal Propulsion engine

Master thesis

Aeilt-Jan Takken

Delft University of Technology



Development of a high-temperature Solar Thermal Propulsion engine

Master thesis

by

**Aeilt-Jan Takken
4212118**

to obtain the degree of Master of Science
at the Delft University of Technology,
to be defended publicly on Tuesday January 19, 2021 at 2:00 PM.

Student number: 4212118
Affiliation: Chair of Space Systems Engineering, Faculty of Aerospace Engineering
Supervisor: Ir. B.T.C. Zandbergen
Thesis committee: Ir. B.T.C. Zandbergen, TU Delft
Prof.dr. E.K.A. Gill, TU Delft
Dr.ir. B.C. Root, TU Delft

An electronic version of this thesis is available at <http://repository.tudelft.nl/>.



Abstract

Miniaturization in spacecraft is an ongoing process in which the launched satellites become smaller and smaller. This trend introduces issues, such as the choice for a reliable and efficient propulsion subsystem. The implementation of engines would enable the spacecraft to perform maneuvers such as orbit changes, drag compensation and attitude control. [Solar Thermal Propulsion \(STP\)](#) has been identified as a promising candidate, due to its theoretical specific impulse being well above that of the best chemical thrusters when hydrogen is the propellant of choice. The concept has never been flown in space but would benefit from ground demonstrations proving that the potential can be realized.

This work will focus on demonstrating the [STP](#) performance. The goal was set to reach a [Sea Level \(SL\)](#) specific impulse of 90.0 s at a continuous mass flow of 300 mg s^{-1} and input power of 250 W. During the project, a demonstration thruster named Solar Thermal Thruster 2 was designed. The resulting engine consisted of a copper heat exchanger and nozzle with a high-powered laser as the irradiation source of choice. Concurrently, a Preliminary Design Tool was developed to assess the performance of [STP](#) engines. Verification and validation was done by comparing the tool outputs to other theoretical and experimental results. Verification was completed, but for validation STT2 experimental results were required.

Preliminary test results of STT2 showed that the motor had some shortcomings, due to concessions made. Erroneously, its heat exchanger had been built with a reduced number of channels, rendering the thruster unavailable for testing. Next to that, the engine suffered from leakages. For further validation of the tool, [Computational Fluid Dynamics \(CFD\)](#) simulations were performed. The thermal part of the tool was validated, but the pressure loss results deviated too much. As such, further experiments are required in this area. In the end, an updated design (STT3) was made of the thruster. The number of channels in the heat exchanger was increased and its mass and area was reduced. It proved to have an [SL](#) specific impulse of 84.9 s, almost meeting the goal set for the thesis. It is recommended that the engine is built and tested at [Delft University of Technology \(DUT\)](#) in order to complete validation of the tool and demonstrate the feasibility of [STP](#).

Acknowledgements

The thesis project that I am presenting to you is the final chapter of my years as an Aerospace Engineering student at TU Delft. Although it took longer than expected to finish this work, I am nonetheless proud to show you the results of countless hours of research, debate and considerations. I am happy to count myself among the alumni of this great university.

Via this way, I would like to thank my supervisor Barry Zandbergen for his unrelenting support in this challenging part of my master's degree. Through his guidance, I was able to conclude the project in a satisfying way with a lot of new insights in the area of experiments and practical research. The weekly meetings were never a bore and always provided me with new material on how to tackle the issues I encountered on the way.

I want to express my sincerest gratitude to my parents who have always been at my side. Their support helped me throughout my whole student life and continues to do so. Next to that, there is an extensive list of people that contributed in some way, both technical and non-technical. There are countless other staff members at the university that helped me find all the small equipment and the facilities that I desperately needed. There are the fellow students in the master room with whom I had many coffee breaks that unfortunately had to continue online at a later stage. There are my friends in and outside Delft, who served as welcome distraction. There are my siblings who always helped to keep me sharp-witted when I was in their presence. There is Robert, who always offered a listening ear on the walks we suddenly made. And finally, there is Jade, who always provided me with emotional support and kept me sane throughout this endeavour.

It has been a pleasure.

*Aeilt-Jan Takken
Delft, January 2021*

Contents

Abstract	iii
Acknowledgements	v
List of Figures	xi
List of Tables	xiv
List of Acronyms	xv
List of Symbols	xvi
1 Introduction	1
2 Research framework	4
2.1 Research background	4
2.1.1 Principles of solar thermal propulsion	4
2.1.2 Summary of research into solar thermal propulsion	5
2.2 Solar Thermal Thruster 1 background	5
2.2.1 Design and manufacturing	5
2.2.2 Experimental results	6
2.2.3 Results discussion	8
2.2.4 Main findings	9
2.3 Research goal	9
2.4 Requirements and constraints	10
2.4.1 Functional requirements	10
2.4.2 System requirements	11
2.4.3 Constraints	11
3 Preliminary Design Tool overview	13
3.1 Requirements	14
3.2 Assumptions	15
3.3 Overview	16
3.4 Verification	17
3.4.1 Verification via thermal model comparison	17
3.4.2 Verification via changing input parameters	19
3.4.3 Verification for NIST relations	20
3.5 Validation	21
3.6 Conclusions & recommendations	21
4 Preliminary Design Tool theory	25
4.1 Heat transfer overview	25
4.2 Convection	26
4.2.1 Propellant convection	26
4.2.2 Inner cavity convection	33
4.2.3 Outer wall convection	35
4.3 Radiation	35

4.3.1 Inner cavity radiation	36
4.3.2 Outer wall radiation	38
4.3.3 Area	38
4.4 Conduction	39
4.5 Pressure loss	40
4.6 Nozzle performance	41
5 Thruster design and hardware	43
5.1 Thruster design	43
5.1.1 Receiver-Absorber Cavity design	43
5.1.2 Nozzle design	49
5.2 Performance	50
5.3 Hardware	50
5.3.1 Receiver-Absorber Cavity hardware	50
5.3.2 Connection pieces hardware	51
5.3.3 Concessions for manufacturing	52
5.4 Cost	54
5.5 Conclusions and recommendations	55
6 Experiment preparation	56
6.1 Planned experiments	56
6.2 Locations	57
6.2.1 Cleanroom	57
6.2.2 Welding facility	57
6.3 Equipment hardware	58
6.3.1 Thermocouples	58
6.3.2 Pressure sensors	59
6.3.3 Mass flow sensor	60
6.3.4 Propellant supply	61
6.4 Test stand hardware	61
6.4.1 Test bench AE-TB-1.1	62
6.4.2 Test bench AE-TB-50m	62
6.4.3 Test bench conclusions & recommendations	70
6.5 Preliminary experiment results	71
6.5.1 Experiment stop	71
6.5.2 Plan for continuation	72
7 Computational Fluid Dynamics modelling	73
7.1 Computational Fluid Dynamics program choice	74
7.2 Quantification of losses to ambient	74
7.2.1 Geometry	74
7.2.2 Mesh	78
7.2.3 Setup	78
7.2.4 Post-processing	82
7.3 Case 1: Solar Thermal Thruster 1, no mass flow and no insulation	85
7.4 Case 2: Solar Thermal Thruster 1, no mass flow and insulation	86
7.5 Case 3: Solar Thermal Thruster 1, mass flow and no insulation	89
7.6 Case 4: Solar Thermal Thruster 2, mass flow and no insulation	93
7.7 Conclusions & recommendations	94
8 Final solar thermal thruster design	96
8.1 Recommendations from previous chapters	96
8.2 Solar Thermal Thruster 3 design	97
8.2.1 Heat exchanger dimensions	97
8.2.2 Channel shape and dimensions	97
8.2.3 Other changes	99
8.2.4 Results	99

8.3 Solar Thermal Thruster 3 performance	99
8.4 Conclusions	101
9 Conclusions & recommendations	103
9.1 Conclusions	103
9.2 Recommendations	104
Bibliography	105
A Technical drawings Solar Thermal Thruster 2	110
B Technical drawings Solar Thermal Thruster 3	119
C Experiment hardware	124
C.1 Futek LRF400 (L2338) data sheet	125
C.2 Futek LSB200 data sheet	126
C.3 RS Pro data sheet	127
C.4 Pressure sensor data sheets	128
C.5 National Instruments USB-6008 data sheet	130
C.6 Scaime CPJ Rail data sheet	132
C.7 Mettler Toledo AG245 data sheet	133
C.8 Zwaluw Fire Sealant 1200 °C data sheet	135
C.9 Saffil M-Fil data sheet	137
D PDT tabular results	139

List of Figures

1.1	Spacecraft launches in the period 2012-2019, split by mass [1].	1
1.2	Propulsion concepts and their characteristics [2].	3
2.1	Main components of an STP thruster (see the second footnote on the previous page).	5
3.1	Specific impulse and nozzle diameter as a function of the expansion ratio.	16
3.2	PDT flowchart, showing its major elements and inputs and outputs.	23
3.3	Case 1: experimental (in red) and theoretical Matlab (in black) Receiver-Absorber Cavity (RAC) temperatures by Leenders [3].	24
3.4	Case 1: PDT RAC temperatures by Takken.	24
3.5	Case 2: experimental (in black) and theoretical Matlab (in red) RAC temperatures by Leenders [3].	24
3.6	Case 2: theoretical Python RAC temperatures by Takken.	24
3.7	Case 3: experimental (in red) and theoretical Matlab (in black) RAC temperatures by Leenders [3]. The axes labels are time (in min) for the horizontal axis and RAC temperature (in K) for the vertical axis. Note that Leenders' experimental and theoretical values do not match well.	24
3.8	Case 3: theoretical Python temperatures by Takken. In blue is the RAC temperature, in orange is the outlet propellant temperature.	24
4.1	Nusselt number versus Reynolds number, for various Prandtl numbers and straight channels. L/D is equal to 0.01.	31
4.2	Nusselt number versus Reynolds number, for various L/D and straight channels. Prandtl number is equal to 0.7.	32
4.3	Nusselt number versus Reynolds number, for various Prandtl numbers and spiral channels. D/Dc is equal to 0.05.	32
4.4	Nusselt number versus Reynolds number, for various D/Dc and spiral channels. Prandtl number is equal to 0.7.	33
4.5	Cone with surfaces 1 and 2. Surface 3, the aperture, is not shown.	37
4.6	Cylinder with surfaces 1 and 2. Surface 3, the bottom wall is not indicated.	37
5.1	Options for cavity heat exchangers [4].	45
5.2	Exploded view of the STT2 heat exchanger.	49
5.3	Disassembled STT2.	52
5.4	Assembled STT2.	52
5.5	STT2 with both machined parts.	54
6.1	Cleanroom at Faculty of Aerospace Engineering (AE).	57
6.2	Thermocouples RS Pro 787-7835. In the background, the corresponding NI DAQ device is shown.	58
6.3	Pressure sensors 3300B16B0A01B000RS and DRTR-AL-20MA-R16B.	59
6.4	Coiled tube to allow the fluid to cool down for the pressure sensor.	60
6.5	PCB connected to one of the Brooks mass flow sensors.	61
6.6	Brooks 5851S mass flow sensor.	62
6.7	Thrust bench TB-1.1 [5].	63
6.8	Thrust bench TB-50m, by Janssens [6].	64

6.9 Thrust bench TB-50m, by Krusharev [7]. The LRF400 sensor is clearly shown in the top right corner.	64
6.10 Thrust bench TB-50m, by Takken. Again, the LRF400 sensor is shown at the bottom.	64
6.11 Connection of the rotating beam to the sensor.	64
6.12 The analog amplifier Scaime CPJ Rail. It has three connections: the right to the power grid (230 V), the middle towards the Data Acquisition (DAQ) device and the left to the RS232 cable of the thrust sensor.	65
6.13 Measuring the weights with the electronic scale Mettler Toledo.	66
6.14 Measuring the sensor voltage output with the use of the weights.	66
6.15 Weight on sensor versus voltage.	67
6.16 Test 1: F_{EM} versus time.	68
6.17 Test 1: averaged F_{EM} over steps of 1 A.	69
6.18 Test 2: F_{EM} versus time.	70
6.19 Test 2: averaged F_{EM} over steps of 0.5 [A].	71
7.1 Solid domain of Ansys physical model of Solar Thermal Thruster 1 (STT1).	75
7.2 Cross-section of Ansys physical model of STT1. Note the smaller hole at the exit, which is on the right bottom of the picture. Furthermore, both inner walls (cone and circular) can be observed.	75
7.3 Fluid domain of Ansys physical model of STT1.	76
7.4 Air domain containing the RAC and fluid domain.	77
7.5 Cross-section of the meshed ambient, RAC and fluid domain.	79
7.6 Closer cross-section of the meshed RAC and fluid domain. Note the two inner walls: the cone inner wall and the small circular inner wall.	80
7.7 Scaled residuals of the simulation to determine convection losses for a case without insulation at an airspeed of 0.001 m s^{-1} . Note the very small oscillation in the energy equation.	82
7.8 Side view of the heated air domain. Note how the upper part of the air in the cavity has a higher temperature than the lower part, due to buoyancy (gravity is pointed down, in the negative y-direction). Airspeed is 0.001 m s^{-1} .	83
7.9 Front view of the heated fluid domain. Again, a small higher temperature pocket is seen at the top of the cavity, in the positive y-direction. Airspeed is 0.001 m s^{-1} .	83
7.10 Area-weighted average temperatures for inner cone, inner circular and outer walls. Necessary to determine the convection losses for an RAC without insulation. Airspeed is 0.001 m s^{-1} .	84
7.11 Convective heat transfer coefficients for inner cone, inner circular and outer walls, for a case without insulation. Airspeed is 0.001 m s^{-1} .	84
7.12 Case 1: area-weighted average temperatures for inner and outer walls. Note the overlaying Python wall temperature.	85
7.13 Area-weighted average temperatures for inner and outer walls, with insulation. Airspeed is 0.001 m s^{-1} .	87
7.14 Area-weighted average convective heat transfer coefficients for inner and outer walls, with insulation. Airspeed is 0.001 m s^{-1} .	87
7.15 Side view of the heated air domain. Note how the upper part of the cavity has a higher temperature than the lower part, due to buoyancy (gravity is pointing down).	89
7.16 Side view of the heated RAC and insulation domains.	89
7.17 Case 3, turbulent subcase. Temperature contour of the fluid domain in side view.	92
7.18 Case 3, turbulent subcase. Temperature along both the upper and lower channel, turbulent subcase. Note that the x-axis, which is in the positive Z-direction, is reversed.	93
7.19 Case 4: cross-section of Solar Thermal Thruster 2 (STT2) showing the temperature in RAC and propellant in laminar flow.	95
8.1 View of STT2.	99
8.2 View of STT3.	99
8.3 Exploded view of the STT3 heat exchanger.	100
A.1 Drawing of STT2 inner cylinder.	111

A.2 Drawing of STT2 outer cylinder.	112
A.3 Drawing of STT2 cap.	113
A.4 Drawing of STT2 spike.	114
A.5 Drawing of STT2 inlet connection piece.	115
A.6 Drawing of STT2 outlet connection piece.	116
A.7 Drawing of STT2 Macor connection piece.	117
A.8 Drawing of the STT2 copper nozzle, from Leenders [3].	118
B.1 Drawing of STT3 inner cylinder.	120
B.2 Drawing of STT3 outer cylinder.	121
B.3 Drawing of STT3 cap.	122
B.4 Drawing of STT3 nozzle.	123

List of Tables

2.1	STT1 measurements from Leenders' paper [8].	7
2.2	STT1 RAC efficiency, enthalpy, propellant and input power, from Leenders' paper [8].	8
2.3	Functional requirements for STT2.	11
2.4	System requirements for STT2.	11
2.5	Constraints for STT2.	12
3.1	Preliminary Design Tool requirements.	14
3.2	Preliminary Design Tool assumptions.	15
3.3	PDT case 1 inputs.	18
3.4	PDT case 2 inputs. Changes relative to Table 3.3.	18
3.5	PDT case 3 mass flow inputs.	19
3.6	Case 3 inputs. Changes relative to Table 3.4.	19
5.1	Main characteristics of Leenders' copper nozzle.	50
5.2	PDT inputs for STT2.	51
5.3	PDT thermal outputs for STT2.	52
5.6	Concessions and their consequences for the manufacturing of STT2.	52
5.4	Component sizes (in mm)	53
5.5	Component mass (in kg)	53
6.1	Sensor voltage output versus mass.	66
7.1	STT1 sizes by Ansys DesignModeler.	75
7.2	Convective heat transfer coefficients per airspeed and emissivities. Results of three simulations with the air domain surrounding the RAC domain.	83
7.3	Inputs and outputs for Ansys case 1.	86
7.4	Convective heat transfer coefficients, view factors and resulting emissivities for case 2.	88
7.5	Averaged wall temperatures and heat flows for case 4.	91
7.6	Averaged propellant temperatures and Nusselt numbers for each region, case 4.	91
7.7	Nusselt number calculations for channel flow, at a Reynolds number of 4550.	92
7.8	Averaged convective heat transfer coefficients, view factors and emissivities for each surface, case 4.	93
8.1	Comparison between channel shapes in terms of heat transfer [9].	98
8.2	Comparison between channel shapes in terms of pressure loss [9].	98
8.3	PDT inputs for STT3.	101
8.4	PDT thermal outputs for STT3.	102
8.5	Properties and results for all three engines.	102
D.1	PDT case 1 RAC temperatures as a function of time.	140
D.2	PDT case 2 RAC temperatures as a function of time.	141
D.3	PDT case 3 RAC temperatures and propellant temperatures as a function of time.	142

List of Acronyms

3mE	Faculty of Mechanical, Maritime and Materials Engineering
AE	Faculty of Aerospace Engineering
AFRPL	Air Force Rocket Propulsion Laboratory
CAD	Computer-Aided Design
CFD	Computational Fluid Dynamics
CNC	Computer Numerical Control
COTS	Commercial Off-The-Shelf
DAQ	Data Acquisition
DEMO	Dienst Elektronische en Mechanische Ontwikkeling
DUT	Delft University of Technology
ECTS	European Credit Transfer and Accumulation System
GUI	Graphical User Interface
IRT	Ideal Rocket Theory
LabVIEW	Laboratory Virtual Instrument Engineering Workbench
MEMS	Microelectromechanical Systems
MLI	Multi-Layer Insulation
MSE	Materials Science and Engineering department
NI	National Instruments
NIST	National Institute of Standards and Technology
NS	Navier-Stokes (equations)
PCB	Printed Circuit Board
PDT	Preliminary Design Tool
RAC	Receiver-Absorber Cavity
RANS	Reynolds-averaged Navier-Stokes (equations)
S2S	Surface-to-Surface
SL	Sea Level
SSE	Space Systems Engineering
STP	Solar Thermal Propulsion
STT1	Solar Thermal Thruster 1
STT2	Solar Thermal Thruster 2
STT3	Solar Thermal Thruster 3
TRL	Technology Readiness Level
UHF	Uniform Heat Flux
UWT	Uniform Wall Temperature
VTDC	Variable-Turn Density Coil

List of Symbols

Symbol	Description	Unit
A_{cs}	Channel cross-sectional area	m^2
A_e	Nozzle exit area	m^2
A_t	Nozzle throat area	m^2
A	Area	m^2
C_d	Discharge coefficient	—
C_μ	Turbulence model constant	—
D_{ap}	Cavity aperture diameter	m
D_{cav}	Cavity average diameter	m
D_c	Spiral diameter	m
D_h	Hydraulic diameter	m
D	Cavity (base) diameter	m
F	View factor	—
F	Thrust	N
I_{sp}	Specific impulse	s
I	Turbulence intensity	—
L_{ch}	Channel length	m
L_s	Characteristic length	m
L	Cavity length	m
MM	Molar mass	kg mol^{-1}
M	Mass	kg
Nu	Nusselt number	—
Pr	Prandtl number	—
Q_{cond}	Conduction heat transfer	W
$Q_{conv,T}$	Convective heat transfer per Kelvin	W K^{-1}
Q_{conv}	Convective heat transfer	W
Q_{loss}	Heat losses	W
Q_{rad}	Radiation heat transfer	W
Q_{res}	Resultant heat power	W
R_A	Universal gas constant	$\text{J mol}^{-1} \text{K}^{-1}$
Re	Reynolds number	—
R	Specific gas constant	$\text{J kg}^{-1} \text{K}^{-1}$
S	Wetted perimeter	m
T	Temperature	K
U_L	Limiting velocity	m s^{-1}
U_{eq}	Equivalent velocity	m s^{-1}
U_e	Exhaust velocity	m s^{-1}
C_{RAC}	RAC heat capacity	$\text{J kg}^{-1} \text{K}^{-1}$
C_p	Specific heat at constant pressure	$\text{J kg}^{-1} \text{K}^{-1}$
f_{DB}	Darcy-Weisbach friction factor	—
g	Gravitational acceleration	m s^{-2}
h	Convective heat transfer coefficient	$\text{W m}^{-2} \text{K}^{-1}$
k	Turbulent energy	$\text{m}^2 \text{s}^{-2}$
k	Thermal conductivity	$\text{W m}^{-1} \text{K}^{-1}$
l	Turbulence length	m
\dot{m}	Mass flow	kg s^{-1}

Symbol	Description	Unit
n	Dittus-Boelter equation coefficient	—
n	Sample size	—
p	pitch	m
p	Pressure	Pa
q	Heat flux	W m ⁻²
r	Radius	m
t _{step}	Time step	s
v	Velocity	m s ⁻¹
ΔH	Change in enthalpy	J kg ⁻¹
ΔT	Change in temperature	K
ΔV	Change in velocity	m s ⁻¹
Γ	Vandenkerckhove function	—
α	Absorptivity	—
α	Thermal diffusivity	m ² s ⁻¹
β	Thermal expansion	K ⁻¹
ε	Emissivity	—
η	Efficiency	—
γ	Specific heat ratio	—
μ	Dynamic viscosity	Pas
ν	Kinematic viscosity	m ² s ⁻¹
ω	Specific turbulent dissipation rate	s ⁻¹
ϕ	Cavity angle	rad
ρ	Density	kg m ⁻³
σ	Standard deviation	—
σ	Stefan-Boltzmann constant	W m ⁻² K ⁻⁴
ξ _F	Nozzle quality correction factor	—

1

Introduction

Space exploration has been dominated by large spacecraft after the launch of the first satellite in 1957, the Sputnik. However, from the late '90s onwards the trend has been increasingly turned towards launching small satellites, also called smallsats [10–13]. This shift is mostly explained by the low cost and development time associated with the smaller spacecraft, the availability of [Commercial Off-The-Shelf \(COTS\)](#) technologies and the development of [Microelectromechanical Systems \(MEMS\)](#)-based components [14, 15]. Figure 1.1 illustrates the miniaturization, where the smaller satellites with a maximum mass of 600 kg make up the bulk of the launches [1]. The smallsats come in many forms, of which the CubeSat as nanosatellite (1-10 kg) and its smaller brother the PocketQube as picosatellite (0.1-1 kg) are prime examples [16]. CubeSats consist of one or multiple $10 \times 10 \times 10 \text{ cm}^3$ cubes and were first envisioned as a low-cost option to perform scientific and technological studies, but are now even considered for use on more sophisticated (commercial) missions [17, 18].

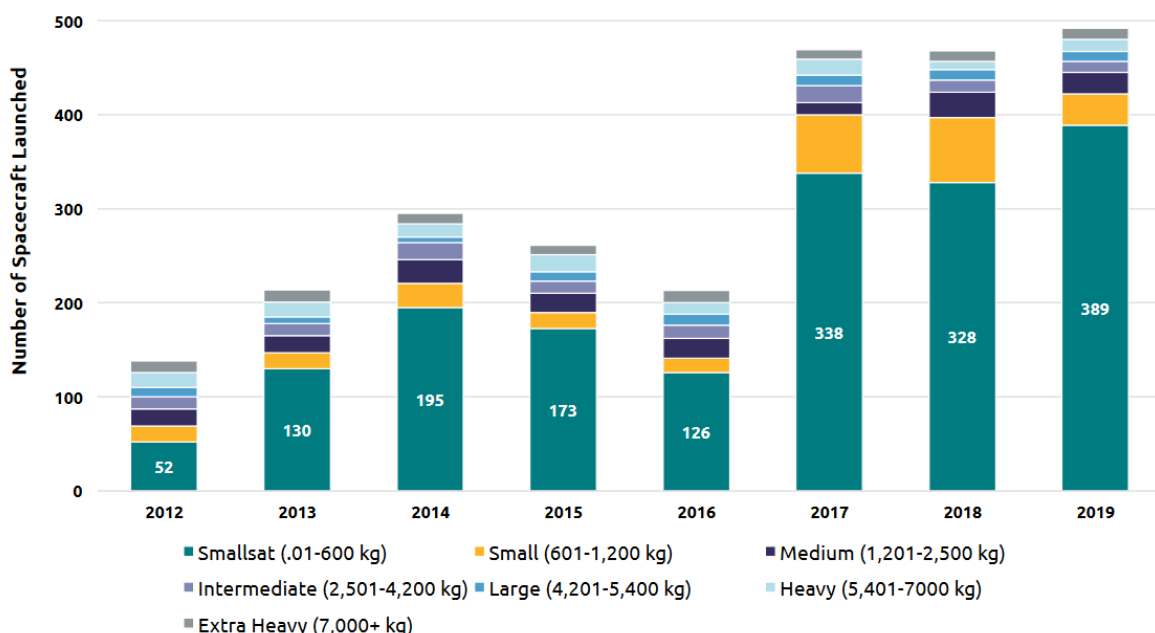


Figure 1.1: Spacecraft launches in the period 2012-2019, split by mass [1].

The shift of the spacecraft mass towards miniaturization is one that is accompanied by challenges. Not all smallsats are deployed on their optimal orbits due to the low number of dedicated launches [1]

and, not unlike other satellite classes, require propulsion, e.g. for orbit changes, drag compensation, attitude control and station-keeping [12]. A dedicated micropropulsion subsystem would thus benefit the mission greatly [19, 20]. A promising candidate for creating thrust on smaller satellites is the concept of solar thermal propulsion [21]. During solar thermal thrusting, a monopropellant is heated by solar irradiation after which it is ejected to create thrust [22]. For the heating, large concentrator systems consisting of mirrors and lenses are used. Then, the concentrated beam is led into the RAC or heat exchanger. In the cavity, the thermal energy can be stored or directly used to increase the propellant's enthalpy. Finally, via a nozzle, the heated propellant is expelled.

STP potentially has a higher specific impulse than the conventional monopropellant and bi-propellant thrusters. The latter are known to have a specific impulse around 150-320 s, while STP could reach up to 860 s according to Leverone et al. [12]. This is since the most promising monopropellant for solar thermal thrusting, hydrogen, has a very low molar mass¹ when compared to typical chemical propellants [23]. For a similar total impulse, this would mean that less propellant mass needs to be brought into space, implying lower launch costs. Alternatively, the flexibility of the spacecraft mission could be enhanced by bringing the same amount of fuel. Hall effect thrusters and ion thrusters, known as electric propulsion, have even higher specific impulses but are limited by the amount of thrust they produce, which is at most 50 mN for the engines designed until now [17]. STP has been demonstrated to generate thrust (pulses) up to 20 N, which in turn is surpassed by the thrust produced by a chemical engine. Thrust is important in the knowledge that it largely determines the time needed to complete a maneuver, e.g. a fast orbit transfer or orbit insertion. Looking at the characteristics, STP thus takes the middle ground between efficient, slow electric propulsion and inefficient, fast chemical thrusting. Compared to a resistojet, where solar light is converted into electrical energy and then converted again to heat, the STP concept eliminates the middle step yielding an efficiency increase in return. These statements are supported by Figure 1.2 [2], which shows various propulsion concepts, their thrust-to-weight ratio and their specific impulses. The figure also shows that the Technology Readiness Level (TRL) of solar thermal thrusting is between 4-6, which indicates that ground tests on the propulsion technology have been conducted [24]. The concept was indeed never flown in space but has been demonstrated successfully in laboratories and in simulations on various occasions, attaining high temperatures up to 2600 K [25]. The largest disadvantage of the concept until now has been the voluminous concentrator system as well as the vulnerability of this component [26]. However, STP clearly is an attractive option for (micro)satellite applications because it delivers specific impulses in excess of chemical thrusters. The challenge is to design a thruster that meets these expectations while tackling the issue of added complexity associated with the large concentrator part.

The research towards STP is of great importance in order to make the concept feasible for (micro)propulsion applications. At Delft University of Technology, practical research has been done on STP. In 2008, H. Leenders designed, manufactured and tested an STP thruster consisting of a Receiver-Absorber Cavity (RAC) and nozzle, illuminating the heat exchanger with a 1000 W theater lamp combined with a convergent lens [3, 8]. The copper engine, dubbed Solar Thermal Thruster 1 (STT1), attained a maximum RAC temperature of 750 K and maximum propellant temperature of 525 K. The highest performance was reached when the propellant (gaseous nitrogen) reached 494 K at a continuous mass flow of 167 mg s^{-1} and RAC input power of 49 W. The highest thrust and specific impulse (both SL) then equalled 81.3 mN and 49.6 s respectively, at a thermal efficiency of 52 %.

The performance reached in those experiments is not competitive in any way: almost half of the inserted heat is lost, while the specific impulse is not close to the aforementioned values in this chapter. The highest possible exhaust velocity (the limiting velocity) for a temperature of 494 K, where the pressure term is ignored, would be 1013 m s^{-1} (see Equation 2.8). This gives a specific impulse of 103.3 s, half of which is reached. Leenders' goal was to demonstrate that thrust could be generated with STP technology at DUT, with little attention to mass, size and performance. The current thesis will reach further. For this project the objective is to design, build and successfully test the successor of the STT1, called STT2, at propellant temperatures that are twice the value reached by Leenders. Those temperatures will at that point be limited by the material's melting point and the hard-soldered connections. To achieve these high temperatures, the thesis will hinge on three main ideas or subgoals:

¹<https://webbook.nist.gov/chemistry/>, visited on 20-11-2020.

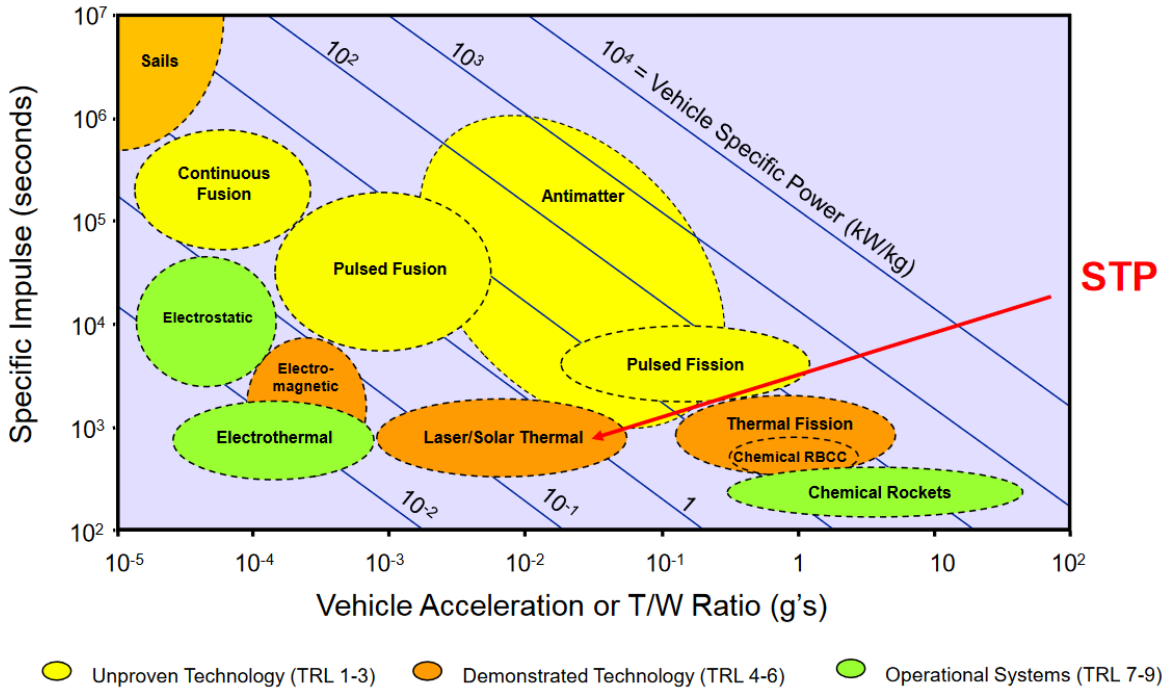


Figure 1.2: Propulsion concepts and their characteristics [2].

increase the temperature of the RAC by increasing the power input from the heat source; increase the thermal efficiency of the heat exchanger by redesigning the piece; and develop a Python tool, the [Preliminary Design Tool \(PDT\)](#), that can predict the [STP](#) engine performance as a result of user design choices.

First of all, the research framework of this project will be shown in Chapter 2. It kicks off with a small background on [STP](#), which is followed by a more thorough analysis of [STT1](#) and the research goal, requirements and constraints for [STT2](#). Then, the [PDT](#) is presented in Chapters 3 and 4, where the first chapter will focus on the theory and models behind the tool while the second chapter will focus on the tool's capabilities. The tool will be verified by models from Leenders' thesis [3] and by discussing the change in output when the input variables are altered. Validation is done using experimental data from Leenders' experiments, combined with the results of experiments on [STT2](#). Because of time constraints, the designed thruster [STT2](#) was already manufactured when the tool was still under development. Chapter 5 will detail this design following from the research goal and requirements. At the end of the chapter the manufactured pieces, both self-made and externally built, are displayed.

Experiment preparations were performed as shown in Chapter 6. After the initial test runs, it was discovered that the thruster had some issues in the channel area, where a small change in the design caused some large unexpected consequences. Furthermore, when trying to remedy leakages in the heat exchanger the thruster got damaged, preventing further experiments on the engine. As such, a drastic change in course was taken and it was decided to replace the actual tests by [CFD](#) simulations in order to validate the [PDT](#) and determine if [STT2](#) would adhere to the set requirements and goal. This analysis is detailed in Chapter 7, which shows the thermal performance of both [STT1](#) and [STT2](#) motors. Finally, now that [PDT](#) is partly validated, a new engine is designed in Chapter 8 which implements the lessons learned from designing and manufacturing [STT2](#). This [Solar Thermal Thruster 3 \(STT3\)](#) engine again has the notable constraint that the engine should be built at [DUT](#). In the end, Chapter 9 gives the conclusions on the research objective and requirements and shows the recommendations for further research into the subject.

2

Research framework

The current chapter will show the research framework of this project. It will kick off with a background on **STP** technology to make the reader familiar with the concept. A small subsection on the research into STP is included in this section as well. It is followed by an extensive section on the performance of the first and up until now only solar thermal thruster built at **DUT** by Leenders, **STT1**. By doing this, the author is able to set a feasible goal for the current project in a next section. In the end the requirements and constraints are derived from the knowledge gained in this chapter.

2.1. Research background

This section will give a small background on both the principles of and research towards solar thermal thrusting. The information will be concise, due to the fact that the workings and research were already thoroughly described in the literature study [27] and the thesis proposal [28] from the same author¹.

2.1.1. Principles of solar thermal propulsion

STP is a propulsion concept proposed to be deployed on (nano)satellites [12, 17, 25, 29]. Figure 2.1 displays the main components of an **STP** engine². The concentrator, made up of a combination of (parabolic) mirror(s) or lenses, collects the solar irradiation which is directed towards the heat exchanger or **RAC** [22]. There, the energy is directly or indirectly absorbed by the propellant. The propellant is then collected in the plenum and expelled via a nozzle, thus creating thrust.

There are a few additions that can be made to the thruster system. Fiber optic cables could be used to decouple the thruster attitude from the Sun direction [30]. A heat storage can be added to provide the spacecraft with high-energy thrust pulses [31]. The thruster system can be extended in order to provide power to the spacecraft as well through a thermal-to-electric energy conversion, a so-called bimodal system [25]. That way, (excess) heat is used to provide electrical energy to the spacecraft, thus mitigating the need for solar panels and possibly batteries.

¹Both documents are retrievable from <https://github.com/AJTRP/AE5810-thesis/tree/AE5810-documents>.

²<https://tinyurl.com/y67pl94g>, accessed on 29-11-2020.

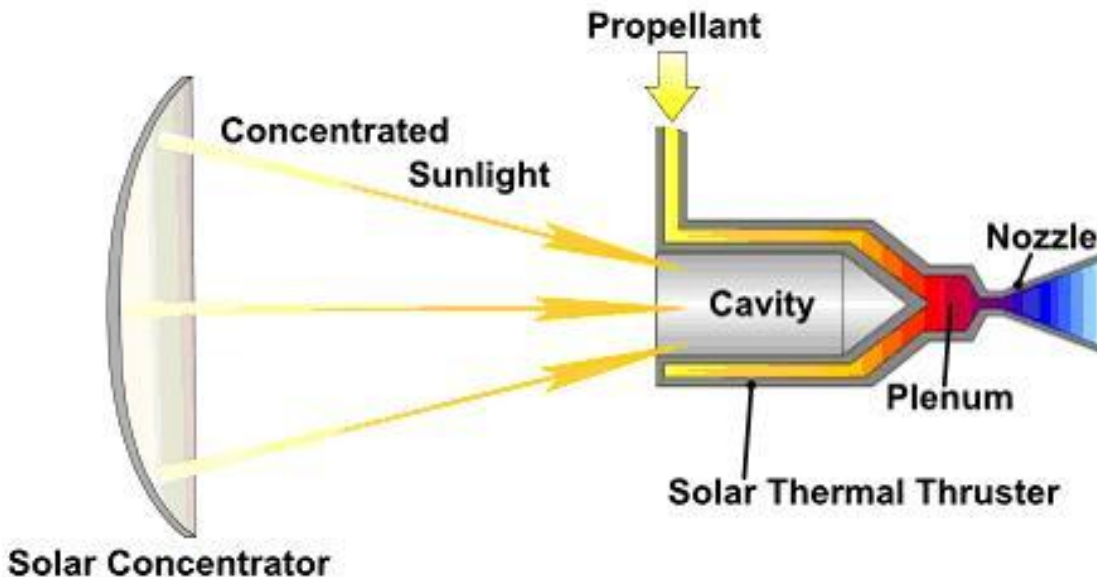


Figure 2.1: Main components of an STP thruster (see the second footnote on the previous page).

2.1.2. Summary of research into solar thermal propulsion

The concept of solar thermal thrusting was already introduced in 1956 [32]. First it was mainly researched by governmental institutes such as the [Air Force Rocket Propulsion Laboratory \(AFRPL\)](#) [22, 26, 33, 34], but starting in the 2000's researchers from universities also started to explore the technology [25, 35–38]. The thruster first consisted of a concentrator subsystem, heat exchanger and nozzle but was later expanded with fiber optic cables, heat storage and power capabilities [30, 39–41]. Propellants of interest were discussed at criteria such as molar mass, heat capacity, storability and toxicity [28]. Hydrogen, ammonia and water are seen as promising candidates. For the heat exchanger's material, rhenium, tungsten and molybdenum were often considered due to their high melting points [42]. STP has never been flown in space. This is mainly due to the risk associated with the voluminous concentrator subsystem and the storability of cryogenic hydrogen [22].

2.2. Solar Thermal Thruster 1 background

Harrie Leenders produced a total of four documents on the subject of solar thermal thrusting in his time at [DUT](#). Together with a fellow student, he modelled the thermal control of an STP-propelled spacecraft in 2006 [43]. In 2007 he finished his literature study [44] and subsequently in 2008 he completed his master thesis [3], which resulted in a paper in association with his supervisor Ir. B.T.C. Zandbergen [8], also the supervisor of the current research. The latter two documents are often cited in this report because of the detailed description of the design methodology, experiment setup and results.

This section will present the design and manufacturing of [STT1](#) and particularly focus on the test results. It will be concise, details and rationale can be found in the document described above. The main findings will be used to improve the current report and prevent the same mistakes from being made twice.

2.2.1. Design and manufacturing

Leenders' goal for his master thesis was to develop and test an STP technology demonstrator at [DUT](#). It was designed to heat a propellant flow of 300 mg s^{-1} to 373.15 K. The assumption was made that of

the incoming 29 W, an arbitrary 80 % would be used to heat the propellant to the aforementioned value without any insulation layer. He designed a thruster consisting of three main elements: concentrator subsystem, heat exchanger and nozzle. For the concentrator subsystem, he used one converging lens in addition to a 1000 W theater lamp as the irradiation source. The lamp was operated for another STP-related study by Pino [45]. The combination would give a focal spot with a diameter of 2 cm at a focal length of 2 cm.

Two nozzles were intended for use during the tests: a glass and a copper one. Both were previously used in other studies. The glass nozzle has a throat diameter of 6.8 mm, an exit diameter of 7.2 mm and a mass of 16 g. This nozzle was mainly added for demonstration purposes; because the glass cannot exceed 473 K, only a few tests were performed with this nozzle attached to the engine. Because of the temperature limit and the non-optimal dimensions (see later in this section), the results of tests with this nozzle are not used in this report. When results are displayed, these are always produced with the copper nozzle attached. The copper nozzle was designed with a throat diameter of 0.66 mm, an exit diameter of 0.77 mm and a mass of 4.5 g. The technical drawing can be found in Appendix A. It was reconstructed for unknown reasons and it turned out to have a throat and exit diameter of 0.58 mm and 0.68 mm respectively. The area ratio, which is the ratio of the nozzle throat and exit area, is thus equal to 1.375 [23].

The heat exchanger has the direct propulsion, indirect absorption configuration [27]. It features eight straight rectangular channels around an open-ended cone. It has a ring on the base of cone for distribution of the propellant. It is made of copper and has a total mass of 0.087 kg. The featured propellant is gaseous nitrogen.

Both the heat exchanger and copper nozzle were manufactured by the DUT in-house workshop, Dienst Elektronische en Mechanische Ontwikkeling (DEMO). This workshop is equipped with advanced Computer Numerical Control (CNC) mills and lathes, operated by experienced users. The glass nozzle, theater lamp and lens were borrowed or already present at the faculty of AE.

2.2.2. Experimental results

All tests on the complete motor were conducted in the cleanroom located at the 8th floor of the faculty of AE. The thruster was tested in different configurations: test were done without and with mass flow and during the latter, insulation was applied around the heat exchanger. Additional equipment used were the test bench TB-AE-1.0 (for more information on this bench, see Jansen [46]), one Futek LSB200 load cell, nine type K thermocouples, two pressure transducers and the Brooks 5851S mass flow controller. Four of the thermocouples were attached at various points of the RAC and averaged to determine the heat exchanger's temperature, another was inserted in the nozzle to find the propellant temperature. One pressure sensor was attached to the nitrogen feed line, the other was attached to the nozzle chamber.

The highest propellant temperature attained during testing was 525 K for a short period of time at a mass flow of 50 mg s^{-1} . The heat exchanger was allowed to heat up to 630-630 K. Thrust and RAC input power for this result are unknown, hence the thermal efficiency cannot be calculated. Next to this, Leenders also tabulated test results from five different mass flow runs, together with the thermal efficiency, measured thrust and propellant pressure at two locations in the engine. These are shown in the upper part of Table 2.1. The lower part shows the calculated specific impulse I_{sp} , nozzle exit pressure p_e , exhaust velocity U_e , equivalent velocity U_{eq} and thrust F . The last row shows the theoretical thrust as calculated by Leenders.

The theoretical values are found using Equations 2.1-2.6 [23]. The involved variables are the propellant temperature in the nozzle chamber T_c , RAC temperature T_{RAC} (both in K), propellant feed pressure p_{feed} , propellant chamber pressure p_c (both in Pa), nozzle throat area A_t , exit area A_e (both in m^2) and mass flow m (in kg s^{-1}). The assumption is made that the ambient pressure p_{amb} is the standard SL value of 1.013 25 bar, while the propellant inlet temperature equals 298.15 K, a value

Table 2.1: STT1 measurements from Leenders' paper [8].

Measurements					
Measurement number	1	2	3	4	5
\dot{m} [mg/s]	77	103	128	154	167
F [mN]	28.9	43.3	59.7	74.5	81.3
T_c [K]	494	480	466	452	445
T_{RAC} [K]	545	514	490	470	460
p_{feed} [bar]	1.97	2.53	3.07	3.61	3.92
p_c [bar]	1.94	2.48	3.02	3.55	3.87
Calculations					
Resulting I_{sp} [s]	38.3	42.9	47.5	49.3	49.6
Theoretical p_e [bar]	0.37	0.47	0.58	0.68	0.74
Theoretical U_e [m/s]	622	613	604	595	590
Theoretical U_{eq} [m/s]	319	423	480	516	531
Theoretical F [mN]	24.6	43.6	61.5	79.4	88.6
Theoretical F [mN] by Leenders	33.5	53.1	72.6	91.8	103.4

used by Leenders in his calculations. The nozzle dimensions from the previous section were used. Note that the pressure values need to be in Pa for the equations below, the thrust in N and the mass flow in kg s⁻¹. The universal gas constant R_A equals 8.314 J mol⁻¹ K⁻¹, the molar mass MM of nitrogen is 0.028 01 kg mol⁻¹ and the specific heat ratio γ at 298.15 K is equal to 1.40³. The resulting Vandenkerckhove function Γ is thus 0.6847.

The equations in this section are derived from the [Ideal Rocket Theory \(IRT\)](#). It hinges on a number of assumptions; the most important are steady, isentropic and one-dimensional nozzle flow, constant propellant heat capacity, homogeneous propellant composition and the propellant obeying the ideal gas law [23]. [IRT](#) allows the use of the equations in this chapter and is used in the preliminary design process. Note that [IRT](#) does not incorporate the effects of thermal losses, pressure losses, change in propellant composition, throat boundary layers and so on. In a later stage, these can be quantified by consulting literature or conducting experiments.

$$\frac{A_e}{A_t} = \frac{\Gamma}{\sqrt{\frac{2\gamma}{\gamma-1} \left(\frac{p_e}{p_c}\right)^{\left(\frac{2}{\gamma}\right)} \left(1 - \left(\frac{p_e}{p_c}\right)^{\left(\frac{\gamma-1}{\gamma}\right)}\right)}} \quad (2.1)$$

$$\Gamma = \sqrt{\gamma} \left(\frac{2}{\gamma + 1}\right)^{\frac{\gamma+1}{2(\gamma-1)}} \quad (2.2)$$

$$U_e = \sqrt{2 \frac{\gamma}{\gamma-1} \frac{R_A}{MM} T_c \left(1 - \left(\frac{p_e}{p_c}\right)^{\left(\frac{\gamma-1}{\gamma}\right)}\right)} \quad (2.3)$$

$$U_{eq} = U_e + \frac{p_e - p_{amb}}{\dot{m}} A_e \quad (2.4)$$

$$F = \dot{m} U_{eq} \quad (2.5)$$

³<https://webbook.nist.gov/>, accessed on 11-03-2020.

$$I_{sp} = \frac{U_{eq}}{g_0} \quad (2.6)$$

Table 2.2 shows the thermal efficiency $\eta_{thermal}$ of the RAC for each of the five measurements, as written down in the paper. Combining this with the mass flow and propellant temperature from Table 2.1 and Equation 2.7, the power input from the thermal lamp to the RAC can be calculated, see the last row of the table. Note that the enthalpy change ΔH is derived from National Institute of Standards and Technology (NIST) properties⁴.

Table 2.2: STT1 RAC efficiency, enthalpy, propellant and input power, from Leenders' paper [8].

Measurement number	1	2	3	4	5
$\eta_{thermal}$ [-]	0.32	0.40	0.45	0.50	0.52
$\Delta H \cdot 10^5 \text{ J/kg}$	2.05	1.90	1.75	1.61	1.53
$Q_p [\text{W}]$	15.8	19.6	22.4	24.7	25.6
$Q_{in} [\text{W}]$	49.2	49.0	49.8	49.4	49.2

$$\eta_{thermal} = \frac{\dot{m} \cdot \Delta H}{Q_{in}} \quad (2.7)$$

2.2.3. Results discussion

From Chapter 1, it was clear that the attained propellant temperature and specific impulse were low in comparison to results from literature. This can be attributed to three main reasons: low thermal efficiency (at most 52 %), low amount of input power (approximately 49 W) and the nozzle not being adapted. The latter can be derived from the fact that the nozzle exit pressure does not equal the ambient pressure for the measurements in Table 2.1. When it does, thrust is maximized in which case the nozzle has a so-called optimum expansion ratio [23]. The exit pressure is dependent on the chamber pressure, which is not a control variable; it cannot be set during the experiments, but it is a result from the combination of propellant properties, mass flow, nozzle throat area and propellant temperature, see Equation 2.9. So despite the temperature decreasing over the measurements (see Table 2.1), the specific impulse does increase because the exit pressure approaches the optimum of 1 atmosphere.

The influence of an adapted nozzle is large. For the fifth measurement, the nozzle exit area would equal $2.74 \times 10^{-7} \text{ m}^2$ if the nozzle had an optimum expansion ratio to ambient (Equation 2.1). The equivalent exhaust velocity would then be 542.4 m s^{-1} (Equation 2.4) which would result in a specific impulse of 55.3 s, which is 11.4 % higher than the value attained during the test run. The highest possible exhaust velocity would be an expansion to vacuum, which is called the limiting velocity U_L in m s^{-1} , see Equation 2.8. For the fifth measurement that would be 98.1 m s^{-1} .

Another thing that was noticed was that the 1000 W theater lamp outputted an irradiation beam of approximately 240 W. Of that number, Leenders estimated that 61 W would be focused by the lens towards the heat exchanger's cavity. However, only 49 W did reach the RAC (see Table 2.2), of which 25.6 W did increase the propellant's enthalpy (for the fifth measurement). So the total system had a thermal efficiency of 2.6 %.

$$U_L = \sqrt{2 \frac{\gamma}{\gamma - 1} \frac{R_A}{MM} T_c} \quad (2.8)$$

⁴<https://webbook.nist.gov/>, accessed on 11-03-2020.

The equations in this section are valid for choked flow only. Choked flow, where the flow becomes supersonic in the divergent part of the nozzle, is reached once the ratio of ambient pressure to nozzle chamber pressure is lower than a value which is dependent on propellant properties, see Equation 2.10. This value is 0.528 at nitrogen's specific heat ratio of 1.40. At a standard SL ambient pressure of 1 atmosphere, a chamber pressure of a minimum 1.92 bar is sufficient, which is barely satisfied in the first measurement.

$$\dot{m} = \frac{\Gamma p_c A_t}{\sqrt{\frac{R_A}{M_M} T_c}} \quad (2.9)$$

$$\left(\frac{p_{amb}}{p_c}\right)_{cr} = \left(\frac{2}{\gamma + 1}\right)^{\left(\frac{\gamma}{\gamma - 1}\right)} \quad (2.10)$$

A few issues arose from the results. Table 2.1 shows the theoretical thrust in the last row as calculated by Leenders. These values could not be reproduced and do not match the calculated values in this report, which are displayed in the second to last row. Furthermore, both rows are also not equal to the measured thrust, shown in the second row. Especially the large differences in both the last rows are an issue; apparently Leenders inserted other properties and measurements in the IRT equations than the current author.

A few explanations can be given for the differences between the three rows: first of all, it is not confirmed that the pressure and temperature at RAC exit are equal to the values in the chamber of the nozzle; there could be some heat and pressure loss in the connecting channel, but this is not substantiated in either thesis or paper. Secondly, the nozzle could suffer from a boundary layer in the throat, which is quantified by the discharge factor. This factor is mentioned in the thesis but could again not be checked. Thirdly, the ambient pressure, ambient temperature and/or inlet propellant temperature could be different than the values stated in this section. A fourth explanation would be that the velocity of the propellant in the chamber was not close to 0.

2.2.4. Main findings

What becomes clear from this section is that documentation of methodology and results is of the utmost importance to any successors who would like to reproduce the obtained values and continue research with those results. It is recommended to clearly state all inputs, results, properties and dimensions when an experiment is conducted, preferably tabulated for a quick overview. In this report, this method will be followed to allow the report to be used in future research.

Furthermore, another lesson learned is that the efficiency of the theater lamp is minor, even with a lens. Only 4.9 % of lamp's rated power of 1000 W reached the RAC after which almost half was lost to the surroundings by convection and radiation in the heat exchanger. There is room for improvement here, both in RAC input power as in thermal efficiency of the heat exchanger itself. Next to that, optimizing the nozzle can also add significantly to the specific impulse. If the budget allows so, constructing a new nozzle for STT2 is preferred over using the copper nozzle from Leenders. The last finding is that DEMO can produce very detailed pieces out of copper. For the design of the new thruster, they will be consulted regarding the possibilities and pricing.

2.3. Research goal

The objective was briefly explained in Chapter 1 as follows: design, build and successfully test the successor of the STT1, called STT2, at propellant temperatures that are deemed to be the maximum

that can be reliably achieved at this university. In the thesis project plan⁵ [28], this goal was quantified: STT2 should reach a SL specific impulse of 62.8 s. However, the specific impulse can be increased beyond that value. With the information from the previous sections, the following research goal is set:

Demonstrate the feasibility of the Solar Thermal Thruster 2 by having a minimum specific impulse at sea level conditions of 90.0 s at a continuous mass flow level of 300 mg s⁻¹.

A small calculation was performed to see if the specific impulse of 90.0 s could be attained under the requirements and constraints. Using IRT and setting the mass flow at 300 mg s⁻¹, about 250 W of input power at a thermal efficiency of 70 % is needed to heat the propellant to 835.3 K (with a propellant inlet temperature of 298.15 K). Then, for an optimally expanded nozzle a pressure ratio of 8.05 (Equation 2.4) and subsequently an area ratio of 1.71 (Equation 2.1) are found. The chamber pressure is 8.2 bar (provided that the ambient pressure is 1 atm) and the nozzle throat diameter and exit diameter are 0.58 mm and 0.76 mm respectively. The thermal efficiency is derived from Leenders. When taking the increase in thermal efficiency in Table 2.2 as a linear trend (which it certainly is not, it has a decreasing increase rate), the thermal efficiency equals 0.72.

Chapter 1 showed that this research goal is hinging on three main pillars or subgoals: increasing the power input, increasing the thermal efficiency and creating a preliminary design tool to allow for accessible evaluation of design choices. These three aspects will be addressed in the next chapters. The goal still allows for changes in the design and experiment outlay: the power source can be altered, additional lenses can be used, more insulation can be applied or another propellant can be used. The mass flow chosen is arbitrary but is set at this level in order to make comparisons to Leenders' thruster, as he chose a similar mass flow for his thesis.

2.4. Requirements and constraints

The research goal stated above is subject to requirements and constraints, which are given in this section. Two types of requirements will be discussed: functional requirements, which outline the direction of this thesis project, and system requirements, which detail the performance the system has to adhere to. The difference between the two types is that the latter can be quantified, while the earlier cannot.

2.4.1. Functional requirements

Table 2.3 shows the functional requirements that were identified in this chapter.

⁵Retrievable from <https://github.com/AJTRP/AE5810-thesis/tree/AE5810-documents>.

ID	Requirement	Rationale
REQ-F-1	An STP thruster system, called STT2, shall be designed.	The goal for this project is to demonstrate a high-temperature STP thruster at DUT.
REQ-F-2	STT2 shall consist of three primary components: the concentrator subsystem, the heat exchanger or RAC and the nozzle.	In order to reduce the complexity of the thruster, no fiber optic cables, thermal storage and/or power subsystem are implemented.
REQ-F-3	STT2 shall heat propellant through the use of concentrated irradiation.	The requirement of solar irradiation is relaxed, because testing when dependent on the Sun adds complexity.
REQ-F-4	STT2 shall generate a thrust force by expelling heated propellant.	The principle of STP is to expel heated propellant via a nozzle.
REQ-F-5	STT2 shall be manufactured and subjected to experiments.	In order to validate the PDT, the designed thruster needs to be built and tested.
REQ-F-6	STT2 shall be manufactured and tested using DUT resources.	Presently, the time allocated to a thesis is 9 months or 42 ECTS, excluding the literature study. The money available is 500 Euros.
REQ-F-7	STT2 shall be designed with a non-toxic propellant.	The cleanroom at AE does not allow testing with toxic propellants.

Table 2.3: Functional requirements for STT2.

2.4.2. System requirements

Table 2.4 shows the system requirements that were identified in this chapter.

ID	Requirement	Rationale
REQ-S-1	STT2 shall have a SL specific impulse of at least 90 s at a mass flow of 300 mg s^{-1} .	See the research goal.
REQ-S-2	STT2's heat exchanger shall reach a temperature of at least 900 K, without propellant flow.	This temperature is necessary in order to heat the propellant to a sufficient degree.
REQ-S-3	STT2's heat exchanger shall heat the propellant to a temperature of at least 850 K at a mass flow of 300 mg s^{-1} .	This temperature is necessary in order to reach the specified specific impulse.
REQ-S-4	STT2's heat exchanger shall have a maximum mass of 0.087 kg.	This is the mass of Leenders' heat exchanger.

Table 2.4: System requirements for STT2.

2.4.3. Constraints

The system requirements are interconnected and are based on constraints found in Table 2.5, which are mostly sensor-related and derived from the literature study⁶ [27].

⁶Retrievable from <https://github.com/AJTRP/AE5810-thesis/tree/AE5810-documents>.

ID	Constraint	Rationale
CON-1	STT2 shall have a maximum heat exchanger temperature of 933 K.	That is the maximum value that hard-soldered connections can withstand according to the DEMO workshop.
CON-2	STT2 shall experience a maximum propellant pressure of 10 bar.	Although some of the pressure sensors that were tested in the literature study could reach up to 16 bar, literature suggests that high-pressure vessels above 10 bar are not recommended in micropulsion [47].
CON-3	STT2 shall have a maximum propellant mass flow of 861 mg s^{-1} .	This is the maximum amount the Brooks 5851S Smart Mass Flow, present at the AE cleanroom, can measure.
CON-4	STT2 shall have a maximum thrust of 1000 mN.	This is the maximum amount various thrust sensors and benches developed at AE can support. See also Chapter 6 .

Table 2.5: Constraints for STT2.

All these values fall within the constraints. There is some room left in the temperature range and the pressure range to accommodate for heat and pressure losses in each component and for nozzle correction factors. After the design for [STT2](#) is finalized in Chapter [5](#), it will be inputted in the preliminary tool built in Chapter [3](#). This will show if the design can actually reach the set specific impulse of 90.0 s.

Note that no ΔV requirement nor volume requirement is given in this chapter. This is purely due to the lack of a dedicated mission for which the thruster is designed. Because the thruster needs to be manufactured at low cost, it can most likely not adhere to any (nano)satellite mission standards.

3

Preliminary Design Tool overview

Designing a solar thermal thruster requires a great deal of work in the areas of conjugate heat transfer, ray tracing, flow characteristics, rocket propulsion and other. This process would be greatly enhanced by the introduction of a design tool that predicts the performance based on certain design choices in the preliminary design phase of an **STP** project. It could help reduce the amount of errors made and assist the user in investigating the performance changes with operating conditions alterations.

This tool has been developed and is explained in this section. It received the name Preliminary Design Tool (**PDT**) and was built in the Python programming language. The code is split into multiple scripts, where one script calls the others when executed. The main script is preceded by the term "MASTER" while all other scripts are preceded by the word "SUB". Because of the large number of scripts, they are not added as an appendix to this report. Instead, all scripts are available online¹ and should be downloaded to one folder in order to execute the full tool. It is encouraged that others use the script as well to assess their **STP** design choices.

The tool consists of three models: a thermal model, pressure loss model and thrust model. The first has been built in great detail, while the other two employ simpler relations which go less in depth. The reason for this is that the focus in this project is on reaching high temperatures in the propellant, in excess of 800 K. The first model will be verified and validated in this chapter as well.

The goal of the tool is to see the impact of design choices on the thermal performance, such as the channel layout, number of channels, propellant, power radiation input, paint and so on. Remember that this design evaluation is one of the three main ideas to bring this thesis to a successful end, see Section 2.3. Assessing the performance will aid the designer in most of the **STP** thruster design decisions. For the thermal model in the **RAC**, the output propellant temperature is the most important output of the tool, as it will indicate the efficiency of heat transfer from solar irradiation to propellant in the **RAC**, thus being a major indicator of the successful application of **STP**.

As stated before, the tool will be built in Python and will have three main themes: heat transfer in the **RAC**, pressure loss in the **RAC** and resulting thrust in the nozzle. Notable models that are not included in this tool are a ray tracing model and a feed system model. Due to time constraints it was chosen to not incorporate these in the tool, however they could be added in the future by other users.

The documentation of the tool will be split into two chapters in this report. This chapter will focus on the requirements, assumptions, layout, inputs, outputs, options, verification and validation of the tool, while Chapter 4 will elaborate on the theory behind the models. The latter chapter will be largely based

¹Retrievable from <https://github.com/AJTRP/AE5810-thesis>.

on literature from sources such as Zandbergen [23], Leenders [3] and to a smaller extent Das [48]. It is strongly recommended to read both chapters to comprehend the capabilities and shortcomings of the tool.

At first, the tool requirements are given, followed by the assumptions used in the models. Then, an overview of the tool is given, including a tool block diagram containing the inputs and outputs. Afterwards, the model will be subjected to cases for verification and validation. In the end, conclusions and recommendations will be presented.

The verification and validation cases will be retrieved from Leenders' thesis [3]. He documented both experimental and theoretical results, which will be compared to the constructed Python tool. Unfortunately, no other cases could be found that approached the structure of this tool. Das built a thermal Matlab tool for her thesis on the design of a solar thermal thruster [48], but this focused to a larger extent on channel characteristics and fiber optic cables. Furthermore, no clear cases could with inputs and outputs were found in her report and it was realized too late to ask for her Matlab code, so her tool is not used for verification and validation.

3.1. Requirements

The tool requirements are given in Table 3.1.

ID	Requirement	Rationale
PDT-R-1	The tool, named Preliminary Design Tool (PDT), shall model STP thrusters of the direct propulsion with indirect absorption configuration.	This configuration was used by Leenders [3] and will also be the configuration for STT2 [28].
PDT-R-2	The PDT shall predict the propellant enthalpy increase in an STP heat exchanger within an accuracy of 10 %.	The thruster's specific impulse scales with the square root of the propellant temperature, so the accuracy for the specific impulse will be 3.2 %. See Equation 2.3.
PDT-R-3	The PDT shall predict the pressure throughout the thruster system.	The pressure in the nozzle chamber and the nozzle exit partly determines the thrust and specific impulse of the thruster (see Section 2.2). Determining the pressure loss is thus key.
PDT-R-4	The PDT shall predict the specific impulse and thrust of the engine.	The goal was set in Chapter 2 to reach a certain specific impulse. The tool should thus indicate if this requirement is met.
PDT-R-5	The PDT shall evaluate the influence of various design inputs, as given in Section 3.3.	The usefulness of the tool is reflected in the amount of inputs it can receive.
PDT-R-6	The PDT shall output various parameters, as given in Section 3.3.	These parameters will determine the performance of the thruster.
PDT-R-7	The thermal model of the PDT shall be transient (time-dependent), in contrast to a steady-state model.	This will allow for verification and validation with Leenders' data, as he has time-dependent thermal results as well [3].

Table 3.1: Preliminary Design Tool requirements.

3.2. Assumptions

The requirements from Section 3.1 are accompanied by the assumptions from Table 3.2, setting the boundaries of the tool.

ID	Assumption	Rationale
PDT-A-1	The heat exchanger will have a cylindrical or conical shape and have a cavity.	These shapes are identified as the most promising by Shoji [4].
PDT-A-2	The heat exchanger will feature one or multiple flow channels, either straight or spiraling.	Other layouts, such as porous material or one channel over the whole surface of the inner RAC, are not considered due to their added complexity.
PDT-A-3	The heat exchanger will be made out of one material.	To reduce complexity.
PDT-A-4	The heat exchanger has an uniform temperature.	Only materials with a high thermal conductivity, such as copper, will be considered for the heat exchanger, see Chapter 5.
PDT-A-5	The surroundings of the heat exchanger will either be still air or vacuum.	Moving air will influence the convection losses on the outside, which adds complexity (see Chapter 4).
PDT-A-6	The incoming radiation will fall on the inner cavity wall and is reflected diffusely.	To reduce complexity. In reality, the collimated beam will be strongly reflected in one particular direction. A ray tracing tool could capture this phenomenon but is considered out of the scope of this thesis.
PDT-A-7	The cavity is oriented towards the side.	Literature for natural convection from cylinders and cones is only available for horizontally oriented geometries [49, 50].
PDT-A-8	The propellant is treated as a single phase fluid.	Some propellants for STP demonstrators are gaseous under standard properties but are stored as liquids [25, 51]. However, this adds complexity to the tool, so it will not be considered.
PDT-A-9	Only conical nozzles will be considered.	Bell nozzles and other nozzles are not considered, because the STT2 nozzle will be conical due to the reduced manufacturing complexity (see Chapter 5).
PDT-A-10	The nozzle is assumed to have ideal expansion, with a minimum exit pressure of 100 Pa.	Ideal expansion cannot be reached in vacuum, as it would require the nozzle to be infinitely long and heavy. See below for the rationale for a minimum exit pressure of 100 Pa.
PDT-A-11	The pipes and nozzle do not experience heat losses nor pressure losses. Also no heat is lost to the surroundings via mounting connections.	It is considered out of the scope of this tool. However, it could be added in the future.

Table 3.2: Preliminary Design Tool assumptions.

Assumption PDT-A-10 requires an extra rationale. At some point, achieving optimum expansion when the ambient pressure approaches zero will cause the nozzle to be too large and heavy. Figure 3.1 shows the specific impulse for increasing expansion ratio. The expansion ratio is defined as the nozzle exit area divided by the nozzle throat area. Input values for the graph are taken from Section

2.3, only the exit pressure was varied. Also shown in the graph is the exit diameter, as well as the maximum achievable specific impulse and the point where an exit pressure of 100 Pa is reached.

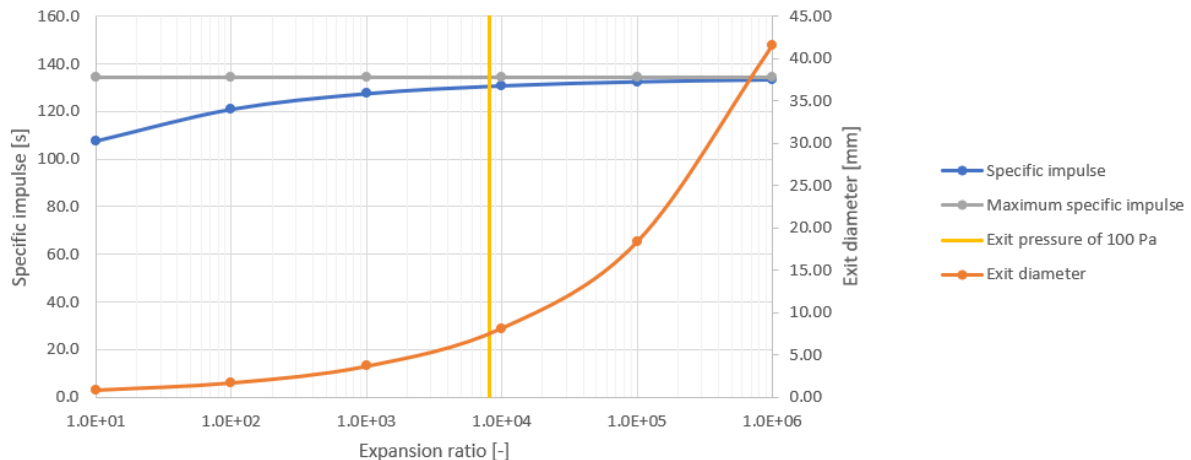


Figure 3.1: Specific impulse and nozzle diameter as a function of the expansion ratio.

The user of the tool is allowed to set the ambient pressure to zero. However, when this is done, the tool will set the exit pressure not at the same level, but at the somewhat arbitrary value of 100 Pa. In the graph it is shown that at that point the specific impulse is very close to the maximum, while the exit diameter is not too large. The user will be able to alter the minimum exit pressure.

3.3. Overview

Figure 3.2 shows the flowchart of the PDT. The rectangular gray blocks represent the user inputs (on the top) and the outputs at the bottom. The hexagonal boxes are the various tool scripts, divided into four coloured parts.

The program requires the user to make a choice for the heat exchanger shape, material, insulation, channel layout and propellant. For the first there are only two options, as stated in assumption PDT-A-1. For the material, the options are copper, molybdenum and tungsten, but these can be expanded by the user. There is the option to apply insulation on the outer side of the heat exchanger, for which two options are available: Saffil M-FIL (see C.9 for the datasheet), also used by Leenders or [Multi-Layer Insulation \(MLI\)](#). There are the straight and spiral options for the channel layout, per assumption PDT-A-2. For the propellant, four propellants can be chosen: nitrogen, water, ammonia and hydrogen. These were identified as promising propellants for STP in the literature study² [52]. All propellants, except for water, will be in the gaseous state when fed to the engine. Water will be in the liquid state and will thus require latent heat for the phase transition to gas. Per assumption PDT-A-8, no two-phase flow is considered for water.

The user inputs leading to the yellow hexagonal block are required for some dimensional inputs to the thermal program. However, these dimensions (mainly heat exchanger mass and surface areas) can also be inputted directly, thus mitigating the use of the yellow block. The reason for that is that the tool simplifies the cavity to a cylindrical or conical shape, so the outputted mass and areas could be off by a large amount. Also, the heating area is comprised of the channel section plus the entrance and exit regions where the manifolds are located. However, the program only determines the channel section heating area, because the manifolds (which can have multiple shapes) require many inputs. To remedy this, the user can thus input the characteristics themselves, for instance by retrieving the values from [Computer-Aided Design \(CAD\)](#) drawings. A part of the main script is dedicated to this override. If one

²Retrievable from <https://github.com/AJTRP/AE5810-thesis/tree/AE5810-documents>.

wants to do a quick analysis however, the built-in dimension calculator can be used.

The power input efficiency shown in the Figure is the ratio of the power that reaches any surface of the heat exchanger divided by the rated output power of the heat source. For instance for the theater lamp from Subsection 2.2.4, the power input efficiency would be equal to 4.9 % or 0.049, because only 49W of the rated power output of 1000W reached the heat exchanger. For the welding laser that will be the heat source of choice for STT2's demonstration, this number can be set to (almost) 100 % because it can accurately direct the collimated beam towards the cavity, see the literature study [52].

The thermal model is given in red. It first calculates the losses to the ambient and the convection heat transfer to the propellant. Then, the remaining power is used to heat the heat exchanger. Afterwards, the program checks if it already reached the end of its run time. If not, it loops again to the beginning of thermal model. After the run time has ended, the pressure loss in the RAC channels is calculated (green block) and the nozzle performance is determined (red block). The yellow square represents where the heat exchanger dimensions are calculated by the script.

As mentioned in the introduction of this chapter, the models and the theory behind the tool are explained in Chapter 4. There, all input parameters will also be detailed.

3.4. Verification

Verification is the process to determine that a model performs as intended by the user and the requirements [53]. Debugging the code and making sure not typos are in are part of this check. Verification for the thermal part of this code will be done by comparing the tool outputs to the theoretical outputs of Leenders' model. Next to that, the tool will be verified by changing some key input parameters and observing the outputs. Finally, the temperature-dependent relations for various parameters such as propellant enthalpy are verified.

Some of the equations presented in Chapter 4 have limitations in terms of the Prandtl number or Reynolds number. These limitations as well as what the variables represent will be explained there. For now, it suffices to know that the three PDT simulations all were within the limits set by these equations. The Prandtl number ranged from 0.720 to 0.728 while the Reynolds number was inbetween 809.2 and 2800.2.

3.4.1. Verification via thermal model comparison

Leenders produced graphs that all contained theoretical and practical results for three main tests he conducted; the first test was a conical cavity with no propellant flow and no insulation, the second a similar case with insulation on the outer sides and the third one a similar case with insulation and mass flow. The theoretical results are derived from Leenders' Matlab model. This model cannot be retrieved and no tabulated data is available from his thesis [3]. However, graphs from his report remain, so these are used as a comparison.

As said before in Chapter 2, Leenders applied four thermocouples at the outer walls of the RAC and took an average to deduce the RAC temperature. The propellant temperature was only measured at the nozzle, so the measured propellant temperature will be lower than the value to which it is heated in the RAC, due to heat losses in the connection pieces and nozzle.

Verification case 1: no mass flow and no insulation

For the first test, the inputs were found in Leenders' report and inserted in the PDT. The dimension inputs were retrieved from CAD drawings. The inputs can be found in Table 3.3. The graph with the

resulting RAC temperatures is found in Figure 3.4, next to the graph with the outputs from Leenders, Figure 3.3. Note that his graph shows two lines, one showing the theoretical results and the other displaying experimental data. The PDT RAC temperature data per 30 s is also shown in Table D.1.

Table 3.3: PDT case 1 inputs.

Name	Symbol	Value	Unit
RAC type	-	"Conical"	-
RAC material	-	"Copper"	-
Insulation	-	"No insulation"	-
RAC channel length	L_{cavC}	0.0501	m
RAC inner length	L_{cavI}	0.0522	m
RAC outer length	L_{cavA}	0.0691	m
RAC inner diameter	D_{inner}	0.0281	m
RAC outer diameter	D_{outer}	0.031	m
RAC aperture diameter	D_{ap}	0.025	m
RAC half angle	ϕ	14	deg
RAC inner cavity area	$A_{RAC,i}$	2.348e-3	m^2
RAC outer cavity area	$A_{RAC,o}$	5.124e-3	m^2
RAC mass	M_{RAC}	0.087	kg
Irradiation time	n_i	16	min
Incoming power	P_{in}	60	W
Incoming power efficiency	η	0.50	-
Absorptivity oxidized copper	α_M	0.70	-
Emissivity oxidized copper	ϵ_M	0.65	-
Ambient temperature	T_{amb}	298.15	K
Ambient pressure	p_{amb}	101325	Pa

The maximum temperature from the PDT is 507.9 K. The curve from the PDT is similar to the theoretical result curve from Leenders, but the maximum temperatures do differ by about 30 K. This can be explained by a difference in model equations, most probably in the calculation of the outer wall convection rate, which is the largest heat loss. However, this cannot be checked due to the fact that the Matlab model is unavailable. The difference is less than the 10 % criterion, so the verification for this case is passed.

Verification case 2: no mass flow and insulation

For case 2, the irradiance was present from 0 to 26 min. No propellant was flowing and M-Fil Saffil insulation (see C.9 for the datasheet) was applied at the outer sides of the RAC, together with aluminium foil at the edge to lower the outer wall emissivity. See Table 3.4 for the inputs for this case. Note that it only shows the changed inputs with respect to Table 3.3.

Table 3.4: PDT case 2 inputs. Changes relative to Table 3.3.

Name	Symbol	Value	Unit
Insulation	-	"Saffil M-FIL"	-
Insulation thickness	t_i	0.040	m
RAC outer diameter	D_{outer}	0.11	m
RAC outer cavity area	$A_{RAC,o}$	5.308e-2	m^2
Irradiation time	n_i	26	min
Emissivity insulation	ϵ_{insu}	0.09	-

The maximum temperature was equal to 727.4 K. The tabulated output data from the PDT can be found in Table D.2. Figure 3.6 shows the outputted graph from the PDT, next to the graph from Leenders in Figure 3.5. The dent at minute 23, Leenders stated, is due to movement of the irradiation

source. The curves again fit and the maximum temperature from the PDT seems to be in the same region as the red curve from Leenders. However, the red curve is slightly more flattened on the highest point than the blue curve. Despite this, the PDT is also deemed verified for this case.

Verification case 3: mass flow and insulation

For the third case, differing amounts of mass flow were applied in the tool. Table 3.5 shows these mass flows and the times that they are occurring. Next to that, Table 3.6 shows the inputs, relative to the inputs of case 2 (Table 3.4). The output data is shown in Table D.3. The graph from the PDT is shown in Figure 3.8, next to the graph from Leenders displaying the RAC temperatures from his model and his experiment. The maximum RAC temperature reached in the PDT simulation is 637.5 K.

Table 3.5: PDT case 3 mass flow inputs.

Mass flow [mg/s]	Start time [min]	End time [min]
75	22	33
100	35	44
125	46	57
150	60	71
175	73	84
200	86	96

Table 3.6: Case 3 inputs. Changes relative to Table 3.4.

Name	Symbol	Value	Unit
Propellant	-	"Gaseous nitrogen"	-
Channel layout	-	"Linear"	-
Number of channels	n_{ch}	8	-
Channel diameter	D_c	0.0006	m
Irradiation time	n_i	95	min
Incoming power	P_{in}	45	W
Propellant feed pressure	p_p	300000	Pa

The model outputs do differ, both in curve as in highest temperature attained. This can be due to the variable radiation input from the theater lamp which Leenders noticed for this case. This is already seen before the first mass flow is applied at minute 22, as the curve of the RAC temperature decreases, while in case 2 it was steeper, towards the maximum temperature of about 710 K. For this reason, the input power was decreased to 45 W in the PDT. This case can thus not be verified, as only the "trend" of applied mass flow is shown, but the temperature numbers hold no real value (and differ more than the criterion of 10 %).

3.4.2. Verification via changing input parameters

In this subsection, key input parameters will be changed to see its effects on the output parameters. As the initial input, the third case is chosen (see Table 3.6) with the only difference that the mass flow is equal to 200 mg s^{-1} for the whole simulation.

Changing RAC inner surface area

The total loss from the inner cavity was minor and only amounted to 0.58 W after the simulation stabilized, of the inputted 30.0 W. When the inner surface area was doubled, this increased to 1.13 W, which seems to be an acceptable consequence. It is almost double the value as it was first, because the extra heat loss also means that the RAC temperature is slightly lower, implying that the extra heat loss is reduced. Indeed, the RAC temperature first was 382.8 K, while it now equals 380.5 K.

Changing RAC outer surface area

The same procedure is executed for the outer surface area. First the insulation outer temperature equalled 308.0 K with a total outer wall loss of 2.75 W. After multiplying the area by two, the outer wall loss increased to 2.87 W with a outer temperature of 303.9 W. This can be explained by the fact that heat loss from the insulation outside is largely countered by the low thermal conductivity of the layer. The layer works as it should.

Changing heating area

For the heating area, the initial values are 17.4 W of power that flows to the propellant, with a RAC temperature of 382.8 K and an almost similar propellant outlet temperature at 381.6 K. Doubling the heating area will only raise the convection heat by a very small amount and will see both temperatures at 381.8 K. This is not surprising: once the propellant flows through the exchanger for an extended period of time, it will reach the same temperature.

Dividing the heating area by ten is another matter: the heat flowing to the propellant is then equal to 12.8 W with an RAC temperature of 474.2 K and a propellant outlet temperature of 359.8 K. The heat reduction, normally going to the propellant, is used to heat the RAC and is then lost to the ambient. This is correct, losses went up with 4.5 W due to the change.

Changing mass flow

Increasing the mass flow with a factor of two will increase the thermal efficiency of the heat exchanger; the resulting power to the propellant is 19.0 W, which is higher than the 17.4 W first reported. This is due to the fact that more cold propellant enters the heat exchanger at the same time, thus extracting more heat. However, the resulting outlet temperature is lower (343.8 K) because the increase in convection heat to the propellant is not a factor two.

Regarding the pressure loss in the channels, this initially was equal to 5332 Pa. This increased to 17 879 Pa because of the doubling of the mass flow. This is explained by the Darcy-Weisbach equation for pressure loss (see Equation 4.48 in Chapter 4), which has a dependency on the propellant flow velocity squared. However, the pressure loss increase is not a factor four, because the Darcy-Weisbach friction factor decreases with higher Reynolds numbers. The Reynolds number (see Equation 4.10) increases because in the increased flow velocity.

3.4.3. Verification for NIST relations

Some variables that are used in the models as presented in Chapter 4 are temperature-dependent. Using NIST³, relations were derived to allow for the determination of the variables when the propellant temperature was known. An example is the propellant enthalpy, which is a measure of the inherent energy the propellant possesses. The temperature can be derived from the enthalpy by the Shomate equation (see footnote). These Shomate equations were all added to the tool and verified by inputting various enthalpies and comparing the result to the NIST website. Whenever such a temperature-dependent relation is introduced in the next chapter, it will be accompanied by a footnote, similar to this section. It indicates that the relation has been verified.

³<https://webbook.nist.gov/>, accessed on 27-11-2020.

3.5. Validation

Validation determines whether a developed tool actually represents real-life experimental results [53]. Validation for the [PDT](#) will be done in two parts: the tool's thermal results are compared to the experimental data from Leenders' three cases and all tool results (including pressure losses and nozzle performance) will be checked by performing experiments on [STT2](#). The latter is explained in more detail in Section 6.1, while the former is done below.

All relevant tables and figures were already referenced in Subsection 3.4.1. For case 1, the [PDT](#) outputs a slightly lower [RAC](#) temperature than the [STT1](#) heat exchanger reached during the experiment. This could be attributed to a different convectional heat transfer coefficient to the ambient, as this is the largest contributor to the heat loss. However, the results are within the 10 % criterion, so this is not seen as an issue. Case 2 also sees a thermal difference which is not too large (again within the criterion), so this is seen as a valid [PDT](#) output as well. Case 3 sees larger differences, due to the propellant convection being overestimated by a larger margin. This can be seen because the "valleys" are too large compared to the actual [RAC](#) temperature.

A possible explanation for this phenomenon is the following: the entrance and exit regions, which are the manifolds where the propellant enters and exits the heat exchanger and is distributed among the channels, is very hard to model due to its unconventional shape. As such, its heating area is simply added to the heating area of the channels. The channel area is very efficient in heat transfer (it is designed for this purpose), so the capability of the entrance and exit regions will be overestimated. Other explanations for the temperature differences could be the experiment input radiation being lower (or having a lower efficiency), slightly different area sizes or the thermal conductivity of the Saffil M-Fil being lower than expected.

Validation for the third case, with mass flow, is thus not completed. To achieve a satisfactory validation for the propellant flow, the experimental results from [STT2](#) have to be used.

3.6. Conclusions & recommendations

The [PDT](#) developed in this chapter allows the user to evaluate an [STP](#) thruster and aid in design choices to increase the performance, mainly thrust and specific impulse. The tool is versatile in various areas, such as heat exchanger shape, dimensions, channel layout and propellant. It has been verified and validated for simulations without mass flow and with an optional layer of insulation applied. Verification of the simulation with mass flow was also (partly) finished, by altering key input parameters which affected the output. It is recommended though to find a similar tool or model to enhance this verification. This could not be achieved in the time that was left for this project. Validation could not be completed for the convectional heat transfer to the propellant. Furthermore, the nozzle performance and the pressure loss in the heat exchanger also need to be validated. In order to do so, experiments on [STT2](#) are needed.

Next to these recommendations, the following list also gives some further commendations to enhance the capabilities and/or accuracy of the [PDT](#):

- Implement a ray tracing model. It will allow for a more accurate determination of the absorbed power in the cavity. By doing so, design choices such as spikes and corrugating walls can be evaluated. Note that this was done by Das [48], so a start could be made there.
- Allow the tool to calculate the effects of two-phase flow, both on pressure loss as on convection in the heat exchanger. Most [STP](#) propellants are stored in the liquid phase due to the high density (and thus low storage volume), so by heating them two-phase flow occurs.
- Model the thermal en pressure losses in other parts of the engine, such as in tubing, mounting and nozzle. That way, the performance can be more accurately predicted.

- Expand the nozzle performance model in order to allow for a more accurate determination of the performance. Now, the tool simply applies two flat penalties to the specific impulse and thrust.
- Extend the tool so that other channel layouts are also accepted. One can think of a porous medium which is inserted in the channels.

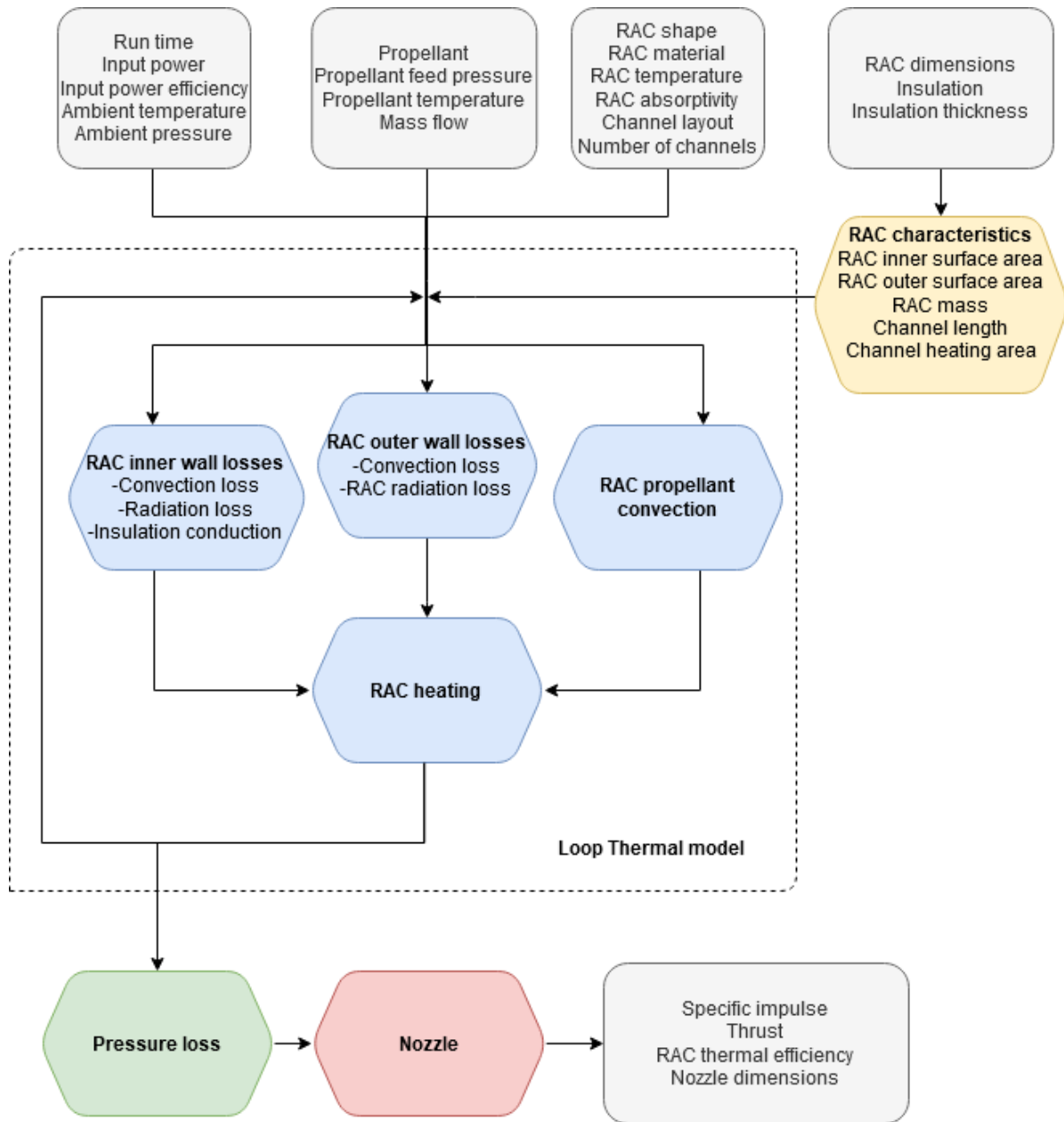


Figure 3.2: PDT flowchart, showing its major elements and inputs and outputs.

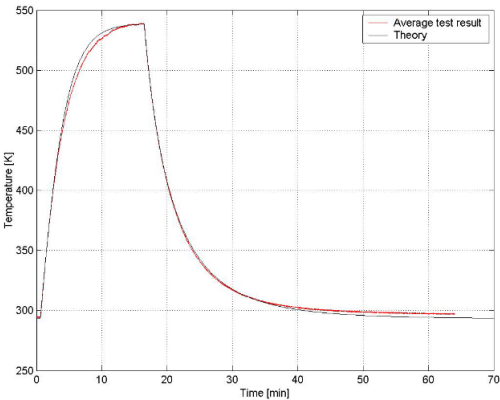


Figure 3.3: Case 1: experimental (in red) and theoretical Matlab (in black) RAC temperatures by Leenders [3].

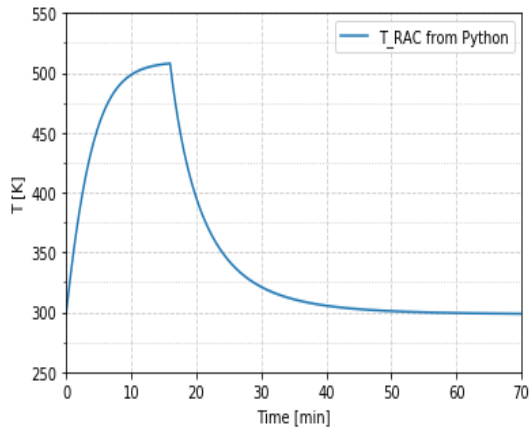


Figure 3.4: Case 1: PDT RAC temperatures by Takken.

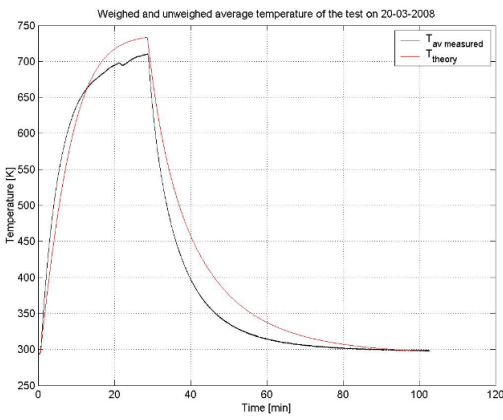


Figure 3.5: Case 2: experimental (in black) and theoretical Matlab (in red) RAC temperatures by Leenders [3].

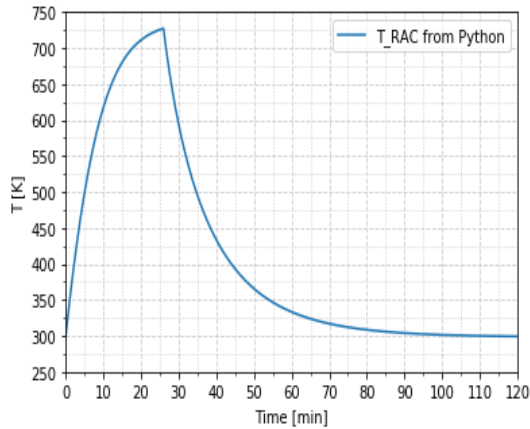


Figure 3.6: Case 2: theoretical Python RAC temperatures by Takken.

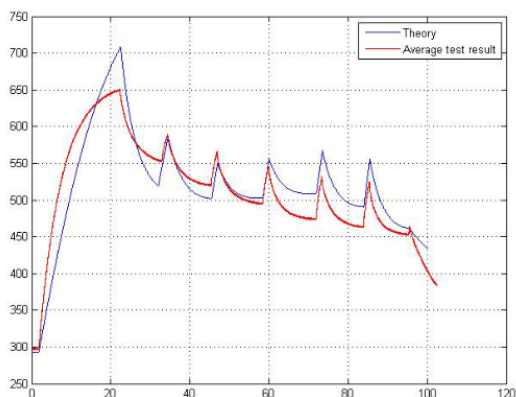


Figure 3.7: Case 3: experimental (in red) and theoretical Matlab (in black) RAC temperatures by Leenders [3]. The axes labels are time (in min) for the horizontal axis and RAC temperature (in K) for the vertical axis. Note that Leenders' experimental and theoretical values do not match well.

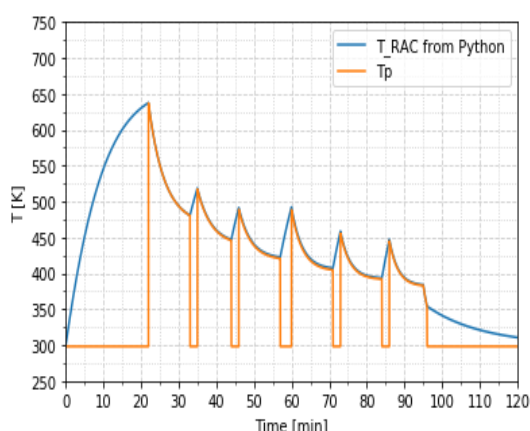


Figure 3.8: Case 3: theoretical Python temperatures by Takken. In blue is the RAC temperature, in orange is the outlet propellant temperature.

4

Preliminary Design Tool theory

The goal, inputs, outputs, verification and validation of the PDT were all dealt with in Chapter 3. The theory, models and equations behind the tool will be explained in this chapter. The chapter is based on the overview as given in Figure 3.2. It starts off with a heat transfer overview, where all heat flows are explained. Then, the three governing heat transfer aspects (convection, radiation and conduction) are discussed, followed by a section on pressure losses in the RAC. In the end, the propellant temperature and pressure are then inputs to calculate the thrust which will be produced in the nozzle.

4.1. Heat transfer overview

The RAC will experience heat transfer in the form of three aspects: convection, conduction and radiation. Convection will account for the losses on both inner and outer walls, while it is also the driving force for the heating of the propellant. Conduction will not be taken into account for the RAC (see assumption PDT-A-4), but it will be if insulation is applied, due to its low thermal conductivity. Radiation is both present on inner and outer walls as well, while it is also the heat input in the RAC.

The heat transfer part of the model will be transient (time-dependent, per requirement) and show the heat gain and losses for each time-step t_{step} in s. These heat flows summed, there will be a resultant heat power Q_{res} (in W), which either will heat up the RAC if positive or lower its temperature if negative as Equation 4.1 shows.

$$\Delta T_{RAC} = \frac{Q_{res} \cdot t_{step}}{M_{RAC} \cdot c_{RAC}} \quad (4.1)$$

Where M_{RAC} is the RAC mass (without insulation) in kg and c_{RAC} is the material's heat capacity in $\text{J kg}^{-1} \text{K}^{-1}$. The resultant power is calculated via Equation 4.2.

$$Q_{res} = Q_{in} - Q_{loss} \quad (4.2)$$

Where Q_{loss} are the power losses, which leave the system in five forms, see Equation 4.3.

$$Q_{loss} = Q_{conv,cavity} + Q_{rad,cavity} + Q_{conv,outerwall} + Q_{rad,outerwall} + Q_{conv,propellant} \quad (4.3)$$

All these variables are in W. Note that the fifth and last form is not really a loss, but the driving principle of the heat exchanger. More information about convection, conduction and radiation is to be found in the subsequent sections.

4.2. Convection

Convection is defined as the heat transfer between a solid and a moving fluid [23]. There are two forms of convection discussed in this section, free (or natural) and forced. The first occurs without the 'forced' motion (e.g. by a pump) of the fluid, for instance when a hot wall is exposed to wind-still cold air. The air heats up, expands, has a lower density and rises, essentially creating its own motion. Forced convection is the other aspect and is the governing principle in e.g. refrigerators, where gas is pumped around to cool down the system.

For this theoretical model, both free and forced convection are encountered. The RAC will experience free convection at the outer walls (either the RAC itself or the surrounding insulation) and in the cavity. It is thus assumed that the surrounding medium (which is air) will be at rest. Forced convection is the driving heat transfer principle to heat up the propellant in the channels. Note that part of this section was already discussed in Section 5.1.

Convection is governed by Equation 4.4.

$$Q_{conv} = h \cdot A \cdot \Delta T \quad (4.4)$$

Where Q_{conv} is the convective heat transfer in W, h is the convective heat transfer coefficient in $\text{W m}^{-2} \text{K}^{-1}$, A is the applicable area in m^2 and ΔT is the temperature difference in K between the hot and cold medium. Note that ΔT is dependent on the application, during the subsequent sections it will be clear what temperature difference is meant.

The equation seen above is very straightforward, but the values of h can range from $10 \text{ W m}^{-2} \text{ K}^{-1}$ to $11\,600 \text{ W m}^{-2} \text{ K}^{-1}$ and beyond, depending on fluid properties, solid dimensions, fluid velocity, fluid viscosity etc. Often these values are based on empirical relations, where the Nusselt number Nu (dimensionless) is used to determine h , see Equation 4.5 [23].

$$h = \frac{\text{Nu} k}{L_s} \quad (4.5)$$

Where L_s is the characteristic length in m and k the thermal conductivity in $\text{W m}^{-1} \text{ K}^{-1}$. Numerous equations exist to calculate the Nusselt number. Subsections about propellant convection, inner cavity convection and outer wall convection are given hereafter to explain the equations used for this model.

4.2.1. Propellant convection

The driving principle for the RAC, essentially a heat exchanger, is convection from the hot wall to the cold propellant. To calculate the power flowing to the propellant, first the Nusselt number and then the convective heat transfer coefficient are calculated according to set of Equations found in 4.6-4.9 [54]. The first equation is a result from assumption PDT-A-4, which states that the heat exchanger's temperature is uniform due to the high conductivity of the material. As such, the Uniform Wall Temperature (UWT) boundary condition is applied (see later in this chapter). Because the temperature difference between channel wall and propellant is changing (most of the times: decreasing), the logarithmic mean temperature difference is introduced as the last term in Equation 4.6. The derivation for the equation is given in Bergman et al. [54].

$$Q_{conv,P} = h_P \cdot A_{ch} \cdot \frac{T_{p,out} - T_{p,in}}{\ln\left(\frac{T_w - T_{p,in}}{T_w - T_{p,out}}\right)} \quad (4.6)$$

$$h_P = \frac{Nu_P k_P}{D} \quad (4.7)$$

$$A_{ch} = \pi \cdot D \cdot L_{ch} \quad (4.8)$$

$$T_b = \frac{T_{p,in} + T_{p,out}}{2} \quad (4.9)$$

Note that L_s has been replaced by the channel diameter D in m. Furthermore, the area A is now the inner wall channel area in m^2 . Note that the wall temperature T_w next to the channel is equal to the RAC temperature T_{RAC} , because it is assumed that the heat exchanger (apart from the insulation) has a uniform temperature due to its high conductivity. The last part of Equation 4.6 is the so-called logarithmic mean and is dependent on the boundary conditions, see further down. Note that k_p is evaluated at the bulk temperature T_b , which is the mean of the incoming propellant temperature $T_{p,in}$ and outgoing propellant temperature $T_{p,out}$, all in K.

The Nusselt number equations still missing above are dependent on a number of factors. These aspects are listed as follows:

- Reynolds number
- Flow regime
- Geometric disturbances
- Channel cross-sectional shape
- Boundary conditions
- Channel layout
- Microchannels

Reynolds number

One of the most important aspects that impacts the Nusselt number is the flow type, which exists in three forms: laminar, transitional and turbulent. The type is dependent on the dimensionless Reynolds number Re , which is given in Equation 4.10 [54]. The Reynolds number is defined as the ratio of inertial forces to viscous forces and is dependent on a characteristic dimension, which in the case of internal flows is the diameter D in m. An internal flow is, in general, laminar for $Re_D \leq 2320$, turbulent for $Re_D \geq 10\,000$ and transitional inbetween. However, Nusselt number equations for certain flow types often give their own ranges for the Reynolds numbers, see later in this chapter.

$$Re_D = \frac{\rho v D}{\mu} = \frac{\dot{m} D}{A \mu} = \frac{4 \dot{m}}{\pi D \mu} \quad (4.10)$$

Here, ρ is the local propellant density (kg m^{-3}), v the propellant velocity (m s^{-1}), \dot{m} the mass flow, A the cross-sectional area of the channel and μ the dynamic viscosity (Pa s). Note that the equation

for mass flow in a circular channel is applied to convert the density and velocity to other variables. Furthermore, μ is evaluated at the bulk temperature T_b (see Equation 4.9). The subscript "D" indicates that the characteristic length for pipe flow is the pipe diameter D .

In general, a turbulent flow has a higher convection heat transfer than a laminar flow. A higher mass flow or lower channel diameter is thus beneficial. However, one should take care that the flow velocity is not too high. Zandbergen [23] gives a relation for an upper limit to the channel gaseous propellant velocity to prevent the so-called water hammer, which is given in Equation 4.11.

$$v_{max} = 175 \left(\frac{1}{\rho} \right)^{0.43} \quad (4.11)$$

Flow regime

Next to the flow type, one also needs to assess whether the flow regime is fully developed or not. Two types of flow development are known: hydrodynamically and thermally. When a flow is hydrodynamically developed, the velocity profile will be constant throughout the pipe. For thermally developed flow, the thermal profile will not change along the axial direction.

In a particular section at the start of the flow, also called the thermal entrance length, the flow has not yet developed and the thermal profile and thus Nusselt number vary. For laminar flow, the entrance length is estimated by Equation 4.12, while for turbulent flow it is given by Equation 4.13 [54].

$$\frac{L_{T,e}}{D} = 0.05 Re_D Pr \quad (4.12)$$

$$\frac{L_{T,e}}{D} = 10 \quad (4.13)$$

Where $L_{T,e}$ is the thermal entrance length in m and Pr is the dimensionless Prandtl number. The Prandtl number is defined as the ratio of momentum diffusivity to thermal diffusivity [54]. The number connects the temperature and the velocity profiles. Large Prandtl number fluids, such as oils, have a longer thermal entrance length than hydrodynamic entrance length; it takes longer for the thermal profile to develop when compared to the velocity profile.

The Prandtl number can be considered as almost constant over a large range of temperatures. For gases, it can be approached using Equation 4.14, but the latter Equation 4.15 is more precise. In those equations, γ is the specific heat ratio (dimensionless), μ the dynamic viscosity (in $\text{kg m}^{-1} \text{s}^{-1}$), c_p the specific heat at constant pressure (in $\text{J kg}^{-1} \text{K}^{-1}$) and k the conductive heat coefficient (in $\text{W m}^{-1} \text{K}^{-1}$).

$$Pr = \frac{4\gamma}{9\gamma - 5} \quad (4.14)$$

$$Pr = \frac{\mu c_p}{k} \quad (4.15)$$

In general, convection heat transfer is higher in the entrance regions. Often, equations for the Nusselt number are averages for the whole pipe length, including the entrance length.

Geometric disturbances

Next to flow type and development of the flow, non-straight aspects such as bends, valves and turns also affect Nusselt number. Often, they create small vortices, causing the flow to enter a turbulent state even at lower Reynolds numbers. Furthermore, the pressure loss is increased in these bends. Leenders suspects that the bend at the entrance caused a turbulent flow in the channels during his experiments, even at lower Reynolds numbers [3]. Meyers [55] argues that the insertion of elements or the roughening of walls could also enhance heat transfer.

Channel cross-sectional shape

Nusselt number equations are susceptible to the shape of the channel cross-section. However, this is often mitigated by using the so-called hydraulic diameter D_h (in m). The hydraulic diameter is determined by Equation 4.16, where A is the cross-sectional area in m^2 and S the wetted perimeter in m of the tube.

$$D_h = \frac{4A}{S} \quad (4.16)$$

The hydraulic diameter is used in equations as the characteristic dimension whenever the tube is non-circular. Notice that for circular channels, D_h will equal the circle diameter D . Note that, for turbulent flow, the equations will have an error of approximately 10 %, while for laminar flow the error is larger [23]. Regarding the latter, Incropera et al. [9] advise to use the tabulated values from their Table 8.1.

Boundary conditions

Two main boundary conditions exist for an RAC: the previously mentioned UWT and Uniform Heat Flux (UHF). The former will be assumed for this model, which simply means that the RAC wall temperature will be considered constant for the whole length of the channel. For laminar flow, the Nusselt number can be considered constant when the flow is fully developed. The values can be found analytically and are given in Equation 4.17 by Meyers [55]. Meyers bases his conclusions on Bergman [54]. The constants can be derived because the assumption is made that there is no advection of thermal energy in the radial direction in steady, laminar flow. For turbulent flow this is not the case, because the thermal energy varies along the radial direction. Because of this, no such analytical solutions exist for turbulent flow; instead, various empirical relations have been established, see later in this chapter.

$$\begin{aligned} Nu_D &= 4.36(UHF) \\ Nu_D &= 3.66(UWT) \end{aligned} \quad (4.17)$$

Note that these values can only be applied for laminar cases and in case that the entrance length is relatively short. In general, the average Nusselt number over the whole pipe will be higher than the values presented here because of the entrance length.

Channel layout

The channel layout options do influence the Nusselt number as well [23]. There are two options available in the PDT: straight and spiraling (see assumption PDT-A-2 in Chapter 3). Bergman et al. [54] suggests that the heat transfer is enhanced due to the centrifugal forces that are introduced in spiral flow.

Microchannels

The last influence on the Nusselt number discussed here are microchannels. This paragraph is added for completeness as microchannels are not considered for the design due to the manufacturing lower limit of 1 mm. According to Morini [56] (also seen in Das [48]), experiments show that the general Reynolds number limits used to distinguish laminar and turbulent flow can differ for very small channels with a hydraulic diameter lower than 1 mm. Das already mentioned the influence of small channels on the Reynolds number in her thesis [48].

Nusselt number equations for propellant convection

Now that the important aspects have been handled, the equations for the Nusselt number used in the model are presented. The equations will be primarily dependent on the Reynolds number. Because this number is dependent on the temperature of the flow (which is not known), the Reynolds number will be calculated based on the inflow temperature (often 298.15 K) using Equation 4.10. This number will then indicate what equation to use, see below.

First of all, the equations for flow in linear channels will be given. For laminar flow in circular channels, Stephan's Equation 4.18 can be used [57]. It is valid for $Re_D \leq 2300$ and Prandtl numbers above 0.1.

$$Nu_D = 3.657 + \frac{0.0677 \left(Re_D Pr \frac{D}{L} \right)^{1.33}}{1 + 0.1 Pr \left(Re_D \frac{D}{L} \right)^{0.3}} \quad (4.18)$$

The equation takes the entrance region into account and is valid for uniform wall temperature. Notice that, for increasing channel length L , the Nusselt number value approaches the value given in Equation 4.17. Stephan's equation gives an average Nusselt number for the whole channel length. Its properties Re_D , Pr and k (to calculate h in Equation 4.7) are evaluated at propellant bulk temperature T_b (see Equation 4.9).

For higher Reynolds number flows in linear channels, the well-known Gnielinski equation given by Rohsenow [58] and Bergman [54] is used to calculate the average Nusselt number. The equation (see 4.19) is applicable for both transitional and turbulent flow in circular tubes for $0.5 \leq Pr \leq 2000$ and for $2300 \leq Re_D \leq 5 \times 10^6$. Other sources such as Taler [59] and Bergman [54] state a higher lower Reynolds number limit, namely 1×10^4 and 3000 respectively. The latter source also indicates that the equation may be used for the UWT boundary condition and that errors are generally within 10 %.

$$Nu_D = \frac{\frac{f_{DB}}{8} (Re_D - 1000) Pr}{1 + 12.7 \left(\frac{f_{DB}}{8} \right)^{\frac{1}{2}} \left(Pr^{\frac{2}{3}} - 1 \right)} \quad (4.19)$$

Here, f_{DB} is the Darcy-Weisbach friction factor (dimensionless) and the subscript "D" stands for the channel circular diameter in m. Several equations exist to calculate the friction factor for transitional and turbulent flow. The one described by Bergman [54] is used, see Equation 4.20. It has an applicable range of $3000 \leq Re_D \leq 5 \times 10^6$, although it will be used in the Gnielinski equation downwards to Reynolds numbers of 2300.

$$f_{DB} = (0.790 \ln (Re_D) - 1.64)^{-2} \quad (4.20)$$

Notice that the Gnielinski equation is used for relatively long tubes, where the effect of the entrance region is negligible. Because this is not the case for the RACs considered in this model, the equation can be modified as stated by Taler [59], see Equation 4.21. By modifying, the Nusselt number is calculated as an average for the whole pipe, including the entrance region.

$$Nu_D = \frac{\frac{f_{DB}}{8} (Re_D - 1000) Pr}{1 + 12.7 \left(\frac{f_{DB}}{8} \right)^{\frac{1}{2}} \left(Pr^{\frac{2}{3}} - 1 \right)} \left(1 + \left(\frac{D}{L} \right)^{\frac{2}{3}} \right) \quad (4.21)$$

For increasing channel lengths L , the modified Gnielinski equation will approach the original equation. Also note that the properties dependent on temperature, being Re_D , Pr and k for calculating h , are again considered at the bulk temperature T_b .

Figure 4.1 shows the Nusselt number versus the Reynolds number for various Prandtl numbers. The Nusselt number increases for increasing Prandtl numbers, which can be attributed to the fact that the thermal entrance length is increased for higher Prandtl numbers, which increases heat transfer to the propellant. Figure 4.2 shows the Nusselt number versus the Reynolds number for various L/D. The Nusselt number increases for increasing L/D for the same reason as above: the relative thermal entrance length with respect to the total length is longer, so the heat transfer increases.

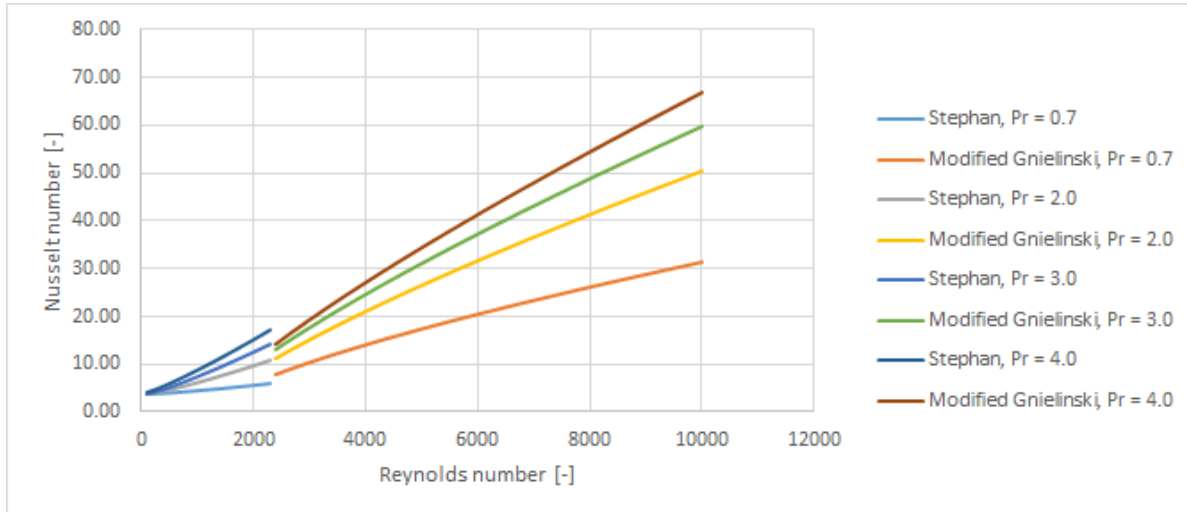


Figure 4.1: Nusselt number versus Reynolds number, for various Prandtl numbers and straight channels. L/D is equal to 0.01.

For turbulent flow in spiral tubing, Rohsenow [23, 58] states that the amount of accurate equations for the Nusselt number is limited. He shows a relation for developed turbulent flow, Equation 4.22, originally from Seban and McLaughlin [60]. It employs similar variables as the previous equations, D_c is the spiral diameter in m. Note that this relation is valid for $1 \times 10^4 \leq Re_D \leq 1 \times 10^5$. No Prandtl number range is given.

$$Nu_D = 0.023 \cdot Re_D^{0.85} \cdot Pr^{0.4} \cdot \left(\frac{D}{D_c} \right)^{0.1} \quad (4.22)$$

For lower Reynolds numbers a relation by Kalb and Seader (from Zandbergen [23]) was found, see Equation 4.23. It is valid for $0.7 \leq Pr_D \leq 5$.

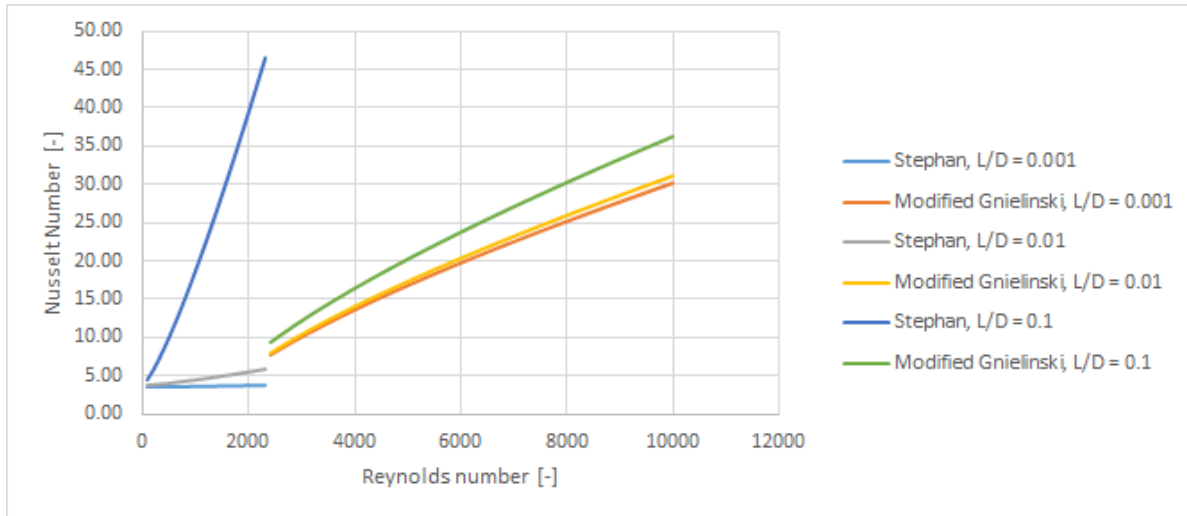


Figure 4.2: Nusselt number versus Reynolds number, for various L/D and straight channels. Prandtl number is equal to 0.7.

$$Nu_D = 0.913 \left(Re_D \left(\frac{D}{D_c} \right)^{0.5} \right)^{0.476} Pr^{0.2} \quad (4.23)$$

Again, both equations for spiral flow are evaluated at bulk temperature, which is a variable for Re_D , Pr and k for calculating h . Ferreira gives more information about convection heat transfer in spiral ducts in his thesis [61].

Figure 4.3 shows the Nusselt number versus the Reynolds number for various Prandtl numbers. The Nusselt number increases for increasing Prandtl numbers, for the same reason as for straight channels. Figure 4.4 shows the Nusselt number versus the Reynolds number for various D/Dc. The Nusselt number increases for increasing D/Dc because the increasing centrifugal forces contribute to the heat transfer [54].

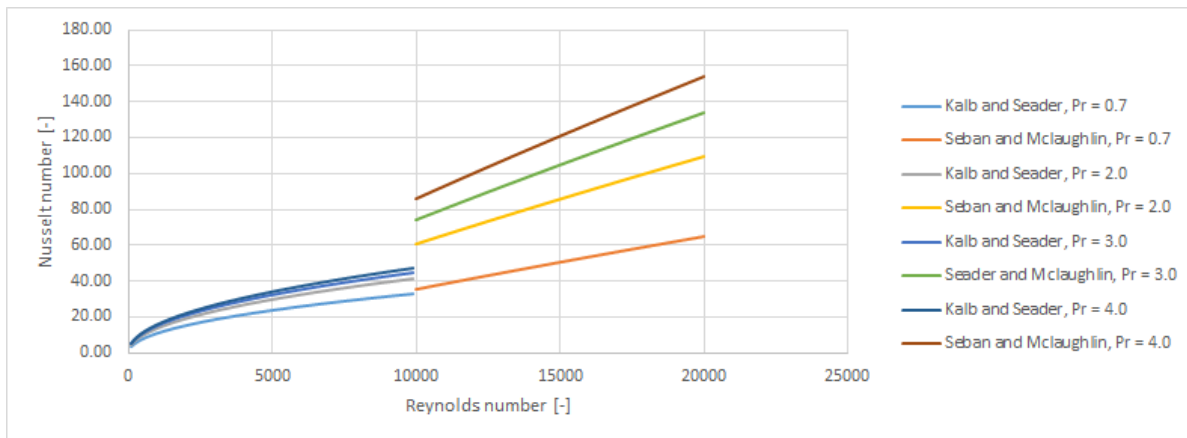


Figure 4.3: Nusselt number versus Reynolds number, for various Prandtl numbers and spiral channels. D/Dc is equal to 0.05.

Propellant outflow temperature calculation

Eventually, all equations from this section will be combined to calculate the outflowing propellant temperature. The bulk temperature T_b will be taken as the only unknown variable. All equations, being Equations 4.6, 4.7, 4.8, 4.9, 4.10, 4.15 and one of the Nu equations 4.18-4.23, will be rewritten to

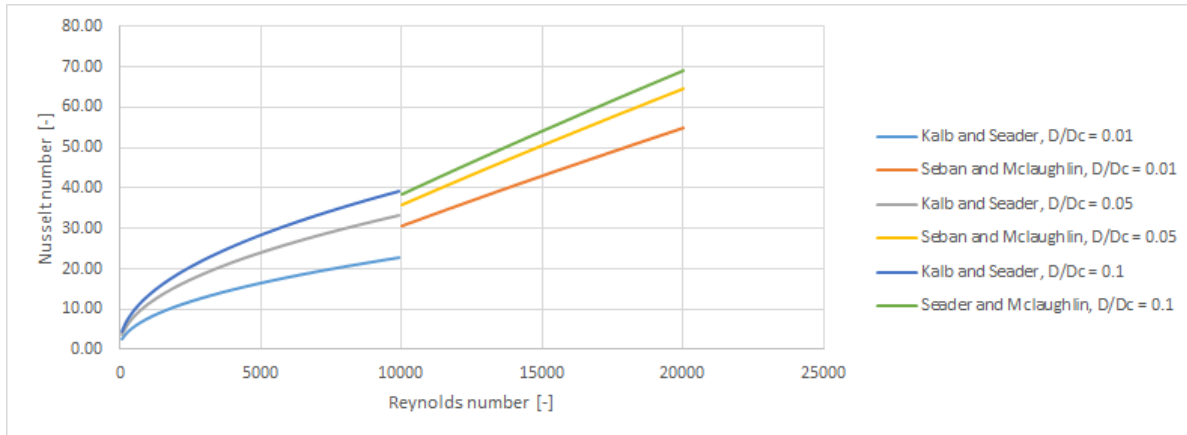


Figure 4.4: Nusselt number versus Reynolds number, for various D/Dc and spiral channels. Prandtl number is equal to 0.7.

have this temperature as the only unknown. Next to that, the properties used in these equations (k , c_p and μ) are added as bulk temperature-dependent equations as well¹. One last equation is needed to relate the power input from Equation 4.6 to the propellant temperature, which is Equation 4.24.

$$\Delta H = \frac{Q_{conv,x}}{\dot{m}} \quad (4.24)$$

Where \dot{m} is the mass flow (in kg s^{-1}) and ΔH is the change in enthalpy of the propellant in J kg^{-1} . This enthalpy increase can then be related to the propellant temperature increase via relations found in NIST². As such, there is a set of equations that can be solved for T_b . However, there is no closed analytical solution, so a built-in optimizer from Python will be used to numerically calculate T_b with an accuracy of 1×10^{-5} K.

4.2.2. Inner cavity convection

In a paper by Paitoonsurikarn et al. [62], a simplified correlation for h for free convection in cavities was found. The authors compared numerical simulation results (performed in Ansys Fluent) to experimental results. The equations hold for an evenly hot cavity which is horizontally oriented with a side opening, which means that the aperture is neither on the top nor bottom. This has influence on the way the hot air "escapes" the cavity. Starting with Equation 4.5, the Nusselt number can then be found using Equation 4.25. It is dependent on the Rayleigh number (dimensionless) which is defined by Equation 4.26.

$$Nu = 0.00324 Ra^{0.447} \quad (4.25)$$

$$Ra = \frac{g\beta\Delta T L_s^3}{\nu\alpha} \quad (4.26)$$

$$T_f = \frac{T_w + T_\infty}{2} \quad (4.27)$$

¹Derived from <https://webbook.nist.gov/>, accessed on 27-11-2020.

²<https://webbook.nist.gov/>, accessed on 11-03-2020.

In the latter equation, g is the gravitational acceleration in m s^{-2} , β is the thermal expansion coefficient in K^{-1} , ν the kinematic viscosity in $\text{m}^2 \text{s}^{-1}$ and α the thermal diffusivity, also in $\text{m}^2 \text{s}^{-1}$. Note that the latter three are all for the surrounding fluid (air) at film temperature, which is the average of the wall or RAC temperature T_w and ambient temperature T_∞ , both in K (see Equation 4.27). The temperature difference mentioned in Equation 4.26 is the actual temperature difference between (bulk) ambient air and the RAC outer wall. Note that no range for Prandtl number is given in the paper, although the equations will only be applied for air as a surrounding medium, so it is assumed to be no issue.

The kinematic viscosity can be calculated by Equation 4.28 [3]. In turn, the found value is used in Equation 4.29 to calculate the thermal diffusivity. The dimensionless Prandtl number Pr used in that equation is found by Equation 4.15. The symbols in the next two equations are the dynamic viscosity μ (in Pas), the density ρ (in kg m^{-3}), specific heat at constant pressure c_p in $\text{J kg}^{-1} \text{K}^{-1}$ and k in $\text{W m}^{-1} \text{K}^{-1}$. Note that again, all these values are evaluated for air at the film temperature and ambient pressure, which is one atmosphere. The equations relating these variables to the film temperature have been derived from NIST³ and have been verified by checking the variable for various temperatures. The user does not have to input the air values manually, they are all calculated by the PDT.

$$\nu = \frac{\mu}{\rho} \quad (4.28)$$

$$\alpha = \frac{\nu}{Pr} \quad (4.29)$$

The definition for the characteristic length L_s is given in Equation 4.30. Here, ϕ is the cavity angle (in rad), D_{cav} the average cavity diameter in m, D_{ap} the aperture diameter (also in m) and L the cavity length in m.

$$L_s = (4.79 \cos^{4.43}(\phi) - 0.37 \sin^{0.719}(\phi)) D_{cav} + (1.06 \cos^{3.24}(\phi) - 0.0462 \sin^{0.286}(\phi)) D_{ap} + (7.07 \cos^{5.31}(\phi) + 0.221 \sin^{2.43}(\phi)) L \quad (4.30)$$

These equations hold for cavities with and without aperture and both for conical and cylindrical ones. However, the prediction error can be up to 50%. A recommendation is thus to find empirical relations that fit the experimental results from the paper better. For now, this is used in the theoretical model. Combining all equation from this subsection leads to h , which can then be used in Equation 4.4.

Note that dynamic viscosity μ is dependent on temperature. It can be related via Sutherland's formula [63], see Equation 4.31.

$$\mu = \mu_0 \frac{T_0 + T_S}{T + T_S} \left(\frac{T}{T_0} \right)^{\frac{3}{2}} \quad (4.31)$$

Where μ_0 (in Pas), T_0 (in K) and T_S (in K) are all constants and reference temperatures found in Crane [63]. The formula is valid for both propellants (not water) and surrounding air. For water, because it vaporizes at some point and thus the equation above cannot be applied, NIST data⁴ was used to extract the relevant μ values and create a polynomial in Microsoft Excel.

³<https://webbook.nist.gov/>, accessed on 11-03-2020.

⁴<https://webbook.nist.gov/>, accessed on 11-03-2020.

The specific heat at constant pressure c_p also changes with temperature for all materials and fluids involved. NIST provides the Shomate equation with coefficients to calculate c_p when the temperature is known, both for propellant and RAC material. The thermal conductivity k is seen as linear with respect to the temperature, and the gradients and intersects for the propellants and the material are both again from NIST and Excel. Because NIST does not provide air data, the temperature dependent values for c_p and k were extracted from The Engineering Toolbox⁵ and polynomials were fitted to the data, again using Excel. These were verified by checking the values at various temperatures and comparing them to NIST⁶ values.

4.2.3. Outer wall convection

The convection coefficient for the outer wall is, similar to inner cavity convection, very susceptible to geometry, temperature, surrounding medium and so on. Equations 4.4, 4.5, 4.26, 4.28, 4.29 and 4.15 are reused, but another expression will be used to quantify the Nusselt number Nu . For a conical geometry this is Equation 4.32 [64], while for a cylindrical shape Equation 4.33 will be used [65]. The subscript "D" in the equations indicates that the used characteristic length L_s is the (base) diameter D in m of the cone or cylinder, because the cylinder is horizontal.

$$Nu_{con} = 0.7 + 0.35 (Ra_D)^{0.125} + 0.51 (Ra_D)^{0.25} \quad (4.32)$$

$$Nu_{cyl} = \frac{2}{\ln \left(1 + \frac{2}{\left(\left(0.518 Ra_D^{\frac{1}{4}} \left(1 + \left(\frac{0.559}{Pr} \right)^{\frac{3}{5}} \right)^{\frac{-5}{12}} \right)^{15} + \left(0.1 Ra_D^{\frac{1}{3}} \right)^{15} \right)^{\frac{1}{15}}} \right)} \quad (4.33)$$

Note that the resulting Nusselt number will be used as an average for the whole outer area of the cone or cylinder, including any end caps and apertures present. The area A in Equation 4.4 will be adjusted to include these surfaces and exclude the apertures.

Again, the resulting outer wall convection heat transfer has its errors compared to the real experimental data. For now, the equations from this subsection are used, but it is recommended to update them accordingly.

4.3. Radiation

Radiation is the heat transfer from a hot to a cold object without the use of a medium, in contrast to conduction and convection which require a medium to transfer heat energy. One calculates the outgoing radiation heat transfer Q_{rad} (in W) of an object by Equation 4.34.

$$Q_{rad} = \epsilon \sigma A (T_1^4 - T_0^4) \quad (4.34)$$

Here, ϵ is the object's emissivity (dimensionless), which is dependent on the material and coating used. A so-called blackbody has an emissivity of 1, while grey objects have one between 0 and 1.

⁵<https://www.engineeringtoolbox.com>, accessed on 07-08-2020.

⁶<https://webbook.nist.gov/>, accessed on 07-08-2020.

σ is the Stefan-Boltzmann constant ($\text{W}/\text{m}^2/\text{K}^4$). The object of temperature T_1 (in K) is completely surrounded by an object of temperature T_0 (in K) for this equation to be true.

Both cavity and outer wall will experience radiation. The outer wall will be hotter than its surroundings, so there will be outgoing radiation. The inner cavity will have the same, but it will also be the location where power flows in via focused (solar) radiation, which is the working principle for STP. First, the inner cavity radiation will be discussed (starting with the outgoing radiation and then the incoming irradiation), followed by the outer wall outgoing radiation.

Note that, in this section, it will be assumed that all walls are grey, meaning that all walls will radiate heat uniformly and diffusely (in all directions). This is in opposition to direct radiation, which is unidirectional.

4.3.1. Inner cavity radiation

The inside of the RAC will experience both outgoing radiation loss and incoming irradiation. In the next two subsections, the theory behind the models that will deal with this form of heat transfer is explained.

Outgoing cavity radiation

Once the heat exchanger starts heating up, its inner wall will have a higher temperature when compared to its surroundings. It will start to radiate heat, which in this case can be considered diffuse (in all directions). However, only the radiation going in the direction of the cooler aperture or opening will contribute to radiation loss. Thus, view factors need to be applied, which indicate the amount of radiation towards a specific wall [23]. The factors F themselves are dimensionless. For various geometrical figures, Howell has derived the view factors equations⁷.

Cone

For the cone, only one surface (the inner cone wall, called surface 1) will radiate heat towards the base (surface 2), see Figure 4.5. If the aperture (or opening), called surface 3, does not cover the whole base, the remaining inner wall next to the aperture (still surface 2) will have the shape of a ring. The aperture is not shown in the figure, but it has a circular shape and is located in the middle .

The expression for the view factor from surface 1 to 1 (thus, to itself) is derived from Howell's expression C-110 and is shown as Equation 4.35. The expression for the view factor from surface 1 to surface 3 is derived from Howell's expression C-117 and is found in Equation 4.36. From deduction, the expression for the view factor from surface 1 to the remaining ring surface 2 is found in Equation 4.37. The inner surface 2 can only radiate towards surface 1, as it is in the same plane as the aperture, hence Equation 4.38.

In all those equations, the parameter r is the radius of the base, r_3 is the aperture radius and h is the height (length) of the cone. All parameters are in m.

$$F_{1-1,cone} = 1 - \left(\frac{1}{1 + H^2} \right)^{\frac{1}{2}}, \quad H = \frac{h}{r} \quad (4.35)$$

$$F_{1-3,cone} = \frac{R^2}{(1 + H^2)^{\frac{1}{2}}}, \quad R = \frac{r_3}{r}, \quad H = \frac{h}{r} \quad (4.36)$$

⁷<https://web.engr.uky.edu/rtl/Catalog/>, accessed on 17-07-2020.

$$F_{1-2,cone} = 1 - F_{1-1,cone} - F_{1-3,cone} \quad (4.37)$$

$$F_{2-1,cone} = 1 \quad (4.38)$$

Cylinder

For a cylinder, two surfaces radiate towards the aperture: the cylinder inner wall (surface 2 in Figure 4.6) and the base wall (surface 3, not shown). Both their view factors towards the aperture (surface 1) have been derived from C-41 and C-82 from Howell and are displayed in Equations 4.39 and 4.40 respectively. All parameters are shown in Figure 4.6 and are again in m.

$$F_{2-1,cyl} = \frac{1 - H^2 - R^2 + (X^2 - 4R^2)^{\frac{1}{2}}}{4RH}, \quad R = \frac{r_1}{r_2}, \quad H = \frac{h}{r_2}, \quad X = H^2 + r^2 + 1 \quad (4.39)$$

$$F_{3-1,cyl} = \frac{1}{2} \left(X - \left(X^2 - 4 \left(\frac{R_3}{R_1} \right)^2 \right)^{\frac{1}{2}} \right), \quad R_1 = \frac{r_1}{h}, \quad R_3 = \frac{r_3}{h}, \quad X = 1 + \frac{1 + R_3^2}{R_1^2} \quad (4.40)$$

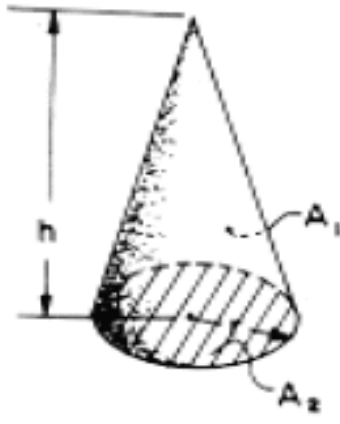


Figure 4.5: Cone with surfaces 1 and 2. Surface 3, the aperture, is not shown.

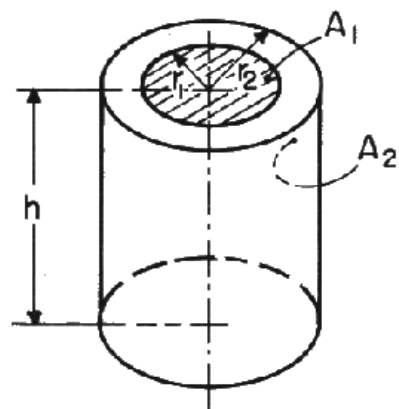


Figure 4.6: Cylinder with surfaces 1 and 2. Surface 3, the bottom wall is not indicated.

Now that the view factors are known for both geometrical figures, one can calculate the radiation loss using the general Equation 4.34, multiplied by the view factor. Note however, that outgoing radiation can also radiate towards other inner walls. Once it reaches this other wall, it will be partly absorbed and partly reflected, according to Equation 4.41 for opaque walls.

$$\rho + \alpha = 1 \quad (4.41)$$

Where ρ is the dimensionless reflectivity and α is the dimensionless absorptivity. Note that, according to Kirchhoff's law, α and emissivity ϵ are equal at some specific known temperature and wave length [23]. However, if both are known, one can take the more accurate α .

Thus, when using multiple inner walls, one starts off with radiation emission from multiple walls, which radiate diffusely and uniformly. The energy partly leaves the system via the aperture but can also fall upon another wall, where the process of absorption and reflection repeats. Python can loop a few times through this process numerically, to approach the final radiation loss from the inner cavity. Conversely, one could use Gebhart factors (also used by Leenders).

Incoming cavity radiation

The incoming power of the **RAC** will be absorbed by the cavity wall according to Equation 4.42. Here, α is the absorptivity (dimensionless), dependent on material, coating and radiation wave length.

$$Q_{in} = \alpha Q_{rad,in} \quad (4.42)$$

However, for an **RAC** it is not as simple as applying Equation 4.42. The non-absorbed energy will be reflected, as only opaque materials will be used which do not transmit the incoming radiation. The reflected energy will partly exit the system, but a part will again fall on an (opposite) wall, repeating the cycle. View factors F (dimensionless) again come into play here, as they indicate the amount of outgoing radiation which falls on another wall (to be absorbed). However, view factors are only applicable in case of a diffuse emitting wall, which radiates in all directions. Calculating the resulting radiation input can be achieved by making a ray tracing model (see e.g. the thesis by Das [48]), but that will be out of the scope for this thesis. So, the assumption is made that the incoming irradiation will be reflected diffusely. In that case, the same method as in the previous subsection will be applied: Python will calculate the radiation gain by looping through a series of radiation absorption, reflection and loss per wall, using the view factors.

Later in the thesis, it was found out that Gebhart factors could also be used to calculate the reflection losses for incoming radiation [23]. They would give similar results as the method above. Because of the small amount of time remaining, it was chosen to keep the current method.

It is recommended for future users of this theoretical model to construct the aforementioned tool in order to find **RAC** shape influences on the radiation absorbed power. When that happens, design choices such as a spike can also be evaluated. Needless to say, reducing the aperture area will decrease the radiation and convection loss.

4.3.2. Outer wall radiation

For the outer wall, radiation is simply calculated by Equation 4.34. In order to do so, it is assumed that the surroundings of the heat exchanger is at a uniform temperature. The temperature of the surroundings will be taken as the cooler temperature, while the **RAC** temperature is the hotter temperature. If an insulation layer on the outside of the heat exchanger is applied, the insulation outer wall temperature instead of the **RAC** temperature is taken.

4.3.3. Area

The involved area of heat transfer is very important, as the amount of power transferred depends on it linearly, see the sections on radiation and conduction. For the two geometrical figures discussed here, the inner and outer areas can easily be determined by simple formulas. However, often in real life the applicable area is much larger than the calculated area, due to the addition of connectors, thicker walls, more insulation etcetera. For instance, in the cases discussed hereafter in this chapter, the calculated outer **RAC** area was 0.0028 m^2 while the actual area equaled 0.0039 m^2 . This is a huge difference, which makes the model output inaccurate temperatures for **RAC** and propellant.

For this model, it is chosen to keep the calculation of areas in there. However, one can override these values by simply adding the areas themselves manually.

4.4. Conduction

Conduction Q_{cond} is the transfer of heat energy through a stationary medium because of temperature differences inside the medium [23]. It is dependent on a material's property, temperature variation and shape, see the next general Equation 4.43.

$$Q_{cond} = k \cdot A \cdot \frac{\Delta T}{t} \quad (4.43)$$

Where k is the material's thermal conductivity in $\text{W m}^{-1} \text{K}^{-1}$, A the area in m^2 , ΔT the temperature difference (in K) between a hot and cold wall and t the wall thickness in m.

The conduction for this model will only be considered in case that insulation is applied. It is assumed that the spread of heat through the RAC will be instantaneous as it is made of high-conductive material. The assumption holds well in case copper is used, as the four thermocouples Leenders attached to his RAC all outputted temperatures close to each other [3].

In case insulation is used, an extra temperature parameter is added (the insulation wall temperature) to the model. In order to calculate this temperature and thus the outer wall losses in the form of convection and radiation, the conduction through the insulation wall will be equated to the outer wall convection and radiation losses. See Equation 4.44.

$$Q_{cond,insu} = Q_{conv} + Q_{rad} \quad (4.44)$$

For a cylinder, Equation 4.45 can be applied to calculate the conductive heat transfer [23]. Unfortunately, no such equation exists for conically shaped insulation, so this equation will apply for that as well.

$$Q_{cond,insu,cylinder} = \frac{2\pi k L}{\ln\left(\frac{R_o}{R_i}\right)} \Delta T \quad (4.45)$$

Where R_o is the outer cylinder radius (in m), R_i the inner one (in m), L is the cylinder length (in m). Note that k is the thermal conductivity of the insulation in $\text{W m}^{-1} \text{K}^{-1}$. It varies with temperature, Equation 4.46 was found by Leenders for the Saffil M-Fil insulation by fitting an exponential line using Excel.

$$k = 0.0665 \cdot e^{\left(0.0015 \frac{T_{RAC} + T_{insu}}{2} - 273.15\right)} \quad (4.46)$$

Equation 4.43 then can be transformed to Equation 4.47.

$$\frac{2\pi k L}{\ln\left(\frac{R_o}{R_i}\right)} (T_{RAC} - T_{insu}) = hA(T_{insu} - T_{amb}) + \epsilon_{insu} \sigma A (T_{insu}^4 - T_{amb}^4) \quad (4.47)$$

There is no closed analytical solution for Equation 4.47, but Python can solve it numerically for the insulation temperature T_{insu} (in K). Afterwards, the convection and radiation loss from the insulation wall can be calculated.

4.5. Pressure loss

An engine's nozzle is designed for a certain chamber pressure. This pressure is a result of other design variables and propellant properties, see Equation 2.9. Before the fluid reaches the nozzle chamber, it will experience pressure loss in the heat exchanger and tubes. The feed pressure is thus the sum of the chamber pressure and this pressure loss and cannot be set as a control variable by the designer; it is merely a result of other chosen design variables, such as mass flow and chamber temperature. This section will show the relations necessary to determine the pressure loss in the RAC channels. Note that the pressure loss in the tubes is not considered, see assumption PDT-A-11.

The pressure drop Δp (in Pa) in the channel(s) can be found using the Darcy-Weisbach equation (see 4.48) [23] for smooth piping.

$$\Delta p = f_{DB} \frac{L}{D} \frac{1}{2} \rho v^2 \quad (4.48)$$

Where f_{DB} is the Darcy-Weisbach friction factor (dimensionless), L is the characteristic length (here: tube length) in m, D is the tube inner diameter in m, ρ is the propellant density in kg m^{-3} and v is the velocity in m s^{-1} . The friction factor is dependent on the Reynolds number Re (based on tube diameter) and several equations exist for both laminar and turbulent flow. For laminar flow in straight pipes (lower Reynolds numbers), the equation by Poisseuille [23, 66] is used, see Equation 4.49.

$$f_{DB} = \frac{64}{Re_D} \quad (4.49)$$

The equation for turbulent flow in straight pipes for range $2300 \leq Re_D \leq 2 \times 10^4$ was given earlier in Equation 4.20, but will be repeated here in Equation 4.50 for clarity.

$$f_{DB} = (0.790 \ln(Re_D) - 1.64)^{-2} \quad (4.50)$$

For laminar flow in spiral tubing, Equation 4.51 from White is recommended by Guo [66] and Zandbergen [23].

$$f_{DB} = \frac{1}{1 - \left(1 - \left(\frac{11.6}{Re_D \cdot \left(\frac{D}{D_C} \right)^{0.5}} \right)^{0.45} \right)^{\frac{1}{0.45}}} \cdot \frac{64}{Re_D} \quad (4.51)$$

For turbulent flow in spiral piping, the relation in Equation 4.52 will be used. It was found by Ito and recommended by Guo [66] and Zandbergen [23].

$$f_{DB} = 0.304 Re_D^{-0.25} + 0.029 \left(\frac{D}{D_C} \right)^{0.5} \quad (4.52)$$

$$Re_{D,cr} = 20000 \left(\frac{D}{D_c} \right)^{0.32} \quad (4.53)$$

Where Re_D can be found using Equation 4.10. D is the tube diameter in m and D_c is the spiral diameter in m. The division of the laminar and turbulent regions in spiral flow will be at the critical Reynolds number from Equation 4.53 [66], where laminar flow occurs below that number and turbulent flow above. The Reynolds number for the friction factor calculation will be evaluated at bulk temperature T_b .

4.6. Nozzle performance

This section will deal with the nozzle performance and nozzle dimensions. Four outputs will be required from this particular script: the thrust, specific impulse, nozzle throat area and nozzle exit area. These outputs can be mostly calculated using equations that were already displayed in Chapter 2. These are the IRT Equations 2.1-2.6 and 2.9. Note that the assumptions for IRT are explained in Section 2.2.

For the tool, it is assumed that the propellant chamber temperature equals the RAC output temperature, as there are no thermal losses in the propellant flow from RAC to nozzle chamber (see assumption PDT-A-11). Next to that, it is also assumed that the nozzle has ideal expansion, so the ambient pressure equals the exit pressure (see assumption PDT-A-10). If vacuum is chosen as the ambient pressure, the exit pressure will be set to 100 Pa in accordance with the explanation in Section 3.2. The user however can alter this value.

In order to take real-life losses into account, the resulting thrust and specific impulse will be multiplied by the correction factor ξ_F [23]. This correction factor is referred to as the "nozzle quality" and ranges from 0.92-1.00. In the tool, the value will be set at an average 0.92 but the user can alter this. Next to this correction factor, the discharge factor C_d is also introduced. This factor is a result of a boundary layer forming in the nozzle throat for low Reynolds number nozzles, below 30 000. This throat Reynolds number Re_T is calculated using Equation 4.54. The discharge factor reduces the mass flow through the nozzle but it will be applied as a penalty to the specific impulse and thrust, similar to the nozzle quality correction factor. The discharge factor has been documented for various gases by Johnson [67], see also the literature study⁸ [27]. From the nitrogen graph, a relation for the discharge factor has been derived which is given in Equation 4.55. Because the graphs are to some extent similar, this relation will be used for all four propellants in the tool.

$$Re_t = \frac{4\dot{m}}{\pi\mu D_t} \quad (4.54)$$

$$C_D = \frac{-3.875}{\sqrt{Re_T}} + 1.000 \quad (4.55)$$

The thrust and specific impulse equations, now corrected for the nozzle quality and discharge coefficient, are found in Equations 4.56 and 4.57 respectively. Further information for the quality factors can be found in Zandbergen [23] and Johnson [67].

$$F = \dot{m}U_{eq}\xi_F C_D \quad (4.56)$$

⁸Retrievable from <https://github.com/AJTRP/AE5810-thesis/tree/AE5810-documents>.

$$I_{sp} = \frac{U_{eq}}{g_0} \xi_F C_D \quad (4.57)$$

The model will take the propellant chamber pressure, temperature and mass flow as inputs. From this, the nozzle throat area and then the nozzle exit area can be calculated. Then, the equivalent velocity will be calculated, which in turn gives the thrust and specific impulse.

5

Thruster design and hardware

This chapter will detail the design, performance, hardware and cost of the solar thermal engine, **STT2**. It kicks off with a section on the design of the two major components of the thruster, the heat exchanger and the nozzle. Because the design had to be completed on a short notice due to limited time, the **PDT** was not yet finished when the thruster was manufactured. Only some **PDT** relations, shown later in this chapter, were used for the design. The section after the thruster design is dedicated to the performance of the thermal thruster as determined by the tool. Then, the manufactured hardware is shown followed by a section on the estimated cost for this project. In the end conclusions and recommendations are given, especially regarding the manufacturing phase.

5.1. Thruster design

STT2 will consist of three main components: concentrator, **RAC** and nozzle, per requirement REQ-F-2. However, the first component can be skipped because the chosen heat source for **STT2**, the welding laser, does not require any concentration devices. The choice for the laser was already made in the literature study [27] and the thesis proposal [28]¹. In those documents, the propellant for **STT2** was also determined, mostly based on the work by Leenders [3] and Leverone [12]: nitrogen. There were three reasons for this choice: the availability of gaseous nitrogen (bottles are present in the **AE** cleanroom), the low cost and because it allows for comparison with Leenders' heat exchanger. The engine could also be used for other propellants (such as carbon dioxide), but the nozzle will most likely not be adapted in those tests due to the different propellant properties.

This section will show the design of the other two main components: the **RAC** and the nozzle. Note that the resulting thruster has to adhere to the requirements and constraints as set in Section 2.4. This will be checked in the subsequent section by the **PDT**.

5.1.1. Receiver-Absorber Cavity design

This subsection will explain the design process for the heat exchanger. First, the material will be chosen, which is followed by the **RAC** configuration, shape and the dimensions.

¹Both documents are retrievable from <https://github.com/AJTRP/AE5810-thesis/tree/AE5810-documents>.

RAC material

The material for the heat exchanger was evaluated by the following criteria: thermal conductivity, density, melting point, heat capacity and manufacturability. From literature, molybdenum, rhenium and tungsten were good candidates [27, 28]. However, they are either expensive, hard to manufacture or hard to find in the right shape. Copper was eventually chosen, due to its high thermal conductivity at the cost of higher density and thus mass. Its heat capacity is also relatively low, which allows the RAC to reach its maximum temperature earlier during start-up.

RAC configuration

The three configurations for the heat exchanger were already explored in the literature study [52]: the direct propulsion with indirect absorption heat exchanger was chosen, because it is the least complex and it was recommended by multiple (student) researchers, including Shoji [4], Leenders [3], Preijde [68] and Das [48]. One of the mentioned reasons is that it is simpler because it does not have to have a transparent window nor does it need to have a separate heat storage. Instead, the heat exchanger can be of a single material, which reduces the risk of thermal stresses and connection issues. Indirect absorption also has less pressure drop than direct absorption [48]. Choosing this configuration will also leave some room to explore indirect propulsion, where the RAC is heated first while the propellant enters later. In that way, even higher efficiencies could be reached. One should stay aware of the possibility of material melting though.

RAC shape

A direct propulsion with indirect absorption heat exchanger can be designed with a cavity or without (flat plate). Constructing the RAC without a cavity is not deemed feasible, due to the high reflectivity losses inherent to the option. Furthermore, the focused light will fall on one spot of the flat plate, which brings the problem of local heat build up with melting as a result or in other words, poor heat distribution. An advantage of the flat plate is that it is easy to manufacture. Literature however favors the cavities [3, 4, 48, 68], often in combination with fiber optic cables. This is due to the reason of reduced mass.

For cavity heat exchangers there are multiple options, see Figure 5.1 [4]. These options have been reduced to three shapes to reduce manufacturing complexity: a conical, cylindrical or spherical cavity. Cavities have the major advantage that the effective heating area is increased; the propellant needs to traverse a longer path around the RAC, which does not necessarily mean that the heat exchanger becomes heavier. One can simply leave the inner room empty. Furthermore, a cavity is an excellent shape for the current heat source, a laser with a tiny focal point. The beam can fall through an aperture in a lid which is located at the start of the cavity and then widen (remember that a laser is not entirely collimated), increasing the heat distribution width. As such, a lid with aperture will be part of the design, because the trade-off between the small mass increase due to the lid and the decreased convection and radiation losses is in favour of the latter. Preijde concluded so, but Leenders never mentioned a lid. That is mostly due to the heat source, which still had a sizable beam focus diameter of 2 cm, even after the lens was included in the system design. A lid would thus not be beneficial but even increase the heat losses, because part of the beam would fall on the outside of the lid and only increase radiation and convection losses. In general, the smaller the lid aperture, the lower the convection and radiation losses [62]. However, one needs to be aware that the aperture should allow (most of) the beam to pass to the cavity.

The three cavity options were extensively traded-off by both Shoji [4] as Preijde [68]. Both concluded that a cylindrical, lidded heat exchanger would be best option. It is not deemed necessary by the author to redo these trade-offs, but a summary will be given of what Preijde found. Shoji in this regard is less reliable, because he modelled the irradiation beam as non-focused; as such, he invented unconventional shapes, such as a horn or outer disc, which only serves to increase the area upon which the beam falls. This only marginally increased the thermal efficiency though. Preijde on

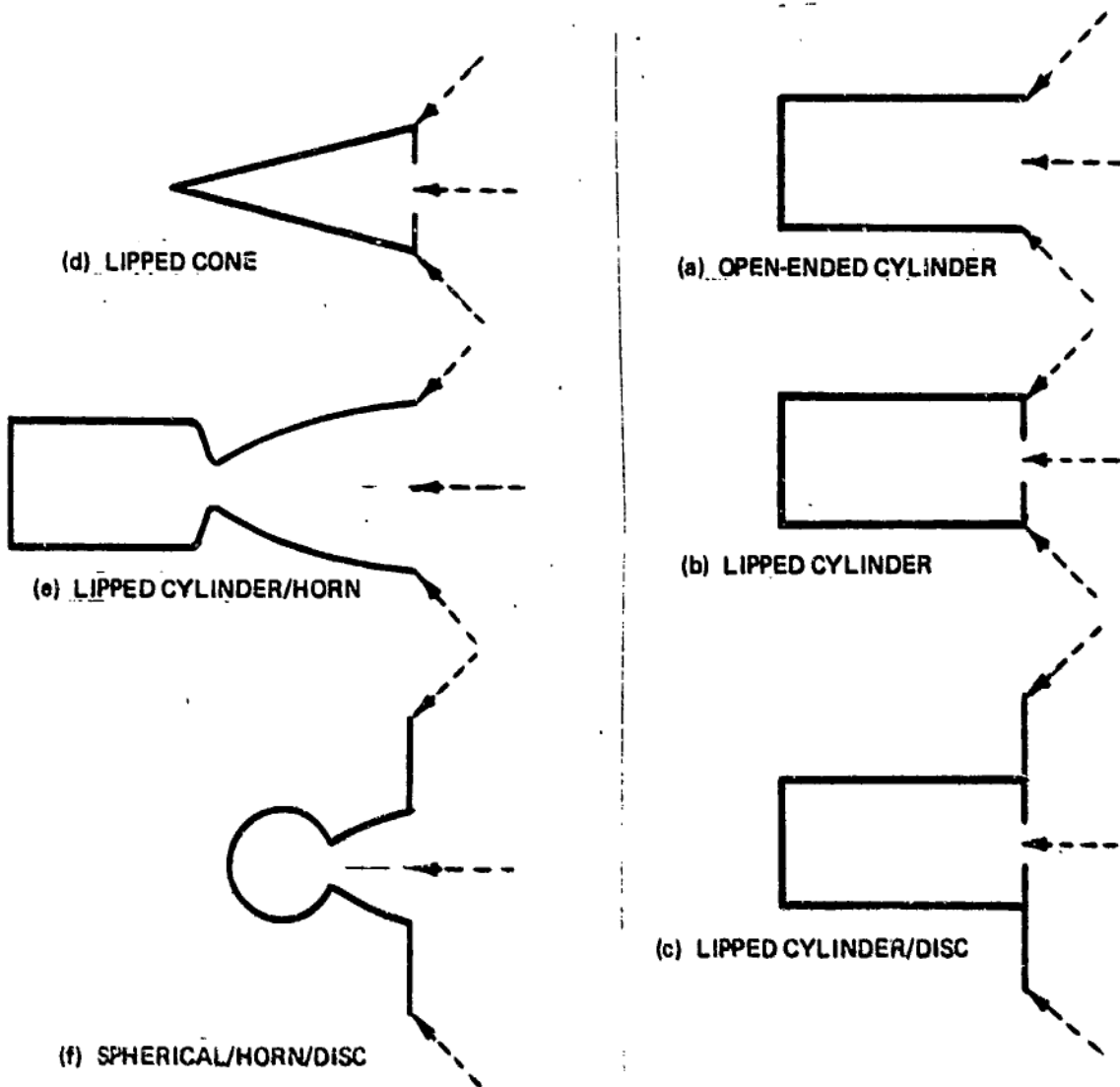


Figure 5.1: Options for cavity heat exchangers [4].

the other hand, did an extensive trade-off between six concepts, each of the cavity options twice with alternatingly ammonia and hydrogen as propellant. The trade-off had six criteria: specific impulse, system-specific impulse, thrust, wet system mass fraction, system volume and system complexity. Preijde built an optimization tool which, with the input of variables such as orbit altitude, solar flux and mass, could automatically calculate those criteria for each concept. For this thesis, the system-specific impulse, wet system mass fraction, system volume and system complexity are important. In the first three categories, the spherical RAC does outperform the other two by a small amount. This is due to the excellent temperature distribution and the high area-to-volume ratio of a sphere. However, when looking at system complexity, or in other words manufacturability, the spherical heat exchanger loses its advantage completely with regards to the other two shapes. Constructing a sphere with etched-out channels is extremely hard, especially when the maker has to rely on DUT workshop machinery. The high area-to-volume ratio of a sphere is also partly mitigated due to the fact that one can hardly fit anything else in the available space outside the sphere; it is not convenient at all.

The latter argument also holds for the conical cavity; although the light distribution is slightly better when compared to the cylindrical cavity, the available space outside the the cone is not easy to use.

Widening a cone to a cylinder will thus increase the mass by a small amount but increase the channel length, which increases the thermal efficiency. Furthermore, a cylinder is easy to construct on a lathe, while a cone is harder because you cannot secure it to the lathe easily. So mainly because of the low complexity combined with a more than reasonable performance, the lidded cylinder will be chosen as the **RAC** shape. This is also supported by Shoji and Preijde as earlier mentioned, but not by Leenders who designed a cone. In Leenders' trade-off, he did not include manufacturability as a criterion, which could be the cause of him leaning towards a cone. In any case, it will also be interesting to compare the results of the cylindrical **RAC** versus the conical heat exchanger.

RAC dimensions

Unfortunately, the dimensions of the **RAC** were very reliant on the maker of the piece. It should be noted that at this point of the project, the author ran into issues regarding manufacturability. Especially the **RAC** formed a problem, because it would become a highly detailed small piece which would require a high amount of experience and man hours on lathes, mills and drills. From the requirements, only €500 is available to conclude a thesis project. While this is more than sufficient for a theoretical thesis, a practical study is different. Not only the manufacturing of **RAC** and nozzle is required, but also the material needs to be bought, next to expenses on propellant, connection pieces, hard soldering, sensors and other. An overview of the costs is found at the end of this chapter.

Because the author was not experienced at all regarding metal machining, **DEMO** was contacted. At various faculties at **DUT**, **DEMO** runs manufacturing workshops with high-end tools. They help out staff and students, but also any commercial institute that might knock on their door. When a sketch of the **RAC** design was shown to them, they estimated that the price would be €1600 for the heat exchanger alone. This was of course not viable. Reducing the amount of detail (for instance by decreasing the amount of channels) would not bring the price down, so another solution had to be found. Via other students and a **DUT** Dreamteam, a master student was found who was willing to manufacture the **RAC** for a price of €300. This was excellent, because it would leave room for the other expenses. However, because the used mills were manual and not **CNC**, many concessions needed to be made on the design. The most important concessions and their consequences are shown in Table 5.6. Especially the requirement that the thickness of the walls needed to be a minimum of 4 mm was a harsh constraint; for comparison, Leenders' **RAC** had walls of approximately 1 mm thick. At this point, it can thus already be stated that the mass requirement, REQ-S-4, cannot be met.

In Section 2.3, it was seen that 175 W was needed to heat gaseous nitrogen from 298.15 K to 835.35 K at a mass flow of 300 mg s^{-1} . For a specific impulse of 90.0 s, a chamber pressure of 8.2 bar is then necessary. This would still satisfy requirements REQ-S-1, REQ-S-2 and REQ-S-3 while not exceeding the pressure constraint, CON-2. The feed pressure would be higher than 8.16 bar to accommodate for pressure losses in **RAC** and tubing, but this will not pose a problem to the experiments as the nitrogen cylinder can provide up to 200 bar. Leenders found pressure losses of 0.05 bar during his runs [8]. Note that higher chamber pressures or higher power input will lead to higher specific impulses, which could be needed to correct for any losses in nozzle or connection pieces.

Because the **PDT** is not yet finished at this point, the goal is to find a first estimate of the channel length. First of all, one needs to decide on the channel lay-out: this could either be linear, spiral or a porous medium. Spiral has the advantage of a longer channel length (thus the heat exchanger could be reduced), while linear is easier to manufacture. Porous has potentially the largest heating area, however it also requires a material that can withstand high temperatures. Next to that, the medium needs to be shaped to fit in between two heated walls. Furthermore, because the fluid 'hits' the medium constantly, the pressure loss will be larger than for the other two options. For now, porous is not considered, but it could be an interesting idea for further research. Leenders did recommend spiral tubing at the end of his thesis, while Preijde also made the recommendation. Thus, spiral will be chosen as the channel configuration.

For construction, it is impossible to make the channels out of the inside of a solid cylinder. So, the

idea was picked up to make the RAC out of three pieces: an inner hollow cylinder with the channels etched out at the outside; an outer hollow cylinder (one end closed) that could fit smoothly over the inner cylinder, so that the channels would be closed off; a cap that would close of the other end of the cylinders. On both sides of the outer cylinder, holes would be made to connect the feed system and nozzle.

Inner cylinder

The inner cylinder is dimensioned at the hand of thermal convection. The convection heat transfer in one channel can be calculated using Equation 4.6 [23]. The assumption is that the RAC wall has a constant temperature for the whole length of the channel. This can be assumed because the heat exchanger has a high conductivity, so heat will spread at a high rate through the RAC. $T_{p,in}$ is set at 298.15 K, while $T_{p,out}$ equals 835.4 K. The latter temperature was established in Section 2.3 as the temperature at which a specific impulse of 90.0 s could be reached. For now it is assumed that the wall temperature T_w is slightly higher than the outgoing propellant temperature, so 850 K. This is well below the melting temperature of copper, which is 1358 K². However, the margin is not that large, as CON-1 shows that the limiting temperature is for the hard-soldered, which can only withstand temperatures up to 933 K.

The convective heat transfer can be found using the dimensionless Nusselt number (see Equation 4.7), which in turn can be calculated using the empirical Gnielinski formula (see Equation 4.19). The latter is valid for Reynolds numbers starting at 2300, although some sources dictate a lower limit of 3000 [54]. The Reynolds number Re_D can be found by using Equation 4.10, while the dimensionless Darcy Weisbach friction factor f_{DB} is calculated using Equation 4.20. The heating area per channel is found from Equation 5.1.

$$A_{ch} = \pi \cdot D \cdot L_{ch} \quad (5.1)$$

In case of a non-circular duct, the diameter D (in m) is replaced by the hydraulic diameter D_h (also in m), see Equation 4.16. In all the used equations, k is the propellant's thermal conductivity in $\text{W m}^{-2} \text{K}^{-1}$ and μ is the propellant's dynamic viscosity, both evaluated at the bulk temperature of the propellant, which is the average of the inlet and outlet temperatures (see Equation 4.9). A_{ch} is the channel cross-sectional area in m^2 and L_{ch} is the channel length for a spiral around a cylinder, from Equation 5.2.

$$L_{ch} = \sqrt{\pi^2 D_{RAC}^2 + L_{RAC}^2} \cdot n_{turns} \quad (5.2)$$

Here, D_{RAC} and L_{RAC} are the heat exchanger's diameter and length respectively, both in m. n_{turns} is the number of turns.

Now that the equations are known, the RAC can be dimensioned. It should be noted that the student who manufactured the RAC advised to make the channels isosceles triangles (with 45 deg angles), with the hypotenuse pointing away from the centre of the cylinder. This was most easy to turn on a lathe according to him, as a chisel has this shape. A standard chisel of width 1.2 mm was chosen, so both sides in the material were 0.849 mm. As such, A_{ch} was 0.36 mm^2 and D_h was 0.497 mm.

The number of channels was set at an arbitrary 6. This is because the Reynolds number would then equal 2428, just above the threshold for the Gnielinski formula. For this calculation, the propellant bulk temperature was assumed to be the average of the inlet propellant temperature and intended outlet propellant, so 566.8 K. The dynamic viscosity for nitrogen is equal to $28.42 \times 10^{-6} \text{ Pa s}$ at that temperature³. A larger amount of channels would lead to lower Reynolds numbers, while a higher

²From <https://webbook.nist.gov/>, accessed on 11-11-2020.

³<https://www.engineeringtoolbox.com>, accessed on 07-08-2020.

amount of channels would be detrimental to the pressure loss. Furthermore, more channels would also imply more work for the manufacturer. The pitch p in m between the channels would be twice the width of the channels, so 2.4 mm. The number of turns could then be found by dividing the RAC length by that number, see Equation 5.3.

$$n_{turns} = \frac{L_{RAC}}{p} \quad (5.3)$$

The diameter of the inner cavity was set at 8 mm to allow for some manufacturing space. The manufacturer agreed to have an outer diameter for the inner cylinder of 13 mm, so the channels were etched out to a maximum depth diameter of 11.8 mm. 175 W of power is needed, so the only unknown would be the length of the RAC channel section. Solving for all variables, the Nusselt number is 8.01, convective heat transfer coefficient is $663 \text{ W m}^{-2} \text{ K}^{-1}$ and the resulting heat exchanger length is 31 mm. However, room is also left at the start and end of the inner cylinder to accommodate for the inlet and outlet. In those areas, the propellant can also heat up, so 10 % is subtracted of the length to reduce the size. A final 28 mm was the result. At that heat exchanger length, each of the six individual channels has a length of 0.090 m.

At the start of the inner cylinder, 5 mm is added to allow a 3 mm sized hole for the inlet. On the other side, 10 mm is added for an outlet of 8 mm. The reason that the outlet is larger is because it makes sure Leenders' nozzle can fit on there, should a dedicated nozzle be too expensive to build. The mass of the inner cylinder is 0.027 kg.

Outer cylinder

The outer cylinder should fit around the inner cylinder and thus has an inner diameter of 13 mm. The outer diameter is 21 mm. The cylinder is open on one end, on the other end it is closed except for the aperture which has a diameter of 4 mm. That way, it allows for some adjustment to the laser focus height, while not being too large to let heat or reflection escape. On the side, the outer cylinder has one hole for the inlet (diameter: 3 mm) and one threaded hole (M8) for the outlet. The mass is 0.092 kg.

Cap

The cap is used to close off the open end of both cylinders, once the inner cylinder is inserted in the outer. The cap is on the inlet side so it also features a 3 mm sized hole. Next to that, it has a threaded hole in the middle, size M6. This allows for a fourth part, which was added later in the design. The mass is 0.050 kg.

Spike

A spike was added, in order to diverge the incoming laser beam and reflect it to the inner side walls. The idea was to make it as sharp as possible, but the manufacturer could only allow a minimum half angle of 20 deg. Furthermore, it was extended in the length because it could otherwise not be clamped in the lathe. The effect of the spike is not yet known, but the added mass of 0.004 kg was minor, so it was constructed as well.

Result

An overview of the heat exchanger dimensions can be found in Table 5.2. The total volume of the heat exchanger amounts to $19\,656 \text{ mm}^3$, which gives a mass of 0.176 kg at a copper density of 8978 kg m^{-3} . This is more than double the amount of Leenders' RAC. As was expected, requirement REQ-S-4 is thus not met, due to the very thick walls required for construction. See Appendix A for the technical drawings of STT2. An exploded view of STT2's heat exchanger is shown in Figure 5.2, pictures of the hardware results are available in Section 5.3.

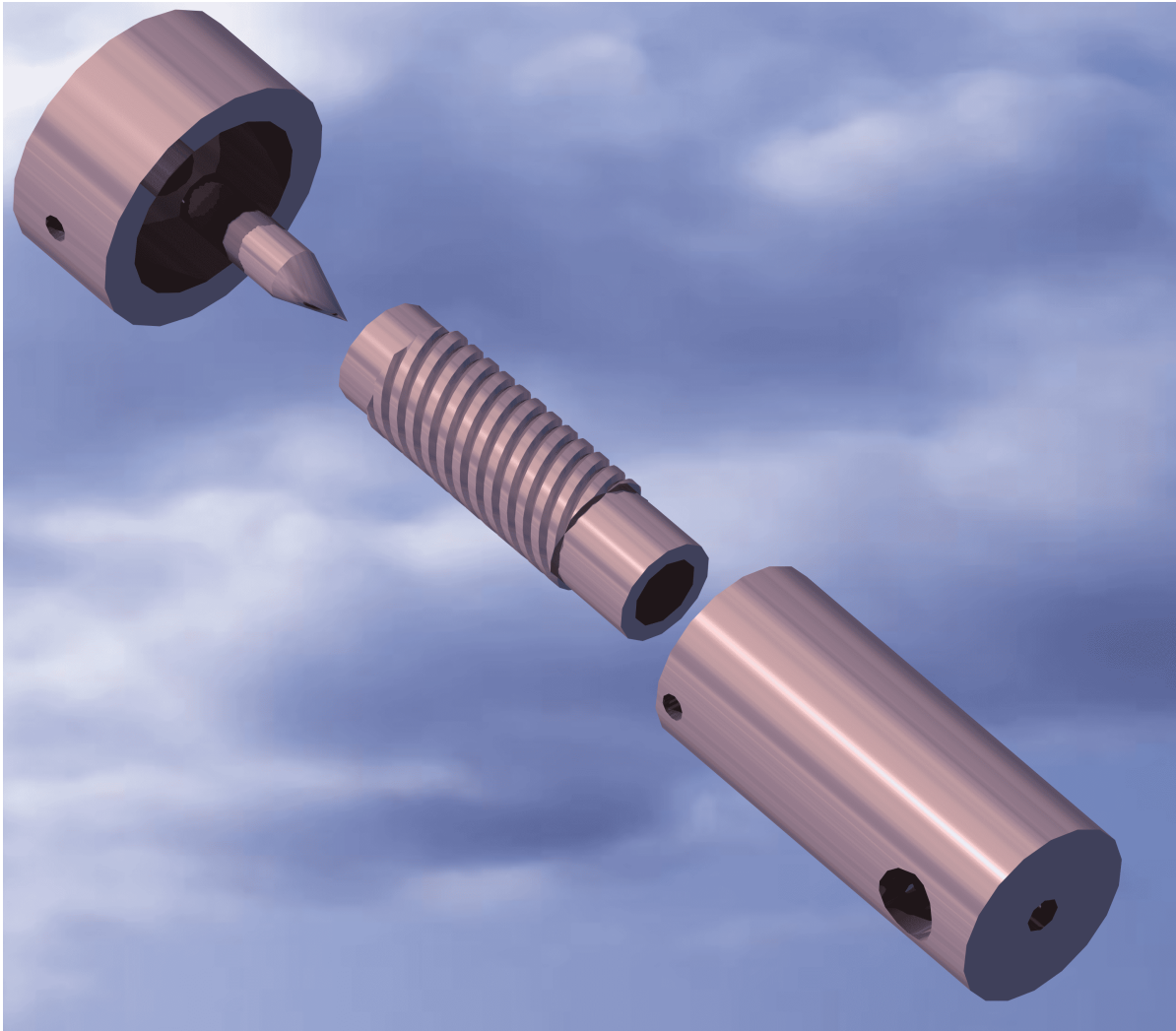


Figure 5.2: Exploded view of the STT2 heat exchanger.

5.1.2. Nozzle design

Originally, the nozzle was designed to be a simple conical one, with the throat and exit diameter determined from [IRT](#). These values were 0.58 mm and 0.76 mm respectively. Zandbergen [23] recommended a convergence half angle of 30 deg and an average divergence half angle of 15 deg. These were thus also incorporated in the nozzle design. The nozzle would be constructed from a solid cylinder with a diameter of 5 mm and length of 20 mm. A hole of diameter 3 mm would be drilled out on one side (not to the end). Then, the nozzle would be drilled out on the other side. However, two issues prevented the final design and manufacturing of the piece: it could not be made accurately as a lack of appropriate tools, experience and funding. Leenders' copper nozzle had similar areas (0.58 mm for the throat and 0.68 mm for the exit) [3], so it was decided to use his nozzle in testing and accept the performance losses, which are only 1.2 %. A drawing of a dedicated nozzle for [STT2](#) was thus not made. However, a drawing of the Leenders' nozzle can be found in [Appendix A](#). [Table 5.1](#) shows the main characteristics of this nozzle.

Table 5.1: Main characteristics of Leenders' copper nozzle.

Material	Copper
Throat diameter	0.58 [mm]
Exit diameter	0.68 [mm]
Convergence half angle	31.4 [deg]
Divergence half angle	15.7 [deg]
Mass	4.5 [g]
Length	22.4 [mm]
Largest diameter	6 [mm]

5.2. Performance

This section will focus on the performance of [STT2](#), as determined by [PDT](#). The inputs are retrieved from section [5.1](#) and inserted in Table [5.2](#). Figure [A.1](#) details the various dimensions; the [RAC](#) channel length is the horizontal length of the channels, 0.028 m in this case. The cavity inner length is the whole length of the cavity, here 0.043 m. The [RAC](#) outer length is not shown in the figure, but it is the total length of the heat exchanger (0.051 m). The inner diameter is equal to 0.008 m, while the outer diameter is the largest diameter (in this case of the cap), which is 0.029 m. The inner and outer areas are retrieved from the [CAD](#) program, CATIA. No insulation is applied.

With these inputs, the tool reaches a steady solution at an [RAC](#) temperature of 780.1 K, propellant temperature of 778.6 K and pressure loss of 1.80 bar, which gives a specific impulse of 77.8 s and thrust of 229 mN. This amounts to a thermal efficiency of 61.6 %, which is lower than the arbitrary 70 % which would bring the specific impulse to 90 s. Table [5.3](#) shows the other thermal outputs for this [PDT](#) simulation. The thermal losses at the outside are relatively high at these [RAC](#) temperatures. Because of this, radiation losses are dominating convection losses.

When the same cylindrical shaped insulation is applied as was for [STT1](#), the thermal efficiency dramatically increases to 89.2 %, which will propel the specific impulse to 86.1 s at a thrust of 253 mN. The reason that the specific impulse does not reach the intended 90 s is because of the large pressure loss of 2.2 bar. It is planned to have these values validated during testing.

5.3. Hardware

This section will focus on the hardware of [STT2](#). First, the [RAC](#) hardware is presented, followed by a section on the connection pieces. In the end, the concessions for the manufacturing of the heat exchanger are given.

5.3.1. Receiver-Absorber Cavity hardware

As was shown in the Section [5.1](#), the design was altered multiple times to allow for the [RAC](#) to be built. Finally, a design was chosen which could be made. It consisted of four parts which are shown in [CAD](#) drawings in Appendix [A](#). All parts were constructed on Dreamhall manufacturing tools, primarily lathes and drills, by a student who was experienced in metal manufacturing.

Figures [5.3](#) and [5.4](#) show the disassembled and the assembled [RAC](#) respectively. Notice the threaded connections and the four parts out of which the heat exchanger is assembled: inner cylinder, outer cylinder, cap and spike. Also be aware of the extended spike, protruding out of the cap. This was necessary in order to clamp the spike in the lathe while the sharp part was made. In Tables [5.4](#) and [5.5](#), the dimensions and mass of the components are shown. As can be seen, the values do differ from the design values, but not by a significant amount. It was checked by inputting the real dimensions in

Table 5.2: PDT inputs for STT2.

Name	Symbol	Value	Unit
RAC type	-	"Cylindrical"	-
RAC material	-	"Copper"	-
Propellant	-	"Gaseous nitrogen"	-
Insulation	-	"No insulation"	-
Channel layout		"Spiral"	-
Number of channels	n_{ch}	6	-
RAC channel length	L_{cavC}	0.028	m
RAC inner length	L_{cavI}	0.043	m
RAC outer length	L_{cavA}	0.051	m
RAC inner diameter	D_{inner}	0.008	m
RAC outer diameter	D_{outer}	0.029	m
RAC aperture diameter	D_{ap}	0.004	m
RAC inner cavity area	$A_{RAC,i}$	1.46e-3	m^2
RAC outer cavity area	$A_{RAC,o}$	5.01e-3	m^2
RAC mass	M_{RAC}	0.173	kg
Irradiation time	n_i	95	min
Incoming power	P_{in}	250	W
Incoming power efficiency	η	1.00	-
Mass flow	\dot{m}	300e-6	kg/s
Propellant feed temperature	$T_{p,in}$	298.15	K
Propellant feed pressure	p_f	816000	Pa
Channel hydraulic diameter	D_h	0.000497	m
Absorptivity oxidized copper	α_M	0.70	-
Emissivity oxidized copper	ϵ_M	0.65	-
Ambient temperature	T_{amb}	298.15	K
Ambient pressure	p_{amb}	101325	Pa

the PDT, but the outputs did not change in comparison to Section 5.2. After the pieces were made and the inner cylinder was inserted in the outer cylinder, it was discovered that they could not be separated anymore. This was not seen as an issue, however the separate dimensions could not be measured.

5.3.2. Connection pieces hardware

Having the heat exchanger and nozzle was not enough to start the experiments. Some connection pieces still needed to be made. Because at this point there was no additional money available from the faculty, it was decided to follow two metal manufacturing courses, on milling and turning. Both were offered to freshmen student at the workshop at the faculty of [Faculty of Mechanical, Maritime and Materials Engineering \(3mE\)](#) and the instructors did allow the author to follow the courses. Both had a time length of four hours, after which the manually operated lathe and mill could be used freely. The author recommends the courses wholeheartedly, as knowledge of the manufacturing process can only enhance the capabilities of an engineer in being.

After the courses, two main pieces were made: the first was a brass object in order to connect the RAC inlet, first pressure sensor and nitrogen feed line; the second was a brass element to connect the second pressure sensor to the nozzle chamber. Both parts are shown in Figure 5.5 and are constructed on a lathe in the [3mE](#) workshop. Brass was chosen as it is cheap and easy to manufacture. Next to that, a ceramic piece from some previous project was reused as a means to connect STT2 to the test stand (see Chapter 6). The piece is made of Macor but could not be milled at the workshop, because of the detrimental effect of the material on the machinery. DEMO eventually manufactured the piece. The CAD drawings of the connection pieces are shown in Appendix A.

Table 5.3: PDT thermal outputs for STT2.

Output	Value
Input power	250.0 [W]
Absorbed power	248.8 [W]
Outer convection loss	26.5 [W]
Outer radiation loss	66.9 [W]
Inner convection loss	1.2 [W]
Inner radiation loss	0.3 [W]
Propellant convection	154.0 [W]
Nusselt number outer convection	7.71 [-]
Nusselt number inner convection	14.1 [-]
Nusselt number propellant convection	22.4 [-]



Figure 5.3: Disassembled STT2.



Figure 5.4: Assembled STT2.

5.3.3. Concessions for manufacturing

As stated in Section 5.1, some concessions had to be made for the manufacturing of the heat exchanger. Table 5.6 shows them and their consequences.

Concession	Consequence
The thickness of the heat exchanger wall needed to be a minimum of 4 mm, instead of the desired 1 mm.	The mass of the heat exchanger will exceed the maximum mass as stated in requirement REQ-S-4.
The channel cross-sectional shape needed to be triangular, because of the form of the milling bit used.	A more optimal shape would be circular or rectangular, see Section 8.2.
The number of channels needed to be reduced from 6 to 1, because that would be cheaper to manufacture.	The pressure loss in the heat exchanger would be tremendously high (see explanation further down).
The spike would be larger than designed, because the part could otherwise not be secured in the lathe.	The part was slightly heavier than designed.

Table 5.6: Concessions and their consequences for the manufacturing of STT2.

The concession with the most impact was the reduction of the number of channels. During meetings with the manufacturer of the heat exchanger, it was indicated that the amount of channels would require extra man hours and would thus cost more. His request was to make one channel instead of six and increase the length sixfold. This was agreed. Later, when the first tests were commenced (see Chapter

Component	Part	Design size	Actual size	Remarks
Inner & outer cylinder	Outer diameter	21.00	21.81	-
	Inner diameter	8.00	7.78	-
	Length	47.00	46.76	-
	Channel diameter	13.00	12.82	-
	Inlet hole diameter	3.00	2.98	-
End cap	Outer diameter	29.00	28.98	-
	Inner diameter	21.00	20.70	-
	Length	14.00	15.20	-
	Aperture	4.00	4.00	-
	Inlet hole diameter	3.00	3.04	-
Spike	Diameter	6.00	5.96	-
	Length	22.24	30.06	Sticks out at the top. No influence on the design, except for mass.

Table 5.4: Component sizes (in mm)

Component	Design mass	Actual mass	Remarks
Inner & outer cylinder	0.119	0.125	Not possible to separate both pieces.
End cap	0.050	0.051	-
Spike	0.004	0.006	Longer spike than designed.
Total	0.173	0.182	-

Table 5.5: Component mass (in kg)

6) it was discovered that due to this alteration the design mass flow rate could not be reached without applying a tremendously high feed pressure. This was because the pressure drop almost neared 31 bar when the design variables were inserted in Equation 4.48. With six channels, this was a mere 0.25 bar. Essentially by having only one small channel, an extra nozzle was introduced in the engine which would be detrimental to its performance. As such, the heat exchanger could not be tested at the indicated mass flow level of 300 mg s^{-1} . No additional funding was available to commission a new heat exchanger, see Section 5.4.

The performance of the manufactured STT2 was also determined by the PDT, under the same circumstances as for the designed STT2. The only differences to the inputs in Table 5.2 were the propellant feed pressure (changed to an arbitrary 50 bar) and the number of channels (changed to 1). Both the outlet propellant temperature and the RAC temperature were equal to 779.5 W (thermal efficiency of 61.7 %). The performance almost equal to the thermal performance of the version with 6 channels. This is not surprising: the very high Reynolds number in the 1 channel version would enhance convection to the propellant. However, the heat losses to the ambient change with changing RAC temperature. So, there was only a tiny margin for a propellant convection increase. In this particular case, the assumption that the RAC has a uniform temperature will likely not hold. Instead, the areas around the channels will likely see higher temperatures, while the surface areas are colder. However, checking this is out of the scope of this thesis. The pressure loss for the heat exchanger with 1 channel was a tremendous 41.0 bar. However, note that this loss is very dependent on the initial feed pressure, see Equation 4.48. With increasing feed pressure, the pressure loss will decrease.

The author realizes that the manufacturing error unfortunately renders the manufactured design almost useless. In Chapter 6, it will be explained that this mistake is only one out of three reasons to divert the thesis into another path; during the initial tests, it was also discovered that the heat exchanger was plagued by leakages. Because of this, the engine could also not be tested at a lower mass flow rate. Next to that, the COVID-19 crisis prevented any large-scale experiments at the faculty of 3mE. In the same chapter, a plan for the continuation of the thesis will thus be shown.

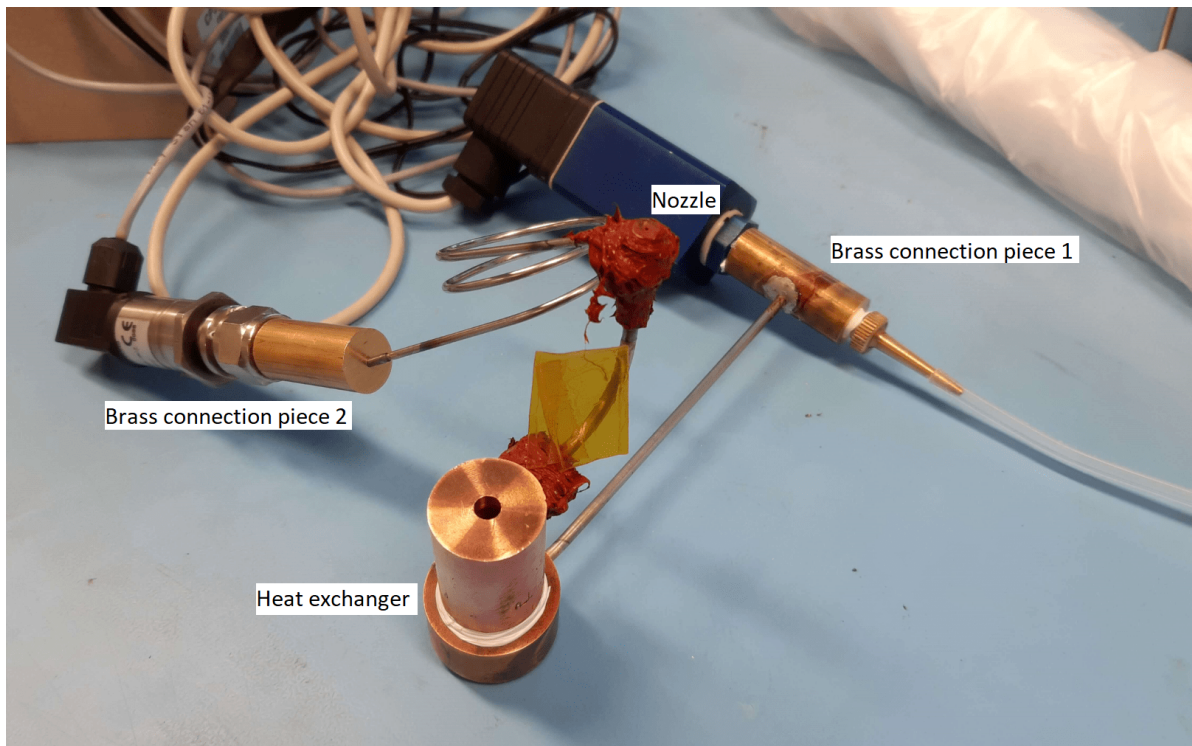


Figure 5.5: STT2 with both machined parts.

5.4. Cost

The list costs are associated with the development and testing of the test motor. These costs would have been out of limits if the concessions during manufacturing had not been made.

- The heat exchanger will be manufactured at the **DUT Dreamhall** by a student at the price of €300. The nozzle is borrowed from Leenders. Various other connection pieces are manufactured by the author himself, see Section 5.3. One hard-soldered connection by **DEMO** costs €50.
- The heat exchanger will be constructed out of copper. It is more convenient to buy the copper in a round solid staff for manufacturing purposes. Also, a margin is necessary, in case of production errors or design changes. A margin of 3 mm is recommended. Because a significant amount of copper will be milled, the estimated length of the staff will be three times 82 mm, which is 246 mm. With a diameter of 30 mm it will cost €60.42 including taxes⁴.
- Some raw material (brass and steel) for the connection pieces (see Section 5.3) is also required and is bought at Firma Kokkelink in The Hague. It amounts to €26.07.
- A bottle of gaseous nitrogen is in the range of €50-€70 at the **DUT Gassenteam**⁵.
- All sensors can be borrowed from the the cleanroom at **AE** or the **3mE Meetshop**.
- Some miscellaneous objects were also bought. An inlet tube, 3 mm outer diameter for €10.75 was purchased at Quartel, located in Pijnacker. Fireproof kit was bought for €14.41⁶. Bolts and nuts were acquired from a local hardware shop for €20.57.

⁴metaalwinkel-metalen.nl

⁵gassenteam-ictfm@tudelft.nl

⁶kitcentrum.nl

The total cost is projected to be €532-€552, which is already in excess of the available resources. It shows that executing a practical thesis can be very challenging and that workarounds and concessions to design are needed to complete the project.

5.5. Conclusions and recommendations

For hardware construction, recommendations are shown. They are listed here:

1. It is advised to have a high level of experience in the area of metal manufacturing before accepting a practical thesis in the area of [STP](#). That way, one can focus on the design and testing instead of spending both time and money on the construction of especially the heat exchanger part of the engine. It was felt that the inexperience of the author held back the design by a large degree.
2. If an external party is chosen for the manufacturing, keep in mind to closely discuss the design with them, at every step. Most of the time, they can tell you what is possible and what is not.
3. Always choose hard-soldered connections over threaded connections. Hard-soldered connections are sturdy, high temperature resistant and leak tight. Furthermore, they are relatively inexpensive, see also Section [5.4](#).
4. The use of kit to remedy leakages is not preferred, due to it expanding and blocking of the inner piece tubes. Where possible, adjust the design to allow for hard-soldered connections.

6

Experiment preparation

This chapter will explain what tests are going to be conducted (Section 6.1), the locations of testing (Section 6.2) and the required equipment (Section 6.3) to bring the experiments to a conclusive end. Next to that, a section is dedicated to the test stand hardware and its calibration. A few small test runs were done in the AE cleanroom, after which serious issues were found which forced the alteration of this project in the later stages. Here, it was decided not to continue with the physical experiments. The last section of this chapter will discuss this change.

6.1. Planned experiments

In Chapter 3, it became apparent that the preliminary tool was still to be validated using experimental results for simulations where propellant flow was present. In order to do so, the following three types of experiments are planned for STT2:

1. Test 1: test with nitrogen flow without illumination.
2. Test 2: test without nitrogen flow with illumination.
3. Test 3: test with nitrogen flow with illumination.

The first test has to be performed in order to validate the performance results at room temperature. The pressure at inlet and just before the nozzle (in the chamber) have to be measured. Together with the geometry of the nozzle, the mass flow and the load sensor readings and the nitrogen characteristics, it should be possible to assess what the performance of the nozzle is. It should be noted that the ambient pressure and the nitrogen chamber temperature are still required for this assessment. The second and third tests will be used to validate the thermal part of the preliminary tool, as told earlier. It should be noted that there is the advantage that the first test without the light source are more flexible locationwise. Instead of using the welding facility this can be done in the cleanroom, located at the eight floor of the faculty of AE, where no technician is needed whatsoever (see Section 6.2). However, the second and third tests are to be performed in the laser welding facility. During the testing, inputs such as input power and mass flow can be varied in order to see their respective impact on the engine performance.

6.2. Locations

Two main locations will be used for the experiments, the cleanroom at the 8th floor of **AE** and the welding facility at the **Materials Science and Engineering department (MSE)** of **3mE**.

6.2.1. Cleanroom

The cleanroom located at **AE** is an ISO 8 cleanroom with the purpose of, among others, providing a professional platform for students to work in¹. It contains a vacuum oven, various sensors and computers and a nitrogen supply to conduct micro-propulsion experiments. The responsible contact person is Mehmet Şevket Uludağ. The cleanroom is accessible to **AE** students at all times, under the condition that they are granted access by the contact person from **Space Systems Engineering (SSE)**. A workshop is attached to the cleanroom, where various tools can be freely used. See Figure 6.1 for the cleanroom.



Figure 6.1: Cleanroom at **AE**.

6.2.2. Welding facility

The welding facility can be found in another part of **DUT**, at **3mE**. It is primarily used for research into welding. It is a closed-off area with a powerful laser which can go up to 8000 Watts in power. The reason it is listed here is because the laser will serve as the illumination source for tests 2 and 3.

¹<https://www.tudelft.nl/en/ae/organisation/departments/space-engineering/space-systems-engineering/facilities/>, accessed on 12-06-2020.

6.3. Equipment hardware

In this section, the required equipment will be listed. The use for it will be explained, as well as various details such as the accuracy, disadvantages and shortcomings. All sensors will be connected to [National Instruments \(NI\) DAQ](#) devices which in turn deliver the data to a desktop or laptop. Most sensors and [DAQ](#) devices, if not all, are borrowed from [3mE's Meetshop](#).

6.3.1. Thermocouples

In order to measure the temperature of the propellant and RAC before, during and after heating, temperature sensors are needed. The data will be used to validate the predictions by the [RAC](#) model. As told before in the literature study [27], the temperature sensors will be thermocouples because of their high availability, medium accuracy and ease of use. The RS Pro 787-7835 is the chosen thermocouple (see Appendix C.3) because of its high temperature range, up to 1100 deg C (see Figure 6.2). The combined thermocouple and [DAQ](#) device may delay the signal by a second (a disadvantage of thermocouples), but that should pose no problem for the tests which will run for multiple minutes.

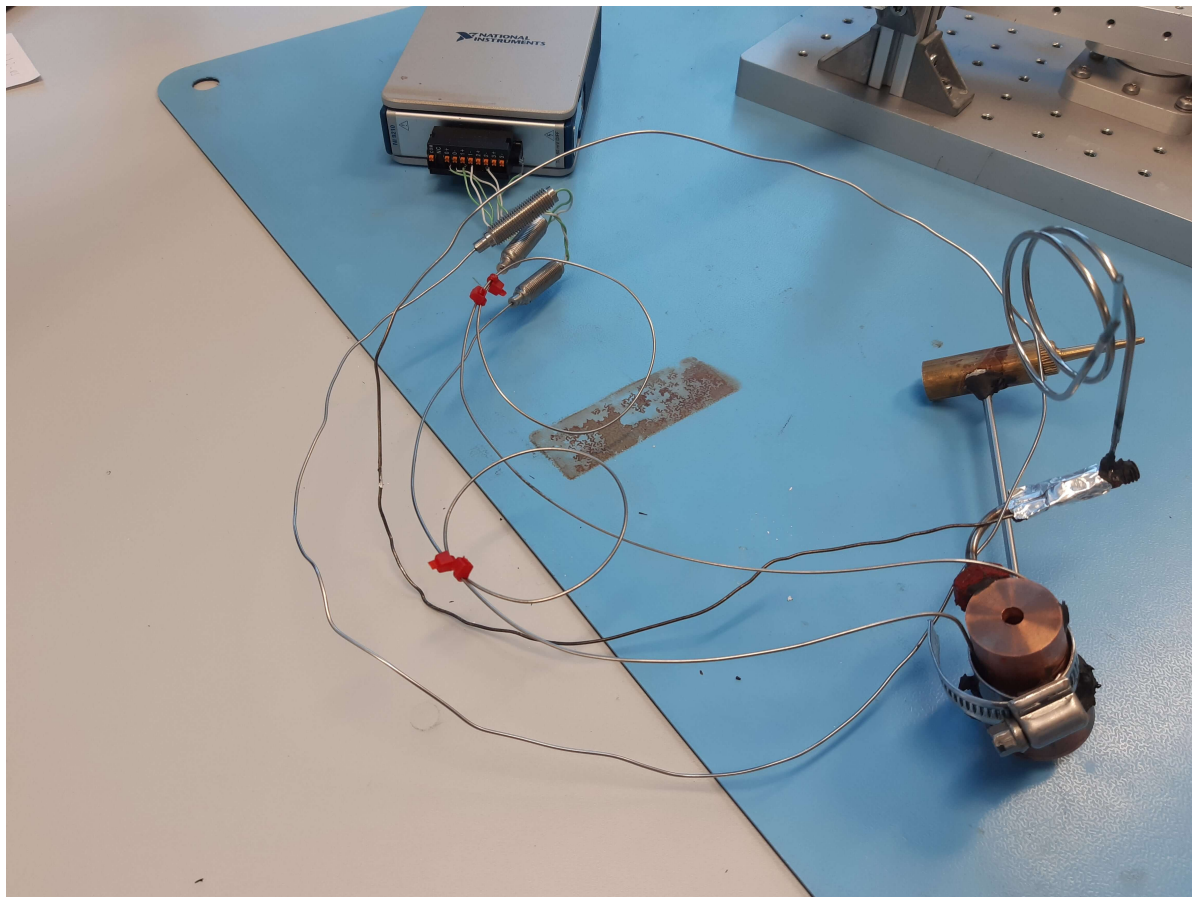


Figure 6.2: Thermocouples RS Pro 787-7835. In the background, the corresponding NI DAQ device is shown.

Because it is hard to directly measure the temperature of a gaseous flow, the sensors will be stuck to the outer and inner surfaces of the [RAC](#) and nozzle where possible. They will be connected to the engine using various methods, such as high temperature kit, steel clamps and hard soldering. Having these measurements, the propellant temperature can be determined or at least estimated.

6.3.2. Pressure sensors

The pressure sensors are necessary to measure the precise pressure of the propellant flowing through the engine. Combined with the temperature readings and mass flow, the pressure will determine what thrust should be delivered by the engine (what in turn is validated by the load sensor). Furthermore, two or more pressure sensors will give means to assess the pressure loss inbetween the two measuring points.

The pressures sensors will impact the design relatively more than the thermocouples, because they will have to be part of the flow to read the pressure. Thus, the amount of sensors will be limited to two, one before the [RAC](#) and one at the nozzle chamber. The sensors themselves have a physical connection in the form of a BSP female thread, G1/8" or G1/4" (see Figure 6.3). These will be connected via brass connection pieces to the engine, more information can be found in the latter subsection.



Figure 6.3: Pressure sensors 3300B16B0A01B000RS and DRTR-AL-20MA-R16B.

The pressure sensors used are the 3300B16B0A01B000RS and the DRTR-AL-20MA-R16B (see Appendix C.4 for the datasheets). The former is an absolute sensor, able to measure up to 16 bars of pressure. It outputs a current, which is converted via a constant resistor (468.8 Ohm) to a voltage which can be read by the [DAQ](#). The latter sensor is a relative one (to atmospheric pressure), again ranging up to 16 bars (over-pressure). A constant resistor of 559.7 Ohm is added to again convert the current output to a voltage output for the [DAQ](#). It should be noted that both sensors require a connection to the grid and operate up to 80 deg C. It is thus adamant that both sensors are shielded from heat flux from the experiment irradiation or convection and radiation. One measure that is taken for the sensor placed after the [RAC](#) is to insert a coiled tube inbetween to allow the fluid to cool down (see Figure 6.4). Be aware that this brings the disadvantage of tubing pressure loss, making the sensor read a slightly decreased pressure than which is present in the nozzle chamber.

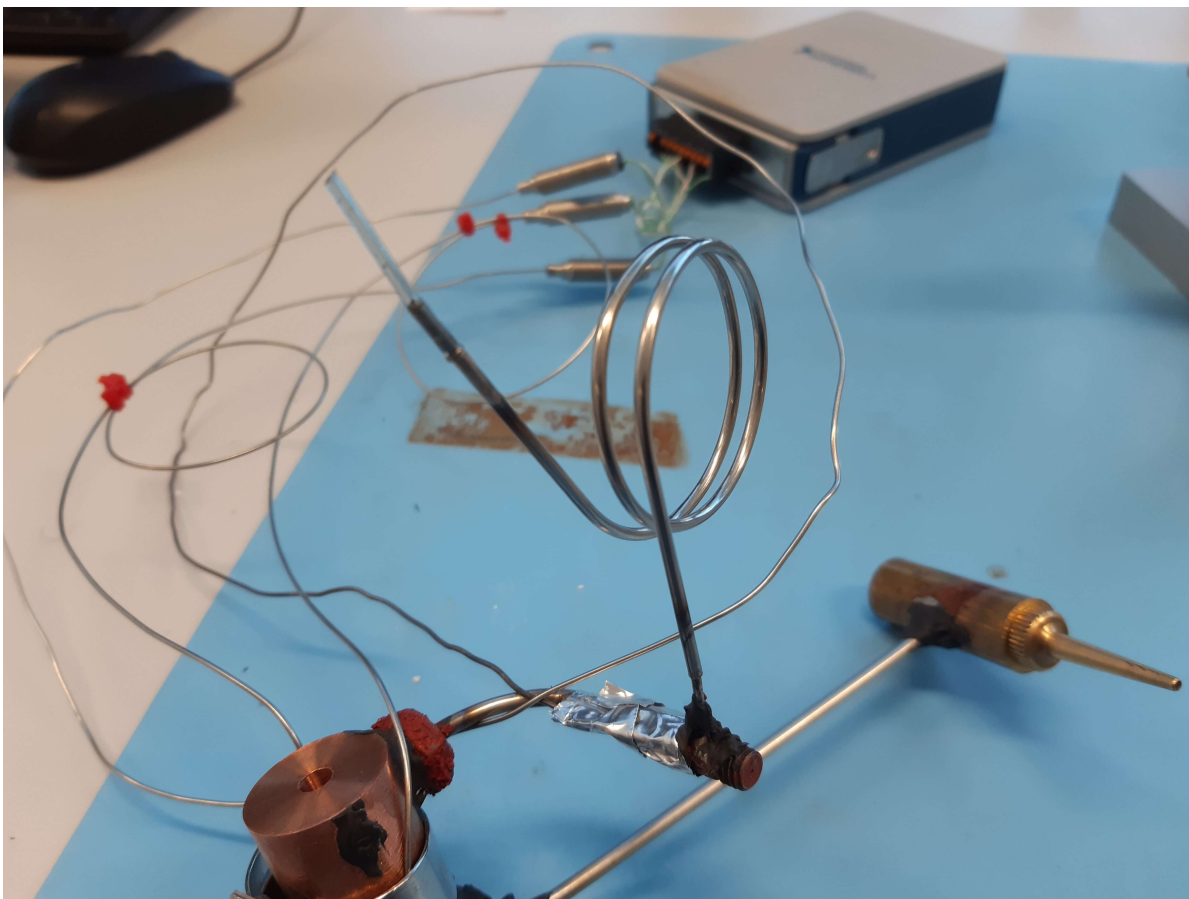


Figure 6.4: Coiled tube to allow the fluid to cool down for the pressure sensor.

6.3.3. Mass flow sensor

The mass flow sensor is a device which is aligned with the propellant flow and measures the mass flow. It is mounted just after the propellant outlet (most likely a gas cylinder). The faculty employs three Brooks mass flow sensors, each overlapping in range (see [27] for more information):

1. Brooks 5850S Smart Mass Flow. Range from 0-144 ml/min of nitrogen, or 0-3.00 mg/s.
2. Brooks 5850S Smart Mass Flow. Range from 0-2 ln/min of nitrogen, or 0-41.69 mg/s.
3. Brooks 5851S Smart Mass Flow. Range from 0-47.3 ln/min of nitrogen, or 0-860.83 mg/s.

All connections to the gas cylinder and the subsequent RAC are similar for the three sensors, which gives some flexibility. The accuracy is listed at 0.5%, but inaccuracy increases at the lower 10% of the range. Hence the overlap of the sensors, to accommodate for this. The sensors are connected to a DAQ device via a Printed Circuit Board (PCB) which is present in the AE cleanroom (see Figure 6.5). It automatically detects which mass flow sensor is connected and outputs a voltage for a similar DAQ as is used for the thermocouples. Note that the output of all three sensors is a current, in a nominal range of 0-20 or 4-20 mA. This should be adjusted for in the voltage read-out, as it reads 0-5 or 1-5 V respectively. See Figure 6.6 for the 5851S version.

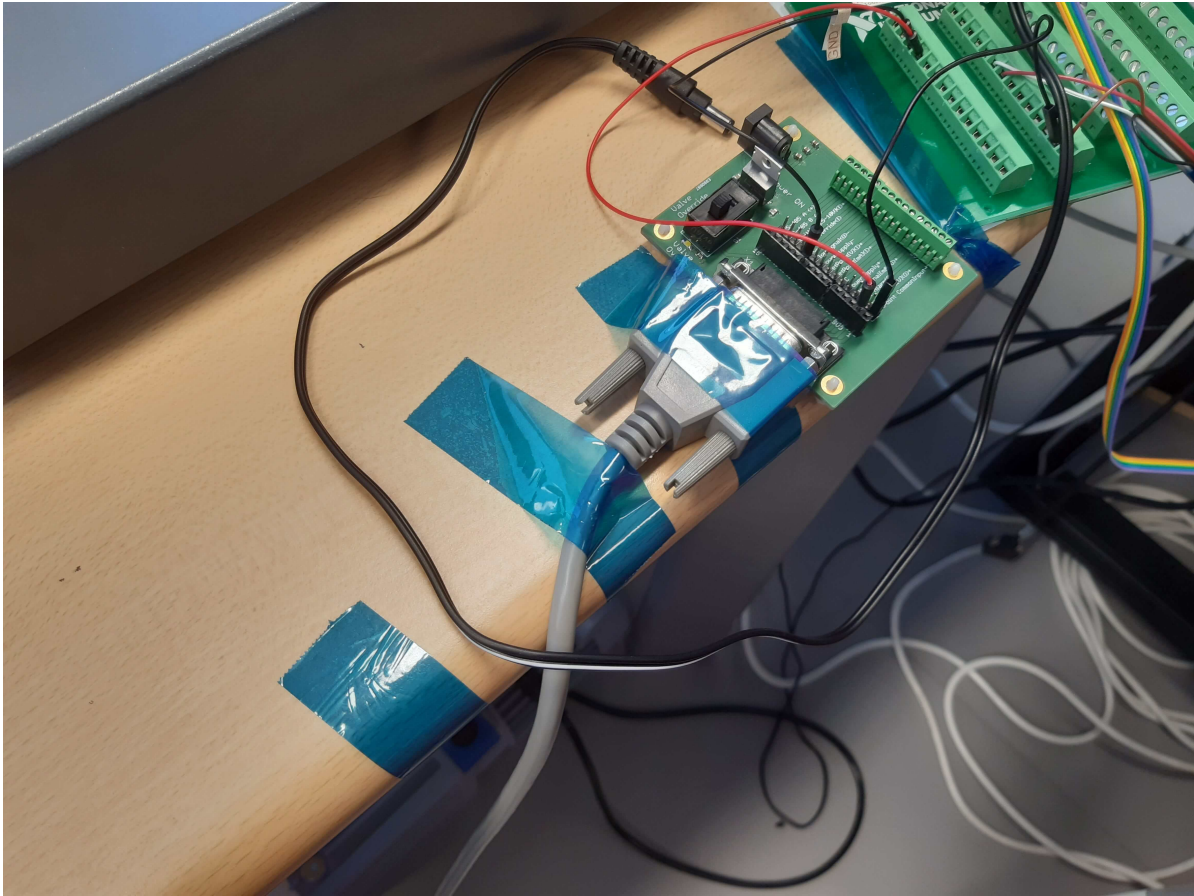


Figure 6.5: PCB connected to one of the Brooks mass flow sensors.

6.3.4. Propellant supply

As stated in the report, gaseous nitrogen will be the designated propellant for the ‘wet’ experiments. It is cheaply available, has no corroding effects on the engine, no two-phase flow and yields intermediate performance in terms of thrust, temperature and specific impulse [27]. The propellant is held in cylinders and is delivered by the [DUT Gassenteam](#). There are multiple purities available: 3.0, 5.0 and 6.0 in increasing purity order.

6.4. Test stand hardware

An overview of the available test stands can be found in the 2016 thesis report of Jansen [46]. Two main candidates are available for the [STT2](#) experiments due to their range: the AE-TB-1.1 and the AE-TB-50m. It should be noted that Leenders measured a maximum hot gas thrust of 104.1 mN, using the then available AE-TB-1.0. From experience it is known that thrust sensors are less accurate in the lower range (about <5 %). Indeed, Leenders shows a large discrepancy in the simulated thermal Matlab model thrust data and the experimental data. It is not apparent whether this is due to an inaccurate sensor or a lacking model validation, as Leenders does not elaborate on the differences.

However, both aforementioned stands will be evaluated hereafter. The thrust bench should adhere to a few requirements: it should be able to hold the engine and thrust sensor (naturally), not cause too much (background) noise and have a low mass and volume to be able to move it.



Figure 6.6: Brooks 5851S mass flow sensor.

6.4.1. Test bench AE-TB-1.1

Federica Valente built a thrust bench named AE-TB-1.1 (short: TB-1.1) for her thesis project in 2007 [5]. This thrust bench fulfilled some of the requirements, having low mass and fitting the engine and load sensor easily due to its modular build (using Boikon profiles). See Figure 6.7 for the thrust bench.

Valente reported a noise of 10-30 mN for the TB-1.1 with a standard deviation of 4.2 mN. The noise was explained by environmental influences, such as building vibrations and air currents. It can be cancelled out by averaging over the range of about five seconds, based on her graphs with experimental data. The bias (or accuracy) has an absolute value of 3 mN for a test case where the expected load was 951.57 mN. She attributes the difference to the visual leveling of the thrust sensor.

Because the thrust level for the current experiments will be in the range of 100 mN to 300 mN, the bias will affect the signal significantly. Hence, another bench was searched for.

6.4.2. Test bench AE-TB-50m

Stef Janssens designed and built a thrust bench for micropulsion test applications, with a usable range of 0.5-50 mN [6]. He aptly named it the TB-50m, see Figure 6.8. The mechanics of the bench are simple: it has a bearing around which a beam revolves. The thruster is mounted on one side, while the thrust sensor will be at the other side. When the thruster fires, the beam will exert pressure on the thruster, which is then translated to a corresponding force. Special measures are to be taken to reduce friction in the beam bearing. This can be done by mounting relatively heavy engine parts directly above the bearing. Also, it should be noted that the thrust needs to be adjusted for the distance of the engine

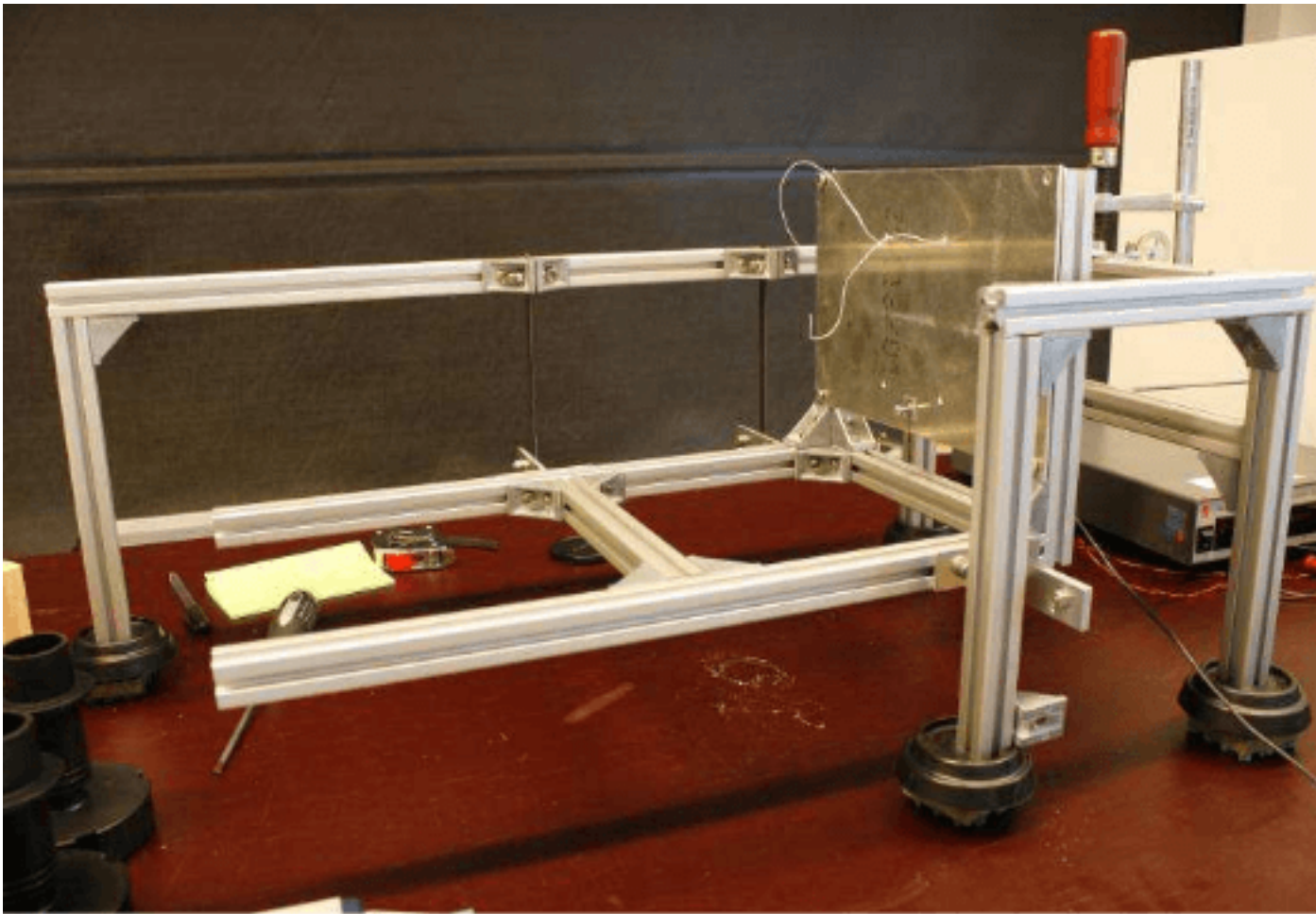


Figure 6.7: Thrust bench TB-1.1 [5].

to the bearing relative to the distance of the bearing to the sensor. Using the law of moments where the distances along the beam are taken into account, the thrust of the engine can be calculated.

The used thrust sensor was the Futek LRF400 (L2338), having an upper limit of 100 mN and a reported accuracy within 2 % (for datasheet, see Appendix C.1). However, Janssens designed the stand for 50 mN, as the lower limit of the TB-1.0 was at that level. He does not elaborate on the applicability of the bench in the 50–100 mN range, but it can be expected that extending the thrust arms would increase the range to 100 mN. Next to this, another issue arose: the bench was disassembled in the past decade. However, in 2015 Krusharev [7] rebuilt it for his own micro-thrust purposes (see Figure 6.9). Again, the LRF400 was the working sensor. Afterwards, again it was disassembled to allow other students to use the parts for their goals.

Both Janssens and Krusharev reported extensively in their theses what components (including datasheets) were used, the capabilities of the bench and the methods of calibration, both for atmospheric conditions and vacuum. This serves as a way to reassemble the stand using the modular Boikon profiles. Again, the LRF400 will be built in but for flexibility, the Futek LSB200 (also advised by Janssens) is also present at the faculty of AE (see Appendix C.2 for the datasheet). This is a higher range thrust sensor, up to 100 g (or 1000 mN). However, the sensor appears to be inaccurate below 15 mN. For now, the lower range Futek LRF400 will be used in the thrust bench. Should it prove to be unsuitable, for example because of higher thrust ranges, the other sensor can be selected. Be aware the the bench will be rebuilt and calibrated around the LRF400; implementing the LSB200 instead is not complicated, as it has a simple thread connection on both sides, similar tot the LRF400. However,

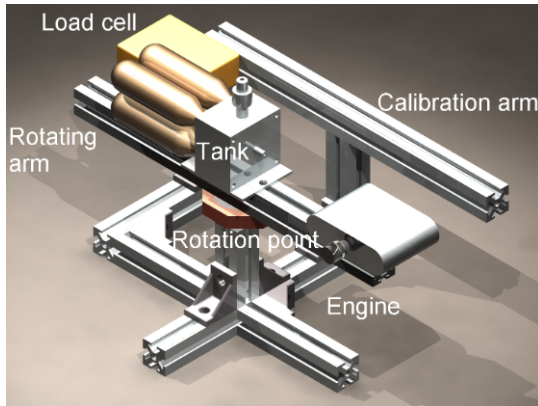


Figure 6.8: Thrust bench TB-50m, by Janssens [6].

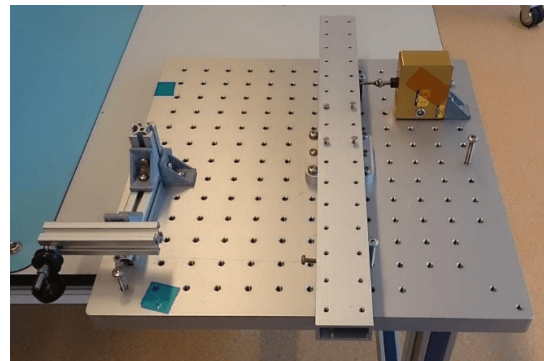


Figure 6.9: Thrust bench TB-50m, by Krusharev [7]. The LRF400 sensor is clearly shown in the top right corner.

the standard thread is different, so another bolt will be necessary.

Rebuilding AE-TB-50m

Thus, the TB-50m was (again) built out of the parts scattered in the AE cleanroom. It has a good resemblance to the Krusharev version, however a few adjustments can be spotted in Figure 6.10; extra Boikon profiles are added for more stability and for more flexibility in the alignment of thruster and sensor. The middle beam is mounted on the bearing used by Krusharev. Figure 6.11 shows the connection of the rotating beam to the sensor.

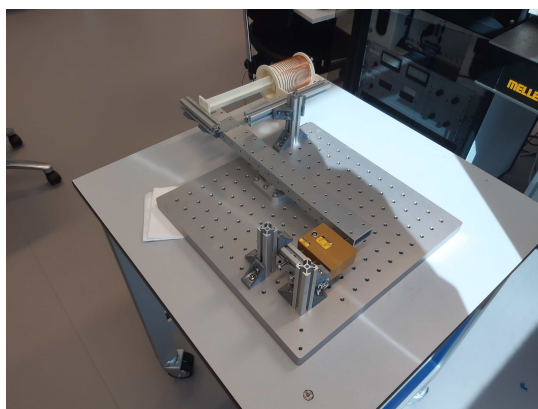


Figure 6.10: Thrust bench TB-50m, by Takken, Again, the LRF400 sensor is shown at the bottom.

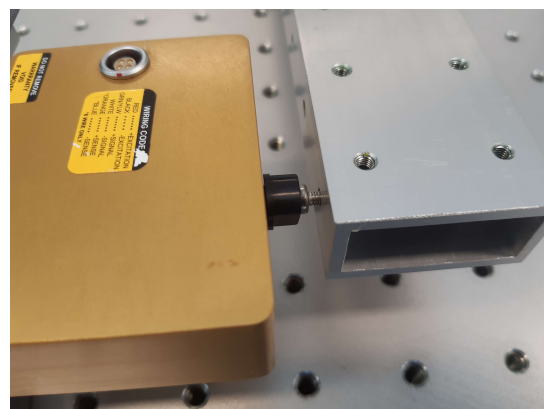


Figure 6.11: Connection of the rotating beam to the sensor.

Because the test stand was rebuilt from scratch, the calibrations performed by earlier users were not valid. As such, they had to be redone. But first, the sensor output was calibrated, see next subsection.

Relating LRF400 sensor output to force

As with Krusharev's stand, the LRF400 sensor will be measuring the thrust exerted by the engine. The sensor will be connected via an RS-232 cable to an NI DAQ USB-6008 device (see C.5 for the datasheet). In turn, the DAQ is connected via an USB cable to a computer. The sensor (Appendix C.1) will have a rated output of 1 mVV^{-1} . For an excitation voltage of 10 V which the DAQ provides, this will only amount to a measurable range of 10 mV, lower than the DAQ's absolute accuracy. As such the analog amplifier shown in Figure 6.12, named Scaime CPJ Rail (see Appendix C.6 for datasheet), was added to the circuit. It boosts the voltage (or current output, per user requirement) to 0-10 V. In

its datasheet, the gain is not displayed, but increasing the rated output from 10 mV to 10 V will give a gain of 1000.

Now, the sensor voltage values are to be related to force values. This will be a linear relationship in the order of $y = ax + b$, where the slope a and the intercept b need to be determined. In order to do this, a set of weights (with known masses) will be applied to the thrust sensor.

At first, a set of weights from the AE cleanroom will be weighed on the Mettler Coledo AG245 electronic scale (for datasheet, see Appendix C.7). The scale has a reported accuracy of 0.1 mg or 1×10^{-3} mN. Figure 6.13 shows the weighing setup and Table 6.1 presents the masses in the first two columns. Note that additional masses in the form of small bolts and nuts were added to the box by a fellow student, which are numbers 5 to 9 in the table. These were measured on the scale as well to increase the number of data points.

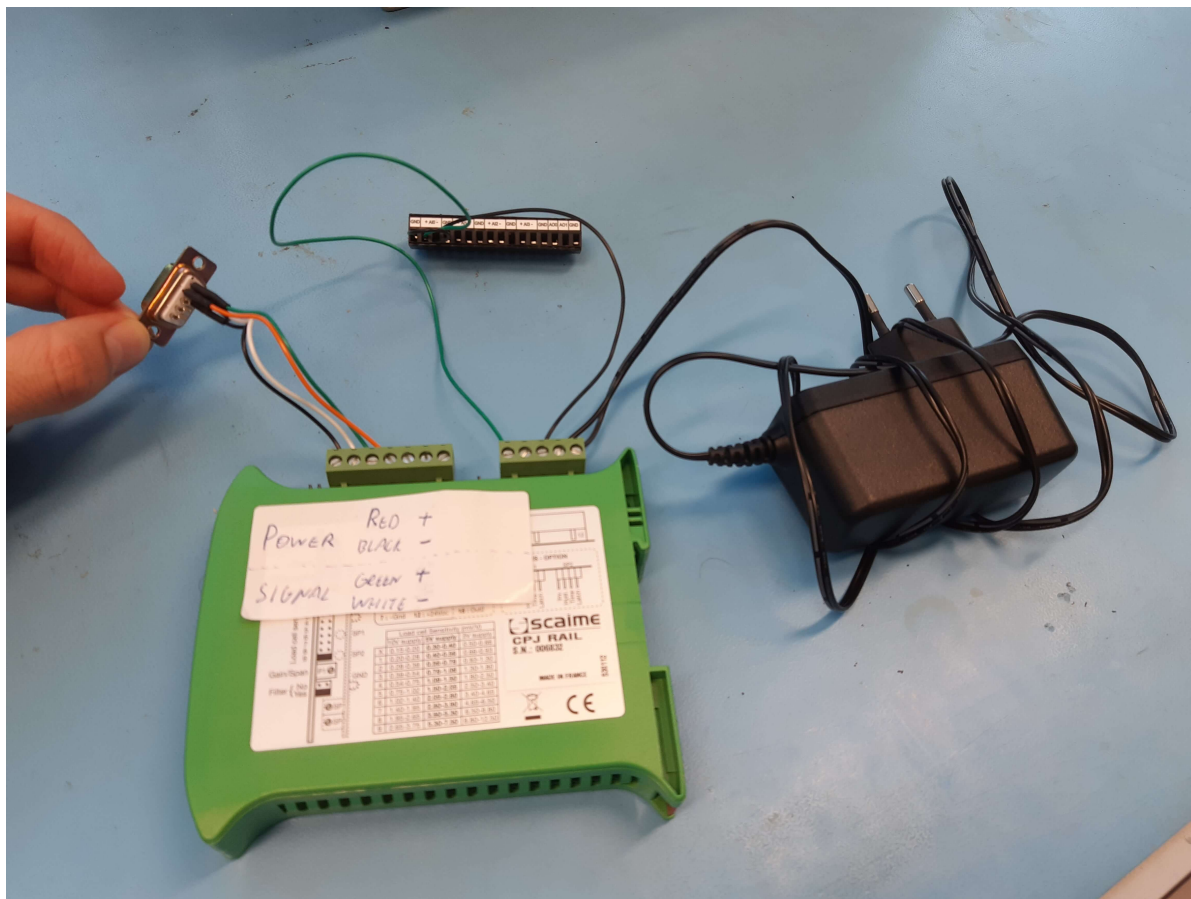


Figure 6.12: The analog amplifier Scaime CPJ Rail. It has three connections: the right to the power grid (230 V), the middle towards the DAQ device and the left to the RS232 cable of the thrust sensor.

Then, those weights were laid on the upright (vertical) force sensor, see Figure 6.14. Using a simple [Laboratory Virtual Instrument Engineering Workbench \(LabVIEW\)](#) script, the voltage output of the sensor via the CPJ Rail and DAQ was read. This gave a relation between the mass and voltage, where the mass can be converted to a force by multiplying the mass with the local gravitational acceleration, assumed to be 9.81 m s^{-2} . See the third column in Table 6.1. Thus appeared a linear regression line between the weights' weight and voltage for the sensor in Equation 6.1. During this test, the sensor did not respond well to the lowest masses (downwards from 0.200 g or 2.0 mN); the readings were fluctuating between values, e.g. for an indicated mass of 0.002 g the readings were either 0.0048 mN or 0.0020 mN. This was not seen as an issue, see further below.



Figure 6.13: Measuring the weights with the electronic scale Mettler Toledo.



Figure 6.14: Measuring the sensor voltage output with the use of the weights.

Table 6.1: Sensor voltage output versus mass.

#	Indicated mass [g]	Measured mass [g]	LRF400 voltage output [V]
1	10	10.0024	8.0705
2	5	5.0017	3.3025
3	2	2.0005	0.4397
4	1	1.0000	-0.5142
5	0.6290	0.6289	-0.8704
6	0.3872	0.3877	-1.1045
7	0.2872	0.2871	-1.1961
8	0.2142	0.2156	-1.2673
9	0.0725	0.0718	-1.3996
10	0.0451	0.0446	-1.4301
11	0.500	0.5002	-0.9925
12	0.200	0.1999	-1.2775
13	0.100	0.0998	-1.3691
14	0.050	0.0498	-1.4199
15	0.020	0.0200	-1.4505
16	0.010	0.0099	-1.4606
17	0.005	0.0048	-1.4708
18	0.002	0.0020	-1.4708

$$V_{LRF400} = 0.0972 \cdot F_{LRF400} - 1.4701 \quad (6.1)$$

For the range of 2-100 mN. Here the force F_{LRF400} is in mN and the voltage V_{LRF400} is in V with an R^2 value of 0.999 998 7, see Figure 6.15. Thus, the regression line fits the data very precisely, despite the fluctuating voltage values for lower masses. Conversely, the force can be made dependent on the voltage, see Equation 6.2.

$$F_{LRF400} = 10.28 \cdot V_{LRF400} + 15.12 \quad (6.2)$$

Again, with force F_{LRF400} in mN and the voltage V_{LRF400} in V. It should be noted that the sensor will not be placed in an upright position in the test stand, but in a horizontal way. When the sensor was rotated 90° during testing, the sensor voltage under rest (so no applied load) did change from -1.47 V (equivalent to 15.12 mN) to -4.09 V (equivalent to 42.10 mN). The latter value in Equation 6.2, the intercept, is thus only valid for vertical measurements, for horizontal measurements the intercept should be adjusted to 42.10 mN. However, the test stand can still be calibrated for the slope value.

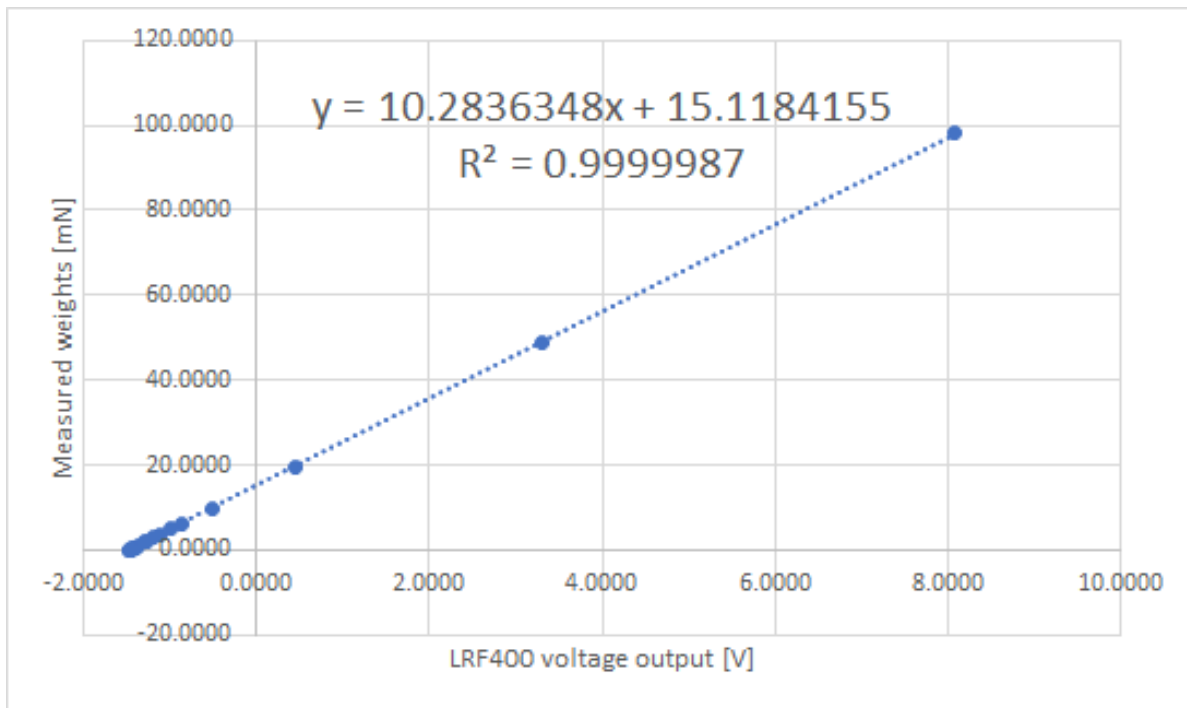


Figure 6.15: Weight on sensor versus voltage.

Calibrating AE-TB-50m

Now that there exists a relation between the sensor voltage output and force, the test stand as a whole can be calibrated. In order to this, two simple experiments were thought of: calibrating by using electromagnetic force, and calibrating by simple weights of which the masses are known (presumably the same weights as used before). Regarding the latter, some low friction pulley of some sorts should be added to the stand over which a wire attached to a basket is suspended. This was executed by Janssens as well, however those parts cannot be found at this instant. Thus, the other way, by electromagnetic force, was used.

At the faculty of AE exists a so-called **Variable-Turn Density Coil (VTDC)**, developed by R. Bijster in 2014 [69]. It creates a homogeneous magnetic field while current runs through the coil which will induce a electromagnetic field if any magnet is inserted. For more details, see his thesis. In 2020, fellow students H. Versteeg [70] and A. Pappadimitriou related the current to the force, which turned out to be 0.826 mNA^{-1} with 3σ confidence bounds of $\pm 0.006 \text{ mNA}^{-1}$, where σ is the standard deviation.

Both the **VTDC** and the actuator holding the magnet are available in the AE cleanroom. Thus, mounting the coil and actuator on the bench provided an easy method to calibrate the bench. In Figure 6.10, the coil and actuator are shown at the top.

The test was setup as follows: a **LabVIEW** script, created by Versteeg, would raise the current from 0 to 20A in steps of 1A. The current would be monitored at a sample rate of 100 Hz and each step would be held onto for 60 s, thus giving 6000 data points per step or 120 000 in total for the test. At the same time, another **LabVIEW** script would save the sensor force readings, adjusted by the aforementioned Equation 6.2 at a pace of 3 Hz, which then gave thrust information for 3,600 data points. These force readings were then adjusted according to Equation 6.3.

$$F_{EM} = F_{LRF400} \cdot \frac{d_1}{d_2} \quad (6.3)$$

Where F_{EM} is the electromagnetic force exerted by the coil-actuator pair in mN, F_{LRF400} is the outputted force of the sensor in mN, d_1 is the distance of the sensor to the centre of the bearing (along the beam) in mm and d_2 is the distance of the centre of the bearing to the actuator (along the beam) in mm. The latter were measured using a caliper and determined as $d_1 = 175.00$ mm and $d_2 = 167.70$ mm.

Then, the resulting adjusted F_{EM} would be averaged for each step of 1 A. The same was done for the current values recorded by Versteeg's script. Thus, these 20 data points were then plotted and a regression line was drawn to determine the slope of the graph. If the test stand adds no significant friction to the measurements and parts are properly aligned, this value should be close to the previously mentioned 0.826 mNA^{-1} value. Please note again that only the slope can be determined from the graph, the intercept is of no value as the sensor is turned sideways to be in the horizontal plane. By surveying previous test runs, the intercept value was manually entered at 42.10 mN, in contrast to the (vertically aligned) value reported in Equation 6.2 of 15.12 mN. As shown before, the intercept is not important as it can be easily determined at the start of experiments or during the analysis afterwards.

In Figure 6.16 the graph with the 3600 data points containing the F_{EM} values is shown versus the time which equaled 20 steps of 60 seconds each at a sample rate of 3 Hz. A significant amount of deviation is detected. Versteeg and Valente suggested that this is the noise induced by building vibrations and any by-passers. Figure 6.17 represents the averaged data per step versus the current. Note that the current was also averaged for the 20 steps, because the actual current running through the coil was not exactly equal to the integers 0, 1, 2.... The slope of this graph equals 0.788 mNA^{-1} with an R^2 of 0.9994, which is 4.72 % off from the reported value by Versteeg and Pappadimitriou. Please note that the intercept value is not exactly zero, although the previously chosen value of 42.10 mN was apparently close.

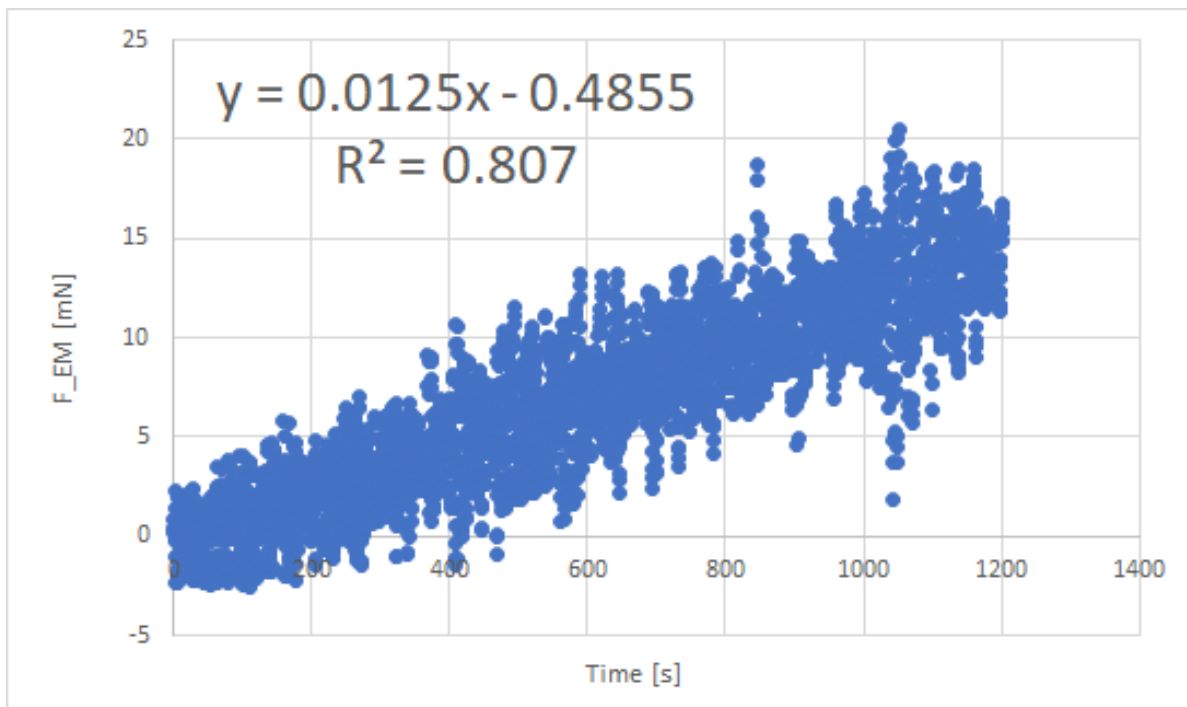


Figure 6.16: Test 1: F_{EM} versus time.

What was later discovered is that, at the higher current range (from 16 A onwards), the coil will heat up and affect the magnetic field. Omitting the data points higher than 16 A would result in a more accurate slope value of 0.800 mNA^{-1} , which only differs by 3.26 % from the coil value.

However, it was decided to redo the test and add more Boikons profiles to secure the sensor and coil better to the base stand. A very precise alignment was also of importance as mentioned by

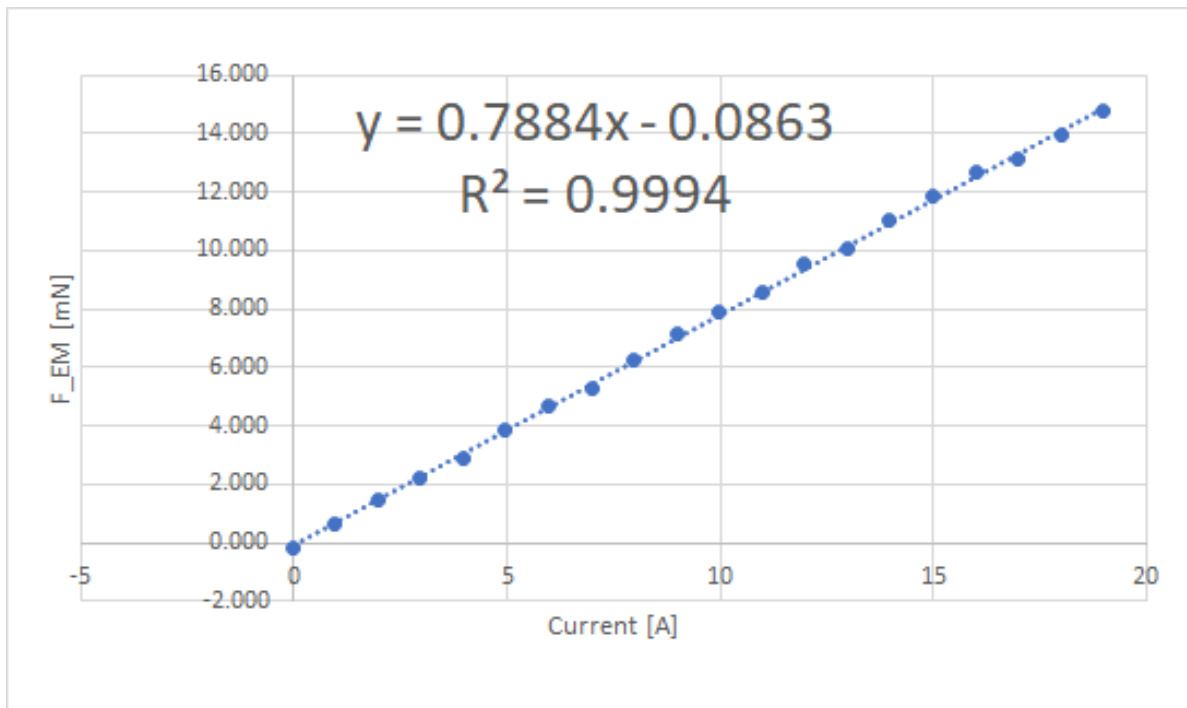


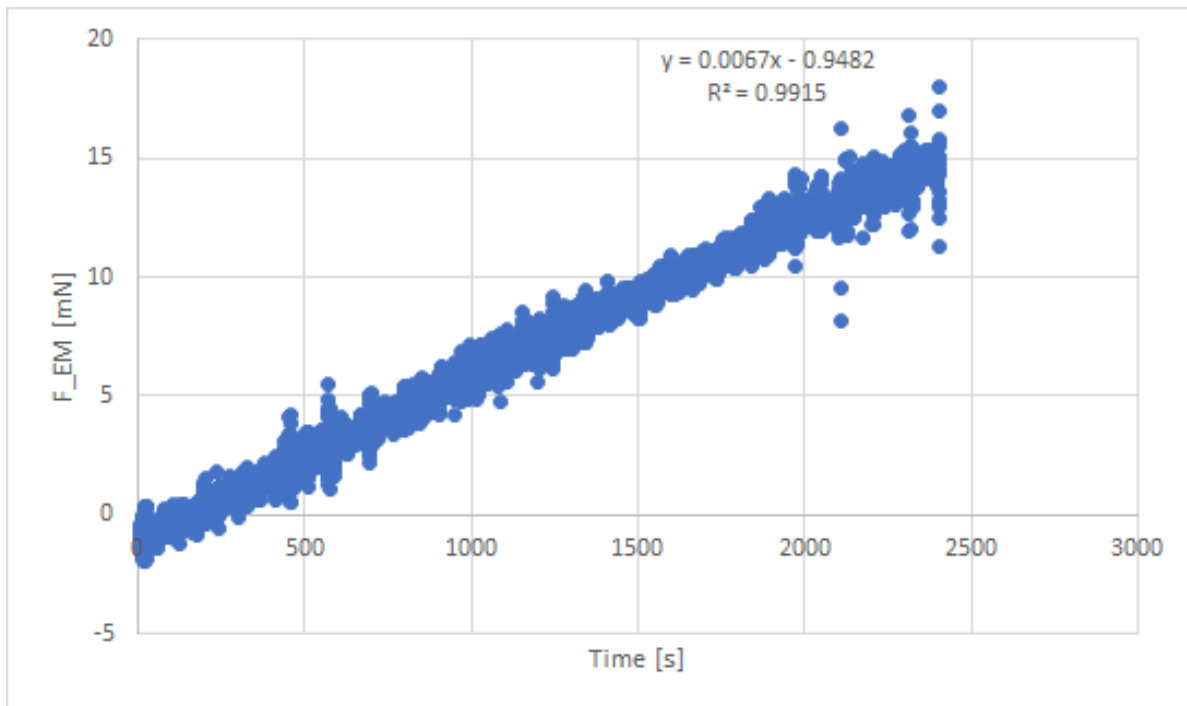
Figure 6.17: Test 1: averaged F_{EM} over steps of 1 A.

Valente in her thesis [5]. Figure 6.10 depicts the stand ready for the second experiment. The test was conducted in the same way as test 1, however now steps of 0.5 A were taken. Distances d_1 and d_2 were measured at 175.00 and 170.91 mm respectively. The intercept (see Equation 6.2) was reset at 53.95 mN. Following the procedure described above, it resulted in the graphs depicted in Figures 6.18 and 6.19.

As seen from Figure 6.18, the noise of the unaveraged data is much lower in test 2 than it was in test 1. Some outliers are seen after 2000 s, this is likely caused by the author entering the cleanroom. Figure 6.19 depicts the slope value of 0.803 mN A^{-1} , already an improvement over the previous 0.800 mN A^{-1} from test 1. However, what is clearly seen in both pictures is again that the temperature has a large effect on the electromagnetic force; the second graph displays an offset starting at 16 A. In fact, at the end of test 2, a smell was detected in the cleanroom which was the coil overheating.

Only taking the force values up to 16 A, gave a precise (R^2 equal to 0.9997) gradient of 0.823 mN A^{-1} , with a very minor difference of 0.31 % with respect to the coil slope of Versteeg and Pappadimitriou. Furthermore, for test 2 σ was calculated for each step of 0.5 A, which consisted of 180 (or 3 Hz over 60 s) data points. These standard deviations were then averaged over the range of 0-16 A, which resulted in a σ of 0.347 mN. Comparing this value to the reported standard deviation of 3.6 mN of TB-1.1 by Valente [5] at a thrust of 948.5 mN, one can see that this is a huge improvement. Be aware that this standard deviation has been asserted for a small range. However, within this range no increase in standard deviation was noticed when increasing the current (and thus thrust). It is expected that the value is still significantly lower when approaching the upper limit of the TB-5m, which is 100 mN.

The standard deviation above is averaged for a varying range of current (and thus thrust). More interesting is to see test 2 as a combination of separate tests at different currents: to be precise a combination of 33 subtests, from 0 A to 16 A. These can be normalized to one and the same current, for instance 10.0 A. Please note that is not possible for the 0 A reading, leaving 32 tests. This allows us to calculate the 3σ (99.7 %) confidence bounds for the mean of these experiments. This indicates that, if the test is redone, with 99.7 % confidence one can say that the mean of this test will fall within the confidence bounds. The mean μ of the 32 subtests (all at 10 A) equals 8.1699 mN, with a σ of 0.2210 mN. Then, the confidence bounds are found by Equation 6.4.

Figure 6.18: Test 2: F_{EM} versus time.

$$F_{LRF,10A} = \left(\bar{\mu} \pm 3 \cdot \frac{\sigma}{\sqrt{n}} \right) = \left(8.1699 \pm 3 \cdot \frac{0.2210}{\sqrt{32}} \right) = (8.1699 \pm 0.1172) = (8.1699 \pm 1.43\%) \quad (6.4)$$

Where n is the amount of samples to calculate the mean thrust. $F_{LRF,10A}$ is in mN. Note that the mean is very close to the desired value of 8.26 mN. The difference is attributed to minor errors in hand measuring the distances and possible interference of the coil connections to the computer, causing variations in the magnetic field. A possible third explanation is that the bench was not leveled horizontally. For this, level sensors were needed but these were forgotten. It is known that tilting the sensor has an effect on the nominal measurements, however if the bench is tilted at the same angle these effects could be cancelled out in the gradient. See the recommendations for further improvements on this.

Because the difference is minor, the bench is considered to be calibrated up until 16 A or equivalently 12.3 mN. The intercept, set at 53.95 mN in the beginning, should be adjusted by 0.80 mN to a value of 54.75 mN.

6.4.3. Test bench conclusions & recommendations

AE-TB-50m was rebuilt and calibrated for the range of 0-12.3 mN. It could not be calibrated for a higher thrust range, because the current was limited to 20 A. Two possible methods to calibrate the bench were discussed in this section. The first one is by electromagnetic force with the use of a combination of coil and magnet actuator, the second is by hanging weights from a wire and (low-friction) pulley. It is recommended to alter the first method to be able to measure higher forces, because the upper limit of the current combination is 20 A or approximately 16.5 mN for a bench which could potentially go to 100 mN. Furthermore, the coil overheats if kept at higher currents (>16 A) for extended periods of time. Altering can be achieved in a number of ways: one can install an actuator having more or stronger magnets or elongate the rotating beam in the direction of the coil.

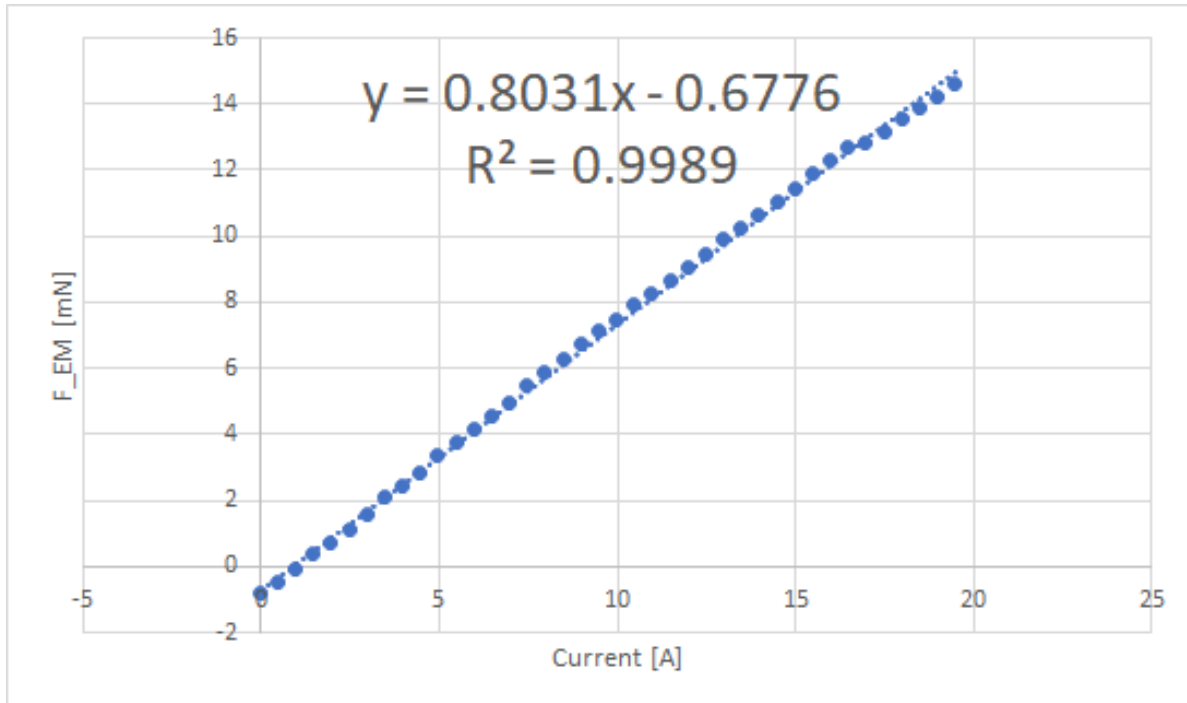


Figure 6.19: Test 2: averaged F_{EM} over steps of 0.5 [A].

It is also advised to recalibrate the bench when a thruster is fit onto the bearing arm. It is not known what the effect would be of the added mass. The two methods described above would be suitable for this. Furthermore, it would be interesting to see what the influence of room temperature would be on the bench output, as Valente already reported an influence of temperature on the readings for her TB-1.1. Next to that, looking into the tilt of the bench would be an improvement, as this could have an influence on the output. Last thing to mention is that the bench can be calibrated in combination with the LSB200 sensor, to see if its range can be extended to 1000 mN.

6.5. Preliminary experiment results

This section will discuss the first preliminary test results. As it turns out, there are some issues with the hardware and the experiment location. The reasons not to commit to further experiments are explained and the subsequent change in plan to finish the project is presented.

6.5.1. Experiment stop

What became apparent in Section 5.3.3 was that the reduction of the number of channels from 6 to 1 proved disastrous to the usefulness of the heat exchanger; the cross-sectional area through which the propellant had to pass was simply too small, which resulted in enormous pressure losses of almost 31 bar or the feed system not delivering enough pressure to overcome the heat exchanger barrier. Next to that, the channel was so small that it approached the nozzle throat area; effectively, an extra nozzle was created inside the [RAC](#).

Next to that flaw, another was discovered during the few test runs that were done in this chapter: the heat exchanger leaked, especially at the inlet and outlet and at the outlet side of the cavity. The latter was because the holes in both cap and outer cylinder should line-up, but when they did, the cap was not entirely screwed on the cylinder. It was tried to remedy this problem with gas tape (teflon) and heat resistant fireplace kit (see Appendix C.8 for the datasheet), which helped to some extent.

However, after a few days the kit was hardened and it appeared to block the channel; unfortunately, the piece could not be opened because of the same kit. This problem could be mitigated in the design by excluding thread connections and allowing hard-soldered connections. When trying to disassemble the [RAC](#) with brute force, the connection to the copper nozzle was broken as well.

A third reason to stop the experiments was because of the COVID-19 pandemic. As such, access to all faculties at [DUT](#) was restricted and no experiments could be carried out at the faculty of [3mE](#) anymore.

6.5.2. Plan for continuation

All the flaws and setbacks combined, it was decided to decommission STT2 and start looking for alternatives to validate the preliminary model presented in the previous chapter. It is a pity that a project which took a lot of resources could not continue, but a new plan was setup. In order to continue validation on the [PDT](#), the physical experiments were altered to simulation, by [CFD](#). These simulations could accurately show what thermal efficiency was gained and what pressure losses would be experienced by the propellant flow. Furthermore, the knowledge gained from the simulations could be used to make a final thruster design, dubbed [STT3](#). Chapter [7](#) will show the [CFD](#) setup, analysis and [STT2](#) results while Chapter [8](#) will focus on that final design.

7

Computational Fluid Dynamics modelling

In the previous chapter, it became clear that validation is still necessary for the [PDT](#), especially in case of propellant flow. However, experiments could not be continued, so another path is chosen: [CFD](#) simulations are to be used for validation. The current chapter will describe the setup and execution of multiple [CFD](#) models. These simulations will be used to assess the heat flows in the [RAC](#). The equations relating to those heat flows, being convection, radiation and conduction, were explained in Chapter 4. Using the [CFD](#) method, these heat flows as calculated by the [PDT](#) can be confirmed and a better view can be acquired regarding the convection heat flow from [RAC](#) to propellant.

[CFD](#) is the numerical analysis of a flowing fluid (gas or liquid) and its properties (temperature, pressure etc.) using computational power. The fluid flow and related heat transfer are governed by the [Navier-Stokes \(equations\) \(NS\)](#) or simpler Euler equations [71]. The [NS](#) equations are partial differential equations consisting of inertial, viscous, external force and pressure terms, derived from the mass, momentum and energy conservation laws [72]. They can be analytically or numerically solved. [CFD](#) does the latter. In general, [CFD](#) analysis follows a procedure where first the physical object which is subject to the simulation is defined. This can be done using [CAD](#) software and is the start of the so-called pre-processing. Then, solid and/or fluid regions are discretized or divided into small elements, which form the mesh. Next, the models that are applicable to the simulation are defined. One can think of the flow type (laminar, turbulent) which needs to be set, if thermal models need to be applied, if radiation is present and so on. Afterwards, the boundary conditions, such as the fluid flow velocity, starting temperatures and applied thermal loads are given. Then, the solver is chosen and the simulation commences. The software computes the relevant equations for each individual element in the mesh and tries to approach a solution (converge) where the differences or residuals between the elements are lowest. Once the simulation has converged, the user can extract the relevant data in the post-processing phase.

First, the [CFD](#) software for the numerical calculations is chosen. Then, multiple sections on the cases from the preliminary tool chapter are presented. These cases will be setup, executed and post-processed. The cases will be used confirm the validity of the [PDT](#). The same criterion for validation as seen in Chapter 3 will be used, namely that the highest heat exchanger temperature as determined by the [CFD](#) simulations should fall within 10 % of the output of the [PDT](#). In the end, conclusions and recommendations on this validation are given. Note that in this chapter, only the heat exchanger or [RAC](#) will be discussed. The focus will be on the heat exchanger because analysing the system as a whole is considered out of scope for this project. For more information about [CFD](#) analysis on nozzles, see fellow students Krusharev [7] and Dickert [73].

7.1. Computational Fluid Dynamics program choice

A number of CFD programs are available for the simulations described in this chapter. The most prominent ones among those are Ansys (Fluent or CFX), Comsol and OpenFoam. The first two are software packages from commercial companies, while the latter is an open-source program which is thus freely available. In previous theses at SSE and in papers related to STP those programs were used for a variety of tasks, such as ray tracing, conjugate heat transfer and nozzle performance. For instance, Krusharev utilized Ansys Fluent in his thesis to determine the thrust and subsequent specific impulse of four different nozzles [7]. Likewise, Ferreira recommended to replace his self-made analytical tool by an Ansys model which he thought could be more accurate [61]. Pino used Ansys not for CFD, but to structurally analyse his solar concentrator, which also happens to be in the area of STP [45]. In various handbooks, such as Tu et al [71], Rohsenow [58] and Zandbergen [23], Ansys (Fluent) is mentioned. Comsol was used by Das to model the incoming radiation of a solar thermal thruster [48] and is also mentioned in the handbooks. OpenFoam was used in the past by students Denies for rocket engine regenerative cooling thermal analysis [74] and Khamis for fluid flow analysis in MEMS thrusters [75]. OpenFoam is regarded by some to have a steeper learning curve, also because it lacks a dedicated Graphical User Interface (GUI) which Ansys and Comsol do possess.

It should be noted that the author of this thesis does not have any prior knowledge in CFD. Thus, after consulting some fellow students and staff at the faculty of AE, the choice was made to use Ansys Fluent. Be aware that this could also have been one of the others, it mainly depends on the experience a user has. A student version of Ansys Fluent can be downloaded from the DUT software website software.tudelft.nl. This version has a maximum amount of 512 000 mesh elements. During simulation setup and running, the manual was used extensively [76]. To get a grip on the software, multiple tutorials were watched, both from Ansys and [youtube.com](https://www.youtube.com).

7.2. Quantification of losses to ambient

In this section, the quantification of thermal losses to the ambient is presented. As could be seen in Chapter 3, the heat exchanger loses heat because of convection and radiation to the ambient, both at the inner as the outer side of the RAC. This section will show the road map on how these losses are determined. Furthermore, this elaborate section will frequently be referred to in later sections, when the setup and execution of the individual cases is discussed. This section will thus show a step-by-step "recipe" on how to properly do a CFD analysis and produce useful results.

The heat exchanger will not be modeled in vacuum, but in air at room properties of 298.15 K and 1 atm. Modeling in vacuum would see the convection loss mitigated but the radiation loss increased dramatically, as the surrounding space is in general modelled at a temperature of 3 K.

Ansys Fluent has been chosen as the solver, but most of the tasks will be performed in Ansys Workbench which serves as a handy means to access all different Ansys modules. It consists of four tasks which are to be executed to complete a simulation: geometry, mesh, setup and post-processing. All four will be explained in detail below.

7.2.1. Geometry

It starts off with the physical model of the RAC of STT1. The CAD drawings are available from Leenders' thesis [3]. Ansys DesignModeler is the CAD module that is integrated within the Workbench. Two RAC domains can be distinguished here: the RAC domain which is the material (in this case: copper) and the fluid or propellant domain (in this case: gaseous nitrogen). The material domain consists of the inner cone, outer cone and propellant ring. These are not modelled as separate entities but as one solid object. Any inconsistencies or minor gaps between the parts are thus not incorporated in the Fluent Model. After the material domain has been constructed, the fluid domain is etched out of the

material.

In Figure 7.1, one can see the RAC. A cross-section is shown in Figure 7.2. The heat exchanger exit is slightly different than the drawings indicate. To simplify things here, the thread has not been modeled but simply constructed as a solid wall containing a hole with a diameter of 3 mm. In normal operations, a bolt containing a hole would be inserted in the exit, so it is expected not to have much impact in terms of mass or thermal performance. Figure 7.3 shows the fluid domain, with the propellant inlet at the left top and the exit at the right bottom. In Table 7.1, relevant sizes coming from the program are shown. Note that the RAC domain inner area is split into an inner cone wall and into an inner circular wall. Irradiation will only fall upon the earlier surface. The density of copper is taken from Fluent as 8978 kg m^{-3} . Note that the mass equals the sum of masses of the individual three parts as described by Leenders [3]. The outer surface area does differ significantly from the value given by Leenders (see also Table 3.3), which is mainly due to the fact that he did not take the ring into account for his calculations.

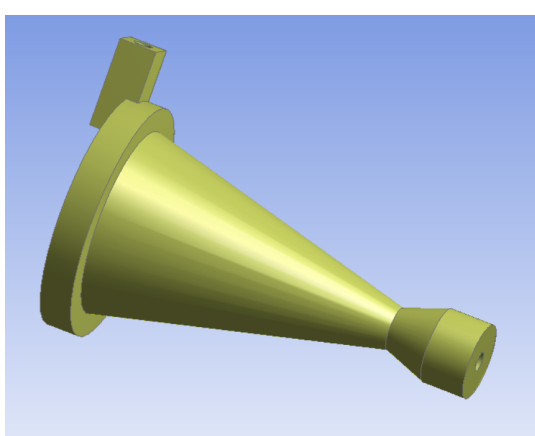


Figure 7.1: Solid domain of Ansys physical model of STT1.

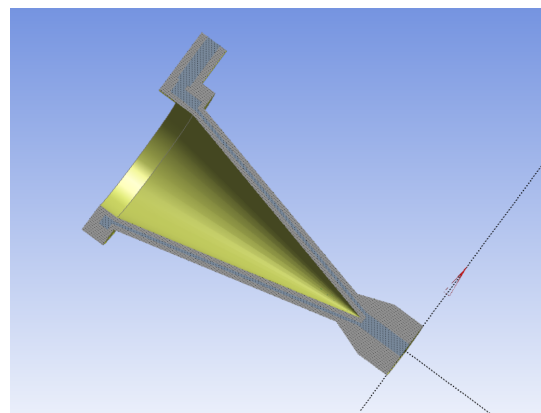


Figure 7.2: Cross-section of Ansys physical model of STT1. Note the smaller hole at the exit, which is on the right bottom of the picture. Furthermore, both inner walls (cone and circular) can be observed.

Table 7.1: STT1 sizes by Ansys DesignModeler.

	Size	Unit
RAC domain inner cone area	2026	[mm ²]
RAC domain circular ring area	322	[mm ²]
RAC domain outer area	5124	[mm ²]
RAC domain volume	9732	[mm ³]
RAC domain mass (copper)	0.0866	[kg]
Fluid domain connection area	1995	[mm ²]

For the quantification of the convection and radiation losses, there are three options in Ansys Fluent: a surrounding ambient domain consisting of air combined with a radiation model, simple equations which require some inputs from the user or a mix of both. All three are explained below.

1. Ambient domain and radiation model

The first option is to build a rectangular "box" around the solid and fluid domain which will represent the surrounding air. See Figure 7.4 for an example. The upper wall of this box will be more distant from the RAC than the other walls, as natural convection from the heat exchanger to the ambient will be modeled as a loss. This way, the plume can develop and will not be hindered by the ambient domain "walls" before it leaves the ambient system. The size of the surrounding ambient domain is based on experience from the author and will be sufficiently large to allow the natural convection loss to develop but not be too large to prevent the amount of mesh cells becoming too large. The radiation is then

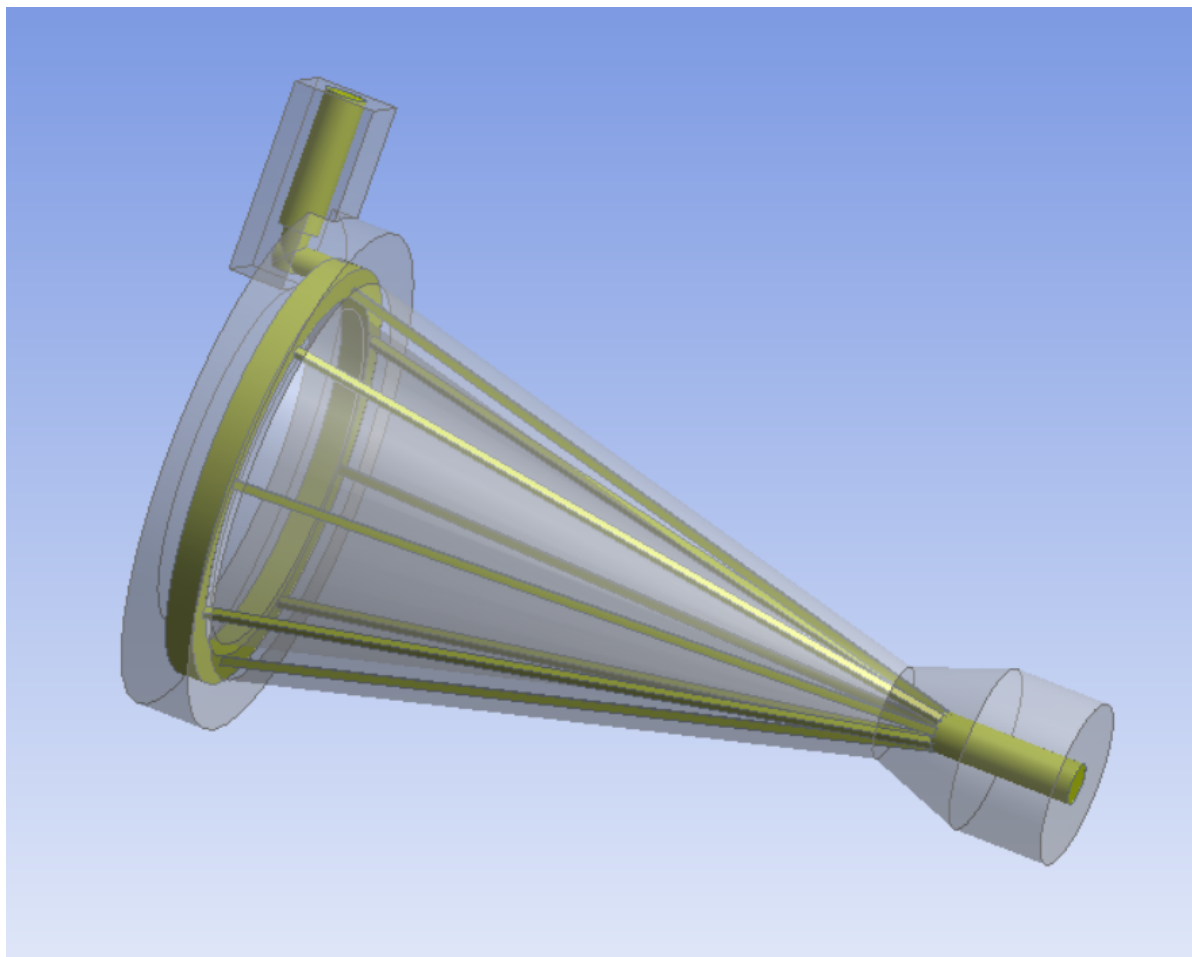


Figure 7.3: Fluid domain of Ansys physical model of STT1.

calculated via the built-in **Surface-to-Surface (S2S)** radiation model from Fluent. The advantage is that it automatically implements the view factor (which is important for the inner cone) so the radiation loss is calculated accurately.

Downsides to this method are the increased computational time and the increase of complexity of the problem. Next to that, the inlet and outlet of the fluid domain need to be elongated so that the start and end outside of the ambient domain. This means that long tubing outside of the **RAC** is needed, which increases the complexity even further. It was surprising to see in a test run that this was needed, but the solver kept diverging because of the fluid "spilling" in the ambient domain. For the definition of divergence, see later in this section.

2. Equations with inputs from the user

Another option is to not model the ambient air surrounding the heat exchanger. This would save a lot of computational power and time and would allow the mesh in the solid and fluid parts to be more refined. Instead, Ansys hands the user the option to enter a convection heat coefficient h (in $\text{W m}^{-2} \text{K}^{-1}$), free stream temperature $T_{\text{inf},1}$ (in K), emissivity ϵ (dimensionless) and external radiation temperature $T_{\text{inf},1}$ (in K) for each surface. Using these four variables, the losses Q_{conv} and Q_{rad} (both in W) for each surface would be automatically calculated depending on the surface temperature T_{surface} (in K) according to Equations 7.1 and 7.2. In those equations, A is the surface area in m^2 and σ is the Stefan-Boltzmann constant ($\text{W/m}^2/\text{K}^4$). Although this is an easy solution which requires minimal computing power, h is usually hard to determine for natural convection (especially in non-

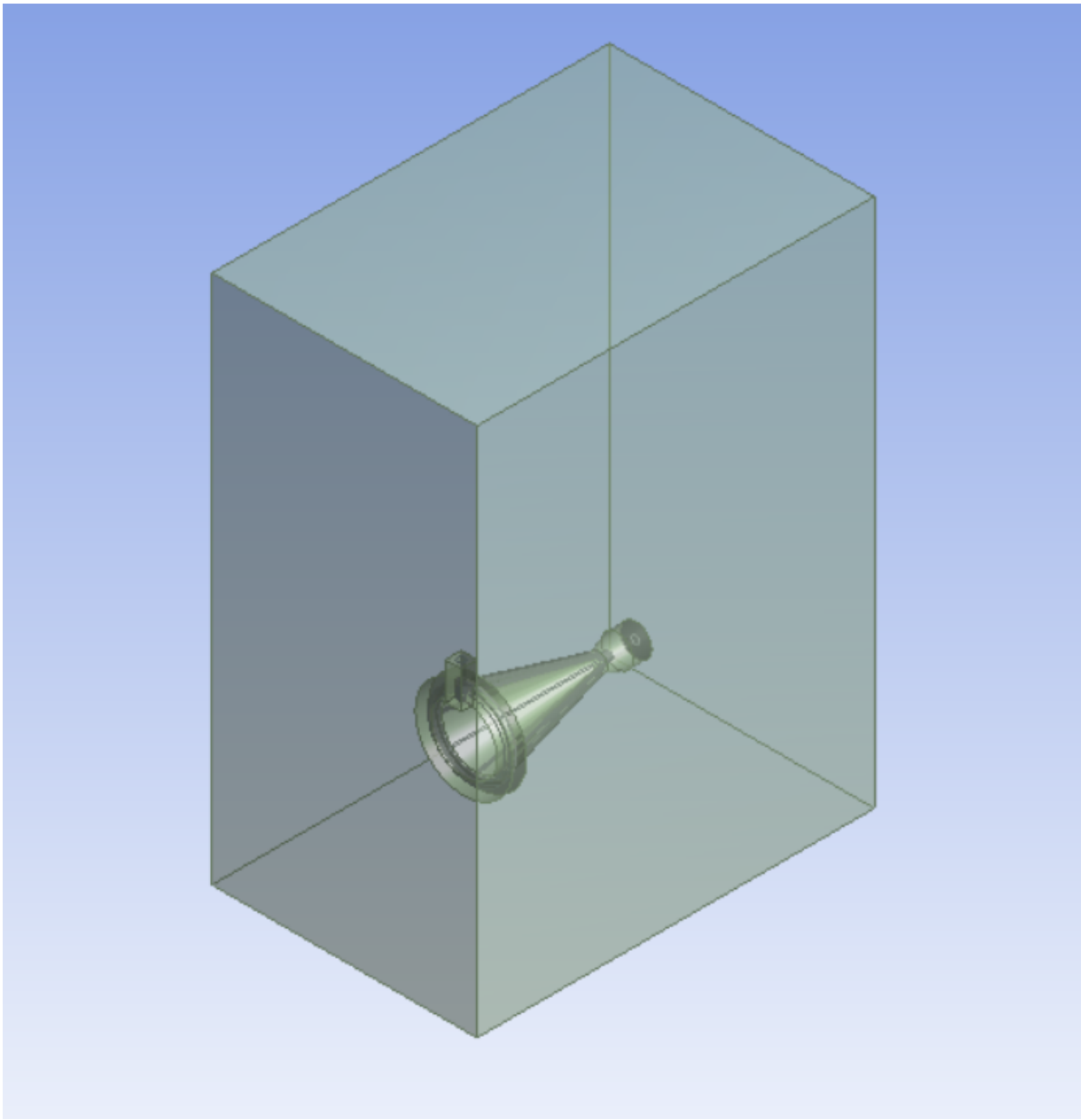


Figure 7.4: Air domain containing the RAC and fluid domain.

standard geometric figures) and view factors are ignored in the radiation term. An approximation of h can however be found from literature. The absence of view factors can be handled by adjusting the emissivity factor if the view factor to the ambient is lower than 1, but it requires some hand calculations.

$$Q_{loss,conv} = hA(T_{surface} - T_{inf,1}) \quad (7.1)$$

$$Q_{loss,rad} = \epsilon\sigma A(T_{surface}^4 - T_{inf,2}^4) \quad (7.2)$$

3. A mix of both

A third option would be a mix of the two: at first the area-weighted average h is to be determined using the ambient domain but without fluid flow. Once this average is determined, the ambient domain can be deleted and the equations stated above can be used to determine the convection coefficient.

Choice for physical model

After some test runs with the physical **RAC**, the third option was chosen. The most prominent reason for this was that the solver did not converge when option 1 was followed. There simply were not enough elements present to both mesh the ambient and the fluid domain properly. Thus, first the convection coefficient h is determined without any propellant flow, then the ambient domain is deleted and the cases can be executed with the application of the earlier determined h to the outer **RAC** walls. The ambient domain will have a length of 110 mm, width of 50 mm and height of 100 mm. It will be placed around the heat exchanger symmetrically, except in the height direction; to account for heated air raising in the domain, it will extend more to the top than to the bottom.

7.2.2. Mesh

In Figure 7.5, a cross-section of the meshed ambient domain (the box), **RAC** domain and fluid domain (somewhat harder to see) is shown. One can see the density of the mesh increasing closer to the object of interest. This is also happening in Figure 7.6, which gives a closer look at the **RAC** and fluid domain. The areas of rapid changes in velocity and pressure of the fluid were automatically meshed denser by the program.

As told above, the mesh should not exceed 512 000 elements due to the student license **DUT** provided. During simulation running, the solution would often not converge because the mesh was too coarse. Convergence in this case is defined as the sum of the scaled residuals decreasing to some lower value, for instance 1×10^{-6} . These scaled residuals are calculated per element and then summed for each variable involved, such as energy (if the energy model is on) or fluid velocity in some particular direction. It is a great way to evaluate if the solution is a sane one. If the energy residuals are low, the solution can be deemed converged.

In order to remedy the divergence of the solution, it was tried to refine the mesh at physical points where the solver would show strange behaviour, such as elements having negative Kelvin temperatures or enormous velocities. This helped to some extent, but eventually applying a symmetry boundary condition was the most useful measure to reduce the number of elements. The object is reflectionally symmetrical and would even be twice symmetrical if not for the fluid inlet which prevents this. The elements that were "freed" were then used to refine the mesh, especially at the boundaries between **RAC** and ambient domain, both at the inner and outer side of the cone. Eventually, this gave way to a converged solution for the determination of h .

7.2.3. Setup

This subsection will deal with the setup of the simulation, including the models, boundary conditions and solver.

Gravity

The gravity will be toggled on, with value of 9.81 m s^{-2} in the negative y-direction. The positive y-direction is where the fluid enters the **RAC**. The gravity is amongst other important to the free convection, as free convection is buoyancy-based which simply means that heated air will rise because its

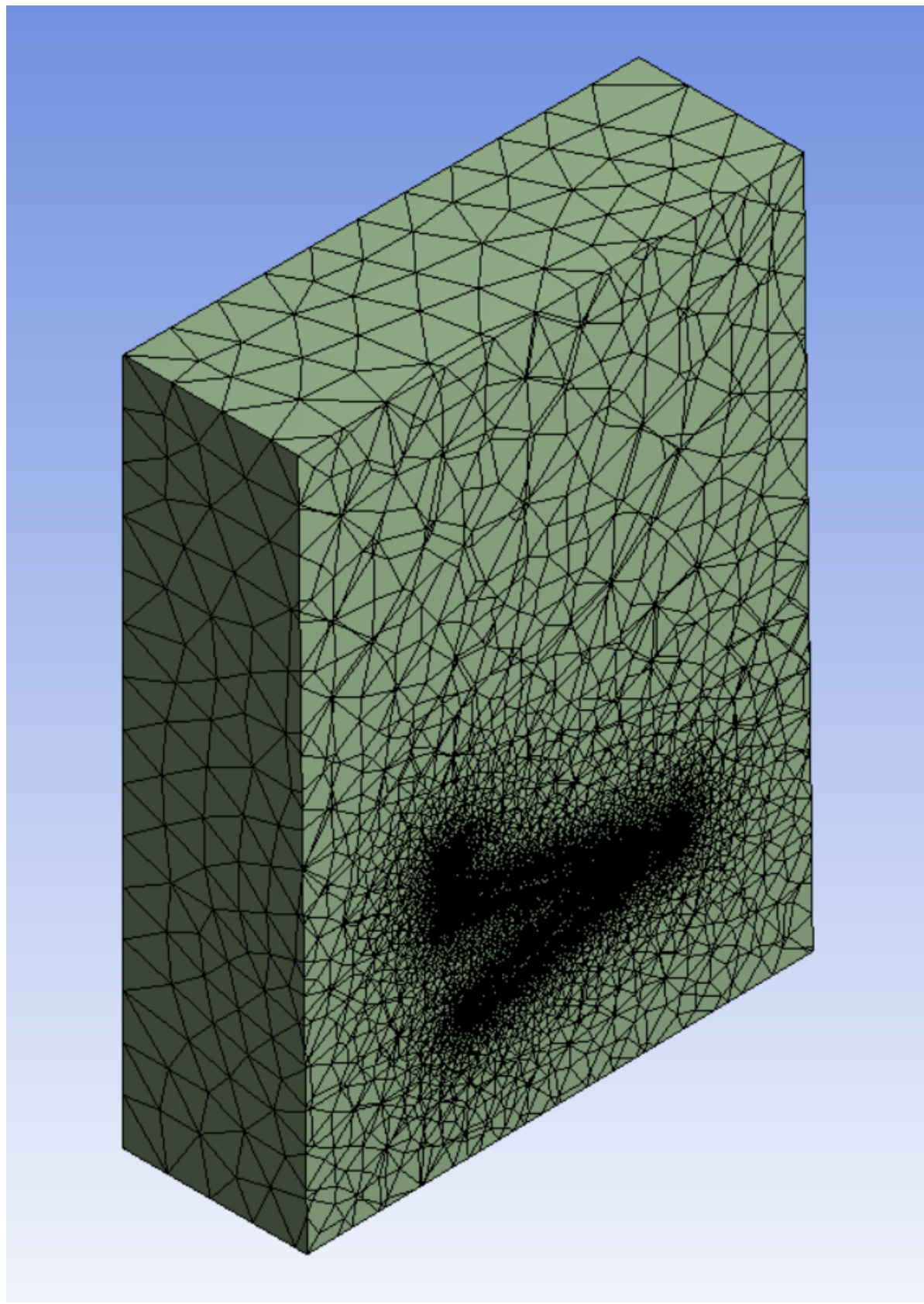


Figure 7.5: Cross-section of the meshed ambient, RAC and fluid domain.

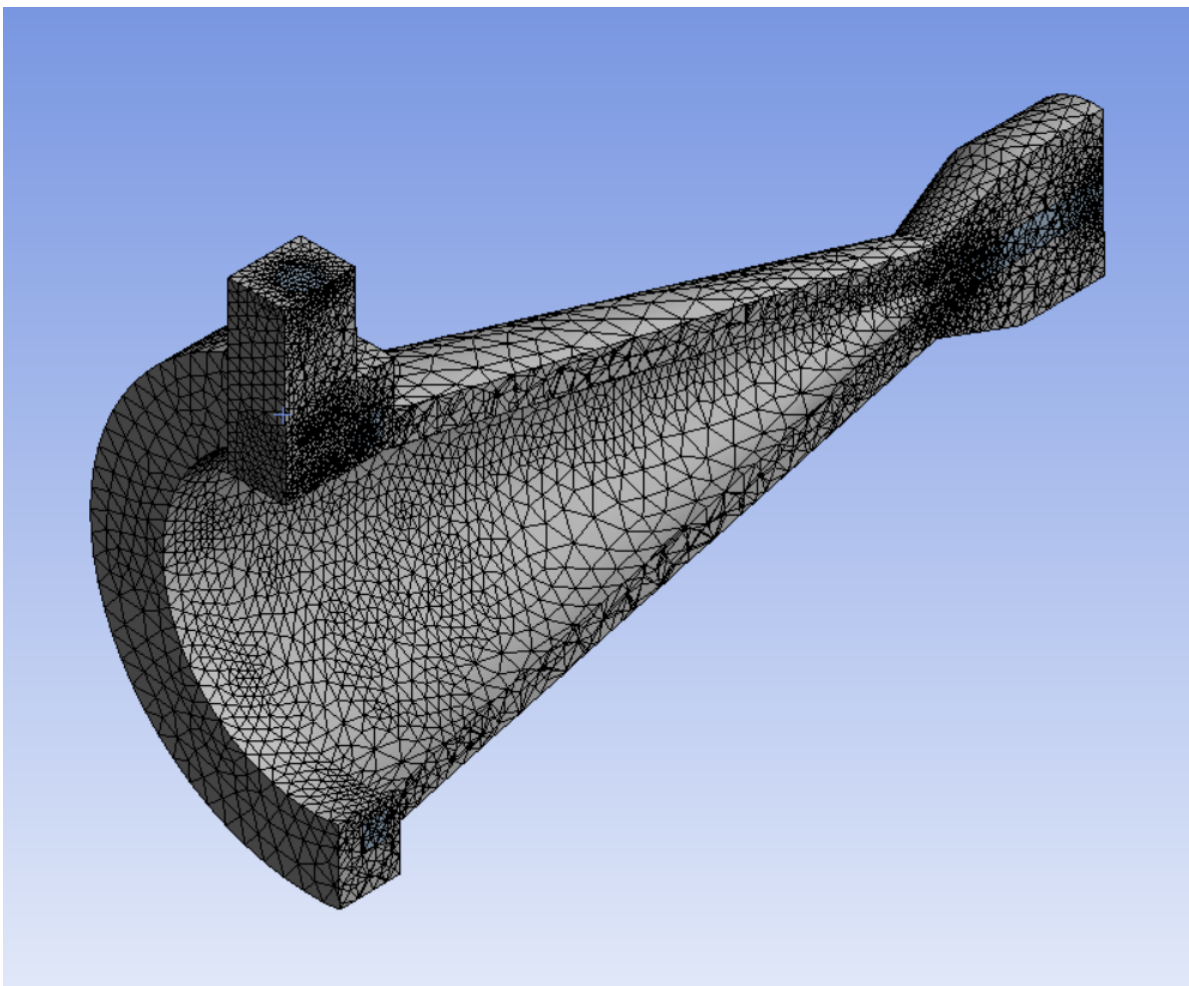


Figure 7.6: Closer cross-section of the meshed RAC and fluid domain. Note the two inner walls: the cone inner wall and the small circular inner wall.

density has been decreased.

Transient or steady-state

The solver can be setup in two ways: the simulation can be done transient (unsteady) or steady-state. The former is a time-dependent simulation, where the applied heat fluxes that go in the system do not necessarily equal the outgoing heat fluxes. Ansys requires a time-step in this situation. Steady-state on the other hand will see the heat fluxes balanced out throughout the system. In steady-state simulations, the object(s) and fluid(s) involved will not change properties (e.g. temperature, pressure) with time. If a transient solver runs for an extended amount of time, it will approach the steady-state solution.

A transient approach will be done for this simulation, so the influence of RAC temperature on h can be discussed.

Materials

Fluent offers a large variety of built-in materials, both fluid and solid. It is easy to rerun a simulation using a different material having e.g. a higher thermal conductivity or lower density to see its effects.

The RAC will consist of copper with a density of 8978 kg m^{-3} , C_p of $381 \text{ J kg}^{-1} \text{ K}^{-1}$ and k of $387.6 \text{ W m}^{-1} \text{ K}^{-1}$. Note that all three are constant and will not change with temperature.

The fluid domain would normally be filled with gaseous nitrogen, which has an ideal gas density (derived thus from the pressure and temperature), k of $0.0242 \text{ W m}^{-1} \text{ K}^{-1}$ and dynamic viscosity μ of $1.663 \times 10^{-5} \text{ Pa s}$. Again, the latter two are constant with temperature and pressure. However, in this simulation which will determine the convection coefficient h , no propellant will be present and the fluid domain will be filled with air, see properties below. It is modelled this way because it is assumed that no tubing is attached so that the channels can fill themselves with air.

The ambient domain consists of air with ideal gas density, constant C_p of $1006.43 \text{ J kg}^{-1} \text{ K}^{-1}$, constant k of $0.0242 \text{ W m}^{-1} \text{ K}^{-1}$ and constant μ of $1.7894 \times 10^{-5} \text{ Pa s}$. The density cannot be set constant, as heated air would not rise due to buoyancy in that case.

Boundary conditions

The boundary conditions will define the constraints of the problem. The first boundary condition is the temperature at which the system will kick off. All domains will start at room temperature, which is 298.15 K . Then, the fluid inlet and outlet will be simple coupled walls which will conduct heat from fluid to ambient and the other way around (if applicable), because there is no propellant flow. The channel walls will also couple the RAC domain and fluid domain, so that heat transfers between those two. The inner and outer RAC walls will both be coupled with the ambient domain, so that convection occurs. Note that no radiation boundaries are applied, only convection and conduction is present in this simulation.

Now, there is a small issue. In an experiment, the room where the test is held is normally very large when compared to the test object. Thus, one can safely assume that the ambient is at a constant temperature. The heated air circulates and air at the starting temperature replaces the moved pocket. However, modelling such a vast room in Ansys is undoable, as it would require enormous amounts of mesh elements and computing power. To remedy this, three simulations will be run. In these simulations, the air domain side walls will have a somewhat arbitrary air velocity input of 0.1 m s^{-1} , 0.01 m s^{-1} and 0.001 m s^{-1} and the air domain top wall will be the pressure outlet of the system. The results will be compared and commented on.

Finally, the inner cone area (one surface) will experience an incoming heat equal to 27.18 W . This was derived from the power input which was used in the cases in Chapter 3. It will be applied as a heat generation rate (in W m^{-3}) over a very small thickness (in m^2) because Fluent unfortunately does not allow a heat flux in a coupled wall.

Initialization

The simulation will be started with an initial guess of all cells, which will be done via standard initialization. The starting temperature will again be set at 298.15 K . The operating pressure is $101\,325 \text{ Pa}$ or 1 atm . The number of time steps will be 300 with 5 iterations per time step. Each time step will be 20 s . The software will thus simulate the model for 6000 s or 100 min .

Solving

The solver ran for approximately 45 min per simulation. For all three simulations, the energy equation residual did converge to a value around 1×10^{-8} , with a very small oscillation. This is due to the natural convection, which brings some instability in the heat leaving via the air domain. It is also due to the fact that the transient solution approached steady-state, which is prevented by again the inherent instability of the natural convection. The temperature of both inner and outer wall did not increase after the 300

time steps for all simulations. Only the latter simulation (for an airspeed of 0.001 m s^{-1}) experienced backflow at the top, which means that air is flowing back in the air domain system. What the effect of this is is not known. In Figure 7.7, the scaled residuals of this simulation are shown. In the further figures down below, the results of the simulation with the lowest airspeed will be shown.

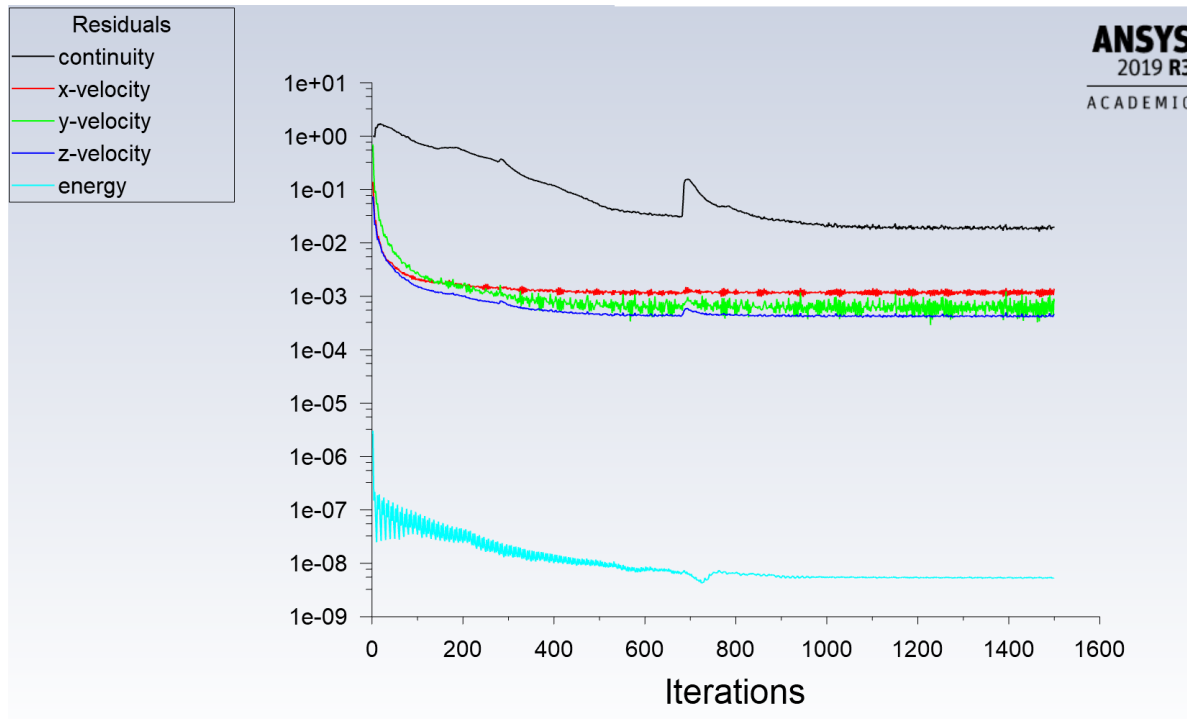


Figure 7.7: Scaled residuals of the simulation to determine convection losses for a case without insulation at an airspeed of 0.001 m s^{-1} . Note the very small oscillation in the energy equation.

7.2.4. Post-processing

In Figures 7.8 and 7.9, the heated fluid domain is shown in side and fronts views respectively (airspeed of 0.001 m s^{-1}). The higher temperature area at the top of the cavity with respect to the bottom can clearly be seen. This is due to buoyancy, note that gravity is pointing down (in the negative y-direction) in the pictures. Next to this, Ansys Fluent outputs a ASCII file which can be read by Excel. Area-weighted averages of both temperature T (in K) and fluxes q (in W m^{-2}) from the inner and outer walls are outputted. From these, the convection coefficient h in $\text{W m}^{-2} \text{ K}^{-1}$ can be calculated using Equation 7.3. In this equation, T_∞ is the ambient temperature in K, which will be equal to 298.15 K. This temperature will also be used as an input for further simulations when it concerns the free-stream temperature related to convection heat transfer.

$$h = \frac{q}{T_{wall} - T_\infty} \quad (7.3)$$

In Figure 7.10, the temperature of both inner and outer walls are shown (0.001 m s^{-1}). The temperature rises smoothly until 80 min, after which it seems to stabilize. Taking the last temperatures after 100 min of flow time, they are 748.42 K, 747.47 K and 747.64 K for the inner cone wall, inner circular wall and outer walls respectively. Be aware that the outer walls consist of multiple surfaces which are (area-weighted) averaged to obtain the current temperature. There will thus be some variation on these outer walls, which are all in connection with the ambient. The resultant temperatures are very close, with the largest temperature difference being 0.95 K. It proves that the assumption from Chapter 3 that the temperature throughout the RAC can be seen as equal in all locations due to the

high thermal conductivity is valid.

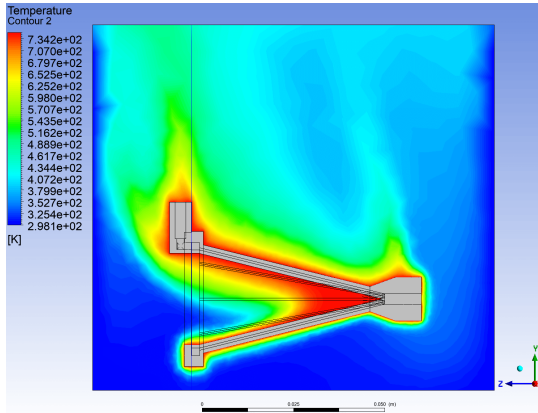


Figure 7.8: Side view of the heated air domain. Note how the upper part of the air in the cavity has a higher temperature than the lower part, due to buoyancy (gravity is pointed down, in the negative y-direction). Airspeed is 0.001 m s^{-1} .

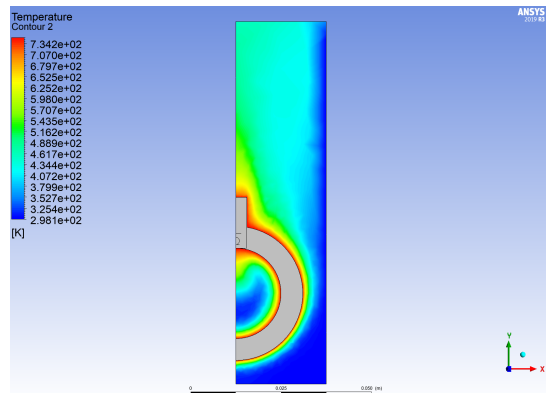


Figure 7.9: Front view of the heated fluid domain. Again, a small higher temperature pocket is seen at the top of the cavity, in the positive y-direction. Airspeed is 0.001 m s^{-1} .

In Figure 7.11, the resulting h for both the inner cone and circular walls and outer walls for all three simulations are shown. Unsurprisingly, the values are higher for the outer than for the inner walls. Air tends to be “blocked” in the inner pocket, which acts as a buffer to cool air entering, thus lowering the convection. The convective heat transfer coefficient, after some initial differences, stabilizes after 40 min. Taking the average after this point yields the results shown in Table 7.2. The values do quite differ, with lower convection loss values with lower airspeed. This is unsurprising, because with lower airspeeds less cold air is forced into the domain. Incropera et al. [9] state a range of $2\text{-}25 \text{ W m}^{-2} \text{ K}^{-1}$ for free convection in gases, so the numbers seem viable. Furthermore, calculations using Equation 7.3 showed that the simulations all outputted 27.10 W, so all approached steady-state.

Table 7.2: Convective heat transfer coefficients per airspeed and emissivities. Results of three simulations with the air domain surrounding the RAC domain.

	$h [\text{W/m}^2/\text{K}]$ at airspeed of 0.1 [m/s]	$h [\text{W/m}^2/\text{K}]$ at airspeed of 0.01 [m/s]	$h [\text{W/m}^2/\text{K}]$ at airspeed of 0.001 [m/s]	View factor to ambient [-]	Adjusted emissivity to ambient [-]
RAC inner cone wall	4.59	3.59	3.29	0.176	0.114
RAC inner circular wall	7.59	7.04	6.44	0.426	0.277
RAC outer walls	13.60	10.48	10.06	1.000	0.650

The values were also compared with the outputs from the equations in the preliminary tool Section 4.2. The Python script outputted, for similar inputs, an h of $1.72 \text{ W m}^{-2} \text{ K}^{-1}$ and $13.63 \text{ W m}^{-2} \text{ K}^{-1}$ for the inner and outer walls respectively. There is no distinction in the two inner walls in the preliminary tool. Both values do not correspond very well. The paper from Paitoonsurikarn [62] was aimed at a cylindrical cavity, which can explain the difference in the conical cavity. For the outer walls, the preliminary tool assumed a geometrical cone, while in reality there is a ring at the inlet and a thickened part at the end of the RAC. For the case following after this subsection, the values for an airspeed of 0.001 m s^{-1} will be used, as this airspeed is more realistic than a higher airspeed which would not be present in a laboratory during testing. However, it is recommended to redo these simulations if more powerful computers and a license allowing for more mesh elements is available. For now, the results here obtained are used, also because the interest lies mostly in the propellant convection domain.

Note that, when a steady-state simulation was executed for an airspeed of 0.001 m s^{-1} , similar

values for the temperatures and h were found after the solution stabilized around 600 iterations.

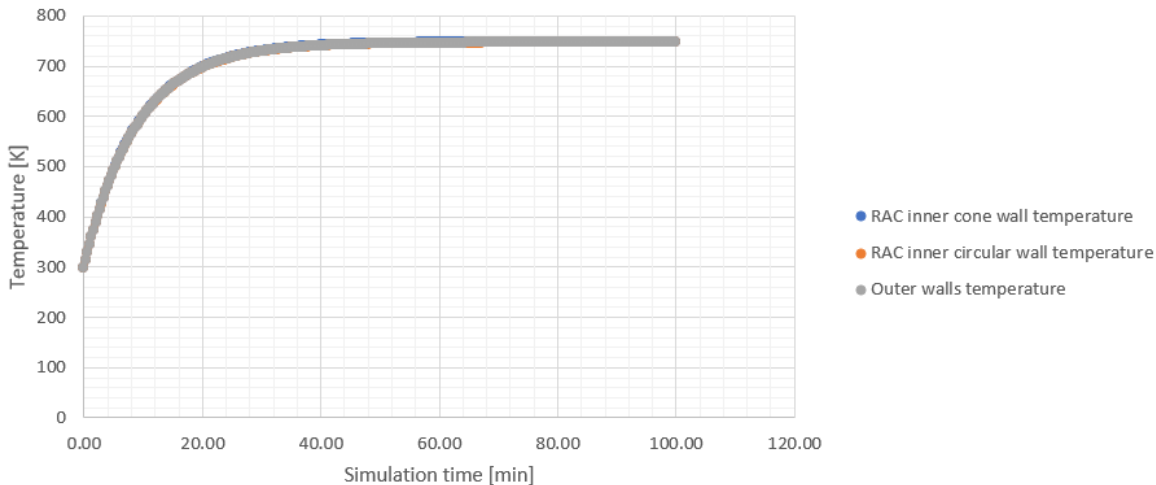


Figure 7.10: Area-weighted average temperatures for inner cone, inner circular and outer walls. Necessary to determine the convection losses for an RAC without insulation. Airspeed is 0.001 m s^{-1} .

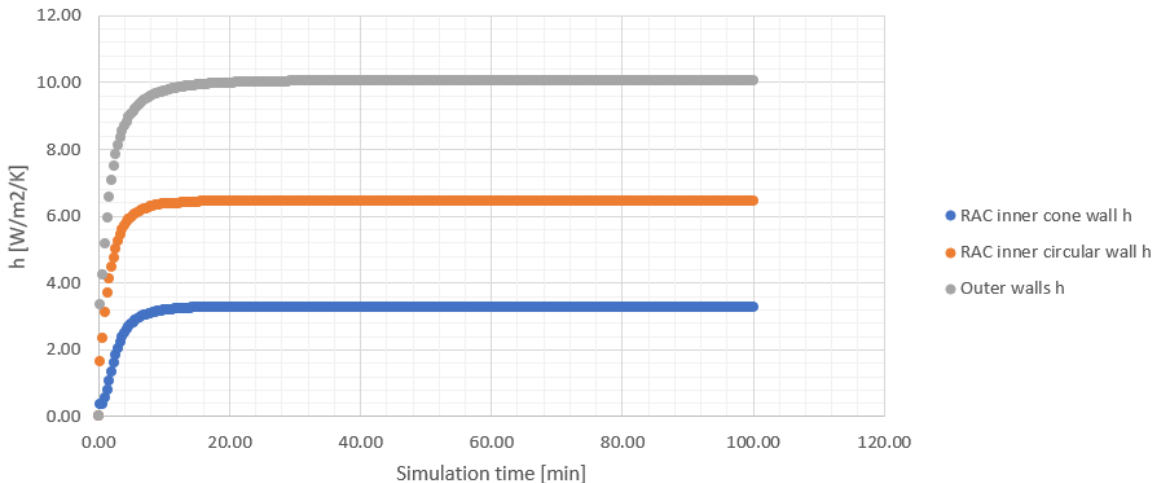


Figure 7.11: Convective heat transfer coefficients for inner cone, inner circular and outer walls, for a case without insulation. Airspeed is 0.001 m s^{-1} .

Now that the convective loss values have been determined, the ambient domain can be deleted. From now on, the convection will be calculated from Equation 7.1. For the other loss to the ambient, which is radiation, Equation 7.2 is used. However, as already stated, no view factors are used by Ansys Fluent when using the boundary condition related to this equation. This is not so much an issue for the outer walls, which radiate towards an ambient of emissivity 1 and 298.15 K as it is for the inner wall (including the inner wall ring). The latter two surfaces will partly radiate back to themselves, which reduces the radiation heat loss. To remedy this, the emissivity of both inner wall surfaces will be multiplied by the calculated view factors for those surfaces. It will thus be assumed that any radiated energy from a surface to itself will be fully absorbed and not reflected, to simplify matters. Note that the outer walls do not fully face towards the radiant; some small surfaces also radiate to other surfaces, but this will be ignored.

7.3. Case 1: Solar Thermal Thruster 1, no mass flow and no insulation

For the first case, which will be a physical RAC model of STT1 with no mass flow and no insulation, the setup from Section 7.2 is copied. The following inputs will differ or need explanation:

- The ambient domain will be deleted.
- All RAC domain walls will have a convection boundary condition with h equal to $3.29 \text{ W m}^{-2} \text{ K}^{-1}$, $6.44 \text{ W m}^{-2} \text{ K}^{-1}$ and $10.06 \text{ W m}^{-2} \text{ K}^{-1}$ for the inner cone, inner circular and outer walls respectively. The free-stream temperature is set at 298.15 K.
- All RAC domain walls will radiate energy towards the ambient. The emissivity of the walls will be 0.65. For the inner two walls (the cone wall and the circular ring), this number will be lower to account for the reabsorbing of the radiated heat. For the cone wall, the view factor to the ambient equals 0.176. Thus, the emissivity will equal 0.114 for this wall. For the circular wall, the view factor to the ambient is 0.426, which gives a resulting emissivity of 0.277 for that wall. The view factors were calculated with the same equations that were used in Subsection 4.3.1.
- The input power on the inner cone wall will equal 27.18 W. This is similar to the input in Chapter 3's cases, where the original input of 60 W would partly miss the RAC, partly be absorbed and partly be reflected back to the ambient (thus lost). See Subsection 4.3.1 for details.
- No propellant is flowing. The fluid domain is filled with air which will be heated by the RAC.
- The solver will still be transient and will run for 150 time steps of 20 s each. The number of iterations per time step is 5.

The solution converges very well (down to an energy residual of 1×10^{-9}), which was to be expected because there is no moving fluid. In Figure 7.12, one can see the temperatures of the three surfaces approaching steady-state around a temperature of 520 K. Again, the three temperatures lie very close to each other, proof of the high copper conductivity.

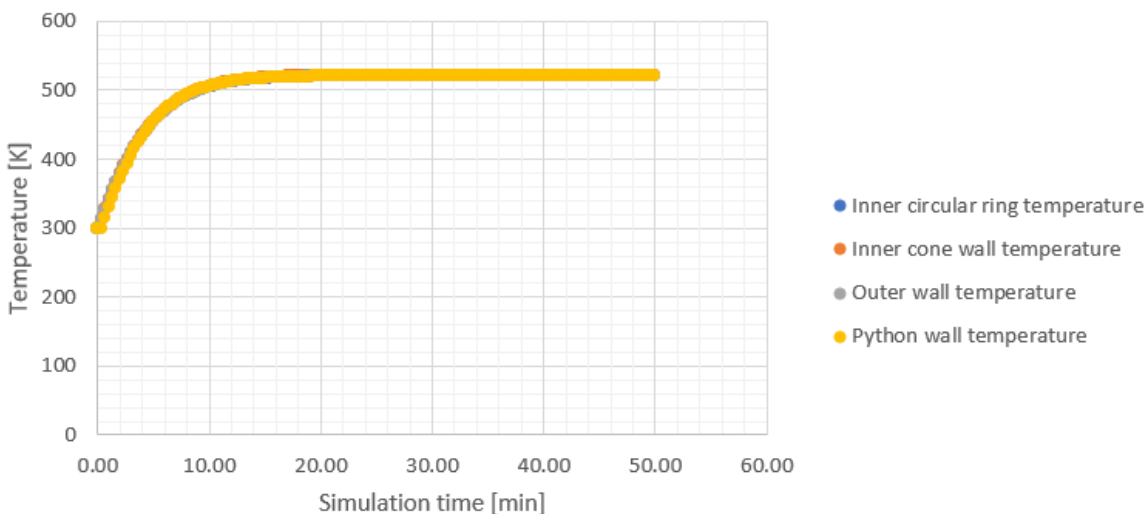


Figure 7.12: Case 1: area-weighted average temperatures for inner and outer walls. Note the overlaying Python wall temperature.

In Table 7.3, the inputs and outputs of the Ansys case 1 simulation are shown for the last time step, which is at 3000 s or 50 min. The radiation and convection heat flow have been checked using

Equations 7.1 and 7.2. One can see the results in the last row of the table, they resemble the values outputted by the Fluent simulation.

Table 7.3: Inputs and outputs for Ansys case 1.

		Inner cone wall	Inner circular wall	Outer walls	Unit
Input power	Input	27.18	0.00	0.00	[W]
Convective heat transfer coefficient	Input	3.29	6.44	10.06	[W/m ² /K]
Emissivity	Input	0.114	0.277	0.65	[-]
Final temperature	Output	522.27	521.18	521.49	[K]
Radiation & convection losses	Output	2.36	0.80	23.99	[W]

Summing the heat flows in last row yields 27.15 W, which is slightly lower than the power input. This means that the solution almost reached steady-state. Comparing the results with case 1 from the preliminary tool in Chapter 3, the final (which is almost steady-state) temperatures do differ, but not by a large amount: 507.9 K calculated by the preliminary tool versus the 521.18-522.27 K from the Fluent simulation. This is explained by the difference in convective heat transfer coefficients between PDT and CFD simulations. For the CFD runs, they are slightly lower. The difference falls within the 10% requirement, so Ansys Fluent does very well on simple heat problems with fixed convection and radiation coefficients and a constant power input.

7.4. Case 2: Solar Thermal Thruster 1, no mass flow and insulation

Case 2 introduces a thick insulation layer around the RAC with a very low conductive heat coefficient. Leenders indicated a cylindrical insulation layer with a diameter of 11 cm and length of 10 cm. He did not exactly state how this layer was placed with respect to the RAC. In the current simulation, the symmetry axis will coincide with the heat exchanger's symmetry axis (without the ring). Lengthwise, the layer will be placed so that on both ends it will stick out equally. A hole is made in the insulation towards the RAC aperture, with a diameter equal to that of the cone base diameter, which is 0.025 m. There are now three inner areas instead of two: the RAC inner cone and the RAC inner circular walls were already known, the circular inner insulation wall is the third. They will all be treated as a separate surface.

At first, the convection coefficients h need to be determined again. The same approach as in Section 7.2 will be used, with the difference that now an insulation layer is applied. The insulation is added as a material in Fluent, with a density of 100 kg m^{-3} and c_p of $1000 \text{ J kg}^{-1} \text{ K}^{-1}$. These two properties are constants, but the thermal conductivity k in $\text{W m}^{-1} \text{ K}^{-1}$ of the Saffil M-Fil will be dependent on temperature in K (see Appendix C.9 for the datasheet). A trendline, Equation 7.4, was created out of the three data points provided using Excel.

The ambient domain will have a length of 155 mm, width of 170 mm and height of 300 mm. It will again be placed around the heat exchanger symmetrically, except in the height direction; to account for heated air raising in the domain, it will extend more to the top than to the bottom.

The input power on the RAC inner cone wall will equal 27.18 W. The airspeed will be 0.001 m s^{-1} , coming from the air domain side walls. For the determination of h , the fluid domain will be united with the RAC domain so that more elements are freed up for critical areas, such as the RAC-insulation and insulation-ambient boundaries.

$$k = 3.125 \cdot 10^{-7}T^2 - 3.232 \cdot 10^{-4}T + 0.2065 \quad (7.4)$$

The solution converges nicely to a residual between 1×10^{-5} - 1×10^{-6} , again with a small oscillation. After 350 time steps of 20 s each (5 iterations per time step) the simulation is stopped. Figures 7.13 and 7.14 show the temperatures and convective heat coefficients respectively of the three earlier mentioned inner surfaces and the outer insulation surface. The coefficients become constant after 40 min. Averaging them from this time on, the coefficients displayed in Table 7.4 are obtained. The sum of the found coefficients are multiplied with the wall area and temperature difference between wall and ambient equals 27.15 K, which is very close to the inputted 27.18 K. The solution is thus almost steady-state. The highest temperature is reached at the inner copper cone wall and equals 796.1 K.

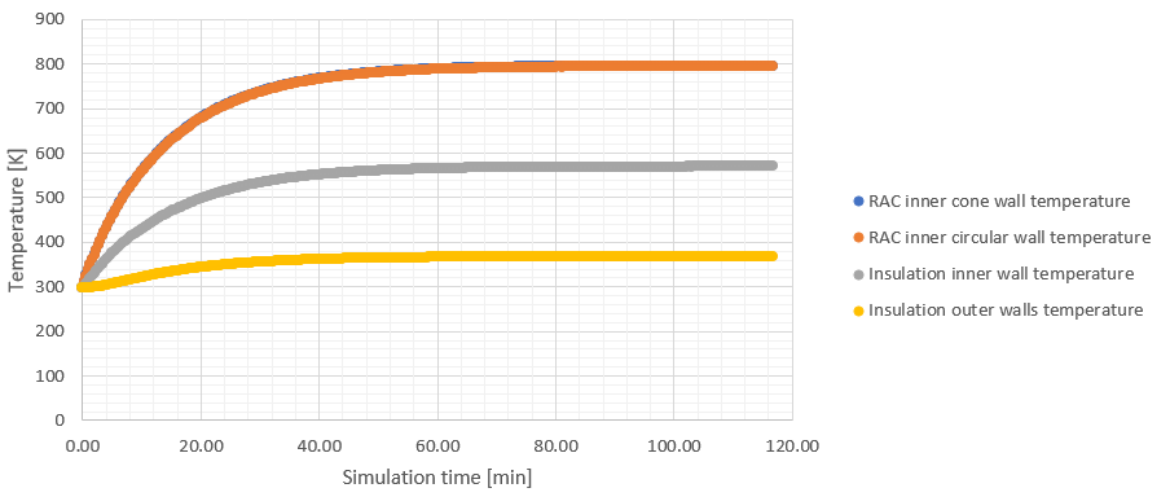


Figure 7.13: Area-weighted average temperatures for inner and outer walls, with insulation. Airspeed is 0.001 m s^{-1} .

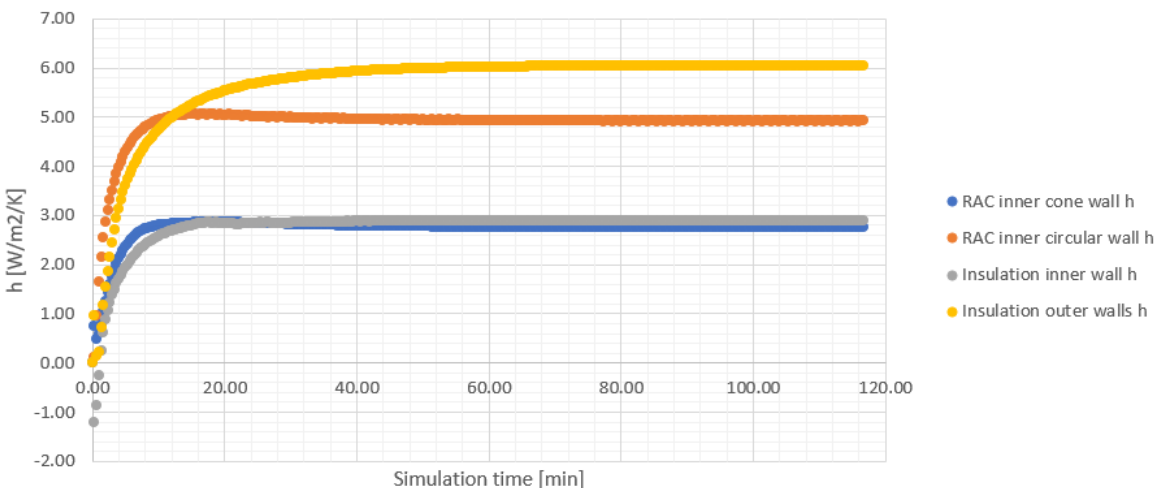


Figure 7.14: Area-weighted average convective heat transfer coefficients for inner and outer walls, with insulation. Airspeed is 0.001 m s^{-1} .

Figures 7.15 and 7.16 show side views of the air domain and the insulation and RAC domains respectively. Note that, in the left picture, the grey mass is the insulation with the hole towards the RAC. As expected, there is a temperature gradient in the insulation due to low thermal conductivity. The heat exchanger on the other hand has a somewhat constant temperature throughout. Notice the asymmetry in the cavity due to buoyancy (gravity is pointing down in the pictures). Next to that, the corners of the insulation do not seem to reduce the convection losses by a large extent, because the

Table 7.4: Convective heat transfer coefficients, view factors and resulting emissivities for case 2.

	h [W/m²/K] at airspeed of 0.1 [m/s]	h [W/m²/K] at airspeed of 0.01 [m/s]	h [W/m²/K] at airspeed of 0.001 [m/s]	View factor to ambient [-]	Adjusted emissivity to ambient [-]
RAC inner cone wall	1.16	2.81	2.76	0.045	0.029
RAC inner circular wall	2.99	4.99	4.93	0.196	0.127
Insulation inner wall	0.44	2.75	2.90	0.243	0.158
Insulation outer walls	11.15	6.56	6.03	1.000	0.090

are at low temperatures (close to room temperature). So, when optimising, cutting of the corners to reduce mass is an option.

The velocity of the incoming air from the sides was 0.001 m s^{-1} . However, to see what the influence of the velocity is, also cases with 0.1 m s^{-1} and 0.01 m s^{-1} were executed. The results are shown in Table 7.4. Both simulations almost reached steady-state, both with convection losses of 27.14 K . The initial airspeed does affect the loss coefficients by a large extent. The focus for this chapter will be more on the convection towards the propellant than the convection to the ambient. For now, the values corresponding with an airspeed of 0.001 m s^{-1} will be used. It is recommended, for future calculations, to increase the size of the air domain to allow for a more accurate assessment of the convection losses.

In the PDT, the equations from Section 4.2 returned steady-state values for h of $6.65 \text{ W m}^{-2} \text{ K}^{-1}$ for the outer insulation walls and $1.76 \text{ W m}^{-2} \text{ K}^{-1}$ for the inner walls. There was no distinction between the different inner walls. Comparing the PDT values to Table 7.4's values at a wind speed of 0.001 m s^{-1} (which is the used wind speed for simulations), the outer wall value differs by 10.3 %. This will result in the outer wall convection heat loss being overestimated by approximately the same amount by the tool, so that is fine within the criterion. The inner value does vary by more than 10 % (the PDT underestimates this loss), but the effect will be minor due to the relatively small inner area. The difference can be due to the different physical model which was inputted in the Python model, because the ring was absent in that case. Next to that, as was previously mentioned, the equations used to determine the value for the tool were mainly applicable to cylindrical cavities, not conical ones.

Now the view factors for the inner three surfaces need to be calculated again. They are added to Table 7.4 and multiplied with the base emissivity, which in this case is still 0.65. However, for the outer insulation walls, the base emissivity is low (0.09 to be precise) because Leenders wrapped the insulation with aluminium foil [3]. As expected, the walls that lie more to the inner side of the system have the lowest view factor and thus emissivity.

So, to execute case 2, boundary conditions for both convection and radiation will be applied to the walls, according to the values in Table 7.4. These values are all with respect to the free stream temperature and room temperature of 298.15 K and a blackbody surrounding (emissivity equal to 1), so no outgoing radiation is reflected back. Again, the ambient domain is deleted to free up computational room for the heat exchanger, fluid and insulation domains. However, the solver did not converge for the aforementioned values. Again, the fluid domain had to be merged with the solid RAC domain, so no channels are present for this case. After these adjustments the solution converged to a scaled residual below 1×10^{-9} . The maximum temperature that was attained was 751.3 K , which is unsurprisingly a bit lower than the value that was read from the plot in Figure 7.13, 796.1 K . This is due to the radiation loss, which was not modelled during the simulations where h was determined.

The maximum RAC temperature as attained during case 2 in Chapter 3.4 was equal to 727.4 K . However, this was not the steady-state temperature, as the curve was not flattened when irradiation

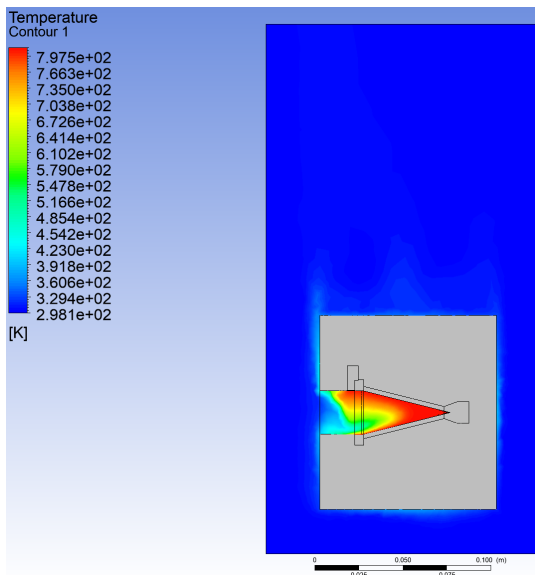


Figure 7.15: Side view of the heated air domain. Note how the upper part of the cavity has a higher temperature than the lower part, due to buoyancy (gravity is pointing down).

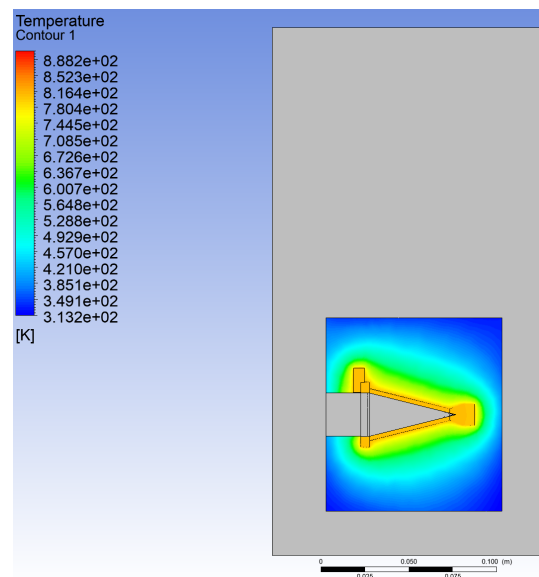


Figure 7.16: Side view of the heated RAC and insulation domains.

was stopped after 26 min. When the tool was run for a longer time, a maximum temperature of 737.6 K was reached. There is but a small difference of 1.9 % when compared to the CFD simulation, which is acceptable within the validation criterion. The difference can be attained to small geometric differences (e.g. the inlet and circular ring) which are not accounted for in the tool.

7.5. Case 3: Solar Thermal Thruster 1, mass flow and no insulation

The third case would normally be similar to the one from Section 3.4. However, various simulation were tried but they all failed due to divergence. When diverging, the outputs were not reliable, due to them going either approaching 1 K or 5000 K. As such, case 3 cannot be executed as planned. However, another case was thought of, where the insulation would be deleted to free up computational space for the heat exchanger and propellant. The convection and radiation values from case 1 will be used to evaluate the heat flow to the ambient. Unfortunately, this also implies that the results cannot be compared to anyone of Leenders' cases, as he tested the RAC with insulation.

Originally, Leenders designed his heat exchanger so that the outlet temperature reached 373.15 K for a mass flow of 300 mg s^{-1} and power input of 29 W, at an efficiency of 80 %, so only 20 % is lost to the surroundings due to convection and radiation.

This case will be redone in Ansys Fluent, as case 4. The boundary conditions will be set as before, with a change in power input and an applied mass flow. The goal of this case is to check the efficiency value and study the effect of laminar and turbulent flow on propellant outlet temperatures. Next to that, it will be interesting to see what the pressure loss is in the RAC. Furthermore, the obtained Nusselt numbers can be compared to literature. The case will be done in steady-state, because the solver unfortunately has a tendency to diverge for transient solutions.

The flow type is very important for the amount of heat that is transferred to the propellant. The flow can be laminar (Re lower than 2300), turbulent (Re higher than 10 000) or transitional (inbetween Reynolds numbers). For the case at hand, the Reynolds number equals 4550 for gaseous nitrogen

at room temperature. Equations 4.10 and 4.16 were used to calculate this number for the channels, which have a square cross-section of 0.6 mm per side.

That means that the flow will have a transitional flow type in the small channels, in theory. However, the flow could also experience turbulent behaviour due to the sharp 90 deg corners at the inlet of the RAC. As such, two simulations will be carried out: one where the propellant is assumed laminar and one where the flow is turbulent. For the latter, a model has to be found; it requires too much computational effort, even for the current generation supercomputers, to solve the NS equations for every eddy at every length scale in the flow [72]. Instead, one uses the Reynolds-averaged Navier-Stokes (equations) (RANS), in which the velocity and pressure are time-averaged, dramatically reducing the simulation time. Ansys Fluent has many of these RANS-models available. Looking at previous theses done in the area of STP at the faculty of AE, no advice on turbulent models was found unfortunately. In literature, for internal flow, the $k-\omega$ model is known to perform well. In this model, k is the turbulent energy in $\text{m}^2 \text{s}^{-2}$ and ω is the specific turbulent dissipation rate in s^{-1} . For details on this, see Argyropoulos et al. [72]. Because the solver is very sensitive to the initial values, they are to be calculated using the equations in 7.5¹. Here, v is the velocity of the flow (in ms^{-1}), I is the turbulence intensity (dimensionless), C_μ is a turbulence model constant (dimensionless) and l is the turbulence length scale (in m).

$$k = \frac{3}{2} (v \cdot I)^2 \quad (7.5a)$$

$$I = 0.16 Re_D^{-\frac{1}{8}} \quad (7.5b)$$

$$\omega = C_\mu^{-\frac{1}{4}} \frac{\sqrt{k}}{l} \quad (7.5c)$$

$$C_\mu = 0.09 \quad (7.5d)$$

$$l = 0.070D \quad (7.5e)$$

Following this, initial values of $38.69 \text{ m}^2 \text{s}^{-2}$ and $270\,394 \text{ s}^{-1}$ for k and ω respectively were calculated. To further speed up convergence for the turbulent simulation, inflation layers were applied at the inside of the channels. These are necessary, because the flow close to the walls sees quick changes in temperature and pressure. To accurately capture this, a high-density mesh is needed in those areas.

For this case, the walls bordering the fluid and RAC domains were split up in three regions: the entrance region, where the propellant flows in and is distributed among the eight channels; the channel region, where the propellant goes through the very small channels; the exit region, where the eight separate flows converge again and leave the system. Doing this, it is possible to see the contribution of each region regarding the heat flow to the propellant. It would be very interesting to see to what extent the flow heats up in each region. Again, the values for convective and radiative heat loss from case 1 were applied to the walls bordering the fictive ambient.

The laminar subcase converged relatively fast in 1000 iterations, which took about 30 min. There was a small oscillation in the temperature and flux terms, so averages were taken starting at 400 iterations. The results are shown in Table 7.5. The first three rows display the losses to the surroundings, the last three rows show the heat flow to the propellant for each region.

Similarly, the turbulent subcase was executed with the k and ω values shown above. It took more than one hour to stabilize the temperatures and fluxes. The results are shown in Table 7.5. There one can observe that the heat flow to the propellant is higher for the turbulent subcase than for the laminar one, which was to be expected. So unsurprisingly, the propellant outlet temperature for the turbulent subcase is also higher, see Table 7.6. The third row displays the propellant temperature after passing

¹https://www.cfd-online.com/Wiki/Turbulence_free-stream_boundary_conditions, accessed on 07-10-2020.

Table 7.5: Averaged wall temperatures and heat flows for case 4.

	Case 4: laminar		Case 4: turbulent	
	Temperature [K]	Heat flow [W]	Temperature [K]	Heat flow [W]
Inner cone wall	381.40	0.73	369.13	0.61
Inner circular wall	379.29	0.23	366.97	0.19
Outer walls	380.45	6.71	368.22	5.59
1. Entrance region	378.87	11.13	366.47	11.41
2. Channel region	381.62	9.90	369.47	11.17
3. Exit region	381.20	0.29	369.64	0.00
Sum of heat flows	-	28.98	-	28.98

the last region, the exit region. The last row shows the efficiency of the heat exchanger; it is almost the predicted 80 % Leenders stated in his thesis [3]. As a result, the outlet propellant temperature approaches the aforementioned 373.15 K.

In Table 7.6, Nusselt numbers for the turbulent case are partly missing. That is due to the propellant temperature at the end of the region surpassing the average wall temperature of that region by a small amount. In that case, the natural logarithm from Equation 4.6 yields invalid results. An explanation for this is two-fold: either the solution is not accurate or the wall temperature is higher at the start of the region, heating the propellant to a temperature which is higher than the wall temperature at the end of the region.

Table 7.6: Averaged propellant temperatures and Nusselt numbers for each region, case 4.

	Case 4: laminar		Case 4: turbulent	
	Nusselt number [-]	Resulting propellant temperature [K]	Nusselt number [-]	Resulting propellant temperature [K]
1. Entrance region	4.70	333.44	6.16	334.38
2. Channel region	7.67	365.10	N/A	370.11
3. Exit region	4.23	366.03	N/A	370.11
Efficiency		73.5%		77.9%

In Table 7.7, the Nusselt numbers are displayed for the channel region. The Reynolds number equals 4550 and the Nusselt numbers are calculated using different methods. Incropera et al. gives the Dittus-Boelter equation (see 7.6) [9]. The coefficient n (dimensionless) equals 0.4 for heating and 0.3 for cooling. It is valid for $0.7 \leq Pr \leq 160$ and $Re_D \geq 10\,000$.

$$Nu_D = 0.023 Re_D^{\frac{4}{5}} Pr^n \quad (7.6)$$

Similarly, the Stephan equation is only applicable for laminar flow. That can directly be seen in Table 7.7, as the Nusselt number from the Stephan equation is significantly lower. Comparing the values with the Nusselt numbers from Table 7.6, there is some discrepancy in the laminar subcase. A strong thermal entrance effect was expected in the channels, raising the Nusselt number, but apparently the thermal boundary layer developed quicker than expected, bringing the value closer to the theoretical 3.66 from Equation 4.17. Unfortunately, the values cannot be evaluated by experiments; Leenders did not state the input power for his tests with mass flow, so those results cannot be used.

For the turbulent subcase, a temperature contour of the fluid domain in side view was taken, see Figure 7.17. Here it can be noticed that the fluid flowing through the lower channel is already more heated than the propellant in the upper channel. This is also seen when plotting the temperature along two lines (sample size of 1000), one through the middle of the upper channel and the other through the middle of the lower pipe, see Figure 7.18.

Table 7.7: Nusselt number calculations for channel flow, at a Reynolds number of 4550.

Method	Equation	Nusselt number [-]
Gnielinski	4.19	15.24
Gnielinski (modified)	4.21	15.97
Dittus-Boelter	7.6	16.83
Stephan	4.22	9.51

Furthermore, which is also supported by the very low contribution of the third region in terms of heat input, the area at the end of the RAC does not see much heat flow. This means that the RAC can be designed smaller, reducing the area (and thus losses to the ambient) and reducing the mass, which is one of the key design criteria for spacecraft propulsion. This reduction of mass will be the subject of the next chapter, where the RAC will be optimized in terms of mass.

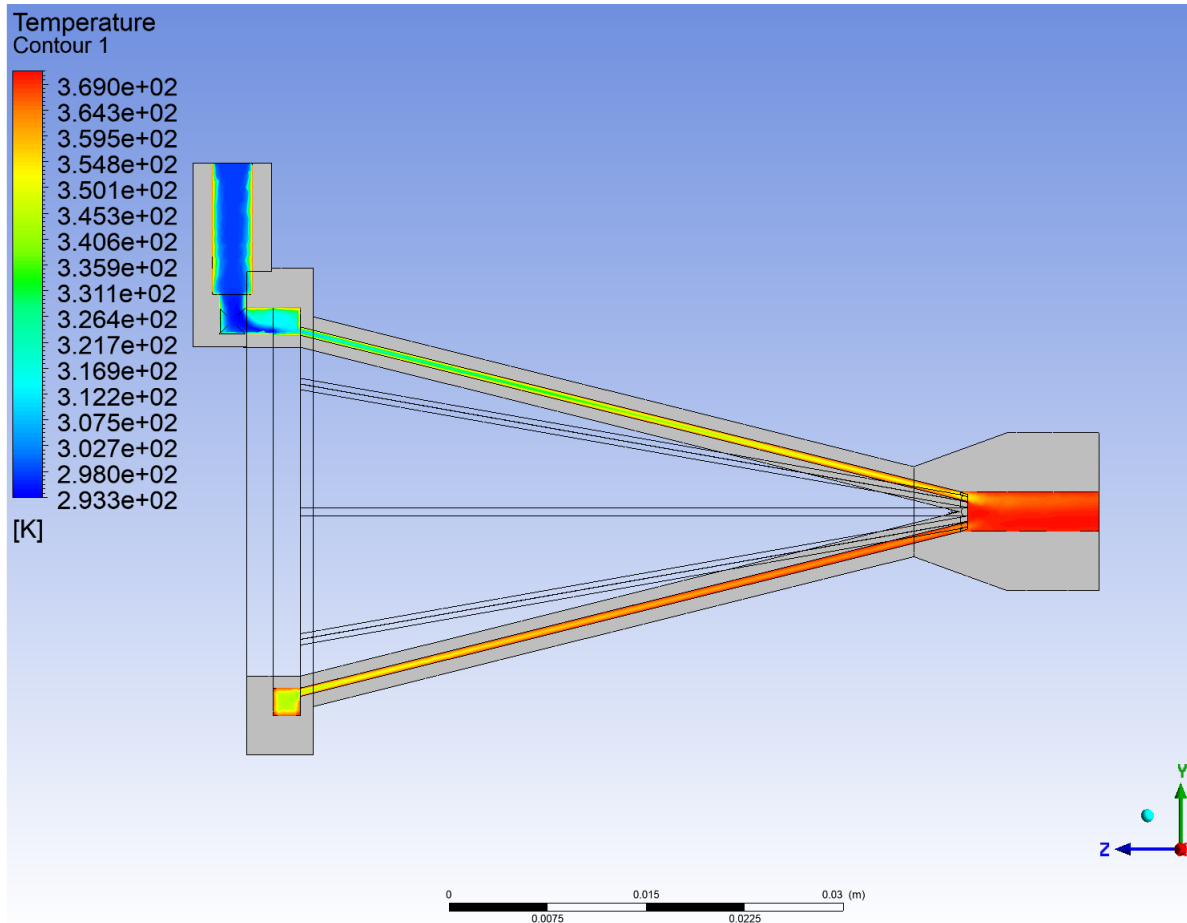


Figure 7.17: Case 3, turbulent subcase. Temperature contour of the fluid domain in side view.

The total pressure loss in the RAC for the turbulent subcase is 37 082 Pa (at an outlet pressure of 101 325 Pa or 1 atm, while for the laminar subcase it is 28 785 Pa. This is quite substantial. From Equations 4.48 and 4.50, one can calculate that the losses in the channels are 18 029 Pa (at room temperature and sea level pressure). This value is for both laminar and turbulent flow. Outside of the channels, there is some additional pressure drop, also due to the bends and corners. Leenders reported a pressure loss in his experiments around 5000 Pa. However, this was for a much lower mass flow, 175 mg s^{-1} . The pressure loss values are thus not validated, but they are in the right direction. Again, experiments on STT1 at a mass flow of 300 mg s^{-1} could validate these results.

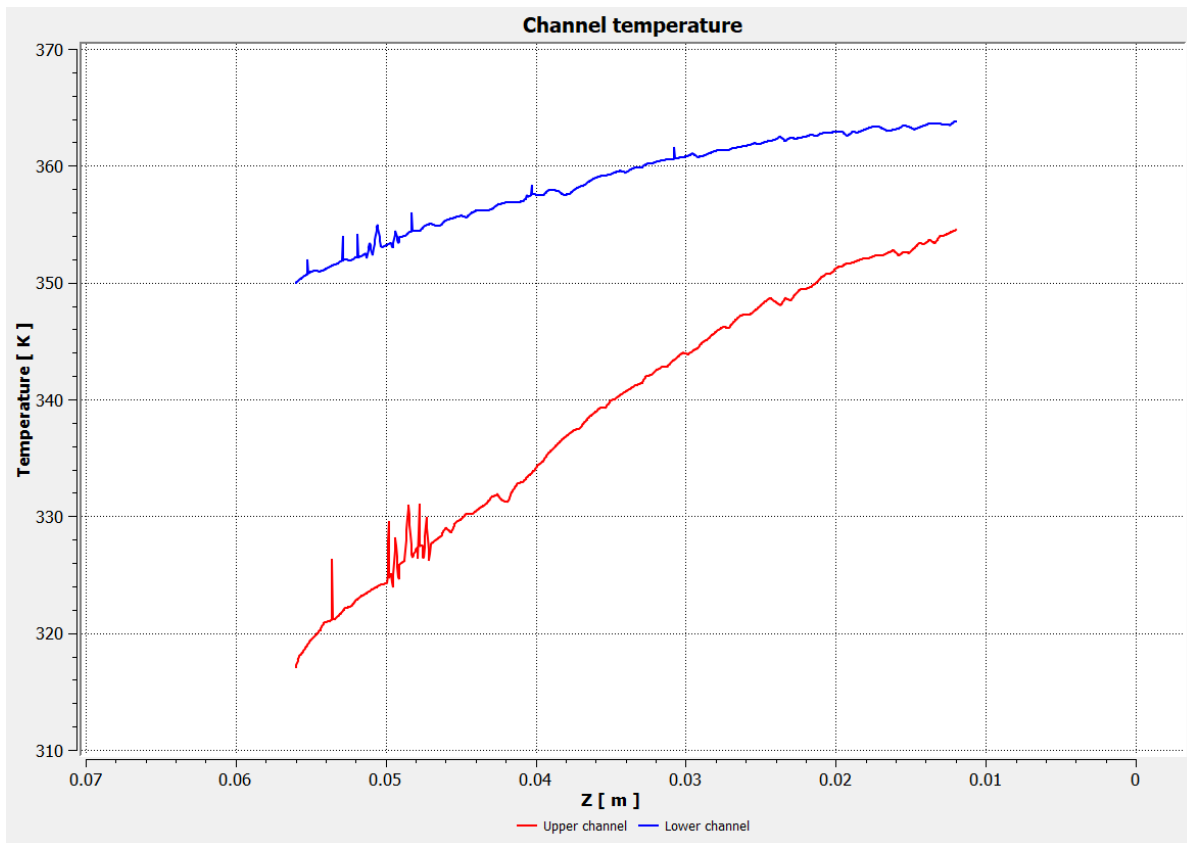


Figure 7.18: Case 3, turbulent subcase. Temperature along both the upper and lower channel, turbulent subcase. Note that the x-axis, which is in the positive Z-direction, is reversed.

7.6. Case 4: Solar Thermal Thruster 2, mass flow and no insulation

In order to validate the STT2 performance output from the PDT in Section 5.2, the engine will be simulated in CFD. At first, the convection losses were simulated per the procedure shown for case 1, see Section 7.2. Similarly, the view factors of all involved surfaces were calculated. Table 7.8 shows the results. Again, the view factor of 0.65 is multiplied with the view factor. It is assumed that the outer walls all have a view factor of 1, despite having some sharp corners. Next to that, the spike walls are assumed to radiate zero power to the ambient.

Table 7.8: Averaged convective heat transfer coefficients, view factors and emissivities for each surface, case 4.

	h [W/m ² /K]	View factor [-]	Emissivity [-]
Entrance ring	0.075	0.2071	0.135
Heated wall	0.005	0.0115	0.007
Bottom ring	0.075	0.0021	0.001
Top ring and spike	0.075	0	0
Outer walls	8.494	1	0.650

Entering the values from Table 7.8 as boundary conditions, a laminar flow simulation was run. It was not possible to apply a symmetry boundary due to the spiral channels rendering the heat exchanger asymmetrical. As such, elements were sparse and had to be carefully applied in the small channel region. Again, an inflation layer was applied, a high-density mesh as quick temperature and pressure changes are seen close to the walls. A turbulent flow simulation unfortunately did not converge; the temperatures oscillated over a large range of more than 100 K. Apparently, this requires a finer mesh

in order to converge [48]. Unfortunately, the Fluent student license does not allow for more elements. It is expected though that the thermal efficiency for the turbulent case would be higher (by 1-4 %), as this was also what was seen in the previous section.

The laminar Ansys Fluent run showed a propellant temperature of 775.3 K at a thermal efficiency of 61.2 % and pressure loss of 1.23 bar. The **RAC** reached temperatures between 800.2-813.9 K. The assumption of uniform wall temperature is thus less valid at higher power inputs. This can be attributed to the fact that the decrease in channels increases the kinetic energy in the channels as the mass flow stays the same. In Figure 7.19, a cross-section of **STT2** is shown for laminar flow. Clearly, the heating of the propellant in the channel area can be observed.

In Section 5.2, the thermal efficiency as determined by the **PDT** was 61.6 %. The **RAC** temperature and the propellant outlet temperature both were 779.5 K. The reported outer wall h was equal to $10.957 \text{ W m}^{-2} \text{ K}^{-1}$. The tool does output a very similar thermal efficiency as the **CFD** simulation. However, the tool does overpredict the convectional heat transfer coefficient to the propellant; that is the reason the **RAC** temperature and propellant temperature are so close, while the **CFD** simulation shows some difference. This overestimation is most likely caused by the fact that the tool regards the entrance and exit regions as thermally efficient as the channels, while in reality they are less suited for propellant heating. Furthermore, the outer wall h differed by 22.5 %. This difference was cancelled in the heat loss to the ambient because the **RAC** outer wall temperature was lower for the **PDT**. Looking at the **RAC** temperature difference, this was at most 4.4 %, which falls within the 10 % validation criterion.

The reported pressure loss by the **PDT** was 1.80 bar. The **CFD** value is thus lower by 31.7 %. When inputting the **CFD** pressure loss manually in the tool, the specific impulse was increased by 5.1 %. This is more than the 3.2 % upon which the temperature validation criterion is based, see Section 3.1. Furthermore, the value found by the tool is only the pressure loss in the channels. Apparently, the pressure loss is thus overestimated by the tool. In order to validate this further, experiments will be needed.

7.7. Conclusions & recommendations

The **CFD** simulations in this chapter validated the thermal part of the **PDT** tool, showing that the **RAC** and outlet propellant temperatures fall within the 10 % validation criterion. However, the pressure loss was not validated, as the tool overestimates this by a large amount. Next to the validation, it was also seen that **CFD** is a welcome addition in the designing process of the **RAC** of an **STP** engine. Although the use is limited due to a student license, it is recommended to carry out **CFD** simulations in order to get more detailed heat transfer and pressure loss values. Especially in entrance and exit areas where it is often hard to predict by the **PDT** what the implications of the intended design are, numerical analysis can help.

To mitigate the risk that results gained from the simulations are deemed useless, the following is recommended. First, the results can be sanity checked by comparing them to literature. If anomalies, when present, can be explained by literature, one can already assume that the outcomes have more value. What is even better is to perform a mesh sensitivity analysis, in which the influence of the mesh is quantified by step wise going from a more coarse to a more fine discretization. Last recommendation for validation is to perform an experiment, after which the results can be compared to the simulation outcome.

The first and third recommendations were partly carried out in this chapter. However, the recommendation still stands to execute more experiments and check the influence of finer meshes, if resources allow. For this thesis that will be out of the scope. Next to that, the designed spike, intended to scatter the incoming radiation, could not be evaluated. Implementing a ray tracing module (as done by [48]), which is possible in Fluent, would also increase the validation of the simulation results.

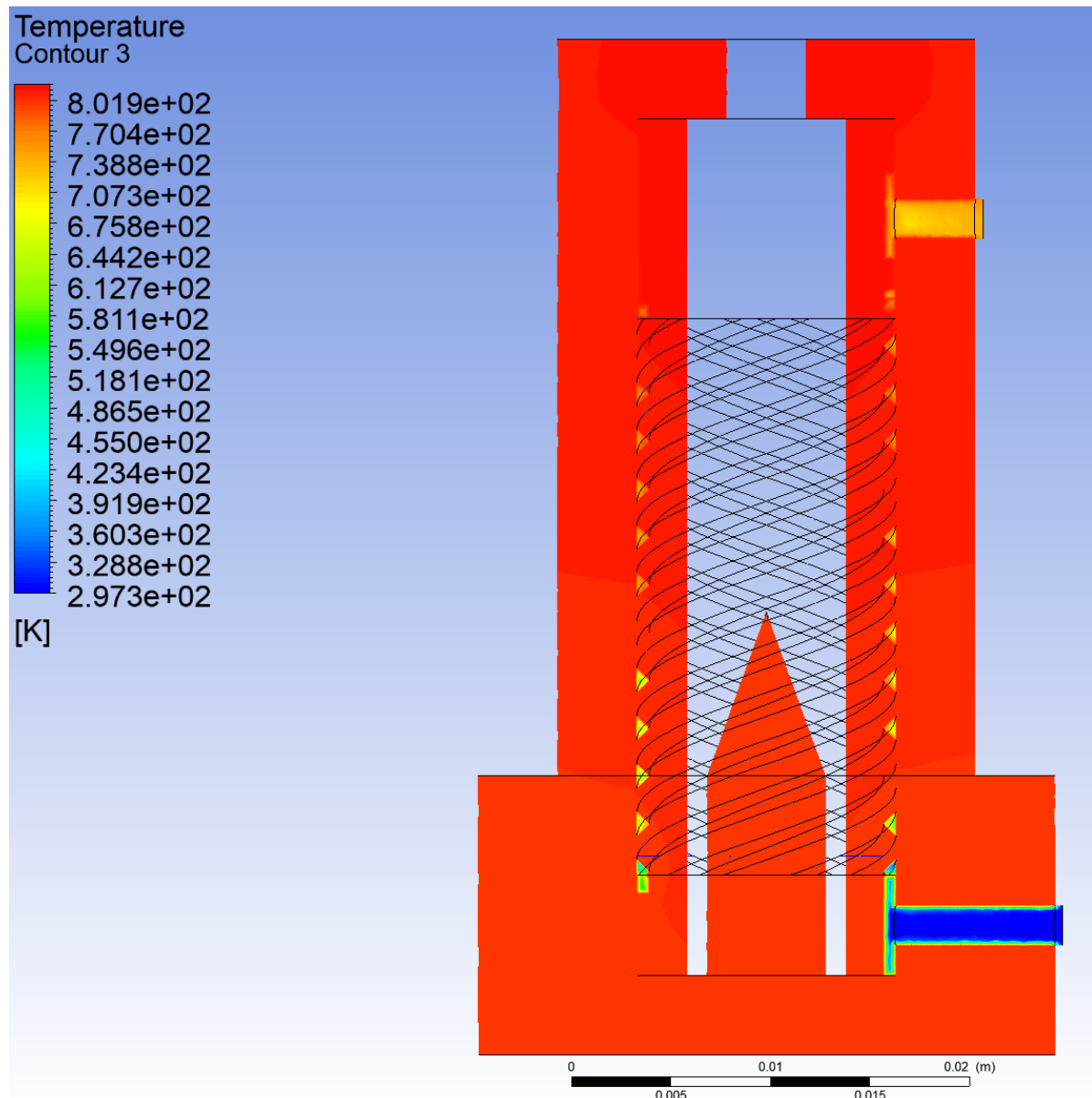


Figure 7.19: Case 4: cross-section of STT2 showing the temperature in RAC and propellant in laminar flow.

8

Final solar thermal thruster design

This chapter will describe the final design of the solar thermal motor. The design will be built on the findings from the previous chapters and be named **STT3** in order to distinguish it from the previous two engines. In the first section, recommendations will be given that were found out during the design, manufacturing and performance analysis of both **STT1** and **STT2**. It will be followed by a section where the resulting design is presented, followed by a performance analysis using both preliminary tool and **CFD** simulation, to assess if the thermal performance meets the requirements set in Chapter 2. Finally, conclusions will be drawn on the results.

The reason to redesign the solar thermal engine is because previous chapters showed that **STT2** does not meet the requirements in both performance and mass. Ultimately, the aim of this chapter is that the design will be the input for a new thesis, wherein the validity of the design is researched by subjecting it to testing. Eventually, raising the nitrogen specific impulse to a **SL** specific impulse of 90.0 s at a mass flow of 300 mg s^{-1} set in Chapter 2 is the goal of the redesign.

8.1. Recommendations from previous chapters

As was explained in Section 6.5, the concessions for the manufacturing of **STT2** disallowed the use of experiments to validate its performance. These flaws need to be prevented in future designs; as such, the preliminary tool from Chapter 3 was fitted with an option to check if the fluid velocity would not become too high in the channels (see Equation 8.1 where ρ is the propellant density in kg m^{-3}).

$$v_{max} = 175 \left(\frac{1}{\rho} \right)^{0.43} \quad (8.1)$$

In Section 5.2 it was seen that the pressure loss in the heat exchanger can become as high as 1.80 bar for **STT2**. This is not acceptable, as Chapter 2 shows that a limited amount of pressure loss is allowed to keep the feed pressure below 10 bar which is the maximum pressure for nanosatellites. Next to that, some of the pressure sensors have 10 bar as the upper limit. These can be replaced by sensors having a larger pressure range, but this will affect the budget. Remember that the design pressure for the nozzle chamber equals 8.16 bar, so any pressure loss before the nozzle is added up to that. An arbitrary 0.50 bar maximum of pressure loss in the heat exchanger is thus set as additional requirement, REQ-S-5. This value will allow for some additional pressure loss in tubing outside the heat exchanger and also some flexibility in altering the mass flow in experiments.

8.2. Solar Thermal Thruster 3 design

STT3 will largely follow the design set in Chapter 5: the heat source, heat exchanger type and shape, heat exchanger material and propellant will remain the same as the choice for those aspects was already discussed in that chapter. As such, the heat source for STT3 will be an indirect absorbing, direct propulsion type with nitrogen as the propellant. Next to that, the heat exchanger will be cylindrical with spirally-shaped channels and made out of copper.

One issue with STT2 was the high mass. As was pointed out before, the wall thickness of STT2's heat exchanger can be reduced from 4 mm to Leenders' 1 mm. Doing this, the mass will dramatically reduce, which probably brings it within acceptable ranges. Another major problem of STT2 was the channel section. Only one channel with a cross-sectional area of 0.36 mm^2 was erroneously designed, which proved to be detrimental to both pressure loss and heat transfer. The amount of channels thus has to be increased, as well as its cross-sectional shape (which is triangular) revised.

8.2.1. Heat exchanger dimensions

The goal of 70 % in thermal efficiency (with input power 250 W) results in a final propellant temperature of 835.3 K at a mass flow of 300 mg s^{-1} and an inlet temperature of 298.15 K. Because of the high thermal conductivity of copper, it is assumed that the wall temperatures are equal in every location. This seems valid, because according to the analysis in Chapter 7 for STT2 the walls had a maximum difference of 13.7 K. So, the outer walls have to have a temperature of at least the final propellant temperature. Only the outer walls of STT2 experienced significant losses (97.7 W), while the other walls did lose a maximum of 0.38 W in total. 153.1 W is currently transferred to the propellant, which is 61.2 %. 70 % amounts to 175 W which needs to be used to heat the propellant. This leaves 75 W for losses. At a convective heat transfer coefficient of $8.494 \text{ W m}^{-2} \text{ K}^{-1}$, wall temperature of 835.3 K, emissivity of 0.65 and ambient temperature of 298.15 K, the outer wall area can be 0.00338 m^2 at most. This is a reduction of 32.5 % when compared to the original 0.0050 m^2 , which is drastic.

STT1 can be roughly seen as two cylinders, the first having diameter 21 mm and length 37 mm, the second (which is the end cap) diameter 29 mm and 14 mm. The outer wall area then amounts to 0.0050 m^2 , a bit more than the aforementioned value due to the aperture. As said before, the thicknesses can and will be reduced (under sufficient manufacturing knowledge), analogous to Leenders' RAC. The outer wall thickness for the smaller cylinder will be reduced from 4 mm to 1 mm, which reduces its diameter by 6 mm and its length by 3 mm. The end cap will have its wall thickness reduced from 4 mm to 2 mm. The resulting outer area is then 0.0029 m^2 , which is more than sufficient to reduce the heat loss. It leaves a margin for an increase in convective heat transfer coefficient and a higher outer wall temperature. Next to that, the channel region heating area is not affected by these changes, so the thermal efficiency could only increase; the channel section length of 28 mm will be unchanged as well as the inner diameter of 11.8 mm where the channels start.

8.2.2. Channel shape and dimensions

In Section 7.6, it became clear that 6 channels for STT2 would lead to large pressure losses but high thermal efficiency as well. This also becomes clear from the Darcy-Weisbach equation for pressure loss (see 4.48) and the Reynolds number equation (see 4.10). As a rule of thumb, the higher the Reynolds number, the higher the amount of heat flowing to the propellant. This is supported by the analysis in Chapter 7, where the turbulent flow sees a higher thermal efficiency than the laminar one, which is also seen in the equations in Subsection 4.2.1. To raise the Reynolds number (with fixed mass flow), one could lower the cross-sectional area by decreasing the diameter (in circular channels). However, this would increase the flow velocity in the channels, which would increase the pressure loss by that same amount squared. Pressure loss versus thermal efficiency is the trade-off here, which is also visible in Incropera et al.'s Table 8.1 [9]. There we observe that a higher Nusselt number is approximately

proportional to the pressure loss in a channel, for laminar flow. Because turbulent flow, above Reynolds numbers of 2300 is still wanted but, this number will be kept as the minimum for channel flow Reynolds numbers.

Three distinct shapes can be distinguished for the channel: circular, square and triangular. As for STT2, they will be milled at the outside of the inner cylinder, at a diameter of 11.8 mm. Incropera's table shows that circular channels have the highest Nusselt number at uniform wall temperature and laminar flow. This is also depicted in Table 8.1, second column. However, the Nusselt number does not incorporate the effect of channel area. Looking at the inner heat exchanger cylinder where the channels have to be made in, a circular cross-section would waste a lot of room on this cylinder; in the same $0.6 \times 0.6 \text{ mm}^2$ "box", the circular channel takes less "room" than the square one. The triangular shape does even worse, see the table's third row where the wetted perimeter S in m is shown. When corrected for this area (perimeter) difference and also for the hydraulic diameter, the triangular channel comes out on top in terms of heat transfer, see last column. For this calculation, the channel length L_{ch} is taken as 1 m and the thermal conductivity as $0.025\ 83 \text{ W m}^{-2} \text{ K}^{-1}$. The heat transfer $Q_{conv,T}$ in W K^{-1} is calculated using Equation 8.2.

$$Q_{conv} = \frac{Nu k}{D_h} \cdot S \cdot L_{ch} \quad (8.2)$$

Table 8.1: Comparison between channel shapes in terms of heat transfer [9].

Channel shape	Nu_{D_h} at uniform wall temperature [-]	S [mm]	D_h [mm]	Q_{conv} [W/K]
Circular	3.66	1.88	0.60	0.297
Square	2.98	2.40	0.60	0.308
Triangular	2.49	1.88	0.35	0.331

However, the effect of pressure loss is far greater for the triangular cross-section. In Table 8.2, the second column shows the values taken from Incropera [9]. The Reynolds number is shown in the third column for an arbitrary 10 channels using Equation 4.10 (μ equals $1.76 \times 10^{-5} \text{ Pa s}$), so the mass flow through each channel is 30 mg s^{-1} . With the use of the cross-sectional area A_{cs} in m^2 and taking the density as 1.135 kg m^{-3} , the flow velocity v in m s^{-1} can be calculated. This eventually gives the pressure losses in the last column of the table using Equation 4.48 for a channel of 1 m in length. There, it can be seen that the triangular option has a far higher pressure loss when compared to the other two.

Table 8.2: Comparison between channel shapes in terms of pressure loss [9].

Channel shape	$f_{DB} \cdot Re_{D_h}$ [-]	Re_{D_h} [-]	f [-]	A_{cs} [mm ²]	v [m/s]	Δp [bar]
Circular	64	3617	0.0177	0.283	93.5	4.90
Square	57	2840	0.0201	0.360	73.4	3.11
Triangular	53	3788	0.0140	0.156	169.6	20.12

Because of the low pressure losses and medium thermal efficiency, the square cross-section is chosen as the channel shape. Note that the square option is harder to manufacture than a triangular one, but easier than the circular option. The dimensions of the channel cross-section will be $0.6 \times 0.6 \text{ mm}^2$ to allow for comparison with Leenders' RAC.

In order to reduce the amount of pressure loss the most, the number of channels needs to be increased. With the current cross-section, the Reynolds number minimum of 2300 allows for 12 channels, which give a Reynolds number of 2367 in each channel. The width between each channel will be 1 mm, so the pitch is 1.6 mm times 12 is 19.2 mm. The width is similar to the wall thickness, so it is expected that this can be manufactured. As said before, the channel section total length is 28 mm, which gives a channel spiral length of 60.8 mm.

8.2.3. Other changes

Next to the changes in heat exchanger dimensions and channel section, the holes at start and end will both have a diameter of 5 mm. That way, tubes with an outer diameter of 5 mm and an inner diameter of 3 mm can be connected. The latter value ensures that the pressure losses are low in these tubes, because the cross-sectional area is 19.6 times the area of one channel. The holes will be extended by 5 mm at a diameter of 5 mm to allow for a solid connection. Simultaneously, both ends of the inner cylinder will be shortened to a length of 3 mm. Threads present in STT2 will be substituted by hard solder connections to prevent leakages. According to DEMO, these connections can withstand 933 K at most, which is sufficient. The spike will be removed, because its use cannot be verified in the upcoming analysis. It could be placed back if a ray tracing tool is used. Now that the spike is removed, one end of the inner cylinder will be closed to prevent leakage on that side.

A nozzle with a throat diameter of 0.58 and an exit diameter of 0.76 mm is designed. It will be made of copper as well, due to the high melting point, easy manufacturability and medium cost.

8.2.4. Results

In Appendix B, the CAD drawings of STT3 are shown. The resulting design has an outer wall area of 0.00274 m², which is smaller than the maximum 0.0038 m². The extra reduction allows for a small increase in coefficient of convective heat transfer to the ambient. The total volume of the RAC amounts to 4852 mm³, which gives a mass of 43.6 g at a copper density of 8978 kg m⁻³, meeting the requirement. In Figures 8.1 and 8.2, both designed heat exchangers of STT2 and STT3 are shown respectively. Note the considerable difference in size, while the scale is equal. Furthermore, the increased hole diameter for both inlet and outlet in STT3 is shown, so that tubes can be connected more easily. An exploded view of STT3's heat exchanger is shown in Figure 8.3.

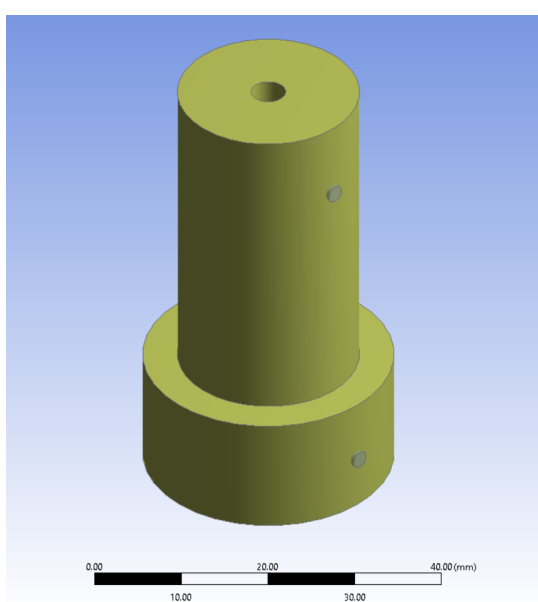


Figure 8.1: View of STT2.

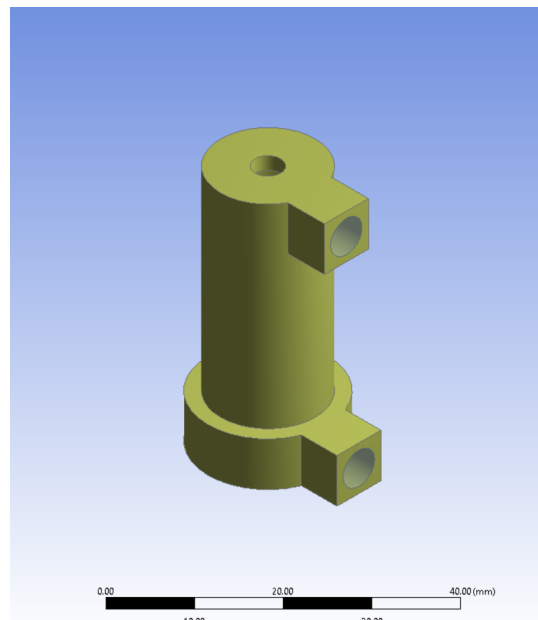


Figure 8.2: View of STT3.

8.3. Solar Thermal Thruster 3 performance

Table 8.3 shows the inputs for the PDT analysis for STT3. The dimensional inputs are based on the figures in Appendix B. From those inputs, the tool calculated a thermal efficiency of 70.8 % and a



Figure 8.3: Exploded view of the STT3 heat exchanger.

pressure loss of 0.22 bar for the heat exchanger. This amounted to a propellant outlet temperature of 846.9 K and a [SL](#) specific impulse of 84.9 s. Other thermal results are shown in Table 8.4.

The same procedure as in Chapter 7 was taken for the [STT3 CFD](#) simulation. First, the wall coefficient of convective heat was calculated by creating a "box of air" around the heat exchanger. Again, the fluid domain is integrated in the [RAC](#) domain to allow for more mesh elements to be placed on critical connecting surfaces, such as the outer walls. The air velocity from the sides is again 0.001 m s^{-1} . The simulation was deemed converged after 500 iterations and outputted a convective heat transfer coefficient of $9.358 \text{ W m}^{-2} \text{ K}^{-1}$ at an ambient temperature of 298.15 K, when averaged over the last 100 iterations. This value is a little higher than the value for [STT2](#), but the decrease in outer wall area fully mitigates this extra loss. Thus, it is to be expected that the total loss (in Watts) for the current design will be less than for [STT2](#). The radiation view factors are calculated for each inner surface. The outer surface is assumed to have a view factor of 1 towards the ambient.

Then, the air box is deleted and the convective and radiative boundary conditions are applied to each wall. The inner cylinder surface will experience a power input of 250 W. After 500 iterations, a thermal efficiency of 68.6 % was reached, which resulted in an outlet propellant temperature of 830.3 K, which is almost the desired value for a specific impulse of 90 s. The pressure loss amounts to 0.43 bar. Again, the temperature falls within the 10 % difference criterion while the pressure loss does not. Experiments

Table 8.3: PDT inputs for STT3.

Name	Symbol	Value	Unit
RAC type	-	"Cylindrical"	-
RAC material	-	"Copper"	-
Propellant	-	"Gaseous nitrogen"	-
Insulation	-	"No insulation"	-
Channel layout		"Spiral"	-
Number of channels	n_{ch}	12	-
RAC channel length	L_{cavC}	0.028	m
RAC inner length	L_{cavI}	0.034	m
RAC outer length	L_{cavA}	0.038	m
RAC inner diameter	D_{inner}	0.0118	m
RAC outer diameter	D_{outer}	0.019	m
RAC aperture diameter	D_{ap}	0.004	m
RAC inner cavity area	$A_{RAC,i}$	1.21e-3	m^2
RAC outer cavity area	$A_{RAC,o}$	2.74e-3	m^2
RAC mass	M_{RAC}	0.0429	kg
Irradiation time	n_i	95	min
Incoming power	P_{in}	250	W
Incoming power efficiency	η	1.00	-
Mass flow	\dot{m}	300e-6	kg/s
Propellant feed temperature	$T_{p,in}$	298.15	K
Propellant feed pressure	p_f	816000	Pa
Channel hydraulic diameter	D_h	0.0006	m
Absorptivity oxidized copper	α_M	0.70	-
Emissivity oxidized copper	ϵ_M	0.65	-
Ambient temperature	T_{amb}	298.15	K
Ambient pressure	p_{amb}	101325	Pa

are welcomed to enhance the tool in the latter area.

8.4. Conclusions

Table 8.5 shows the properties and results of both PDT and CFD analysis for all three engines. The results are from simulations with 250 W of input power, nitrogen mass flow of 300 mg s^{-1} and SL ambient properties. The first thing that is visible is the large differences in preliminary tool outcomes and CFD results for the pressure losses. For STT1, an interesting detail is that the thermal efficiency is lower for the CFD analysis than for the preliminary tool results. This could perhaps be due to varying Reynolds numbers in the channels; however, validation experiments could be of great assistance here, as could it be for all (pressure loss) results.

Another thing that becomes apparent is that STT2 is not at all competitive with respect to STT1 because of the higher mass. However, the thermal efficiency is higher for STT2 than for STT1 at the cost of more pressure loss. STT3 on the other hand outperforms STT1 and STT2 on all areas, be it size, mass or performance. So, this new design is recommended for future manufacturing and testing at DUT. The most prominent downside for the engine are the small details. However, STT1 could be built at DUT and STT3 does not have any smaller details than Leenders' RAC, so it is believed that STT3 can one day be tested at this university.

Table 8.4: PDT thermal outputs for STT3.

Output	Value
Input power	250.0 [W]
Absorbed power	249.0 [W]
Outer convection loss	19.5 [W]
Outer radiation loss	51.2 [W]
Inner convection loss	1.0 [W]
Inner radiation loss	0.3 [W]
Propellant convection	177.0 [W]
Nusselt number outer convection	5.69 [-]
Nusselt number inner convection	11.0 [-]
Nusselt number propellant convection	15.1 [-]

Table 8.5: Properties and results for all three engines.

	STT1	STT2	STT3
RAC material [-]	Copper	Copper	Copper
RAC mass [g]	87	182	44
RAC length [mm]	69	51	38
RAC largest diameter [mm]	37	29	19
RAC number of channels [-]	8	6	12
Channel cross-sectional shape [-]	Square	Isosceles triangle	Square
Channel length [mm]	52.5	77.3	60.9
Channel cross-sectional area [mm²]	0.36	0.36	0.36
Nozzle throat diameter [mm]	0.58	0.58	0.58
Nozzle exit diameter [mm]	0.68	0.68	0.76
Propellant	Nitrogen	Nitrogen	Nitrogen
PDT: Thermal efficiency [%]	54.6	61.6	70.8
CFD: thermal efficiency [%]	50.4	61.2	68.6
PDT: pressure loss [bar]	0.17	1.80	0.22
CFD: pressure loss [bar]	0.46	1.23	0.43

9

Conclusions & recommendations

This chapter will describe the conclusions, followed by the recommendations.

9.1. Conclusions

The project was kicked off as a practical study towards solar thermal thrusting. In Chapter 1, STP was identified as a suitable propulsion candidate for (micro)satellite applications. In Chapter 2, the goal was set to construct and successfully demonstrate a high-temperature engine and bring the SL specific impulse to 90.0 s at a continuous nitrogen mass flow of 300 mg s^{-1} . The thruster would be named STT2. The goal was dependent on three subgoals: increasing the power input, increasing the thermal efficiency and developing the PDT which would allow for evaluation of design choices.

In Chapters 3 and 4, the PDT was constructed, verified and validated. However, validation could not be entirely completed for the tool, as the propellant outlet temperatures and pressure losses were in disagreement with theoretical and experimental outputs from other sources. As such, validation would be done by conducting experiments on STT2. The thruster was designed and built in Chapter 5. Its SL specific impulse equalled 77.8 s according to the PDT, mainly due to the lower thermal efficiency and larger pressure loss than expected. Because the engine had to be finished in a limited time span, it was designed before the PDT was finished. Many concessions to the manufacturer had to be made, so the heat exchanger mass exceeded the mass requirement. Next to that, the reduction in the number of channels caused the RAC to experience a very high pressure loss, which would prove to be detrimental to the engine's performance.

In Chapter 6, during the experiment preparations, it was also discovered that the heat exchanger had severe leakages. When trying to remedy this, the engine was damaged beyond repair. Because the welding laser facility was also closed down, experiments were cancelled. A new plan was made to validate the PDT by CFD simulations on the RAC in Chapter 7. The simulation outputs showed good accordance with the PDT thermal results, but the differences in pressure loss were too large. Furthermore, the nozzle performance was not simulated. The PDT was thus validated for the thermal part, but not for the pressure and nozzle performance section.

With the partly validated tool, a new thruster named STT3 was designed in Chapter 8. PDT analysis showed that the motor had a SL specific impulse of 84.9 s. Thus, the goal for the thesis was almost reached. The expectation is that this thesis serves as the input for a next master student who is willing to pick up the STT3 design, manufacture the pieces and test them in the laser welding facility at 3mE when possible again.

9.2. Recommendations

The foremost recommendation that is to be given is to construct [STT3](#) and validate the [PDT](#) pressure loss and performance results. When this is done, the results could help to improve the Python tool while also showing if the extensive effort needed for the [CFD](#) analysis pays itself back. Next to this recommendation, a list stating several other commendations is given below. These are derived from the recommendations that were already given at the end of each chapter.

- The [PDT](#) would benefit from a ray tracing model. Furthermore, allowing the evaluation of two-phase flow would enhance the tool capabilities. Next to that, the accuracy of results would benefit from thermal and pressure losses in tubes also being implemented.
- The [CFD](#) analyses would benefit from larger simulations, where finer meshes are implemented. That way, turbulent flow can be evaluated to a more accurate degree.
- For the construction of [STT3](#), it is recommended to have practical experience in metalworking and that a problem-solving mindset is required. Next to that, additional funding is required in order to order externally built pieces. Try the department of [AE](#) or look for other sponsors outside of the university.

Bibliography

Most of the TU Delft thesis reports are retrievable from <https://repository.tudelft.nl/>.

- [1] Bryce Space & Technology, *SmallSats by the Numbers 2019*, (2019).
- [2] H. P. Gerrish Jr, *Solar Thermal Propulsion at MSFC*, Tech. Rep. (Marshall Space Flight Center, 2016).
- [3] H. C. M. Leenders, *Development of a solar thermal propulsion system*, Tech. Rep. (MSc thesis report TU Delft, 2008).
- [4] J. M. Shoji, *Solar Rocket Component Study*, Tech. Rep. (Rockwell International, Canoga Park, 1985).
- [5] F. Valente, *Development and verification of test set up for microthrusters testing*, Tech. Rep. (MSc thesis report TU Delft, 2007).
- [6] S. Janssens, *Design of a micro propulsion test bench*, Tech. Rep. (MSc thesis report TU Delft, 2009).
- [7] I. Krusharev, *Micro - Thruster Development: Propulsion System for the DelFFi Mission*, Tech. Rep. (MSc thesis report TU Delft, 2015).
- [8] H. Leenders and B. Zandbergen, *Development of a Solar Thermal Thruster System*, 59th International Astronautical Congress (2008).
- [9] F. Incropera, D. DeWitt, T. Bergman, and A. Lavine, *Fundamentals of Heat and Mass Transfer (6th edition)* (John Wiley & Sons, 2007).
- [10] S. W. Janson, *25 Years of Small Satellites*, 25th Annual AIAA/USU Conference on Small Satellites (2011).
- [11] A. Freeman, *Exploring our solar system with CubeSats and SmallSats : the dawn of a new era*, *CEAS Space Journal* **12**, 491 (2020).
- [12] F. Leverone, A. Cervone, and E. Gill, *Cost analysis of solar thermal propulsion systems for microsatellite applications*, *Acta Astronautica* **155**, 90 (2019).
- [13] A. Perera-Webb, A. Da Silva Curiel, and V. Zakirov, *The changing launcher landscape - A review of the launch market for small satellites*, in *IAC* (2017) pp. 11987–11990.
- [14] A. Poghosyan and A. Golkar, *CubeSat evolution: Analyzing CubeSat capabilities for conducting science missions*, *Progress in Aerospace Sciences* (2017), [10.1016/j.paerosci.2016.11.002](https://doi.org/10.1016/j.paerosci.2016.11.002).
- [15] T. A. Grönland, P. Rangsten, M. Nese, and M. Lang, *Miniaturization of components and systems for space using MEMS-technology*, *Acta Astronautica* **61**, 228 (2007).
- [16] M. A. Silva, D. C. Guerrieri, A. Cervone, and E. Gill, *A review of MEMS micropropulsion technologies for CubeSats and PocketQubes*, *Acta Astronautica* **143**, 234 (2018).
- [17] D. B. Scharfe and A. D. Ketsdever, *A Review of High Thrust , High Delta-V Options for Microsatellite Missions*, in *45th AIAA/ASME/SAE/ASEE Joint Propulsion Conference*, August (2009) pp. 1–14.
- [18] P. Tortora, *Small satellites beyond boundaries*, *CEAS Space Journal* **12**, 489 (2020).

- [19] A. R. Tummala, *An Overview of Cube-Satellite Propulsion Technologies and Trends*, MDPI (2017), [10.3390/aerospace4040058](https://doi.org/10.3390/aerospace4040058).
- [20] K. Lemmer, *Propulsion for CubeSats*, in *Acta Astronautica* (Elsevier Ltd, 2017) pp. 231–243.
- [21] F. Etheridge, *Solar Rocket System Concept Analysis*, Tech. Rep. (AFRPL, 1979).
- [22] F. G. Kennedy, *Solar Thermal Propulsion for Microsatellite Manoeuvring*, Tech. Rep. (University of Surrey, Surrey, 2004).
- [23] B. Zandbergen, *AE4S01 Thermal Rocket Propulsion reader (version 2.06)* (TU Delft, 2017).
- [24] J. C. Mankins, *Technology Readiness Levels, White Paper (April)* Advanced Concepts Office. Office of Space Access and Technology. NASA., 5 (1995).
- [25] F. Leverone, A. Cervone, M. Pini, E. Gill, and P. Colonna, *Feasibility of an Integrated Solar Thermal Power and Propulsion System for Small Satellites*, IAC (2017).
- [26] C. C. Selph, AFRPL, Tech. Rep. (AFRPL, 1981).
- [27] A. Takken, *Literature study*, Tech. Rep. (TU Delft, 2019).
- [28] A. Takken, *Project Proposal and Plan*, Tech. Rep. (TU Delft, 2019).
- [29] T. Nakamura, D. Sullivan, J. A. Mcclanahan, J. M. Shoji, R. Partch, and S. Quinn, *Solar Thermal Propulsion for Small Spacecraft*, (2004) pp. 1–11.
- [30] P. Henshall, P. Palmer, and A. Baker, *Solar Thermal Propulsion Augmented with Fibre Optics: A System Design Proposal*, 41st AIAA/ASME/SAE/ASEE Joint Propulsion Conference & Exhibit, 1 (2005).
- [31] M. R. Gilpin, *Phase-Change Thermal Energy Storage and Conversion : Development and Analysis for Solar Thermal Propulsion*, in *48th AIAA/ASME/SAE/ASEE Joint Propulsion Conference*, August (2012) pp. 1–11.
- [32] K. A. Ehricke, *The solar-powered space ship*, Convair Astronautics (1956).
- [33] F. G. Kennedy and P. L. Palmer, *Preliminary design of a micro-scale solar thermal propulsion system*, in *38th AIAA/ASME/SAE/ASEE Joint Propulsion Conference & Exhibit*, July (2002) pp. 1–11.
- [34] F. Kennedy, P. Palmer, and M. Paul, *Results of a Microscale Solar Thermal Engine Ground Test Campaign at the Surrey Space Centre*, in *40th AIAA/ASME/SAE/ASEE Joint Propulsion Conference and Exhibit*, July (2004) pp. 1–11.
- [35] H. Sahara, K. Watanabe, M. Shimizu, and Y. Nakamura, *Single-Crystal Molybdenum Solar Thermal Propulsion Thruster*, *Trans. Japan Soc. Aero. Space Sci.* **46**, 180 (2003).
- [36] H. Sahara, M. Shimizu, K. Osa, K. Watanabe, and Y. Nakamura, *Solar Thermal Propulsion for Microsatellites End-of-Life De-Orbiting*, (2003) pp. 1–8.
- [37] H. Sahara and M. Shimizu, *Solar Thermal Propulsion System for Microsatellites Orbit Transferring*, in *40th AIAA/ASME/SAE/ASEE Joint Propulsion Conference and Exhibit*, July (2004) pp. 1–7.
- [38] M. R. Gilpin, D. B. Scharfe, A. P. Pancotti, and M. P. Young, *Molten Boron Phase-Change Thermal Energy Storage to*, in *Distribution* (2011).
- [39] P. Henshall and P. Palmer, *Solar Thermal Propulsion Augmented with Fiber Optics: - Technology Development*, in *42nd AIAA/ASME/SAE/ASEE Joint Propulsion Conference & Exhibit*, July (2006) pp. 1–12.
- [40] T. Nakamura, R. Krech, J. McClanahan, J. Shoji, R. Partch, and S. Quinn, *Solar Thermal Propulsion for Small Spacecraft - Engineering System Development and Evaluation*, in *41st AIAA/ASME/SAE/ASEE Joint Propulsion Conference & Exhibit* (2005).

- [41] J. D. M. Malloy, R. F. Rochow, and J. B. Inman, *Hybrid solar rocket utilizing thermal storage for propulsion and electrical power*, (1994).
- [42] B. Xing, K. Liu, M. Huang, and M. Cheng, *High efficient configuration design and simulation of platelet heat exchanger in solar thermal thruster*, *Journal of Thermal Science* **23**, 246 (2014).
- [43] H. C. M. Leenders and P. Batenburg, *Thermal control of a solar thermal propulsion system*, Tech. Rep. October (TU Delft, 2006).
- [44] H. C. M. Leenders, *Solar thermal propulsion Literature study*, Tech. Rep. (TU Delft, 2007).
- [45] D. M. Pino, *Solar Concentrator Demonstrator for PocketQubes*, Tech. Rep. (MSc thesis report TU Delft, 2016).
- [46] E. Jansen, *Improvement and validation of test stand performance for novel micropulsion systems*, Tech. Rep. (MSc thesis report TU Delft, 2016).
- [47] A. Cervone, B. Zandbergen, D. C. Guerrieri, M. A. Costa, I. Krusharev, and H. Zeijl, *Green micro-resistojet research at Delft University of Technology: new options for Cubesat propulsion*, *CEAS Space Journal* (2016), 10.1007/s12567-016-0135-3.
- [48] K. Das, *Design and Thermal Analysis of a Solar Thermal Thruster*, Tech. Rep. (MSc thesis report TU Delft, 2018).
- [49] S. W. Churchill and H. H. Chu, *Correlating equations for laminar and turbulent free convection from a horizontal cylinder*, *International Journal of Heat and Mass Transfer* **18**, 1049 (1975).
- [50] Z. Atayilmaz and I. Teke, *Experimental and numerical study of the natural convection from a heated horizontal cylinder*, *International Communications in Heat and Mass Transfer* **36**, 731 (2009).
- [51] B. Y. Xing, M. C. Huang, M. S. Cheng, and K. Liu, *Influence of Thermal Decomposition of Ammonia Propellant in Solar Thermal Propulsion*, *Applied Mechanics and Materials* **598**, 257 (2014).
- [52] A. Takken, *Thesis Proposal and Plan*, Tech. Rep. (TU Delft, 2019).
- [53] S. J. Aboud, M. Al Fayoumi, and M. Alnuaimi, *Verification and validation of simulation models*, *Handbook of Research on Discrete Event Simulation Environments: Technologies and Applications*, 58 (2009).
- [54] T. Bergman and A. Lavine, *Fundamentals of Heat and Mass Transfer (8th edition)*, 8th ed. (Wiley, 2017).
- [55] J. Meyers, *ME 144 : Heat Transfer Internal Convection (v1.0)*, (2011).
- [56] G. L. Morini, *Laminar-to-turbulent flow transition in microchannels*, *Microscale Thermophysical Engineering* **8**, 15 (2004).
- [57] H. Baehr and K. Stephan, *Heat and Mass Transfer* (Springer, 2006).
- [58] W. M. Rohsenow and J. R. Hartnett, *Handbook of heat transfer* (McGraw-Hill, 1999).
- [59] D. Taler and J. Taler, *Simple heat transfer correlations for turbulent tube flow*, *E3S Web of Conferences* **13**, 1 (2017).
- [60] R. A. Seban and E. F. McLaughlin, *Heat transfer in tube coils with laminar and turbulent flow*, *International Journal of Heat and Mass Transfer* **6**, 387 (1963).
- [61] R. Ferreira, *Development and Testing of a Water Microresistojet*, Tech. Rep. (MSc thesis report TU Delft, 2008).
- [62] S. Paitoonsurikarn and K. Lovegrove, *On the study of convection loss from open cavity receivers in solar paraboloidal dish applications*, *Proceedings of ANZSES* **0**, 154 (2003).

- [63] Crane Company, *Flow of fluids through valves, fittings and pipe* (Crane Company, 1979).
- [64] P. Oosthuizen, *Free Convective Heat Transfer From Horizontal Cones*, ASME , 5 (1973).
- [65] R. J. Goldstein, U. Madanan, and T. H. Kuehn, *Simplified correlations for free convection from a horizontal isothermal cylinder*, *Applied Thermal Engineering* **161**, 113832 (2019).
- [66] L. Guo, Z. Feng, and X. Chen, *An experimental investigation of the frictional pressure drop of steam-water two-phase flow in helical coils*, *International Journal of Heat and Mass Transfer* **44**, 2601 (2001).
- [67] A. N. Johnson, P. I. Espina, G. E. Mattingly, and C. L. Merklet, *Numerical characterization of the discharge coefficient in critical nozzles*, Tech. Rep. (University of Tennessee Space Institute, 1998).
- [68] J. J. Preijde, *Design of a Solar Thermal Power-Propulsion System for a Small Satellite*, Tech. Rep. January (MSc thesis report TU Delft, 2015).
- [69] R. Bijster, *Design, Verification and Validation of a Micropulsion Thrust Stand*, Tech. Rep. (MSc thesis report TU Delft, 2014).
- [70] H. Versteeg, *Novel fabrication method for a hot gas supersonic micro-thruster*, Tech. Rep. (MSc thesis report TU Delft, 2020).
- [71] J. Tu, G.-H. Yeoh, and C. Liu, *Computational Fluid Dynamics* (Elsevier, 2008).
- [72] C. D. Argyropoulos and N. C. Markatos, *Recent advances on the numerical modelling of turbulent flows*, *Applied Mathematical Modelling* **39**, 693 (2015).
- [73] Z. Dickert, *GOX-Ethanol Resonance Ignition System Design*, Tech. Rep. (MSc thesis report TU Delft, 2020).
- [74] L. Denies, *Regenerative cooling analysis of oxygen/methane rocket engines*, Tech. Rep. (MSc thesis report TU Delft, 2015).
- [75] K. Khamis, *Comparative Study between MEMS and Conventional Thrusters for Small Spacecraft Micropulsion*, Tech. Rep. (Msc thesis report TU Delft, 2019).
- [76] ANSYS Fluent Tutorial Guide 18, *ANSYS Fluent Tutorial Guide 18*, *ANSYS Fluent Tutorial Guide 18* **15317**, 724 (2018).

A

Technical drawings Solar Thermal Thruster 2

The [CAD](#) drawings of Solar Thermal Thruster 2 are shown in this appendix. It consists of the following eight drawings:

1. Figure A.1: the inner cylinder of the [RAC](#) part.
2. Figure A.2: the outer cylinder of the [RAC](#) part.
3. Figure A.3: the cap of the [RAC](#) part.
4. Figure A.4: the spike of the [RAC](#) part.
5. Figure A.5: the connection piece for connecting the inlet of the [RAC](#) part to the feed line and inlet pressure sensor.
6. Figure A.6: the connection piece for connecting the outlet of the [RAC](#) part to the outlet pressure sensor.
7. Figure A.7: the Macor piece for securing the [RAC](#) part to the thrust bench.
8. Figure A.8: the copper nozzle. Note that this drawing is taken from Leenders [3].

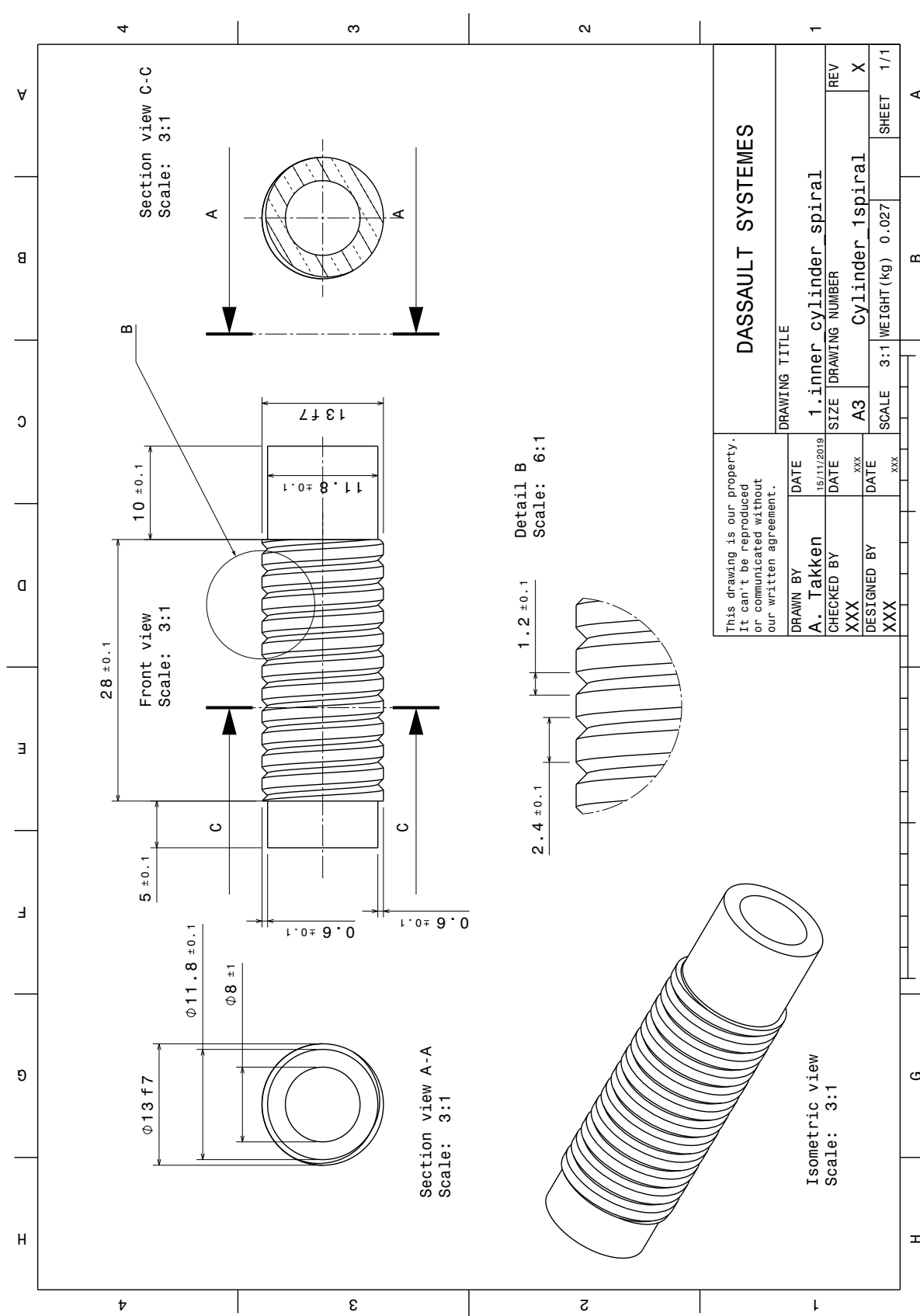


Figure A.1: Drawing of STT2 inner cylinder.

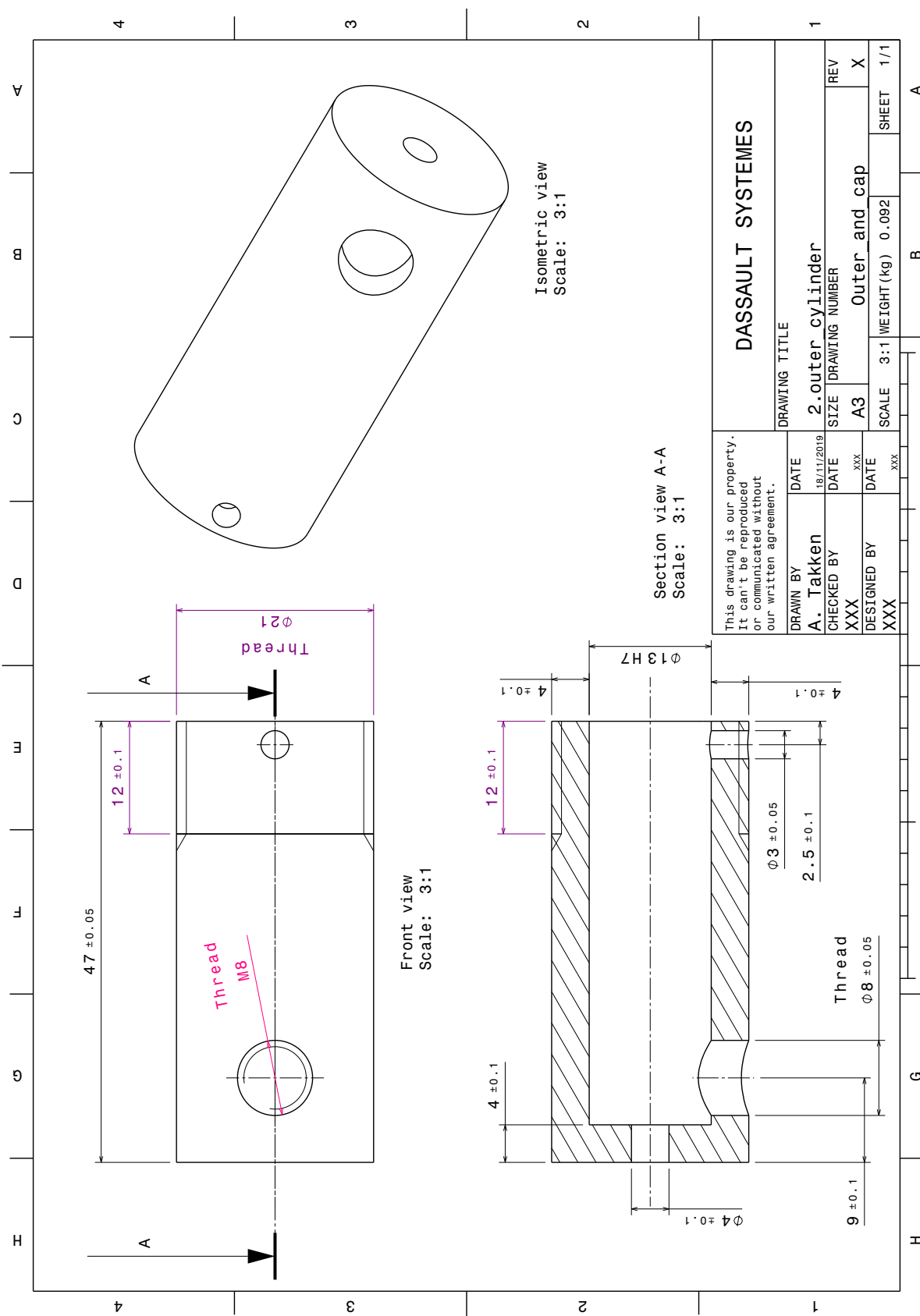


Figure A.2: Drawing of STT2 outer cylinder.

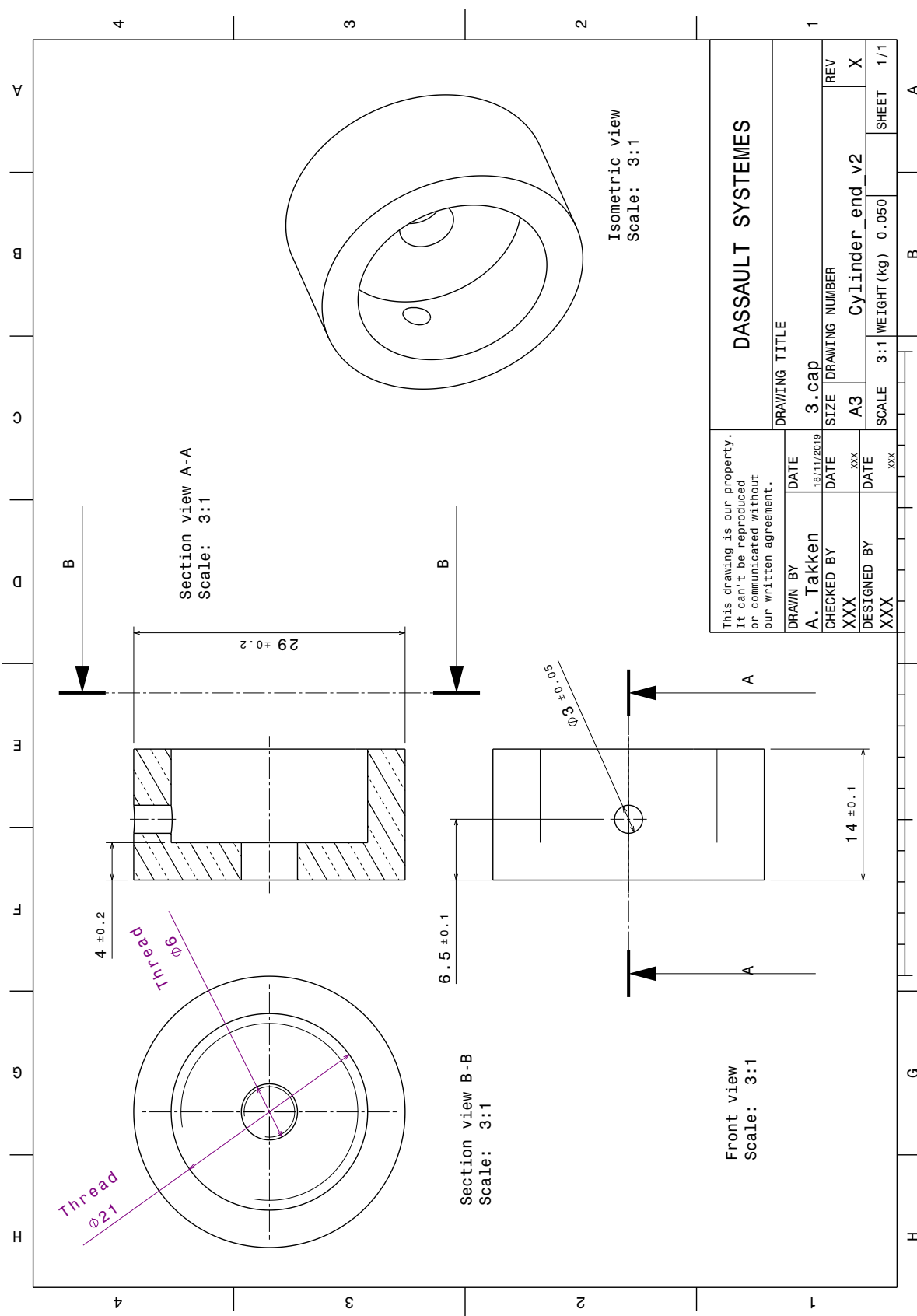


Figure A.3: Drawing of STT2 cap.

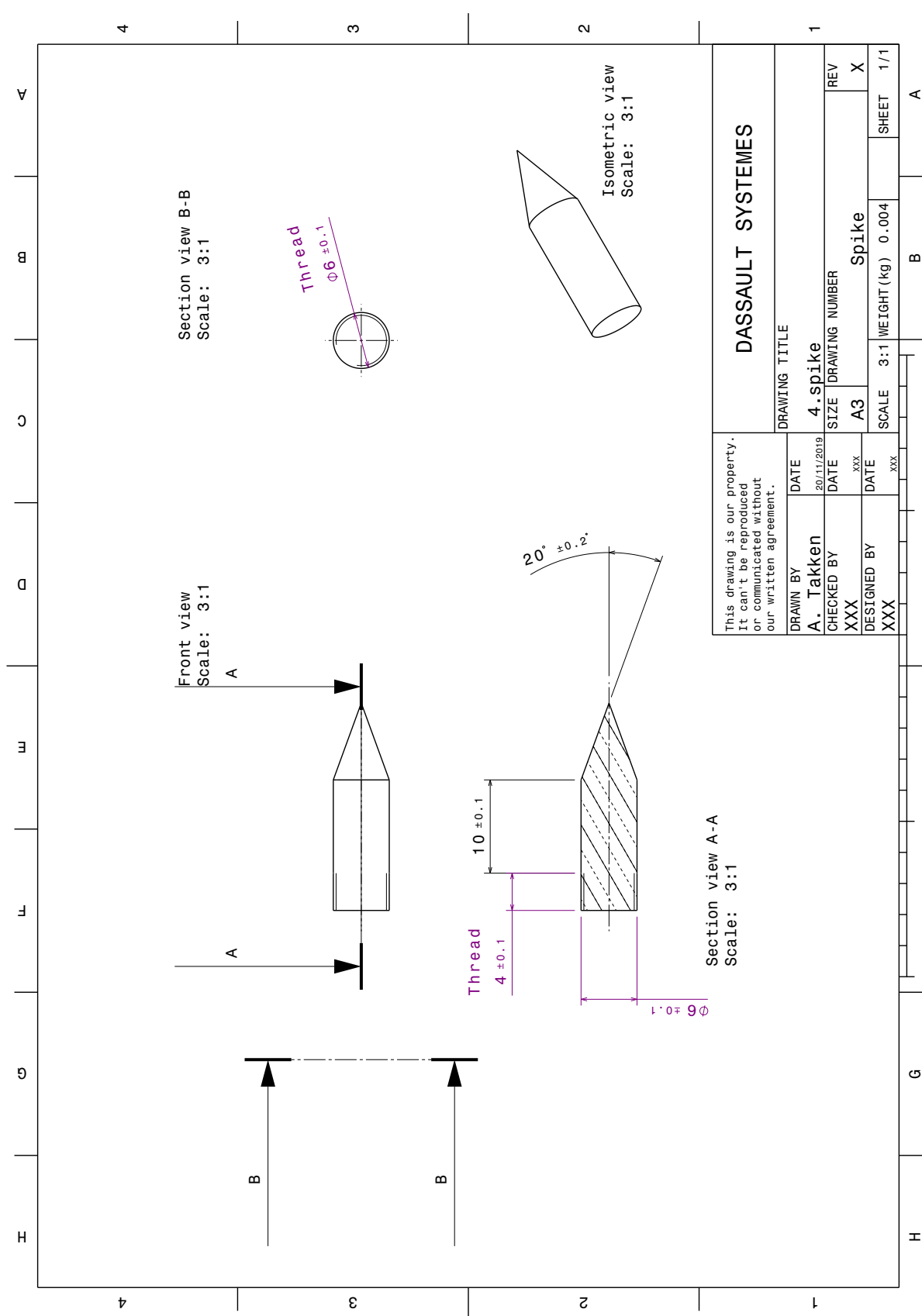


Figure A.4: Drawing of STT2 spike.

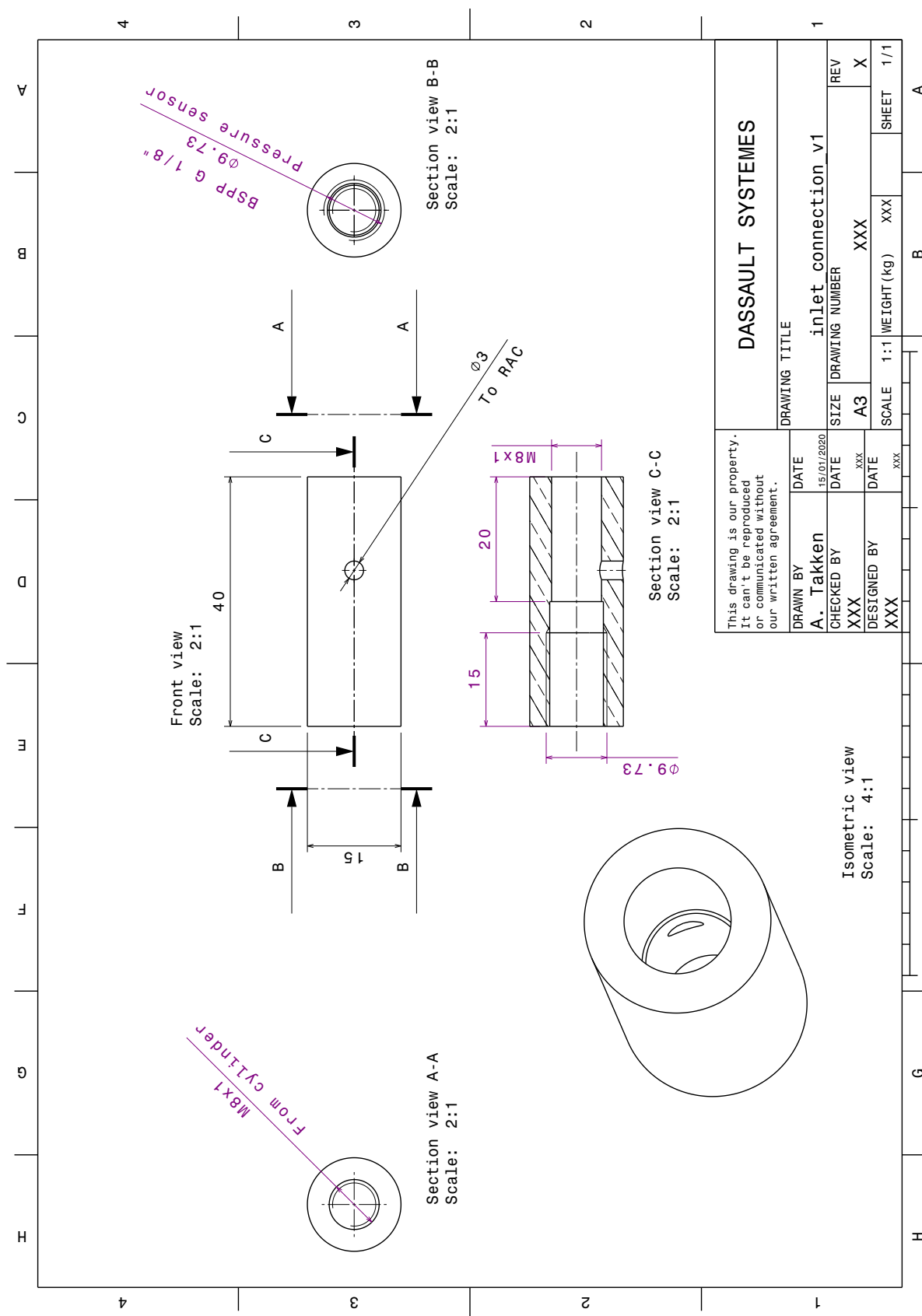


Figure A.5: Drawing of STT2 inlet connection piece.

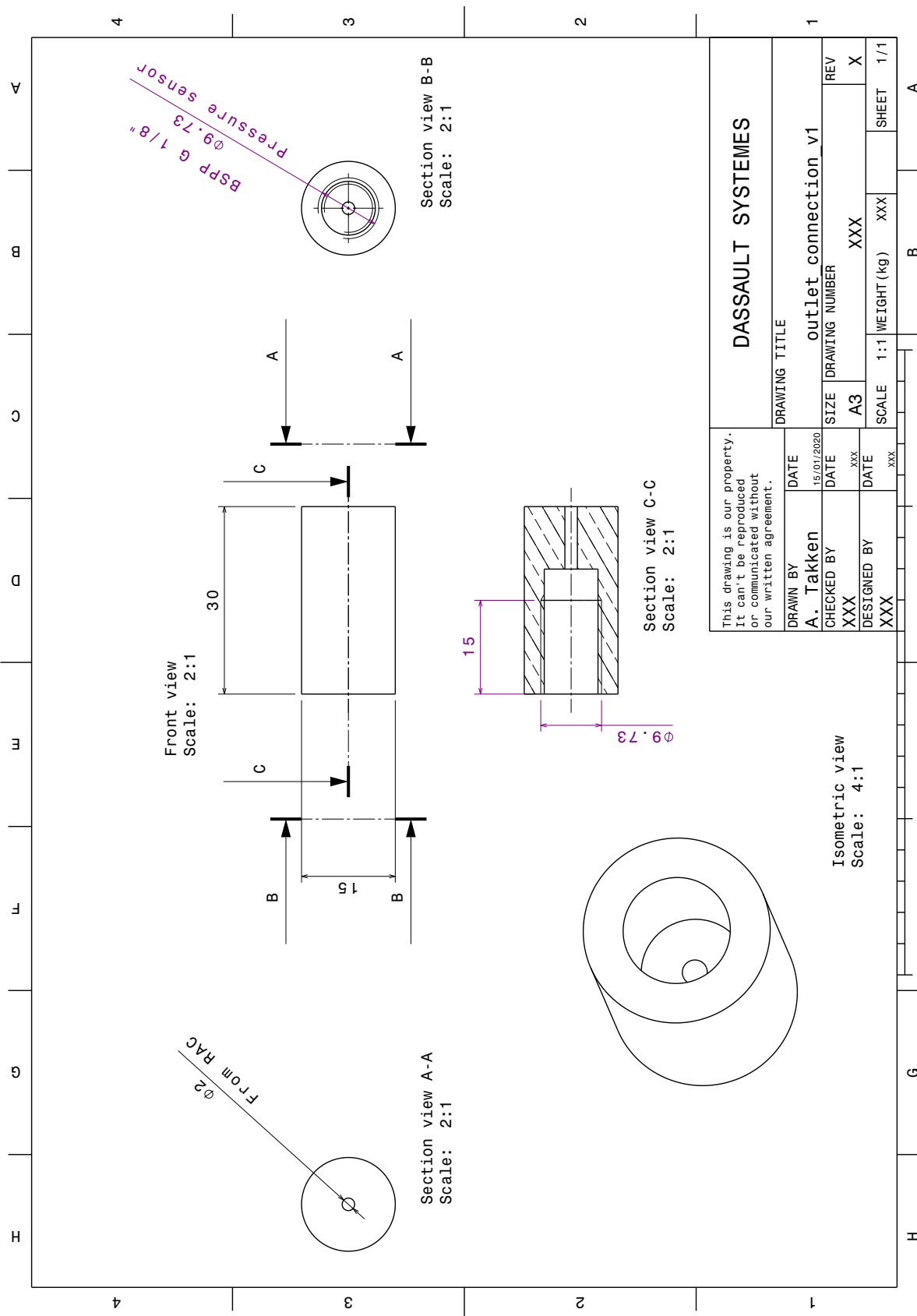


Figure A.6: Drawing of STT2 outlet connection piece.

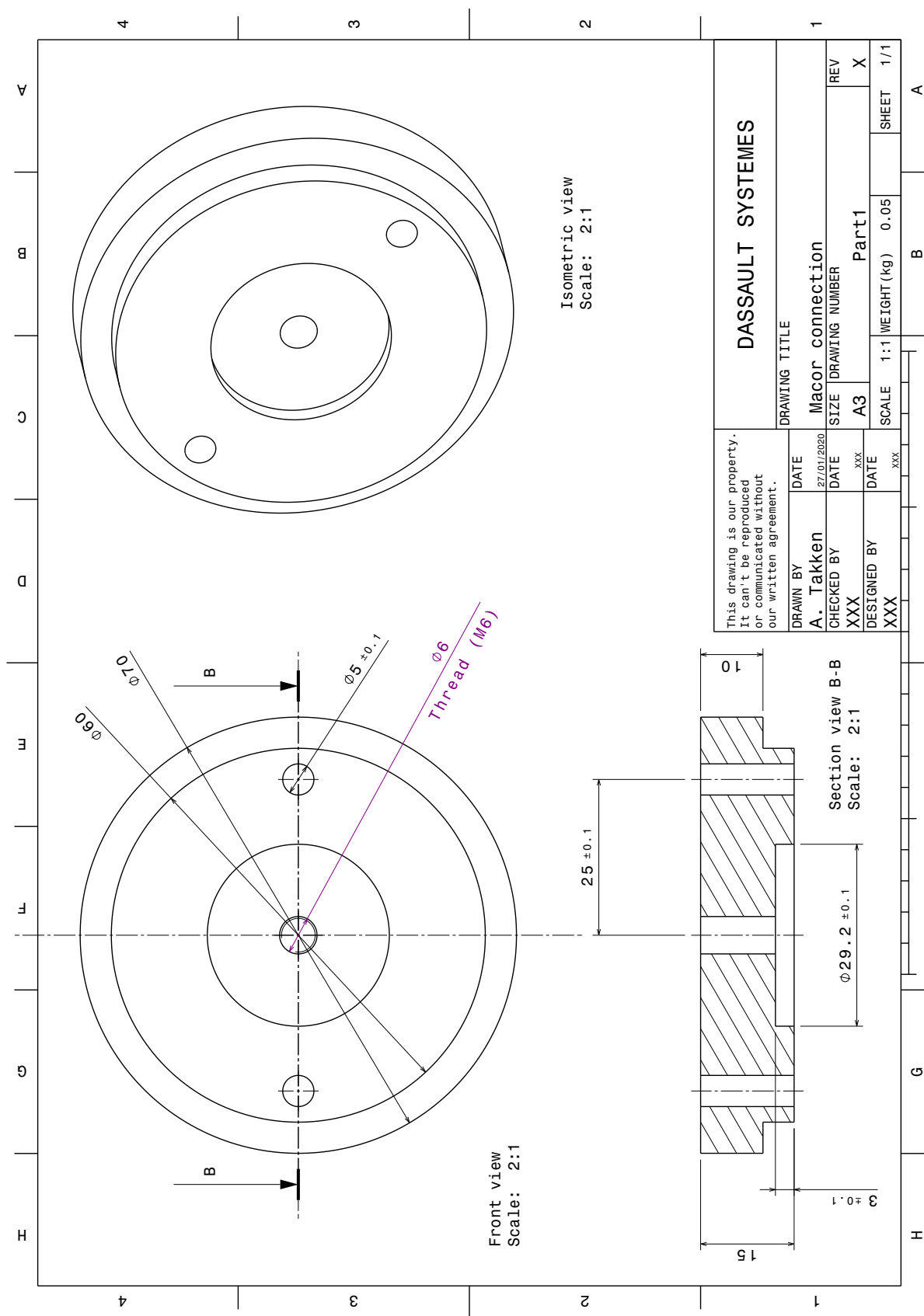


Figure A.7: Drawing of STT2 Macor connection piece.

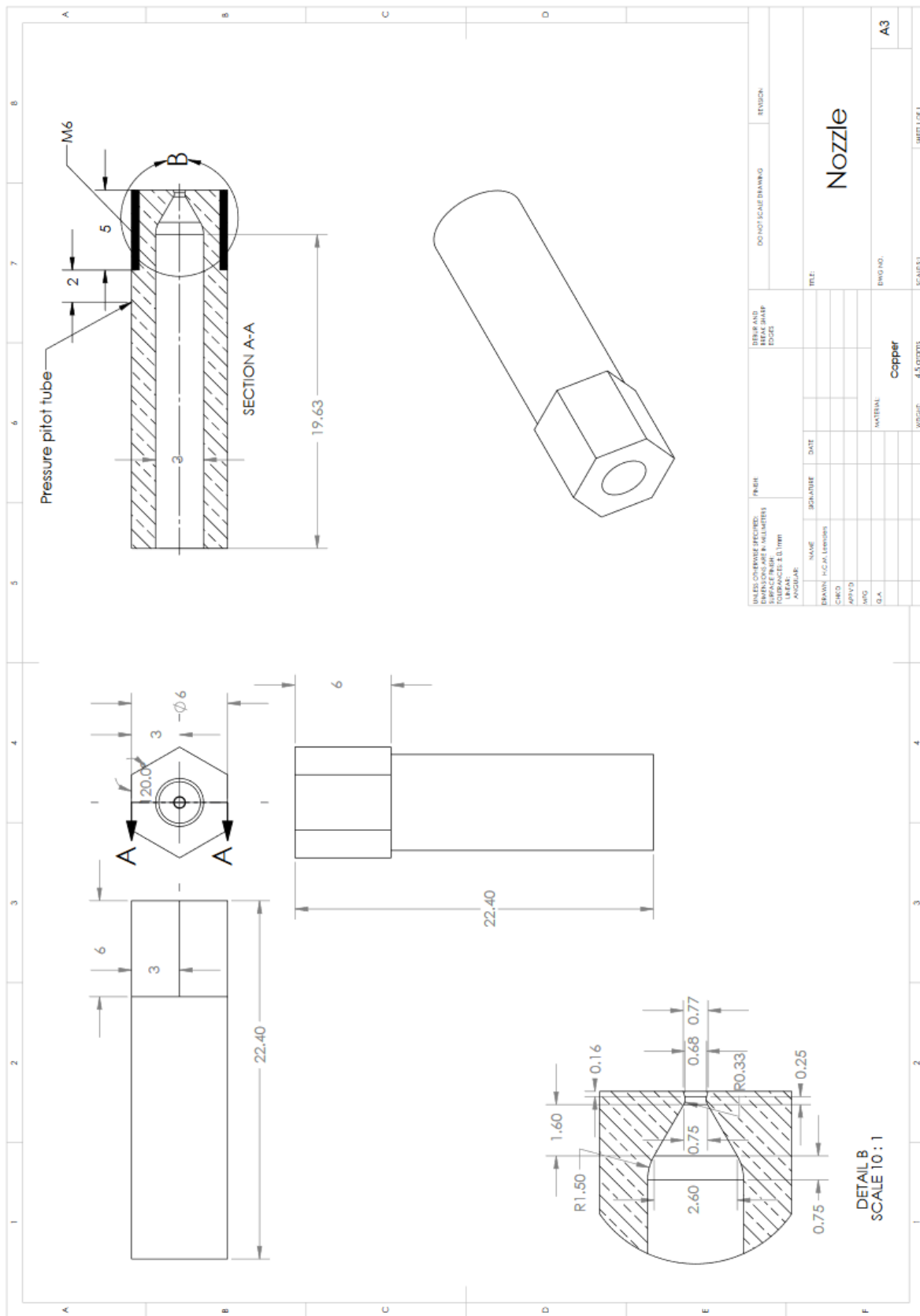


Figure A.8: Drawing of the STT2 copper nozzle, from Leenders [3].

B

Technical drawings Solar Thermal Thruster 3

The [CAD](#) drawings of Solar Thermal Thruster 3 are shown in this appendix. It consists of the following four drawings:

1. Figure [B.1](#): the inner cylinder of the [RAC](#) part.
2. Figure [B.2](#): the outer cylinder of the [RAC](#) part.
3. Figure [B.3](#): the cap of the [RAC](#) part.
4. Figure [B.4](#): the nozzle.

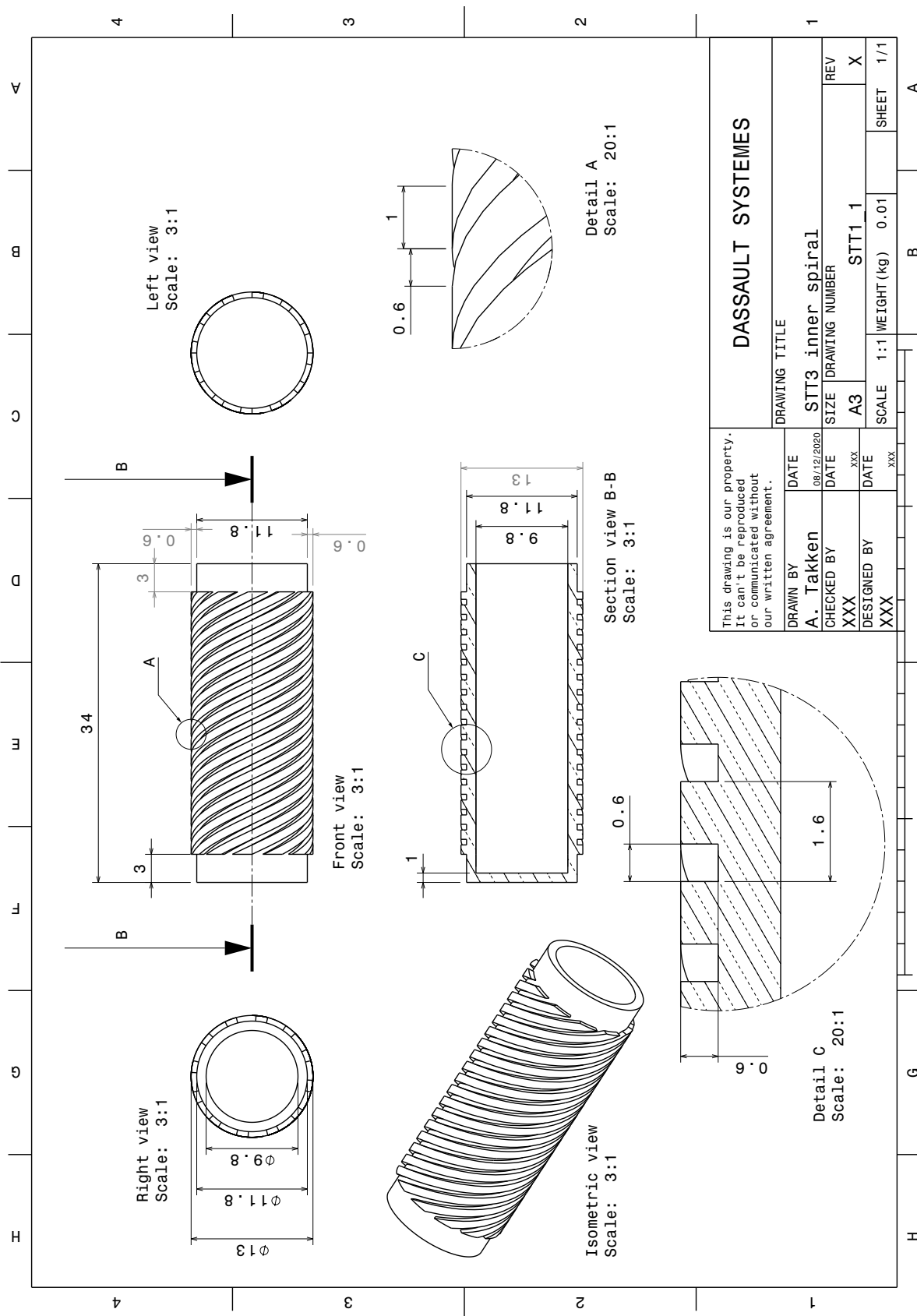


Figure B.1: Drawing of STT3 inner cylinder.

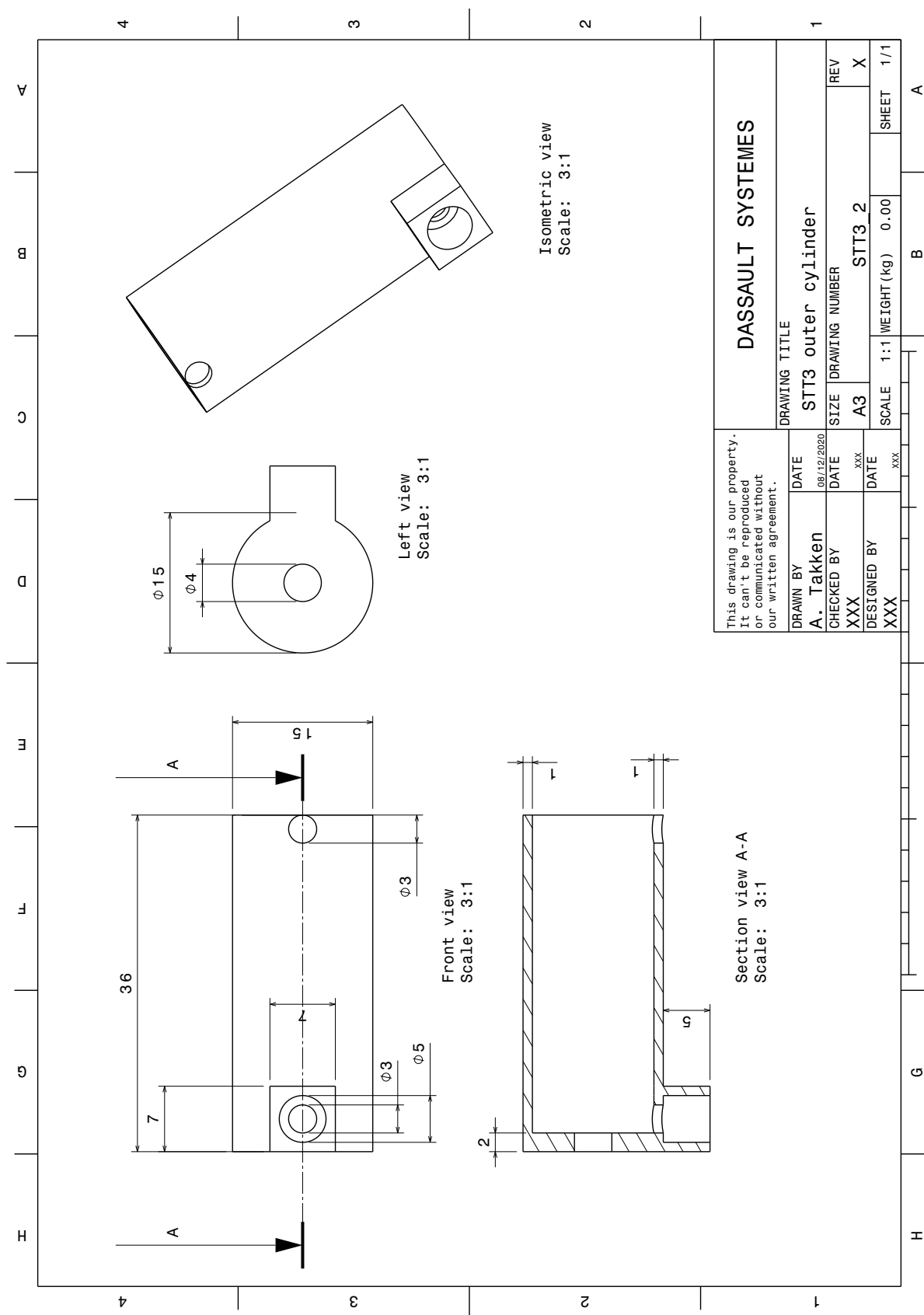


Figure B.2: Drawing of STT3 outer cylinder.

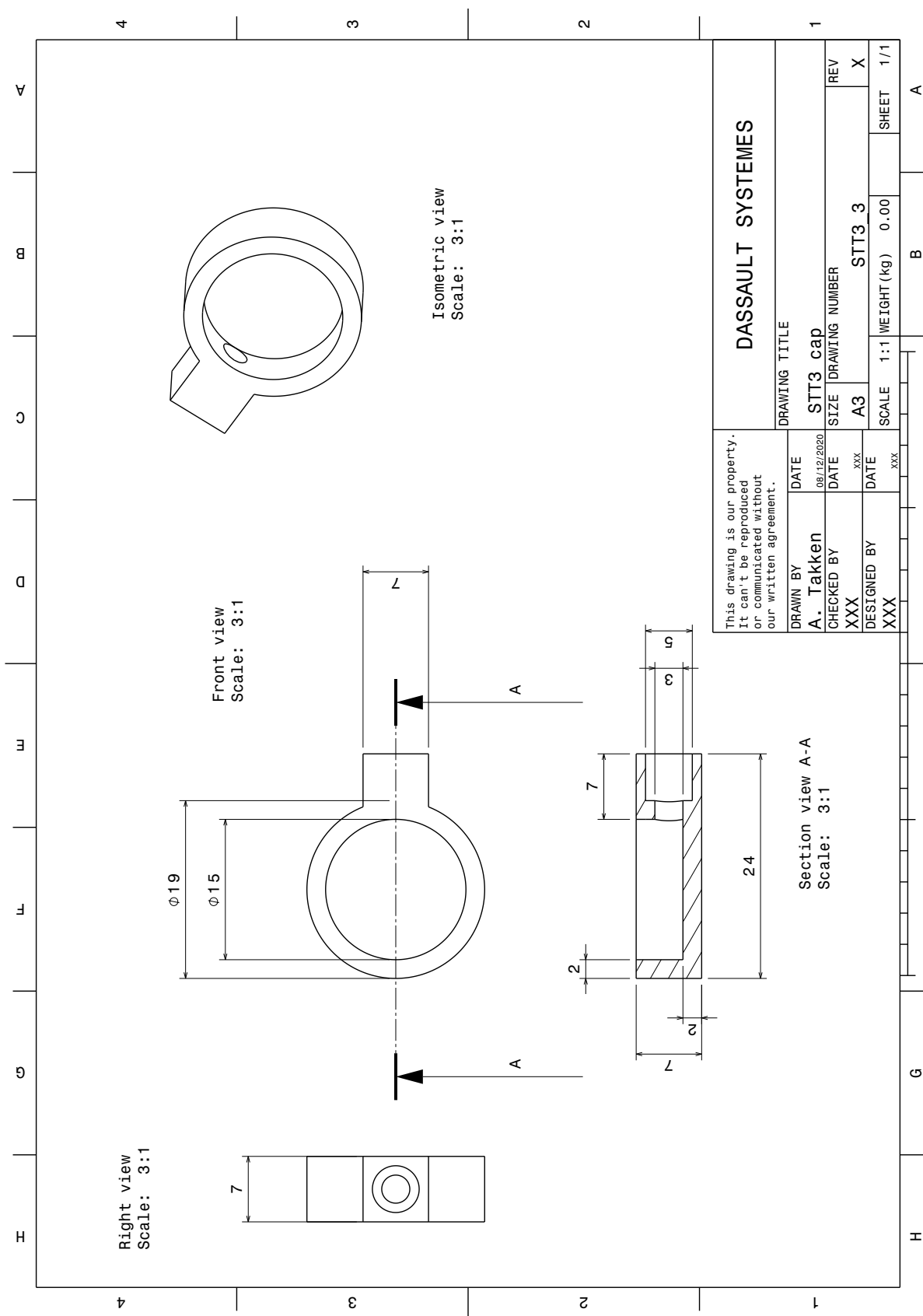


Figure B.3: Drawing of STT3 cap.

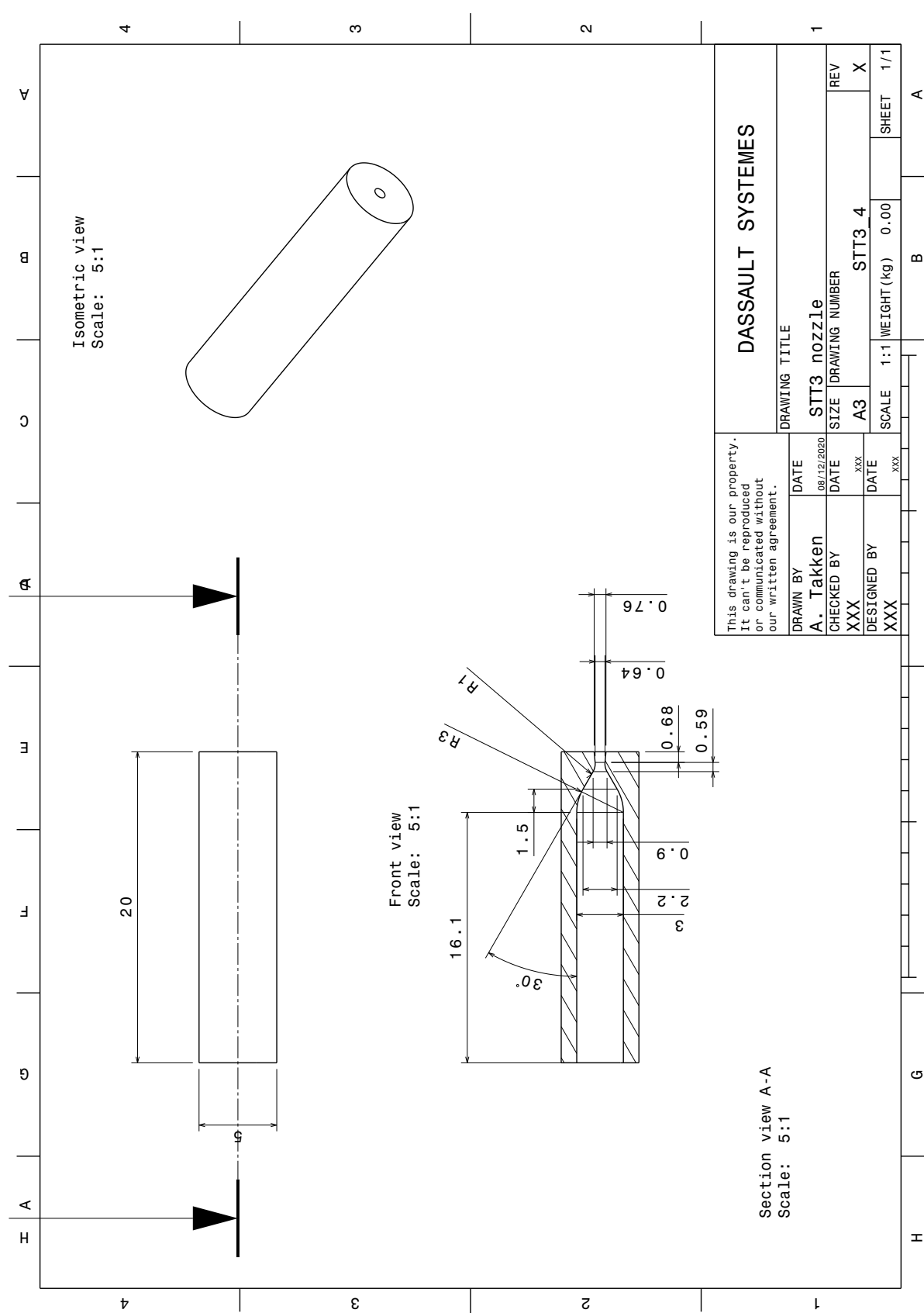


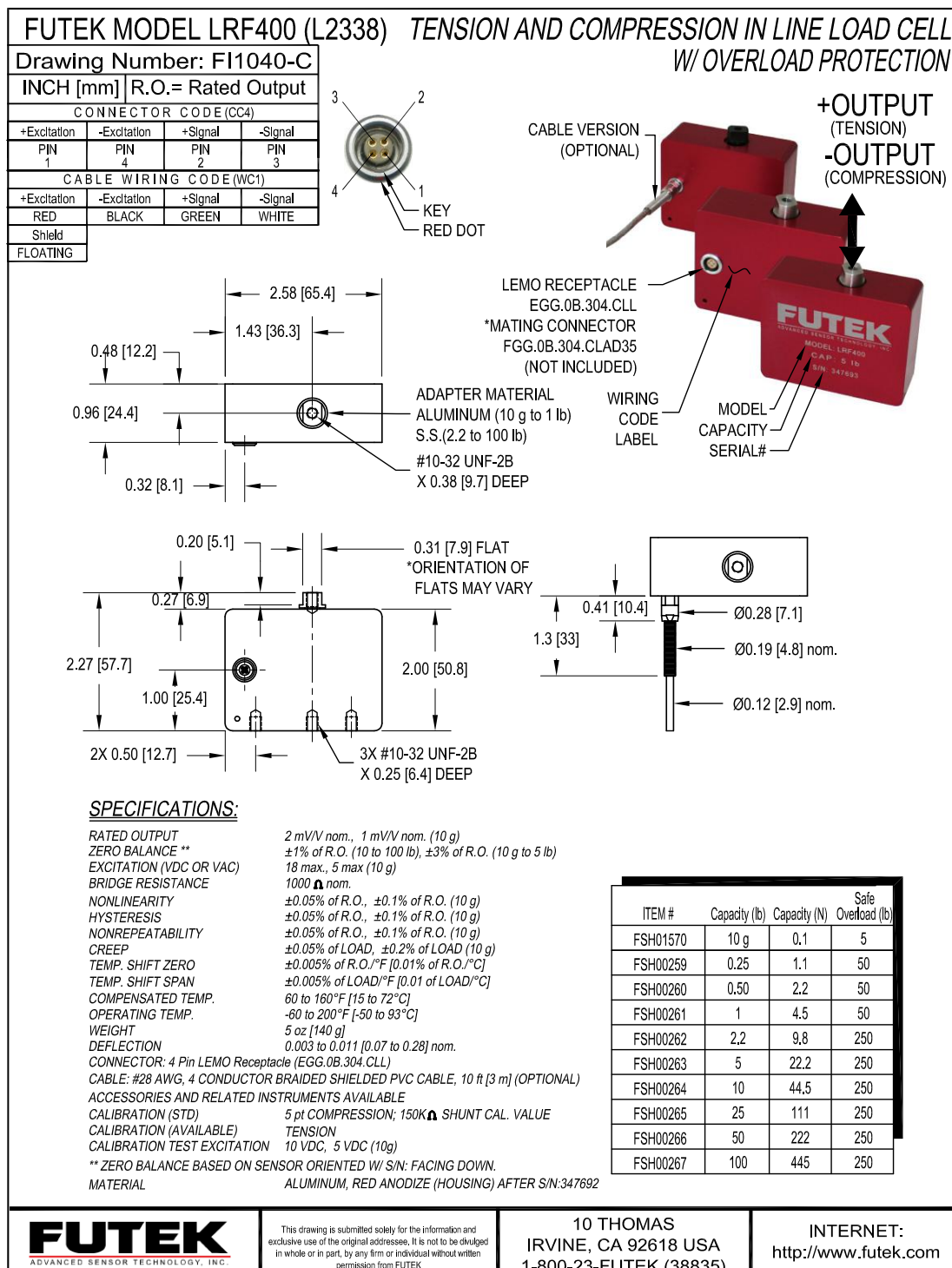
Figure B.4: Drawing of STT3 nozzle.

C

Experiment hardware

Below, the data sheets of all used sensor equipment, insulation and kit are shown. They were all used in the test runs at some point, except for the insulation. Most sensor equipment is borrowed for free from the Meetshop, located at the faculty of [3mE](#).

C.1. Futek LRF400 (L2338) data sheet



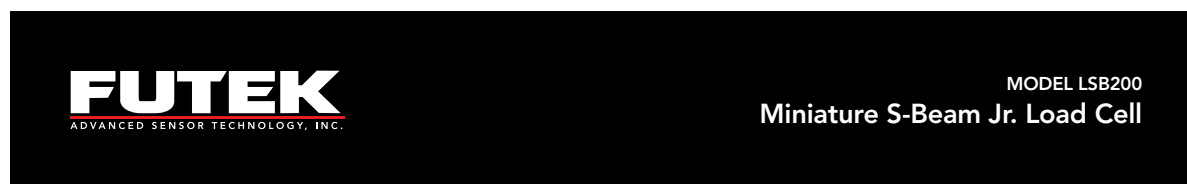
FUTEK
ADVANCED SENSOR TECHNOLOGY, INC.

This drawing is submitted solely for the information and exclusive use of the original addressee. It is not to be divulged in whole or in part, by any firm or individual without written permission from FUTEK

10 THOMAS
IRVINE, CA 92618 USA
1-800-23-FUTEK (38835)

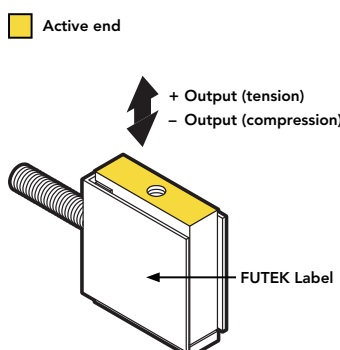
INTERNET:
<http://www.futek.com>

C.2. Futek LSB200 data sheet



FEATURES

- Up to 10 times the overload protection
- Overload is available in Tension and Compression
- Light weight
- Notable nonlinearity
- Loads up to 100 lb (445 N)
- Miniature size



SPECIFICATIONS	
PERFORMANCE	
Nonlinearity	±0.1% of RO
Hysteresis	±0.1% of RO
Nonrepeatability	±0.05% of RO
ELECTRICAL	
Rated Output (RO)	See chart on third page
Excitation (VDC or VAC)	10 max
Bridge Resistance	See chart on third page
Insulation Resistance	≥500 MOhm @ 50 VDC
Connection	#29 AWG, 4 conductor, spiral shielded silicone cable, 5 ft [1.5 m] long
Wiring Code	WC1
MECHANICAL	
Weight (approximate)	0.3 oz [9 g]
Safe Overload	1000% of RO 200% tension only (50–100 lb)
Material	Aluminum (10 g–10 lb), stainless-steel (25–100 lb)
IP Rating	IP40
TEMPERATURE	
Operating Temperature	-60 to 200°F [-50 to 93°C]
Compensated Temperature	60 to 160°F [15 to 72°C]
Temperature Shift Zero	±0.01% of RO/°F [0.018% of RO/°C]
Temperature Shift Span	±0.02% of Load/°F [0.036% of Load/°C]
CALIBRATION	
Calibration Test Excitation	5 VDC
Calibration (standard)	5-pt Tension
Calibration (available)	Compression

C.3. RS Pro data sheet

**ENGLISH****Datasheet**

IEC Mineral Insulated Thermocouples with Threaded Pot

Type 'K' with threaded pot & tails – 310 stainless steel or Inconel® Alloy 600 sheath



- Mineral insulated Type 'K' Thermocouple
- Choice of 310 stainless steel or Inconel® Alloy 600 sheath
- Highly flexible, sheath can be bent/formed to suit many applications and processes
- 0.5mm diameter fast response option, other diameters include 1.0, 1.5, 3.0 & 6.0mm
- Insulated hot junction
- Probe temperature range -40°C to +1100°C
- M8 x 1.0mm fine pitch threaded pot seal (200°C)
- M8 locknuts available as an option (see below)
- 100mm tails, PFA twin twisted 7/0.2mm, colour coded to IEC 584

Specifications

Sensor type:	Type 'K' (Nickel Chromium/Nickel Aluminium) to IEC 584
Construction:	Flexible mineral insulated probe with 310 stainless steel or Inconel® Alloy 600 sheath with M8 x 1.0mm fine pitch threaded pot seal & tails
Element/hot junction:	Single element, junction insulated from sheath (offers protection against spurious electrical signals)
Termination:	100mm PFA twin twisted 7/0.2mm tails, +green/-white colour coded in accordance with IEC 584
Probe temperature range:	-40°C to +1100°C >1.0mm diameter -40°C to +750°C – 1.0mm diameter and below
Pot seal rating:	200°C

RS014/0816

C.4. Pressure sensor data sheets

OPERATION MANUAL

Industrial pressure transmitter with voltage or current output



Description



Characteristic features

- Product variants from vacuum to 100 bar FS
- For measurement of relative pressure
- Output standard signal of 0...10 V or 4...20 mA
- Temperature compensated
- Robust, medium resistant models
- Simple assembly
- Water and oil resistant
- Enclosure IP65

Typical areas of application

- Food technology
- Pneumatics
- High pressure
- Fuel pumps
- Gases
- Fuel cells

Features

The pressure probe of series DRTR convert the measured values in the form of calibrated and temperature compensated standard signal of 0...10 V or 4...20 mA. The delivery spectrum covers a wide pressure range from vacuum to 100 bar FS with 12 variants of different measuring ranges (see table).

Through a precise calibration at 7 measuring points, an outstanding accuracy and a very low temperature residual error is achieved.

The probes are ideally suitable for measurement of static and dynamic relative pressure in liquids or gases. Typical areas of application are in the field of pneumatics, hydraulics and other industrial applications.

The robust probe housing with enclosure type IP 67 is made of anodised aluminium and is provided with a 1/4" internal thread for connection to the medium.

The electric connection is done with an industrial plug as per DIN 43650. The model with current signal is connected through a current loop. The model with voltage output requires an auxiliary supply.

Besides the standard variants, customer specific models for absolute pressure with other type of calibration, ratio metric voltage output and also with digital output signal are also available. Further information on OEM-models can be obtained on request!

In general the B+B pressure sensors are medium resistant. However we recommend to prove the media compatibility with critical mediums such as electroplating applications (iron trichloride) or oils with undefined additives .

Technical Data

Industrial pressure transmitter

Measuring range	0...+100 bar, 6 types
Bursting pressure	See table
Residual error linearity / hysteresis	< ±0,2 % FS
Temperature coefficient	TCO < ±0,015 % FS / K
Operating temperature range	-20...+80 °C
Sensor material	Ceramics, Al2O3
Housing material	Aluminium AlMgPbCu, blue anodised
Seal	Viton
Pressure connection	1/4" female thread
Dimensions	30 x 30 x 89 mm
Connection	4-pole industrial connection, DIN 43650
Protection	IP65
Model 4...20 mA	
Output signal	4...20 mA, Two-Wire
Permissible load	R _A [Ω]=(U _V [V]-10V)/0,02 A
Model 0...10 V	
Output signal	0...10 V, Three-Wire
Auxiliary power	12...30 V DC / 5 mA

Technical changes reserved
0141 0316-180 14.08.2015

B+B Thermo-Technik GmbH | Heinrich-Hertz-Straße 4 | D-78166 Donaueschingen
Fon +49 771 83160 | Fax +49 771 8316-50 | info@bb-sensors.com | bb-sensors.com



OPERATION MANUAL

Industrial pressure transmitter for measuring absolute pressure DRTR-ED-XX_A



Description



Technical data

DRTR-ED-R

Measuring range	1...+50 bar, 6 Types
Overload	See table
Residual error Linearity/Hyst.	< ±0.4 % FS
Temperature coefficient	TCO < ±0.015 % FS / K TCG < ±0.010 % FS / K
Application temp. range	-20...+80 °C
Sensor material	Ceramics, Al ₂ O ₃
Housing material	Stainless steel 1.4305 optional 1.4571
Seal	Viton
Pressure connection	G 1/4" male thread
Dimensions	(LxWxH) 89x50x30 mm
Power supply connection	4-pole industrial plug, DIN 43650
Protection	IP65
CE-conformance	2014/30/EU
EMV-noise emission	EN 61000-6-3:2011
EMV-noise withstanding	EN 61000-6-1:2007
Model 4...20 mA	
Output signal	4...20 mA, 2-wire
Permissible load	R _a [Ω] = (U _v [V] - 10V) / 0.02 A
Model 0...10 V	
Output signal	0...10 V, 3-wire
Power supply	12...30 V DC / 5 mA

Characteristic features

- Variants from vacuum to 50 bar FS
- For measuring absolute pressure
- Output standard signal 0...10 V or 4...20 mA
- High-quality industrial design in stainless steel
- Robust, media-resistant design
- Temperature compensated
- Easy to install
- Water and oil resistant
- IP65 protection

Areas of application

- Pneumatics
- Hydraulics
- Industrial applications
- Machinery and plant technology
- Automation technology

Features

The stainless steel series pressure sensor DRTR-ED transfer the measured value as a calibrated and temperature compensated standard signal 0...10 V or 4...20 mA. The product range covers 6 graded measuring range variants of the pressure range from vacuum to 50 bar Full Scale (FS) (See table).

From a precise calibration of 7 measurement points at 3 different temperatures, an excellent precision and a very low temperature residual error is achieved. The sensors are ideal for measuring both static and dynamic absolute pressure in liquids and gases. Typical applications for this sensor is in the field of pneumatics, hydraulics and other industrial applications.

The robust housing of the sensor with IP65 protection is made out of stainless steel and has a G 1/4" male thread media port.

The electrical connection is an industrial plug according to DIN 43650. The version which needs current signal gets this through the power loop. The version with voltage output requires a separate power supply. In addition to the versions with 4...20 mA and 0...10 V variants with digital output signal and stainless steel case, relative pressure versions are also available.

Technical changes reserved
0141 0316-140 20.04.2016

B+B Thermo-Technik GmbH | Heinrich-Hertz-Straße 4 | D-78166 Donaueschingen
Fon +49 771 83160 | Fax +49 771 8316-50 | info@bb-sensors.com | bb-sensors.com



1/2

C.5. National Instruments USB-6008 data sheet

SPECIFICATIONS

USB-6008

8 AI (12-Bit, 10 kS/s), 2 AO (150 Hz), 12 DIO USB Multifunction I/O Device

Definitions

Warranted specifications describe the performance of a model under stated operating conditions and are covered by the model warranty.

The following characteristic specifications describe values that are relevant to the use of the model under stated operating conditions but are not covered by the model warranty.

- *Typical* specifications describe the performance met by a majority of models.
- *Nominal* specifications describe an attribute that is based on design, conformance testing, or supplemental testing.

Specifications are *Typical* unless otherwise noted.

Conditions

Specifications are valid at 25 °C unless otherwise noted.

Analog Input

Analog inputs

Differential	4
Single-ended	8, software-selectable
Input resolution	
Differential	12 bits
Single-ended	11 bits
Maximum sample rate (aggregate)	10 kS/s, system dependent
Converter type	Successive approximation
AI FIFO	512 bytes
Timing resolution	41.67 ns (24 MHz timebase)



Timing accuracy	100 ppm of actual sample rate
Input range	
Differential	$\pm 20\text{ V}^1, \pm 10\text{ V}, \pm 5\text{ V}, \pm 4\text{ V}, \pm 2.5\text{ V}, \pm 2\text{ V}, \pm 1.25\text{ V}, \pm 1\text{ V}$
Single-ended	$\pm 10\text{ V}$
Working voltage	$\pm 10\text{ V}$
Input impedance	$144\text{ k}\Omega$
Overtoltage protection	$\pm 35\text{ V}$
Trigger source	Software or external digital trigger
System noise²	
Differential	
$\pm 20\text{ V}$ range	5 mV_{rms}
$\pm 1\text{ V}$ range	$0.5\text{ mV}_{\text{rms}}$
Single-ended, $\pm 10\text{ V}$ range	5 mV_{rms}

Table 1. Absolute Accuracy at Full Scale, Differential

Range (V)	Typical at 25 °C (mV)	Maximum over Temperature (mV)
± 20	14.7	138
± 10	7.73	84.8
± 5	4.28	58.4
± 4	3.59	53.1
± 2.5	2.56	45.1
± 2	2.21	42.5
± 1.25	1.70	38.9
± 1	1.53	37.5



Note Input voltages may not exceed the working voltage range.

¹ $\pm 20\text{ V}$ means that $|\text{AI+} - (\text{AI-})| \leq 20\text{ V}$. However, AI+ and AI- must both be within $\pm 10\text{ V}$ of GND. Refer to the *Taking Differential Measurements* section of the *NI USB-6008/6009 User Guide* for more information.

² System noise measured at maximum sample rate.

C.6. Scaime CPJ Rail data sheet

Conditionneur de signal analogique
Analog signal conditioner

CPJ / CPJ2S

±10 V/0-10 V / 4-20 mA



Version Rail DIN
DIN Rail Version

- Conditionne jusqu'à 4 capteurs à jauge de contrainte (350Ω)
- Capteur 4 ou 6 fils
- Sortie tension ($\pm 10 \text{ Vdc}$ ou $0-10 \text{ Vdc}$) et sortie courant ($4-20 \text{ mA}$)
- Signal d'étalonnage par shunt
- 2 seuils sur relais en option (CPJ2S)

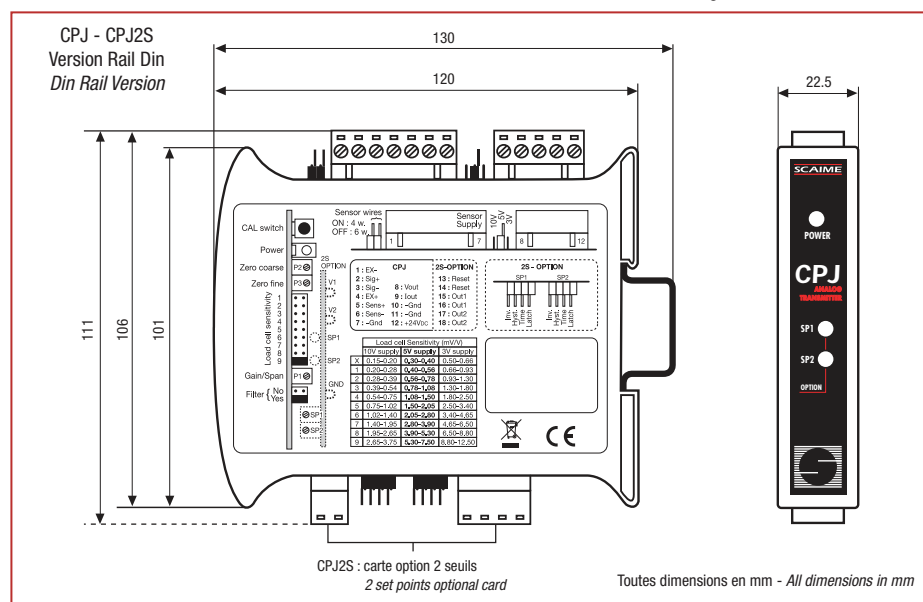
- The CPJ is able to run up to 4 strain gauge load cells (350Ω)
- 4 or 6 wire load cell
- Voltage output ($\pm 10 \text{ Vdc}$ or $0-10 \text{ Vdc}$) and current output ($4-20 \text{ mA}$)
- Shunt calibration signal
- 2 set points on relays optional version CPJ2S



Version Carte
Board Version



Version Boîtier IP65
IP65 Housing Version



C.7. Mettler Toledo AG245 data sheet

Technical data and optional equipment

68

7 Technical data and optional equipment

7.1 Technical data of the AG balances

Power supply

Power supply with AC/AC adapter national power cable	115 V, -20%+15%, 50/60 Hz, 230 V, -20%+15%, 50/60 Hz,	195mA, 90mA,	Sec: 12V, 50/60Hz, 1.25A Sec: 12V, 50/60Hz, 1.25A
---	--	-----------------	--

Fusing

Temperature switch

Power supply AG balance

9.5–17.5 V, 50/60 Hz, 7 VA or 9–20 V =, 7 W

Use only with a tested AC adapter with SELV output current.

Ensure correct polarity

Ambient conditions for AG balances

Height above sea level	up to 4000 m
Temperature	5–40 °C
Atmospheric humidity	80% RH @ +30 °C
Overtoltage categor	II
Pollution degree	2

Standard equipment

Balance complete with feedthrough for weighing below the balance, fitting for antitheft device and integrated short-form operating instructions, protective cover for keypad and display, cleaning brush, AC adapter, holder for AC adapter, power cable, operating instructions, draft shield element (AG135, AG285 only)

Technical data	AG64	AG104	AG135	AG204
Readability	0.1 mg	0.1 mg	0.1 mg/0.01 mg ¹⁾	0.1 mg
Maximum capacity	61 g	101 g	101 g/31 g ¹⁾	210 g
Taring range	0...61 g	0...101 g	0...101 g	0...210 g
Repeatability (s)	0.1 mg	0.1 mg	0.1 mg/0.02 mg ¹⁾	0.1 mg
Linearity ²⁾	±0.2 mg	±0.2 mg	±0.2 mg/±0.03 mg ¹⁾	±0.2 mg
Stabilization time (typical)	3 s	3 s	3 s/12 s ¹⁾	3 s
Adjustment	internal, fully automatic motorized initiation (FACT) and test possibility for checking the sensitivity			
• with internal weight	100 g	100 g	100 g	200 g
• with external weights	50 g	50/100 g	20/50/100 g	50/100/200 g
Sensitivity				
• Temperature drift ²⁾	±1.5 ppm/°C	±1.5 ppm/°C	±1.5 ppm/°C	±1.5 ppm/°C
• Long-term drift ³⁾	±0.003 %	±0.003 %	±0.003 %	±0.003 %
Display	backlit LCD	backlit LCD	LCD, not backlit	backlit LCD
Interface	LocalCAN universal interface			
Weighing pan	ø 85 mm, stainless steel			
Effective height above pan	240 mm			
Dimensions (w/d/h) balance	205 x 330 x 310 mm			
Net weight/with packaging	4.9 kg/7.25 kg			

Technical data	AG204 DR®	AG245**	AG285
Readability	1 mg/0.1 mg ¹⁾	0.1 mg/0.01 mg ¹⁾	0.1 mg/0.01 mg/0.01 mg ¹⁾
Maximum capacity	210 g/81 g ¹⁾	210 g/41 g ¹⁾	210 g/81 g/41 g ¹⁾
Taring range	0...210 g	0...210 g	0...210 g
Repeatability (s)	0.5 mg/0.1 mg ¹⁾	0.1 mg/0.02 mg ¹⁾	0.1 mg/0.05 mg/0.02 mg ¹⁾
Linearity ²⁾	±1 mg/±0.2 mg ¹⁾	±0.2 mg/±0.03 mg ¹⁾	±0.2 mg/0.1 mg/±0.03 mg ¹⁾
Stabilization time (typical)	3 s	3 s/15 s ¹⁾	3 s/15 s ¹⁾
Adjustment	internal, fully automatic motorized initiation (FACT) and test possibility for checking the sensitivity		
• with internal weight	200 g	200 g	200 g
• with external weights	50/100/200 g	40/100/200 g	40/100/200 g
Sensitivity			
• Temperature drift ²⁾	±1.5 ppm/°C	±1.5 ppm/°C	±1.5 ppm/°C
• Long-term drift ³⁾	±0.003 %	±0.003 %	±0.003 %
Display	backlit LCD	LCD, not backlit	LCD, not backlit
Interface	LocalCAN universal interface		
Weighing pan	ø 85 mm, stainless steel		
Effective height above pan	240 mm		
Dimensions (w/d/h) balance	205 x 330 x 310 mm		
Net weight/with packaging	4.9 kg/7.25 kg		

¹⁾ Values in the fine range (AG135, AG245, AG285) or DeltaRange (AG204 DeltaRange®)

²⁾ In the temperature range 10 ... 30°C

³⁾ Sensitivity deviation/year after first-time startup with self-calibration FACT switched on

** Production phaseout form June 2000

C.8. Zwaluw Fire Sealant 1200 °C data sheet

Den Braven

Technische Datasheet

Zwaluw Fire Sealant 1200 °C Hittebestendige pasta



Product Omschrijving

Zwaluw Fire Sealant 1200 °C is een pastavormig product dat door droging uithardt tot een niet elastische afdichting die bestand is tegen hoge temperaturen.

Voordelen

- Bestand tegen hoge temperaturen tot 1200 °C
- Lijmen en voegen van vuurvaste stenen

Applicaties

Zwaluw Fire Sealant 1200 °C is ontwikkeld voor het afdichten van aansluitvoegen in kachels, open haarden en ovens. Fire Sealant 1200 °C is een verhardend, niet elastisch product geschikt voor toepassingen waar geen beweging optreedt.

Gebruiksaanwijzing

Bij de eerste blootstelling aan hoge temperaturen wordt geadviseerd om de temperatuur geleidelijk op te voeren. Eventueel nog aanwezig vocht in de Fire Sealant 1200 °C kan tot blaasvorming leiden.

Aanvullende informatie

Applicatie temperatuur	+ 5 °C to + 40 °C
Basis	Sodium Silicate
Dichtheid	2,0 g/ml
Temperatuur bestendigheid	+ 1200 °C
Uithardingstijd	1 - 4 days
Vorstbestendigheid gedurende transport	Up to - 15 °C

Deze waarden zijn typische eigenschappen en kunnen variëren van +/- 3%

Beperkingen

- Niet geschikt voor PE, PP, PC, PMMA, PTFE, zachte kunststoffen, neopreen en bitumineuze ondergronden
- Niet geschikt voor continue waterbelasting

Oppervlakte voorbereiding en afwerking

Aanbrengtemperatuur: + 5 °C tot + 40 °C (geldt voor omgeving en ondergronden). Ondergronden dienen schoon, droog, vet- en stofvrij en draagkrachtig te zijn. Ondergronden goed ontvetten met Zwaluw Cleaner. Bijzonder poreuze ondergronden dienen licht bevochtigd te worden. Ondergronden vooraf altijd testen op hechting. Glad afwerkbaar met Zwaluw Finisher.

Schoonmaken

Vers materiaal en gereedschap kunnen worden gereinigd met behulp van Zwaluw Cleaner. Uitgehارد materiaal kan alleen mechanisch worden verwijderd. Handen kunnen worden gereinigd met Zwaluw Wipes.

Kleur(en)

- Zwart

Verpakking

- Koker

Voor productspecificaties, raadpleeg de Product Detail Pagina



Den Braven Benelux B.V.
Denariusstraat 11, 4903 RC Oosterhout
+31 (0) 162491000 info@denbraven.nl

28-06-2018 13:44:01 UTC



Den Braven

Technische Datasheet



Zwaluw Fire Sealant 1200°C

Hittebestendige pasta

Houdbaarheid

In ongeopende originele verpakking, tussen + 5°C en + 25°C, tot 9 maanden houdbaar na productiedatum mits bewaard op een droge plaats.

Gezondheid & Veiligheid

Het productveiligheidsblad dient te worden gelezen en begrepen voor gebruik. Productveiligheidsbladen zijn beschikbaar op aanvraag en via de Den Braven websites.

Waarborg & Garantie

Den Braven garandeert dat haar product, binnen de houdbaarheidstijd, in overeenstemming is met de specificaties.

Disclaimer

Alle informatie in dit document en in al onze gedrukte en digitale publicaties is gebaseerd op onze huidige kennis en ervaring en is het uitsluitend (intellectuele) eigendom van Den Braven. Het document (en de daarin vervatte vinding (en)) mag uitsluitend met de uitdrukkelijke schriftelijke toestemming van Den Braven worden gekopieerd, aangedaan getoond of op andere wijze worden vervelvuldigd, openbaregemaakt en/of gebruikt. De technische gegevens in dit document worden gegeven bij wijze van indicatie en zijn niet uitputtend. Den Braven is niet aansprakelijk voor enige (directe of indirecte) schade als gevolg van eventuele (redactionele) fouten, onvolledigheden of onjuistheden in de inhoud van dit document. Daaronder wordt mede verstaan, maar is niet beperkt tot, onjuistheden of onvolledigheden die het gevolg zijn van technologische veranderingen of onderzoek tussen de datum van publicatie van dit document en de datum waarop het product wordt verkregen. Den Braven behoudt zich het recht voor om wijzigingen aan te brengen in formuleringen. Den Braven is niet aansprakelijk voor enige (directe of indirecte) schade als gevolg van het gebruik van het in dit document weergegeven product. Voor het aanbrengen en gebruiken van het product dient de gebruiker de informatie van dit document en andere documenten met betrekking tot onze producten, te lezen en te begrijpen. De gebruiker is verantwoordelijk voor het uitvoeren van alle nodige tests om er zeker van te zijn dat het product geschikt is voor de wijze van toepassing. Wij hebben geen invloed op de wijze van aanbrengen van het product en de omstandigheden tijdens opslag en



Den Braven Benelux B.V.
Denariusstraat 11, 4903 RC Oosterhout
+31 (0) 162491000 info@denbraven.nl

28-06-2018 13:44:01 UTC

C.9. Saffil M-Fil data sheet



SAFFIL M-FIL PRODUCT DATA SHEET



Introduction

M-FIL blanket is formed from high temperature MULLITE fibres. It has been specifically designed for demanding applications and has a classification temperature of 1600°C. M-FIL blanket utilises an innovative stitching/self needling process, which produces a product with significantly improved gas erosion characteristics.

These and other properties make M-FIL suitable for the most demanding high-end insulation applications.

Health and Safety

Mullite fibres are not subject to European legislation 97-69EC. M-FIL has been designed and made to give not only a narrow band of fibre diameter distribution but also does not form crystobalite when exposed to high temperatures.

Properties and Benefits

M-FIL blanket exhibits all the benefits associated with SAFFIL products. It's lightweight, low thermal mass properties enables it to cope with the most demanding industrial insulation applications.

Thermal conductivity

Controlled fibre diameter and low-shot has a direct bearing on thermal conductivity of fibre products. M-FIL is a significantly better insulator than other fibres by up to 50% in some cases. M-FIL is increasingly being used as fuel costs escalate and cost saving solutions are required. M-FIL more than meets these needs by cost effectively providing a stable, long lasting thermal barrier.

Chemical Resistance

M-FIL shows a good resistance to chemical attack and shows very good resistance to alkali and low Ph.

Thermal Shock Resistance.

The low heat storage and fibrous structure avoid the problems normally caused by thermal shock. Faster cycle times are possible that offer advantages in the form of reduced fuel consumption and increased capacity.

Typical Applications.

M-FIL blanket can be used in most module configurations. Modules can be supplied to any specification and anchoring systems installed / designed to your specific requirements.

M-FIL blanket is flexible and resilient and can be used for expansion gaps, seals and thermal backing in kilns.



SAFFIL

M-FIL - Technical Data

Classification Temperature	°C	1600		
Properties measured at ambient (23°C / 50% RH)				
Colour		White		
Solubility in water		Insoluble		
Odour		Odourless		
Fibre diameter (median)	Micron	3.0 - 3.5		
Shot content (Non fibrous material)		negligible		
Tensile Strength	kPa	38		
Bulk Density	g/cm³	0.1		
Properties when exposed to high temperature				
Melting Point	°C	2000		
Thermal Conductivity				
Temp	800	1000		
W/mK	0.22	0.30		
	1200	0.41		
	1400	0.54		
Standard Availability				
Rolls (Nominal)	Density (Kg/m³)	Length (mm)	Width (mm)	Thickness (mm)
	100	7200	620	25

Standard Packaging:- M-FIL is supplied in rolls packed in cardboard cartons (570 x 570 x 670mm)

The values given herein are typical average values obtained in accordance with accepted testing methods and are subject to normal manufacturing variations. They are supplied as a technical service and are subject to change without notice.

Head Office Address

SAFFIL Ltd
 Pilkington Sullivan Site,
 Tanhouse Lane,
 Widnes,
 Cheshire.
 WA8 0RY
 UK

Tel + 44 (0) 151 422 6700
 Fax + 44 (0) 151 422 6701
 Web <http://www.saffil.com>



D

PDT tabular results

Below, the tabulated temperature data for the PDT simulations in Section 3.3 is shown.

Table D.1: PDT case 1 RAC temperatures as a function of time.

Time [min]	Temp RAC [K]	Time [min]	Temp RAC [K]	Time [min]	Temp RAC [K]
0.00	298.15	24.00	350.16	48.00	301.41
0.50	322.08	24.50	346.49	48.50	301.26
1.00	344.15	25.00	343.13	49.00	301.12
1.50	364.23	25.50	340.04	49.50	300.98
2.00	382.37	26.00	337.20	50.00	300.85
2.50	398.62	26.50	334.59	50.50	300.73
3.00	413.11	27.00	332.19	51.00	300.61
3.50	425.95	27.50	329.97	51.50	300.50
4.00	437.26	28.00	327.92	52.00	300.40
4.50	447.20	28.50	326.02	52.50	300.30
5.00	455.88	29.00	324.26	53.00	300.21
5.50	463.43	29.50	322.64	53.50	300.12
6.00	469.99	30.00	321.13	54.00	300.03
6.50	475.67	30.50	319.73	54.50	299.95
7.00	480.57	31.00	318.42	55.00	299.87
7.50	484.78	31.50	317.21	55.50	299.80
8.00	488.40	32.00	316.08	56.00	299.73
8.50	491.51	32.50	315.03	56.50	299.66
9.00	494.17	33.00	314.05	57.00	299.60
9.50	496.45	33.50	313.14	57.50	299.53
10.00	498.40	34.00	312.28	58.00	299.48
10.50	500.05	34.50	311.49	58.50	299.42
11.00	501.47	35.00	310.74	59.00	299.37
11.50	502.68	35.50	310.04	59.50	299.32
12.00	503.70	36.00	309.39	60.00	299.27
12.50	504.58	36.50	308.77	60.50	299.22
13.00	505.32	37.00	308.20	61.00	299.18
13.50	505.95	37.50	307.66	61.50	299.14
14.00	506.49	38.00	307.15	62.00	299.10
14.50	506.95	38.50	306.68	62.50	299.06
15.00	507.34	39.00	306.23	63.00	299.02
15.50	507.67	39.50	305.81	63.50	298.99
16.00	507.95	40.00	305.41	64.00	298.96
16.50	486.60	40.50	305.04	64.50	298.92
17.00	468.18	41.00	304.69	65.00	298.89
17.50	452.13	41.50	304.36	65.50	298.86
18.00	438.05	42.00	304.05	66.00	298.84
18.50	425.63	42.50	303.75	66.50	298.81
19.00	414.60	43.00	303.47	67.00	298.78
19.50	404.76	43.50	303.21	67.50	298.76
20.00	395.96	44.00	302.96	68.00	298.74
20.50	388.06	44.50	302.73	68.50	298.71
21.00	380.94	45.00	302.51	69.00	298.69
21.50	374.50	45.50	302.30	69.50	298.67
22.00	368.67	46.00	302.10		
22.50	363.38	46.50	301.92		
23.00	358.56	47.00	301.74		
23.50	354.17	47.50	301.57		

Table D.2: PDT case 2 RAC temperatures as a function of time.

Time [min]	Temp RAC [K]						
0.00	298.15	30.00	594.84	60.00	333.33	90.00	303.87
0.50	322.42	30.50	582.41	60.50	332.22	90.50	303.70
1.00	345.71	31.00	570.65	61.00	331.16	91.00	303.55
1.50	368.02	31.50	559.51	61.50	330.13	91.50	303.39
2.00	389.35	32.00	548.95	62.00	329.13	92.00	303.24
2.50	409.74	32.50	538.92	62.50	328.16	92.50	303.10
3.00	429.19	33.00	529.40	63.00	327.23	93.00	302.96
3.50	447.73	33.50	520.33	63.50	326.33	93.50	302.82
4.00	465.38	34.00	511.70	64.00	325.46	94.00	302.69
4.50	482.16	34.50	503.48	64.50	324.62	94.50	302.56
5.00	498.11	35.00	495.64	65.00	323.80	95.00	302.44
5.50	513.24	35.50	488.15	65.50	323.01	95.50	302.32
6.00	527.57	36.00	481.00	66.00	322.25	96.00	302.20
6.50	541.14	36.50	474.18	66.50	321.51	96.50	302.08
7.00	553.97	37.00	467.65	67.00	320.80	97.00	301.97
7.50	566.09	37.50	461.40	67.50	320.11	97.50	301.87
8.00	577.52	38.00	455.42	68.00	319.44	98.00	301.76
8.50	588.29	38.50	449.69	68.50	318.79	98.50	301.66
9.00	598.42	39.00	444.21	69.00	318.16	99.00	301.56
9.50	607.95	39.50	438.95	69.50	317.56	99.50	301.47
10.00	616.89	40.00	433.91	70.00	316.97	100.00	301.37
10.50	625.28	40.50	429.08	70.50	316.40	100.50	301.28
11.00	633.15	41.00	424.43	71.00	315.85	101.00	301.20
11.50	640.51	41.50	419.98	71.50	315.32	101.50	301.11
12.00	647.40	42.00	415.70	72.00	314.80	102.00	301.03
12.50	653.84	42.50	411.60	72.50	314.30	102.50	300.95
13.00	659.85	43.00	407.65	73.00	313.82	103.00	300.87
13.50	665.46	43.50	403.85	73.50	313.35	103.50	300.80
14.00	670.70	44.00	400.21	74.00	312.90	104.00	300.72
14.50	675.57	44.50	396.70	74.50	312.46	104.50	300.65
15.00	680.11	45.00	393.33	75.00	312.03	105.00	300.58
15.50	684.33	45.50	390.08	75.50	311.62	105.50	300.52
16.00	688.26	46.00	386.96	76.00	311.22	106.00	300.45
16.50	691.92	46.50	383.95	76.50	310.83	106.50	300.39
17.00	695.31	47.00	381.06	77.00	310.45	107.00	300.33
17.50	698.46	47.50	378.27	77.50	310.09	107.50	300.27
18.00	701.38	48.00	375.58	78.00	309.74	108.00	300.21
18.50	704.10	48.50	373.00	78.50	309.40	108.50	300.15
19.00	706.61	49.00	370.51	79.00	309.07	109.00	300.10
19.50	708.95	49.50	368.11	79.50	308.75	109.50	300.04
20.00	711.11	50.00	365.79	80.00	308.43	110.00	299.99
20.50	713.11	50.50	363.56	80.50	308.13	110.50	299.94
21.00	714.97	51.00	361.41	81.00	307.84	111.00	299.89
21.50	716.68	51.50	359.34	81.50	307.56	111.50	299.84
22.00	718.27	52.00	357.33	82.00	307.28	112.00	299.80
22.50	719.75	52.50	355.41	82.50	307.02	112.50	299.75
23.00	721.11	53.00	353.54	83.00	306.76	113.00	299.71
23.50	722.37	53.50	351.75	83.50	306.51	113.50	299.67
24.00	723.53	54.00	350.01	84.00	306.27	114.00	299.63
24.50	724.61	54.50	348.34	84.50	306.03	114.50	299.59
25.00	725.61	55.00	346.73	85.00	305.80	115.00	299.55
25.50	726.53	55.50	345.17	85.50	305.58	115.50	299.51
26.00	727.38	56.00	343.66	86.00	305.37	116.00	299.47
26.50	706.66	56.50	342.21	86.50	305.16	116.50	299.44
27.00	687.38	57.00	340.80	87.00	304.96	117.00	299.40
27.50	669.39	57.50	339.45	87.50	304.76	117.50	299.37
28.00	652.56	58.00	338.14	88.00	304.57	118.00	299.34
28.50	636.78	58.50	336.87	88.50	304.39	118.50	299.30
29.00	621.96	59.00	335.65	89.00	304.21	119.00	299.27
29.50	608.00	59.50	334.47	89.50	304.04	119.50	299.24

Table D.3: PDT case 3 RAC temperatures and propellant temperatures as a function of time.

Time [min]	Temp RAC [K]	Temp prop [K]	Time [min]	Temp RAC [K]	Temp prop [K]	Time [min]	Temp RAC [K]	Temp prop [K]	Time [min]	Temp RAC [K]	Temp prop [K]
0.00	298.15	298.15	30.00	494.09	493.75	60.00	492.30	298.15	90.00	394.02	392.76
0.50	316.37	298.15	30.50	491.22	490.87	60.50	478.33	475.01	90.50	391.81	390.57
1.00	333.91	298.15	31.00	488.65	488.29	61.00	466.63	463.40	91.00	390.03	388.81
1.50	350.75	298.15	31.50	486.37	486.00	61.50	456.80	453.67	91.50	388.60	387.39
2.00	366.92	298.15	32.00	484.33	483.95	62.00	448.56	445.51	92.00	387.46	386.26
2.50	382.40	298.15	32.50	482.51	482.13	62.50	441.63	438.66	92.50	386.53	385.34
3.00	397.24	298.15	33.00	480.88	480.50	63.00	435.82	432.91	93.00	385.79	384.61
3.50	411.42	298.15	33.50	490.43	298.15	63.50	430.94	428.09	93.50	385.20	384.01
4.00	424.98	298.15	34.00	500.27	298.15	64.00	426.84	424.04	94.00	384.72	383.54
4.50	437.93	298.15	34.50	509.62	298.15	64.50	423.39	420.63	94.50	384.33	383.16
5.00	450.29	298.15	35.00	518.50	298.15	65.00	420.50	417.77	95.00	384.02	382.85
5.50	462.07	298.15	35.50	508.57	507.48	65.50	418.07	415.37	95.50	367.48	367.03
6.00	473.29	298.15	36.00	499.92	498.81	66.00	416.03	413.36	96.00	354.11	353.76
6.50	483.98	298.15	36.50	492.37	491.25	66.50	414.31	411.66	96.50	352.30	298.15
7.00	494.14	298.15	37.00	485.77	484.64	67.00	412.87	410.24	97.00	350.54	298.15
7.50	503.80	298.15	37.50	480.01	478.88	67.50	411.66	409.04	97.50	348.85	298.15
8.00	512.97	298.15	38.00	474.98	473.84	68.00	410.64	408.04	98.00	347.22	298.15
8.50	521.67	298.15	38.50	470.58	469.44	68.50	409.78	407.20	98.50	345.64	298.15
9.00	529.93	298.15	39.00	466.74	465.59	69.00	409.06	406.49	99.00	344.12	298.15
9.50	537.75	298.15	39.50	463.38	462.23	69.50	408.46	405.89	99.50	342.65	298.15
10.00	545.16	298.15	40.00	460.44	459.29	70.00	407.95	405.39	100.00	341.23	298.15
10.50	552.17	298.15	40.50	457.86	456.71	70.50	407.53	404.97	100.50	339.86	298.15
11.00	558.79	298.15	41.00	455.61	454.46	71.00	407.17	404.62	101.00	338.54	298.15
11.50	565.06	298.15	41.50	453.65	452.49	71.50	420.92	298.15	101.50	337.26	298.15
12.00	570.97	298.15	42.00	451.92	450.77	72.00	434.05	298.15	102.00	336.02	298.15
12.50	576.55	298.15	42.50	450.42	449.26	72.50	446.59	298.15	102.50	334.83	298.15
13.00	581.82	298.15	43.00	449.10	447.95	73.00	458.54	298.15	103.00	333.67	298.15
13.50	586.79	298.15	43.50	447.94	446.79	73.50	446.84	444.53	103.50	332.56	298.15
14.00	591.47	298.15	44.00	446.93	445.78	74.00	437.22	435.06	104.00	331.48	298.15
14.50	595.87	298.15	44.50	458.87	298.15	74.50	429.30	427.26	104.50	330.44	298.15
15.00	600.02	298.15	45.00	470.25	298.15	75.00	422.78	420.84	105.00	329.43	298.15
15.50	603.92	298.15	45.50	481.08	298.15	75.50	417.42	415.56	105.50	328.46	298.15
16.00	607.59	298.15	46.00	491.38	298.15	76.00	413.01	411.21	106.00	327.52	298.15
16.50	611.05	298.15	46.50	481.17	478.98	76.50	409.38	407.63	106.50	326.61	298.15
17.00	614.29	298.15	47.00	472.44	470.27	77.00	406.40	404.69	107.00	325.73	298.15
17.50	617.33	298.15	47.50	464.96	462.82	77.50	403.95	402.27	107.50	324.87	298.15
18.00	620.20	298.15	48.00	458.55	456.44	78.00	401.93	400.28	108.00	324.05	298.15
18.50	622.88	298.15	48.50	453.07	450.97	78.50	400.27	398.64	108.50	323.25	298.15
19.00	625.40	298.15	49.00	448.36	446.29	79.00	398.90	397.29	109.00	322.48	298.15
19.50	627.76	298.15	49.50	444.33	442.28	79.50	397.78	396.19	109.50	321.74	298.15
20.00	629.98	298.15	50.00	440.88	438.85	80.00	396.86	395.27	110.00	321.02	298.15
20.50	632.06	298.15	50.50	437.92	435.90	80.50	396.10	394.53	110.50	320.32	298.15
21.00	634.01	298.15	51.00	435.38	433.38	81.00	395.48	393.91	111.00	319.64	298.15
21.50	635.84	298.15	51.50	433.20	431.22	81.50	394.96	393.40	111.50	318.99	298.15
22.00	637.55	298.15	52.00	431.34	429.36	82.00	394.54	392.99	112.00	318.35	298.15
22.50	618.42	618.57	52.50	429.74	427.77	82.50	394.20	392.64	112.50	317.74	298.15
23.00	601.56	601.64	53.00	428.37	426.41	83.00	393.91	392.36	113.00	317.15	298.15
23.50	586.67	586.68	53.50	427.19	425.24	83.50	393.68	392.13	113.50	316.57	298.15
24.00	573.50	573.45	54.00	426.18	424.23	84.00	393.48	391.94	114.00	316.02	298.15
24.50	561.82	561.73	54.50	425.32	423.37	84.50	407.83	298.15	114.50	315.48	298.15
25.00	551.47	551.34	55.00	424.57	422.64	85.00	421.55	298.15	115.00	314.96	298.15
25.50	542.29	542.12	55.50	423.94	422.00	85.50	434.66	298.15	115.50	314.45	298.15
26.00	534.12	533.93	56.00	423.39	421.46	86.00	447.16	298.15	116.00	313.97	298.15
26.50	526.87	526.64	56.50	422.92	420.99	86.50	434.57	432.94	116.50	313.49	298.15
27.00	520.41	520.16	57.00	422.52	420.60	87.00	424.43	422.90	117.00	313.03	298.15
27.50	514.67	514.40	57.50	435.58	298.15	87.50	416.27	414.82	117.50	312.59	298.15
28.00	509.55	509.26	58.00	448.05	298.15	88.00	409.71	408.32	118.00	312.16	298.15
28.50	504.99	504.69	58.50	459.93	298.15	88.50	404.43	403.08	118.50	311.74	298.15
29.00	500.93	500.62	59.00	471.26	298.15	89.00	400.18	398.87	119.00	311.34	298.15
29.50	497.32	496.99	59.50	482.04	298.15	89.50	396.76	395.49	119.50	310.95	298.15